FUNDAMENTAL STUDY OF THE DESIGN AND DEVELOPMENT OF IRON BASED ALLOYS FOR BIODEGRADABLE IMPLANT DEVICE APPLICATION

by

Sung Jae Chung

B.S. in Materials Science and Engineering, Hanyang University, 2002

M.S. in Materials Science and Engineering, Hanyang University, 2004

Submitted to the Graduate Faculty of

the Swanson School of Engineering in partial fulfillment

of the requirements for the degree of

Doctor of Philosophy

University of Pittsburgh

2016

UNIVERSITY OF PITTSBURGH

SWANSON SCHOOL OF ENGINEERING

This dissertation was presented

by

Sung Jae Chung

It was defended on

July 6, 2016

and approved by

Ian Nettleship, Ph.D., Associate Professor, Department of Mechanical Engineering and Materials Science, University of Pittsburgh

John A. Barnard, Ph.D., Professor, Department of Mechanical Engineering and Materials Science, University of Pittsburgh

Jung-Kun Lee, Ph.D., Associate Professor, Department of Mechanical Engineering and Materials Science, University of Pittsburgh

Arif Sirinterlikci, Ph.D., Professor, Department of Engineering, Robert Morris University

Dissertation Director: Prashant N. Kumta, Ph.D., Edward R. Weidlein Chair Professor, Department of Mechanical Engineering and Materials Science, Bioengineering, Chemical and Petroleum Engineering, University of Pittsburgh

FUNDAMENTAL STUDY OF THE DESIGN AND DEVELOPMENT OF IRON-BASED ALLOYS FOR BIODEGRADABLE IMPLANT DEVICE APPLICATION

Sung Jae Chung, PhD

University of Pittsburgh, 2016

Biodegradable metals have been widely studied in recent years as potential biomedical implant materials which exhibit higher mechanical properties than degradable polymers while corroding over time to alleviate known complications such as stress-shielding, infection, permanent physical irritation and secondary removal/revision surgeries that is inherent to permanent and bio-inert metallic biomaterials. Specifically, iron (Fe), magnesium (Mg), and their alloys are the two main classes of metals that have been considered as promising candidates for degradable load and non-load bearing bone implants, cardiovascular stents, and other implantable medical devices. However, most of the research on Fe and Fe based alloys have reported very slow degradation rate in physiological environments while Mg and Mg based alloys under rapid degradation. Hence, controlling the degradation rates of these metals has been a key challenge limiting the technological development and implementation of these systems requiring more fundamental studies to be conducted. There is therefore the need to modify the chemical composition and microstructural characteristics through the appropriate alloying techniques with suitable alloying elements. Some studies have been conducted to overcome these limitations but the degradation rates and cytocompatibility of the two main classes of metals are still far from levels necessary for implementation in clinical applications. An alternative approach is therefore needed to develp metallic materials with improved degradation behavior wihle maintaining ithe

desired biocompatibility. Although Fe and Mg have been studied separately as degradable implants, there are no reports on the Fe-Mg binary alloy system for use as biodegradable metallic materilas because of the thermodynamic immiscibility of Fe and Mg under ambient conditions. In this dissertation, novel non-equilibrium alloys, particularly in the Fe-Mg binary system with additional elements, have been proposed and studied for their desirable corrosion and cytocompatible properties.

The first part of this dissertation focuses on the formation of amorphous alloys in the Fe-Mg binary alloy system through the process of high energy mechanical alloying (HEMA) followed by pulsed laser deposition (PLD) in order to overcome the limitations of the immiscibility of Fe-Mg. In the second part of this dissertation, an alloy development strategy to accomplish high degradation rates, antiferromagnetic behavior and good cytocompatibility is presented. Thus, manganese (Mn), calcium (Ca) and zirconium (Zr) were selected and added as alloying elements, which include the following two aspects: (i) Electrochemical considerations to increase the corrosion rates by electrochemical modification of the Fe matrix; (ii) addition of Mn to introduce anti-ferromagnetic characteristics to the alloy for exploring biological applications.

Powders and thin layers were characterized for their composition/structure and evaluated potential for biomedical applications using preliminary in vitro cytocompatibility and corrosion experiments. For Fe-Mg binary alloy, uniform corrosion of $Fe_{70}Mg_{30}$ amorphous thin layer was observed and the corrosion current density value was approximately 8 fold higher than pure Fe. The direct and indirect cytotoxicity results indicated that $Fe_{70}Mg_{30}$ amorphous thin layer has no cytotoxicity to MC3T3-E1, hMSCs, HUVECs and NIH3T3 cell lines. Similarly, addition of Ca, Zr and Mn indicate good cytocompatibility with suitable modifications in the corrosion rates

TABLE OF CONTENTS

LIST OF TABLES

LIST OF FIGURES

PREFACE

To my parents, wife, children and family:

Hayoon & Jinsoon, Kanghwi & Bongsim, Hyeyeon, Lynn, Charlotte & Nathan, Youjung, Kyungjae & Seoyoung

Whose love and support for me have shaped me into the person I am today

Firstly, I thank God for giving me strength and wisdom to get through all the hurdles during my graduate studies in the United States.

I would like to express my heartfelt gratitude to my advisor, Prof. Kumta, for his continuous support, encouragement and valuable suggestions that played a vital role during my research studies and it has been an honor being his student. His knowledge, insights and enthusiasm in doing research is something that I always look up to and hope to follow in my life.

I would also like to thank the rest of my PhD thesis committee – Dr. Ian Nettleship, Dr. John A. Barnard, Dr. Jung-Kun Lee, and Dr. Arif Sirinterlikci, for their insight and advice ever since the start of my PhD. I learned a great deal with each collaboration and interaction we shared.

Special thanks to Boeun Lee, Drs. Abhijit Roy, Daeho Hong, Nicole Ostrowski and Da-Tren Chou for their constant support and guidance as great co-workers/friends throughout my Ph.D. I would further like to extend my thanks to all the post-docs, graduate students, technicians and administrative assistants in Prof. Kumta's group for their support, camaraderie and making

the lab a great place to work. I am grateful to all my friends who have made my life cheerful and memorable at Pittsburgh.

Pittsburgh has been my hometown in the United State as I had all children and spent the longest time in this city. With all good memories that I had in Pittsburgh, I look forward to a new beginning of my career.

1.0 INTRODUCTION

1.1 BIODEGRADABLE METALS

During the past few years significant advances have been made in the development of biodegradable metallic materials for biomedical applications, such as temporary prostheses, cadivascular stents, and three-dimensional porous structures such as scaffolds for tissue engineering [1-7].

1.1.1 Classical biomaterials

Biomaterials are used to make devices to replace a part or a function of the body and it has had a long history of clinical employment [8]. Initially, the most important biomaterial was metal for the skeletal applications including wires and pins made from iron (Fe), gold (Au), silver (Ag) and platinum (Pt) [9]. These early metal devices were used to fix bone fractures [10]. Subsequently, the evolution of medical implants was closely linked to the development of new materials. In the 1930s, stainless steels and cobalt-chromium alloys were introduced and these metallic “bio-inert” alloys are associated with permanent applications such as bone fixation devices and joint replacements [9]. Metal has excellent combination of strength, stiffness and ductility, which are superior to that of polymers or ceramics at the site of high mechanical loading. Therefore, they are used for the clinical employment as implants in the treatment of

temporary clinical problems, which are mainly includes two applications. One area is the prosthesis such as a tooth, a facial bone, the palate, hip, or knee, and another is the fixation of structures such as screws, plates, wires, intramedullary nails and stents [2, 3, 11-13]. Their high strength guarantees good primary stability after surgery, and their fracture toughness, ductility and high fatigue limit are also beneficial in applications.

Table 1.1. Commonly used biomaterials for biomedical applications [9].

Material	**Advantages**	**Disadvantages**	**Examples**
Metals	Strong Tough Ductile	Corrosion Density Processing	Joint replacement Dental roots Orthopedic fixation Stents
Polymers	Resilient Easy to fabricate	Not strong Not rigid Time-dependent deformation (creep: stress relaxation) Degradation	Dental implant Blood vessels (e.g. vascular grafts) Joint socket (knee, shoulder) Ear, nose Soft tissues in general
Ceramics	Biocompatible Inert Strong in compression	Brittle- fractures easily in tension	Dental implants Orthopedic implants (some)
Composites	Strong Tailor made	Processing	Joint implant Heart valves

At present, not only metals but all classes of materials, which includes ceramics, polymers and composites, are used as biomaterials for various purposes. Table 1.1 lists the various applications and their advantages and disadvantages in the human body [9]. However, as the medical science has advanced to fulfil the demand for better implant devices, it is desirable that implantable medical devices also possess bioactivities or bio-functionalities such as blood compatibility and bone conductivity [14]. Each material is selected and deployed for its specific

advantages. For example, the hydroxyapatite coatings on dental implants provide excellent bone ingrowth and consequently stable long-term tissue integration despite poor mechanical strength [15] and for the need to modify surface of metals in order to improve blood compatibility with polyethylene terephthalate [16]. Recently many researchers continue to study about novel metallic biomaterials includes those composed of nontoxic and allergy free elements like Ni-free stainless steel [17].

Polymeric biomaterials offer the main advantage over metals or ceramics in processing to form various shapes. Basically, there are two kinds of these biomaterials: (i) classical inert polymers such as polymethylmethacrylate (PMMA), poly amide or nylon, polyethylene (PE), etc. and (ii) absorbable polymers such as polyglycolic acid (PGA) and polylactic acid (PLA), etc [14]. Besides being employed in their bulk, they are often made into thin layer or coating onto metal surfaces with tailored mechanical and physical properties. The recent development exploits absorbable polymers for use as drug delivery carriers loaded with a specific drug in the form of coating, for example drug eluting stents [14, 18].

Ceramics biomaterials provide inertness, high compressive strength and aesthetic appearance. They can be classified into: (i) inert bio-ceramics such as zirconia, alumina, aluminum nitrides and carbon, (ii) bioactive ceramics such as hydroxyapatite, bio-glass, etc. and (iii) biodegradable/ resorbable ceramics such as calcium aluminates, calcium phosphates, etc. The inherent surface qualities of ceramics have been exploited to make implants such as dental crowns. The high specific strength and blood compatibility of carbon makes carbon often used for heart valves leaflets. Many bio-ceramics have been also applied as coating onto metal surfaces including diamond like carbon, nitrides, bio-glasses and hydroxyapatites [19].

Composite biomaterials can be made with metals, polymers or ceramics as their matrix, and reinforced with one of these materials. Composites allow control over material properties where a combination of stiff, strong, resilient but lightweight can be achieved all together. Bone is a composite of the low elastic modulus organic matrix reinforced with the high elastic modulus mineral “fibers” permeated with pores filled with liquids. Other examples include orthopedic implants with porous structures, dental filler, and bone cement composed of reinforced PMMA and ultra-high molecular weight PE [20].

1.1.2 Concept for biodegradable metals

Traditionally, most metallic implants are developed from corrosion resistant materials such as stainless steels, titanium (Ti) and cobalt (Co)-chromium (Cr) based metallic “bio-inert” alloys. They are associated with permanent applications which includes joint replacements and stents. However, some implants must be removed when they are no longer needed, e.g. osteosynthesis plates and screws. Permanent implants are also accompanied by long-term risks and side effects. In cardiovascular stents, for example, these include permanent physical irritation, chronic inflammatory reactions, in-stent restenosis, and mismatches in mechanical behavior between stented and non-stented vessel areas [21-23]. Therefore, patients with these permanent implants suffer from these kinds of unavoidable short and long term clinical problems and additional pain and discomfort from implant removal or revision surgeries [24-26]. In many osteosynthesis applications, for example, the implant needs to be removed after one or two years and the patient has to undergo the pain of a second surgery and accept risks such as re-fracture, neurovascular injuries or even implant failure. From an economic point of view this also means considerable costs for health care systems and implant removal accounts for up to 30% of

orthopedic procedures [27]. Stainless steel or Co–Cr alloys contain allergens such as nickel (Ni), Co or Cr. Although these alloys possess high corrosion resistance, wear or unfavorable conditions in the area of metal to metal contact like screw heads on plates can increase the release of metal ions. This may stimulate sensitivity to the various metal components or allergic reactions, e.g. localized eczema near the implant site [28]. A prominent current example of permanent implant application is the coronary stent. This field is booming since the first attempts were conducted by Sigwart et al [29]. Stents are metallic wire meshes which by means of a balloon catheter are introduced into narrowed arteries to keep the lumen open. Although stents are successfully and widely deployed they do have some risks. Bare metal stents are associated with a 20~30% restenosis rate, which requires re-intervention [30]. Drug eluting stents were developed to minimize the risk of restenosis. However, there are indications that these stents present a higher risk of late thrombosis, which can lead to a heart attack or sometimes death [31]. It has also been observed that remodeling of the vessel occurs within a period of 6~12 months, meaning that after that period the supporting function of the stent is actually no longer required [32, 33]. For these reason, in a number of clinical applications a metal that degrades when no longer needed would be highly desirable to circumvent the disadvantage of permanent implant materials.

Biodegradable metals, on the other hand, degrade in vivo, either via hydrolytic reactions, resorption or electrochemical reactions [9]. In general, this can be described as the breakdown of a material mediated by a biological system [34], with appropriate host response elicited by released corrosion products, and then dissolve completely upon fulfilling the mission to assist with tissue healing with no implant residues [14]. This concept is similar with the context of polymeric materials and ceramics [9]. Recently, however, a concept of biodegradable metals has

been developed which questions the traditional paradigm that metallic biomaterials must be corrosion-resistant [35, 36]. Ideally biodegradable metals should feature a tradeoff between mechanical integrity and degradation. The temporary support should be maintained until healing is completed and hence the degradation progress must be tailored such that mechanical integrity does not deteriorate too fast [37]. In the case of bone fracture, the required time for hard bone union should be varied greatly depending on the configuration or location of fracture, soft tissues and patient characteristics [35]. Therefore, biodegradable metals use their corrosion properties as an advantage, flying in stark contrast to the convention of developing metals which are designed to be as inert as possible. This degradation must occur in a controlled manner so that while the implant is degrading and its strength diminishes, load is gradually transferred to the healing bone tissue until it completely disappears once the tissue has fully healed. This profile of gradual degradation and reduction in mechanical support from a high initial point is shown in Figure 1.1 [35].

In addition, the degradation progress may not cause any accumulation of degradation products around the implant or in systemic organs, and degradation products may not produce any adverse effects. In these respects, it is obvious that biodegradable metals can only be used in small, lightweight implants. Accordingly, research has mainly focused on the development of degradable stents or small screws or plates for osteosynthesis. Figure 1.2 gives an overview of the selected examples.

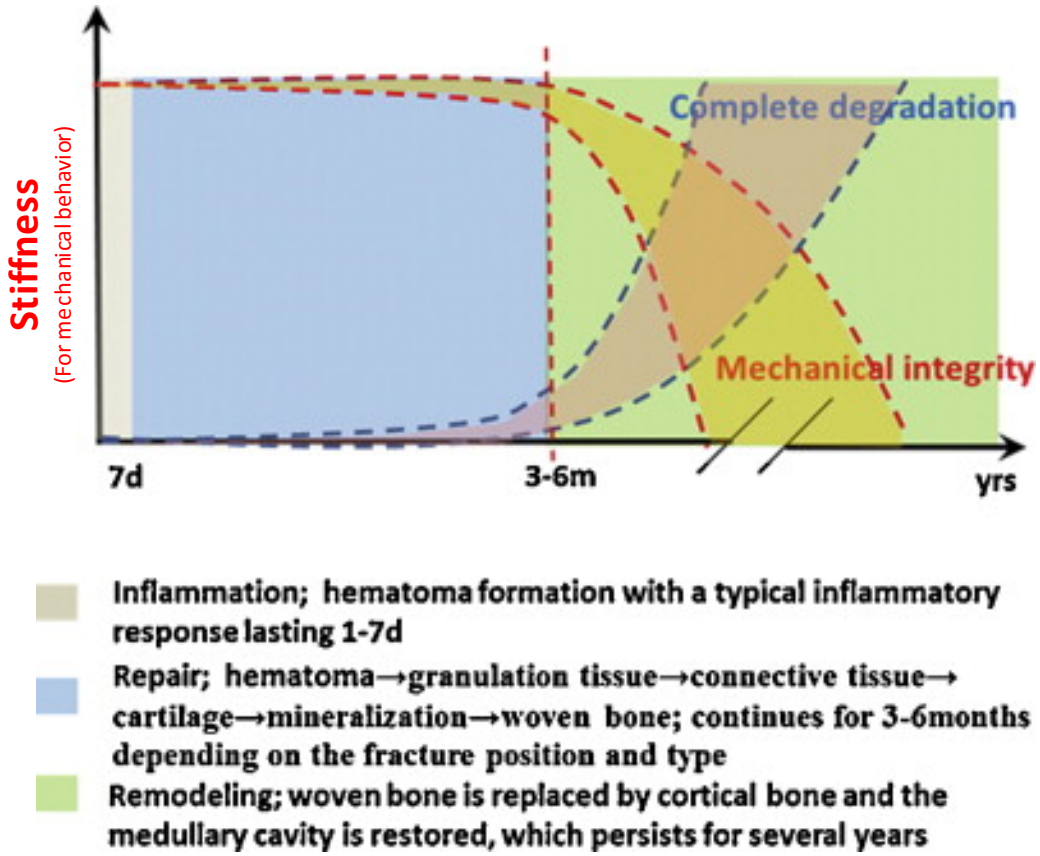

Figure 1.1. The schematic diagram of degradation behavior and the change of mechanical integrity of biodegradable metallic implants during the bone healing process. Used with permission of [35].

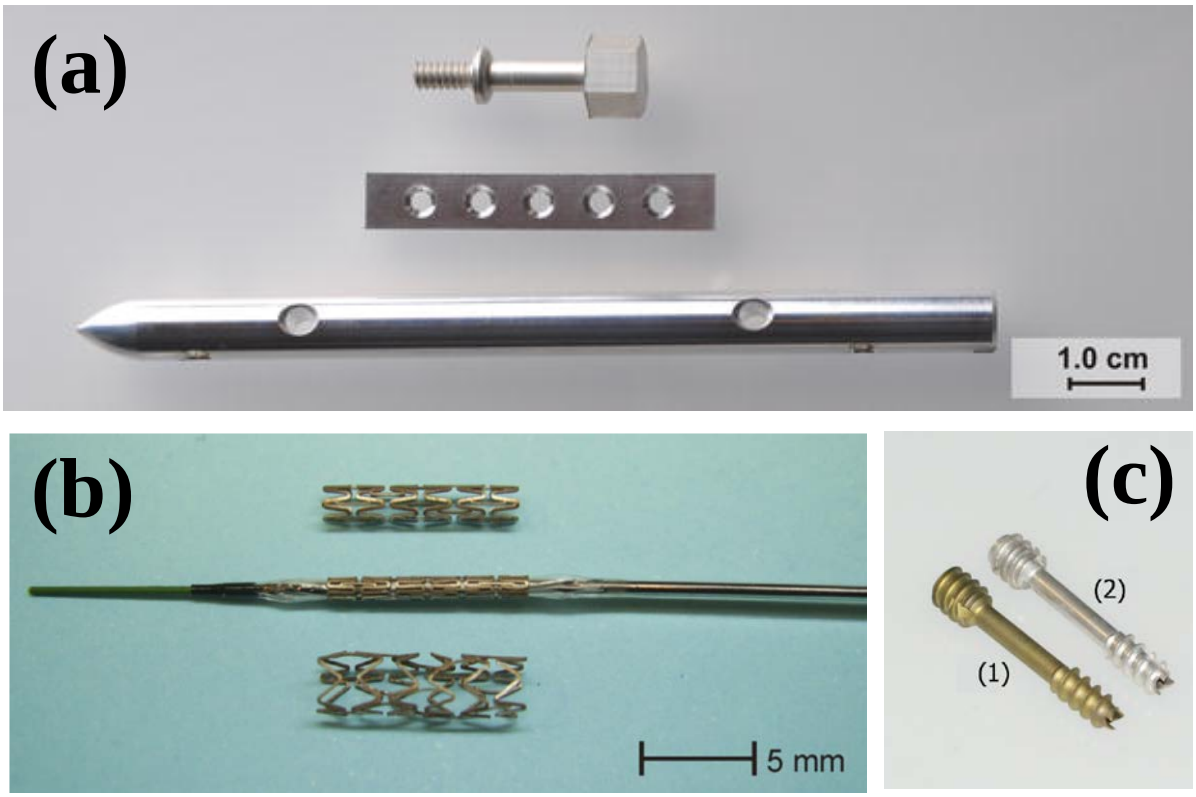

Figure 1.2. (a) different orthopedic implant geometries made of magnesium alloys. Used with permission of [38], (b) Fe-35Mn stents at three conditions: (up) as descaled, (middle) as crimped over balloon, and (bottom) as expanded [39] and (c) The two cannulated screws with the same design. 1) The titanium screw (Fracture compressing screw, Königsee Implantate GmbH, Am Sand 4, 07426 Allendorf, Germany), 2) MAGNEZIX® Compression Screw (Syntellix AG Schiffgraben 11, 30159 Hannover, Germany). Used with permission of [40].

1.2 IRON AND ITS ALLOYS AS BIODEGRADABLE METALS

Both polymeric and metallic materials possess the property profile required for the above-mentioned applications. Metals, however, are superior to polymers in mechanical performance [2, 3]. Among metals, Mg and Fe have both been considered for degradable implants because they are essential trace elements in the human body [7, 13, 21, 41-43]. On the other hand, superior mechanical properties of pure Fe or Fe-based alloys are more attractive as biodegradable implants compared to Mg-based alloys [35, 44].

1.2.1 General remarks

Fe has several vital functions in the body. It serves as a carrier of oxygen to the tissues from the lungs by red blood cell hemoglobin, as a transport medium for electrons within cells, and as an integrated part of important enzyme systems in various tissues [45]. The physiology of iron has been extensively reviewed [46]. Most of the iron in the body is present in the erythrocytes as hemoglobin, a molecule composed of four units, each containing one hemoglobin group and one protein chain [47]. The structure of hemoglobin allows it to be fully loaded with oxygen in the lungs and partially unloaded in the tissues (e.g. in the muscles). The iron-containing oxygen storage protein in the muscles, myoglobin, is similar in structure to hemoglobin but has only one hemoglobin unit and one globin chain [48]. Several iron-containing enzymes, the cytochromes, also have one hemoglobin group and one globin protein chain. These enzymes act as electron carriers within the cell and their structures do not permit reversible loading and unloading of oxygen. Their role in the oxidative metabolism is to transfer energy within the cell and specifically in the mitochondria [49]. Other key functions for the iron-containing enzymes

include the synthesis of steroid hormones and bile acids; detoxification of foreign substances in the liver; and signal controlling in some neurotransmitters, such as the dopamine and serotonin systems in the brain [46]. Fe is reversibly stored within the liver as ferritin and hemosiderin whereas it is transported between different compartments in the body by the protein transferrin [50].

The suitability of Fe as a degradable implant material has been studied in various *in vitro* and *in vivo* settings using variety of cells and animal models [13, 21, 26, 42, 43, 51-54]. In an initial *in vivo* study by Peuster et al. [21], stents produced from pure iron were implanted in the descending aorta of New Zealand white rabbits. The main findings were that no pronounced neointimal proliferation and no significant inflammatory response in the stented vessel occurred during the 18-month follow-up but the concentration of Fe ions in the body should not reach higher than 50μg/ml to avoid cell toxicity and death [54, 55]. A subsequent study over 12 months reported on the biocompatibility of Fe stents implanted in the descending aorta of mini pigs [42]. It was concluded that Fe is a suitable material for degradable stents and does not cause local or systemic toxicity. However, it was also concluded that its overall degradation rate is too low, and is not matched with the tissue healing period. It has become the major drawback to limit their further applications [42, 56].

Different degradation behavior between Fe and Mg depends on the oxygen availability. Generally, Fe is corroded in an oxygen absorption corrosion mode based on the following reactions:

$$Fe \rightarrow Fe^{2+} + 2e^{-} \text{ (anodic reaction)} \quad (1.1)$$

$$2H_2O + O_2 + 4e^{-} \rightarrow 4OH^{-} \text{ (cathodic reaction)} \quad (1.2)$$

$$2Fe + 2H_2O + O_2 \rightarrow 2Fe(OH)_2 \text{ (overall formation)} \quad (1.3)$$

The anodic partial reaction usually proceeds rapidly in media [57]. In oxygen-containing aqueous solutions in the pH-range between 4 and 10, the reduction of dissolved oxygen is the cathodic reaction. These conditions apply to most of the potential implantation sites in a living body. The reduction reaction (1.2) and, coupled to it, the oxidation reaction (1.1) proceed as rapidly as dissolved oxygen reached the metal surface [56]. The formation of Fe oxides has been identified as the major inhibitor for a faster degradation [58]. Additionally, other degradation products layers (Fe hydroxides, Fe carbonates and Fe phosphate), which are relatively denser than Fe oxide, greatly hinder transport of the oxygen toward the fresh Fe surface which would be necessary for further degradation [56, 59, 60] . Attempts to accelerate the degradation kinetic of Fe have been explored through alloying with other elements, thermomechanical treatment, surface modification, composites and novel/new fabrication methods [35, 61]. It will be introduced in the next section.

Moreover, there is another challenge to overcome limitations of Fe and Fe based alloy as biodegradable material. Its ferromagnetic characteristics that can seriously limit magnetic resonance imaging (MRI) capabilities of Fe based alloy. Therefore, ideal alloying elements should change this natural property to make Fe alloys compatible with high magnetic field that generated by MRI which has become widely used for post implantation monitoring and diagnostic [62].

1.2.2 Recent developments of biodegradable Fe-based alloys

In the field of biodegradable metals mainly Fe and Mg and their alloys have been investigated in a number of *in vitro* and *in vivo* studies [39, 63]. Both Fe and Mg are essential elements in the human body; adult men normally contain approximately 3~5g of Fe [45] and 21~28g of Mg -

muscle and soft tissues accounting for almost half of this and bone for slightly more than half [64]. Mg based alloys are well established as material for temporary implant applications, and have already undergone human clinical trials in the field of osteosynthesis [40] and in particular stent applications [65-67]. However, Mg based alloys are known to exhibit too rapid degradation rates in physiological environments.

In addition, hydrogen gas may be formed during the degradation process. This can generate gas cavities at the implantation side which can be problematic in healing [68]. Although Mg based alloys have been developed which have acceptable strength and ductility values, materials with better mechanical performance would also be strongly desirable. Compared with Mg based alloys, Fe based alloys have similar mechanical properties to stainless steel and are more attractive from a structural point of view which are summarized in Table 1.2.

In this respect, Fe and in particular its alloys have been proposed as a promising alternative [39, 63]. Fe based alloys possess superior mechanical properties compared to Mg, enabling versatile implant design and fabrication of filigree structures. Compared to Mg based alloys, Fe is also radio opaque, which in stents facilitates placement via coronary angioplasty. The main drawback of Fe in contrast to Mg, however, is its rather slow degradation rate in physiological media [39, 63]. Hence, research has focused on the development of new kinds of Fe based biodegradable materials by modifying the chemical composition, microstructure, and surface of Fe with diverse manufacturing process technologies including casting, powder metallurgy, electroforming, and 3D printing, to achieve a faster degradation and improved MRI compatibility, as illustrated in Figure 1.3. For example, powder metallurgy Fe–Mn alloy had a faster in vitro degradation compared to the same alloy produced by casting because of the powder metallurgy process porosity increasing the degradation rate.

Table 1.2. Summary of the properties of reported Fe-based biodegradable metals. Used with permission of [35].

Material		YS (MPa)	UTS (MPa)	Elongation (%)	χ_0 (μm3/kg)	Ref.
Pure Fe	Cast	–	–	–	–	
	Annealed (550 °C)	140 ± 10	205 ± 6	25.5 ± 3	–	[52]
	Electroformed	360 ± 9	423 ± 12	8.3 ± 2	–	[52]
	ECAPed (8 passes)	–	470 ± 29	–	–	[43]
	P/M	–	–	–	–	[69]
	SPS	–	–	–	–	[70]
Nitride Fe		561.4	614.4	–	–	[71]
Fe–10Mn/forged + ht2[a]		650	1300	14	–	[72]
Fe–10Mn–1Pd/forgerd + ht2[a]		850	1450	11	–	[72]
Fe–30Mn/cast		124.5	366.7	55.7	–	[73]
Fe–30Mn–6Si/cast		177.8	433.3	16.6	–	[73]
Fe–30Mn/forged		169	569	60	0.16	[74]
Fe–30Mn–1C/forged		373	1010	88	0.03	[74]
Fe–3Co/rolled[a]		460	648	5.5	–	[61]
Fe–3W/rolled[a]		465	712	6.2	–	[61]
Fe–3C/rolled[a]		440	600	7.4	–	[61]
Fe–3S/rolled[a]		440	810	8.3	–	[61]
Fe–20Mn/P/M		420	700	8	0.2	[75]
Fe–25Mn/P/M		360	720	5	0.2	[75]
Fe–30Mn/P/M		240	520	20	0.2	[75]
Fe–35Mn/P/M		230	430	30	0.2	[75]
Fe–0.6P/P/M		–	–	–	–	[69]
Fe–0.05B/P/M		–	–	–	–	[69]
Fe–5W/SPS		–	–	–	–	[70]
Fe–1CNT/SPS		–	–	–	–	[70]
316L SS		190	490	40	0.5	[75]

[a] The chemical composition was in atom percentage, while the others were in weight percentage.

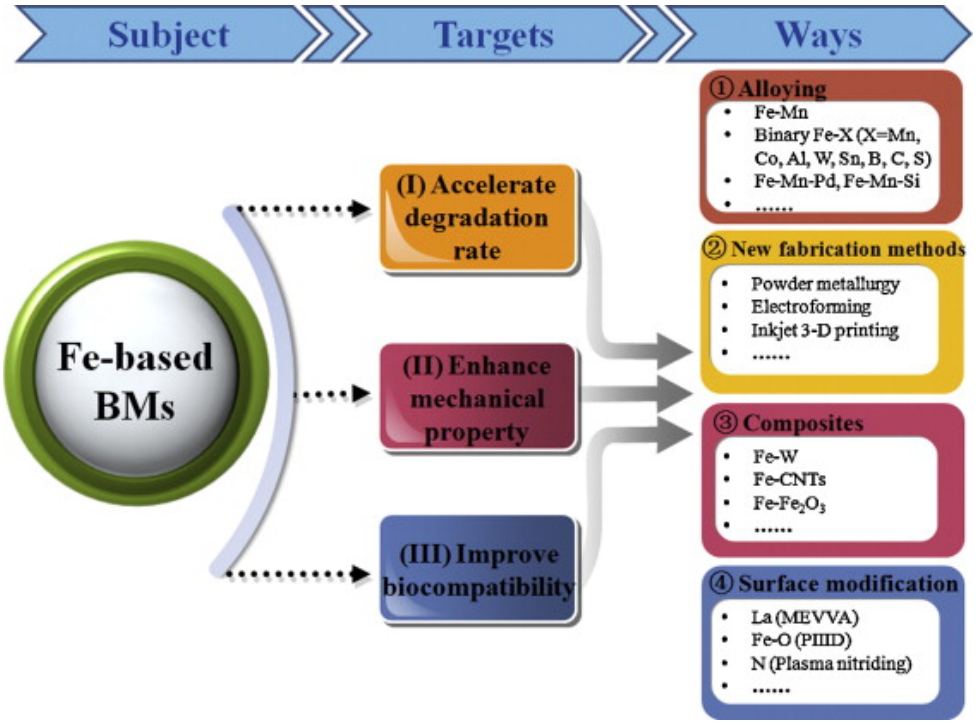

Figure 1.3. Status of present research on Fe-based biodegradable metals. Used with permission of [35].

In this respect, Fe and in particular its alloys have been proposed as a promising alternative [39, 63]. Fe based alloys possess superior mechanical properties compared to Mg, enabling versatile implant design and fabrication of filigree structures. Compared to Mg based alloys, Fe is also radio opaque, which in stents facilitates placement via coronary angioplasty. The main drawback of Fe in contrast to Mg, however, is its rather slow degradation rate in physiological media [39, 63]. Hence, research has focused on the development of new kinds of Fe based biodegradable materials by modifying the chemical composition, microstructure, and surface of Fe with diverse manufacturing process technologies including casting, powder metallurgy, electroforming, and 3D printing, to achieve a faster degradation and improved MRI compatibility, as illustrated in Figure 1.3. For example, powder metallurgy Fe–Mn alloy had a

faster in vitro degradation compared to the same alloy produced by casting because of the powder metallurgy process porosity increasing the degradation rate. Electroformed iron also showed a faster *in vitro* degradation compared to Armco® Fe fabricated by casting since the electroformed material had a much finer microstructure with increased volume of grain boundaries, which are more susceptible to corrosive attack [13]. Alloying, subsequent processing, and heat treatment are common approaches to modify the mechanical, corrosion, and ferromagnetic properties of pure Fe [58]. Table 1.3 gives an overview of the various strategies proposed.

First, for alloying, Hermawan et al.[7, 75] developed a Fe-Mn alloy containing 35wt.% Mn using powder metallurgy methods which have an increased corrosion rate with respect to pure iron [5] and these alloys, showed low inhibition of fibroblast cell metabolic activity in cell viability test. Fe-Mn-Pd alloys are also showed to reveal a degradation resistance that is one order of magnitude lower than observed for pure iron by Schinhammer et al. [72]. Xu et al. added 1 wt.% of carbon into Fe-30Mn alloy that showed lower magnetic susceptibility and better mechanical properties than Fe-30Mn alloy [74]. Moreover, the effect of various alloying elements of pure iron has been reported to recommend suitable elements for iron biomaterials such as Co, W, C, and S [61]. However, Alloying Fe with other elements such as Mn, C, Si, and Pd improved its degradation rate, but their biocompatibility is uncertain at higher concentrations of the alloying elements [76]. Wegener et al. [69] investigated binary Fe–X (X= P, B, Ag) alloys using a powder metallurgical fabrication route. B and P were chosen as they can increase the sintering density. Ag was selected because Ag and Fe are not soluble and Ag particles were expected to act as local galvanic corrosion spots. Feng et al. [71] used plasma nitriding to improve the strength of Fe and thus to decrease implant dimension. They also expected that fine

dispersed particles of Fe and N could induce micro-galvanic corrosion. Huang et al. investigated Fe-5Pd and Fe-5Pt alloys produced via spark plasma sintering (SPS). They observed that the materials investigated exhibit a greatly increased degradation rate and improved mechanical properties compared to Fe [77].

Second, surface modifications, as proposed by Zhu et al [78] for surface modification, Fe-O thin films synthesized on a pure iron surface by plasma immersion ion implantation and deposition (PIII&D), which effectively improved both the corrosion resistance and biocompatibility. Lanthanum (La) ion implanted pure Fe by metal vapor vacuum arc (MEVVA) [79] have been shown in improvement of corrosion resistance and biocompatibility. In addition, Fe was also coated with micro-patterned Au disc arrays and produced a more uniform corrosion with an almost four times higher degradation rate than the uncoated ones [80]. Chen modified the microstructure of commercial pure Fe using plasma nitride and then showed the improvement in corrosion resistance [81].

Finally, some novel and new fabrication methods such as electroforming technique [51, 52], powder metallurgy [69], equal channel angular pressing (ECAP) technique [43] and 3D printing [82] are suggested to fabricate pure Fe foil or Fe-based alloys which showed faster degradation than pure iron obtained from conventional casting technique. Recently researchers reported that newly designed biodegradable Fe-X composites (X= W, CNT, Pd, Pt, Mg, Bioceramic) were prepared by spark plasma sintering (SPS) [70, 77], powder metallurgy [76] and cold drawn method [83-85]. Another attempt was making composite of Fe with Fe_2O_3 to create more phase/grain boundaries which theoretically act as active sites for accelerating degradation [86].

Table 1.3. Overview of various strategies for developing a biodegradable Fe based alloy.

System	Method	Approach/Aim	Ref. (year)
Fe-Mn	Alloying by HEMA	Addition of Mn within solubility limit of Fe, to reduce standard electrode potential of Fe–Mn alloys compared to pure Fe	[6] (2007)
Fe	Plasma nitride	The microstructure of commercial pure Fe modified by plasma nitride and corrosion resistance is improved	[81] (2008)
Fe	metal vapor vacuum arc (MEVVA)	Lanthanum ion was implanted into pure Fe by MEVVA to improve its corrosion resistance and biocompatibility	[79] (2009)
Fe	plasma immersion ion implantation and deposition (PIII&D)	Fe-O thin layer was synthesized by PIII&D in order to improve corrosion resistance and biocompatibility	[78] (2009)
Fe-Mn-Pd	Alloying + heat treatments	Addition of Mn to reduce standard potential and minor addition of Pd to form noble precipitates to induce micro-galvanic corrosion. Improved strength via heat treatments to reduce implant dimensions	[72] (2010)
Fe	Electroforming of Fe sheets	Evaluation to increase degradation rate of Fe via electroforming	[52] (2010)
Fe	Commercial pure iron was fabricated via ECAP through severe plastic deformation	Study corrosion rate and enhance biocompatibility through nano-crystalline Fe produced by ECAP	[43] (2010)
Fe–X (X= Mn, Co, Al, W, Sn, B, C, S)	Alloying	Feasibility of different binary Fe alloys for use as degradable biomaterial	[61] (2011)
Fe–30Mn–1C	Vacuum induction melting	Show high degradation rate compared with Fe-30Mn, lower hemolytic ratio, better anticoagulation property and less platelet adhesion as well as good cell compatibility	[74] (2011)
Fe–X (X= P, B, Ag) and Fe-Ag-P	Alloying by powder metallurgy	Development of a degradable Fe-based alloy with the idea of using them as matrix material of cellular structures producible via powder metallurgy	[69] (2011)

Table 1.3 (continued)

Fe-Mn-C Fe-Mn-C-Pd	twinning-induced plasticity(TWIP) steel via vacuum induction furnace	Combination of high strength and ductility by strain hardening. Exceed the performance of SS, Ti or Co-Cr alloys	[87] (2012)
Fe based bulk metallic glass (BMG)	Arc-melting and cold suction casting with water cooled Cu mold	More corrosion resistance than 316L SS and high cell viability value of Fe based BMG	[88] (2012)
Fe-X composites (X=W, CNT)	spark plasma sintering (SPS)	Improve strength and induce galvanic corrosion through the incorporation of the X-Phase	[70] (2013)
Fe-Mn	Inkjet-3D printing	Generate complex, customizable parts from powder Corrode more rapidly than pure Fe Good *in vitro* cytocompatibility	[82] (2013)
Fe–N	Alloying via vacuum plasma nitriding of Fe	Improve strength via nitriding to reduce implant dimension; formation of Fe/N-particles to induce galvanic corrosion	[71] (2013)
Fe–Fe_2O_3 composite	spark plasma sintering (SPS)	Fe–5Fe2O3 composite is a promising alternative for biodegradable stent material with elevated corrosion rate, enhanced mechanical properties, as well as excellent biocompatibility	[86] (2014)
Fe–Pd, Fe–Pt	Alloying via spark plasma sintering (SPS)	Acceleration of degradation rate through the addition of Pd or Pt	[77] (2014)
hydroxyapatite(HA) coated porous Fe	Porous Fe sheet via the polymer space holder method HA coating via dip coating method	effect of HA in enhancing cytocompatibility of the surface inhibition effect of the coating on degradation	[89] (2014)
Fe-bioceramic composites	powder metallurgy and sintering	Slightly increased their corrosion rate compared to that of pure Fe and increase of cellular activity composites have the potential to be used for biodegradable bone implant applications	[76] (2014)
Fe coated with micro-patterned Au disc arrays	vacuum sputtering	more uniform corrosion with an almost four times higher degradation rate than the uncoated ones	[80] (2015)
Fe–Au / Fe–Ag composites	powder metallurgy and sintering	increase the corrosion rate of the iron matrix and change the corrosion mode into more uniform one No significant toxicity for cells	[90] (2015)

1.2.3 Degradation behavior of Fe based alloys in physiological media

When a metal is implanted it comes into contact with soft or hard tissue and is continuously exposed to corrosive body fluid, which among other things contains dissolved oxygen, sodium chloride, phosphate, carbonates, calcium, other salts, and complex organic compounds such as proteins. In order to simulate *in vivo* conditions in lab-scaled tests, simulated physiological media are used, such as Hank's solution (HS), simulated body fluid (SBF), and phosphate buffered saline (PBS). Degradation behavior is typically investigated by means of immersion tests, where mass loss or dissolved ion concentrations as a function of immersion time are measured to evaluate degradation rates. Electrochemical methods including potentiodynamic polarization measurements and impedance spectroscopy are also often utilized to determine degradation rates. These methods also allow characterization of the corrosion process involved. Table 1.4 summarizes the degradation rates of Fe and various Fe based alloys which were introduced in the previous sections.

There are big discrepancies in measured degradation values of Fe in Table 1.4. These may relate to differences in the measurement conditions employed, such as the test media (HS, SBF or PBS), buffering system, test method (immersion or potentiodynamic polarization), dynamic or static test conditions, and the time periods investigated. However, despite the lack of comparability between the different investigations it is clear that alloys containing Mn and/or Pd as alloy elements exhibit an increased *in vitro* degradation rate compared to Fe.

Table 1.4. Comparison of the in vitro degradation rates of Fe and various Fe based alloys.

Alloy	Test medium	Test method	Degradation rate		Ref.
			Reported	Converted (mm/year)	
Pure Fe Cast	–	–	–	0.008	
Fe	HS	PD	16 μA/cm^2	0.2	[75] (2010)
Fe–25Mn	HS	PD	40-90 μA/cm^2	0.52	
Fe–35Mn	HS	PD	37-55 μA/cm^2	0.44	
Fe	SBF	IM	0.0026 mg/cm^{2}h	0.03	[72] (2010)
Fe–10Mn	SBF	IM	0.011 mg/cm^{2}h	0.12	
Fe–10Mn–1Pd	SBF	IM	0.038 mg/cm^{2}h	0.42	
Fe	HS	PD	8.96 μA/cm^2	0.1	[73] (2011)
Fe–30Mn	HS	PD	10.7 μA/cm^2	0.12	
Fe–30Mn–6Si	HS	PD	24.7 μA/cm^2	0.29	
Fe	PBS	PD	10.887 μA/cm^2	0.13	[71] (2013)
Nitride Fe	PBS	PD	19.365 μA/cm^2	0.225	
Fe	HS	PD	0.652 μA/cm^2	0.016	[70] (2013)
Fe–5W/SPS	HS	PD	6.392 μA/cm^2	0.138	
Fe–1CNT/SPS	HS	PD	8.397 μA/cm^2	0.177	
Fe	HS	IM	0.044 mg/cm^{2}h	0.02	[77] (2014)
Fe-5Pd	HS	IM	0.074 mg/cm^{2}h	0.03	
Fe-5Pt	HS	IM	0.120 mg/cm^{2}h	0.06	

HS: Hank's solution SBF: Simulated body fluid PBS: Phosphate buffered saline
PD: Potentiodaynamic polarization method IM: Immersion test

For example, according to Hermawan et al.[75] the following mechanisms are involved during the degradation of Fe-Mn alloys in physiological media (Figure 1.4). The initial reaction after immersion of the alloy in the fluid involves the dissolution of the metal (oxidation) given by the two anodic partial reactions in Figure 1.4(a):

$$Fe \rightarrow Fe^{2+} + 2e^{-} \text{ (anodic reaction)} \quad (1.4)$$

$$Mn \rightarrow Mn^{2+} + 2e^{-} \text{ (anodic reaction)} \quad (1.5)$$

In aerated aqueous solutions, the reduction dissolved oxygen is the partial cathodic reaction:

$$2H_2O + O_2 + 4e^{-} \rightarrow 4OH^{-} \text{ (cathodic reaction)} \quad (1.6)$$

The partial anodic or cathodic reactions, however, can only proceed as fast as one of the two limiting reactions. The dissolved metal ions may further react with hydroxyl ions (OH^{-}) forming hydroxide layers (hydrous metal oxides in Figure 1.4(b)). In the following the reactions are given for the main constituent Fe:

$$Fe^{2+} + 2OH^{-} \rightarrow Fe(OH)_2 \text{ or } FeO{\cdot}H_2O \text{ (product formation)} \quad (1.7)$$

$$4Fe(OH)_2 + O_2 + 2H_2O \rightarrow 4Fe(OH)_3 \text{ or } 2Fe_2O_3{\cdot}6H_2O \text{ (product formation)} \quad (1.8)$$

From the literature it is known that the corrosion products of iron in aqueous solutions typically comprise a layered structure which consists of $Fe_2O_3{\cdot}nH_2O$ on surface layer, $Fe_3O_4{\cdot}nH_2O$ in the middle and $FeO{\cdot}nH_2O$ at the bottom [75]. A similar structure has been revealed in many *in vitro* studies, where a layer of brownish red degradation products, indicating the formation of hematite (Fe_2O_3), has been observed over a black layer reflecting the formation of magnetite (Fe_3O_4) or wustite (FeO).

During the course of degradation, pits on the metal surface emerge, along with an increased concentration of Cl^{-} at the degradation surface. Hermawan et al. proposed that Cl^{-} ions from the immersion media diffuse through the porous oxide layers to the metal surface to

compensate for the increased Fe^{2+} or Mn^{2+} concentration in Figure 1.4(c). The Cl^- ions may subsequently react with metal ions, according to the following equation:

$$Fe^{2+} + 2Cl^- \rightarrow FeCl_2 \quad (1.9)$$

The metal chloride may also react with water to form hydroxide and free hydrochloric acid:

$$FeCl_2 + H_2O \rightarrow Fe(OH)_2 + HCl \quad (1.9)$$

The pH value locally decreases and it leads to the formation of pits. As the degradation process continued, the precipitation of Ca and P rich layers deposit onto the hydroxide layers in Figure 1.4(d).

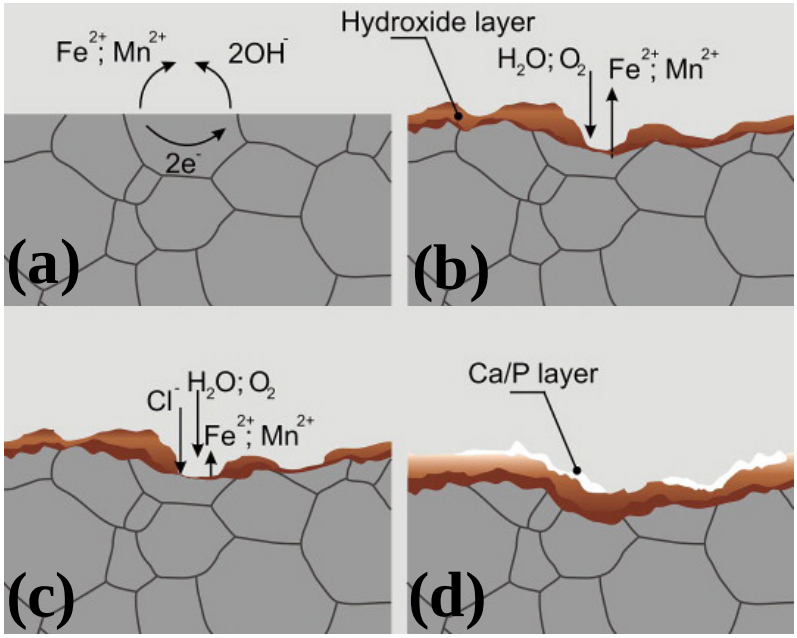

Figure 1.4. Illustration of the corrosion mechanisms for Fe–Mn alloys: (a) initial corrosion reaction, (b) formation of hydroxide layer, (c) formation of pits, and (d) formation of calcium/phosphorus layer. Used with permission of [75].

1.2.4 Electrochemical considerations in alloy design for Fe based degradable materials

As mentioned above for the degradation behavior of Fe-Mn system by way of example, metallic degradation response occurs via the electrochemical reaction upon introducing the metal to an aqueous environment wherein metals give away electrons and form positive ions during the anodic dissolution of the metal and a cathodic reaction takes place, leading to the formation of a corrosion product. In keeping with the concept of development of new compositions for controlling the corrosion of the Fe alloys, various alloy systems have been investigated to date in Table 1.3. The purpose of adding alloying elements to Fe as discussed earlier is mainly to increase the corrosion resistance. It is closely related with design strategy for Fe based degradable material which are proposed by Schinhammer et al [72].

The approach to achieving increased degradation rates takes into account two criteria which influence the corrosion susceptibility of the metal:

1. The addition of less noble alloying elements within the solubility limit in Fe to make the Fe matrix more susceptible to corrosion.
2. The addition of noble alloying elements to generate small and finely dispersed precipitates that act as cathodic sites towards the Fe matrix, inducing micro-galvanic corrosion.

To satisfy criterion (1), the standard electrode potentials listed in Table 1.5 must be taken into account. This is an orderly arrangement of potentials for all metals; the more negative values correspond to more reactive metals [91, 92]. The position of a given element in the series is determined by the equilibrium potential of the metal in contact with an aqueous solution with its ions at a concentration equal to unit activity. Although this situation rarely occurs in practice, it is a useful aid in establishing a ranking among the different elements.

Many metals listed in the standard electrode potentials are less noble than Fe. Usually, most of these were not considered further, however, as either their solubility in Fe (e.g. Li, Mg, Ti) or their biocompatibility (e.g. Al, Cr) is limited [72]. However, in line with this observation, Mn was chosen in first to meet criterion (1) because it possesses a distinctly lower reduction potential (E_{Mn} = –1.18 V) than Fe (E_{Fe} = –0.44 V) and shows high solubility in Fe. Because Fe and Mn form a solid solution, the standard potential of the Fe–Mn alloy is expected to decrease with increasing Mn content [93]. The same approach was previously reported by Hermawan et al. [6, 7] and was based on metallurgical and toxicological considerations. It corresponds to criterion (1) by considering Mn a suitable alloying element, and is clearly a step in the desired direction.

The potential of criterion (2) has already been illustrated in systems such as Al-Cu, where precipitates (Al_2Cu) are formed that are nobler than the Al matrix and thus reduce the alloy's corrosion resistance [94]. The efficiency of such an approach can be enhanced by reducing the size of the precipitates and distributing them homogeneously in the matrix. Here the degradation rate is expected to increase, while the material maintains homogeneous "macroscopic" degradation behavior. The elements available for pursuing criterion (2) are all those in the standard electrode potential which are nobler than Fe (Table 1.5). The requirement that small and homogeneously distributed precipitates be formed imposes additional restrictions on the choice of element. Despite no consideration being reported in the literature for use of Mg as an alloying elements to meet criterion (1) [72], for this dissertation Mg is used as alloying element of these Fe alloy, which will be discussed in the following section.

Table 1.5**.** Selected standard electrode potentials of metal in aqueous solution at 25 °C relative to the standard hydrogen electrode [92, 95].

Electrode reaction	*E°(V)*
$Pt^{2+}(aq) + 2\ e^- \rightarrow Pt(s)$	≈ 1.2
$Pd^{2+}(aq) + 2\ e^- \rightarrow Pd(s)$	0.987
$Ag^{2+}(aq) + 2\ e^- \rightarrow Ag(s)$	0.800
$Cu^{+}(aq) + e^- \rightarrow Cu(s)$	0.521
$Cu^{2+}(aq) + 2\ e^- \rightarrow Cu(s)$	0.342
$2H^{+}(aq) + 2\ e^- \rightarrow H_2(g)$	0.000
$Sn^{2+}(aq) + 2\ e^- \rightarrow Sn(s)$	-0.136
$Ni^{2+}(aq) + 2\ e^- \rightarrow Ni(s)$	-0.25
$Co^{2+}(aq) + 2\ e^- \rightarrow Co(s)$	-0.28
$Cd^{2+}(aq) + 2\ e^- \rightarrow Cd(s)$	-0.403
$Cr^{3+}(aq) + e^- \rightarrow Cr^{2+}(aq)$	-0.41
$Fe^{2+}(aq) + 2\ e^- \rightarrow Fe(s)$	-0.44
$Ga^{3+}(aq) + 3\ e^- \rightarrow Ga(s)$	-0.53
$Cr^{3+}(aq) + 3\ e^- \rightarrow Cr(s)$	-0.74
$Zn^{2+}(aq) + 2\ e^- \rightarrow Zn(s)$	-0.763
$Cr^{2+}(aq) + 2\ e^- \rightarrow Cr(s)$	-0.91
$Mn^{2+}(aq) + 2\ e^- \rightarrow Mn(s)$	-1.18
$V^{2+}(aq) + 2\ e^- \rightarrow V(s)$	-1.18
$Zr^{4+}(aq) + 4\ e^- \rightarrow Zr(s)$	-1.53
$Ti^{2+}(aq) + 2\ e^- \rightarrow Ti(s)$	-1.63
$Al^{3+}(aq) + 3\ e^- \rightarrow Al(s)$	-1.66
$Mg^{2+}(aq) + 2\ e^- \rightarrow Mg(s)$	-2.37
$Na^{+}(aq) + e^- \rightarrow Na(s)$	-2.714
$Ca^{2+}(aq) + 2\ e^- \rightarrow Ca(s)$	-2.87
$Sr^{2+}(aq) + 2\ e^- \rightarrow Sr(s)$	-2.89
$Ba^{2+}(aq) + 2\ e^- \rightarrow Ba(s)$	-2.9
$Rb^{+}(aq) + e^- \rightarrow Rb(s)$	-2.925
$K^{+}(aq) + e^- \rightarrow K(s)$	-2.925
$Li^{+}(aq) + e^- \rightarrow Li(s)$	-3.045

1.3 IRON-MAGNESIUM: AN IMMISCIBLE SYSTEM

1.3.1 Thermodynamic phase diagram in Fe-Mg system

According to the common phase diagrams in Figure 1.5, Fe and Mg are almost immiscible at ambient pressure [96]. In the liquid phase, the solubility of Mg in Fe is on the order of 0.025 atomic percent (at. %). The maximum solid solubility of Fe in Mg is 0.00041 at. % and the Fe content in Mg at the eutectic point is less than 0.008 at. % [97]. Moreover, below 1273 K, the solubility of Mg in α-Fe is below the detection limit and only about 0.25 at. % Mg is soluble in δ-Fe at the monotectic temperature [98]. Solubility of Mg in Fe is possible only at high pressures and temperatures [96]. Below 1000° C, Mg does not dissolve in Fe. The immiscibility of Fe and Mg at ambient conditions is in line with the well-known Hume-Rothery rules, in which atomic size difference above 15 % between the alloy constituents limits solid solution formation [99]. The enthalpy of mixing in the Fe-Mg system is +18 kJ/mol [98]. This system is convenient for Mössbauer studies since it contains Fe [100]. Indeed, based on semi-empirical thermodynamic calculations, Yelsukov et al. obtained 6 kJ/mol for the enthalpy of formation for $Fe_{0.93}Mg_{0.07}$, compared to 20 kJ/mol calculated for the corresponding Fe-Mg nanocomposites [101].

1.3.2 High energy mechanical alloy (HEMA) of immiscible Fe-Mg system and other system.

Despite the negligible solubility of Mg in Fe, several Fe-rich metastable Fe-Mg solid solutions have been synthesized. According to the pioneering work by Hightower et al. [102] mechanical

alloying produced Fe-Mg substitutional solid solutions with up to 20 at. % Mg in α-Fe. Later, Dorofeev et al.[100, 101] found the formation of about 5~7 at. % Mg in α-Fe supersaturated solid solution [101]. Additionally, Dubrovinskaia et al, found that pressure can facilitate the solid solution formation and then reported that the solubility of Mg in α-Fe was increased to 4 at.% at pressures around 20 GPa and temperature up to 2273 K [103]. The solution of Mg in the bcc-structured Fe-based alloy increases the lattice parameter by approximately 2.4% with respect to that of pure iron [103].

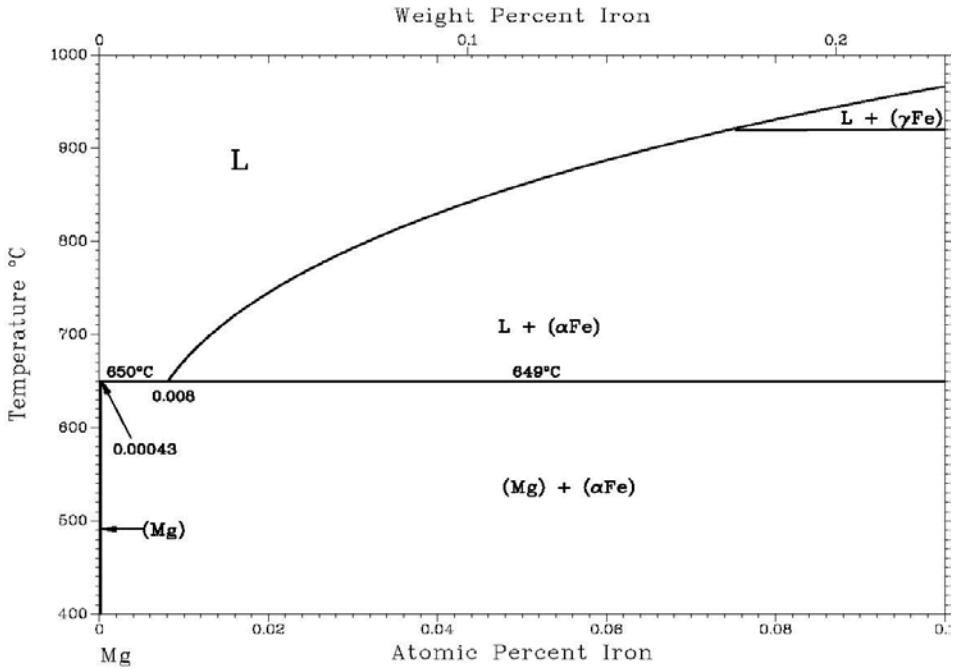

Figure 1.5. Assessed Fe-Mg phase diagram in the Mg-rich region. Used with permission of [96].

In contrast to systems with negative heats of mixing, in the great majority of systems with positive heats of mixing non-equilibrium processing results in the formation of supersaturated solid solutions rather than amorphous phases [104]. Examples are systems which have very

limited equilibrium solid solubility and which do not form intermetallic phases, such as Cu–Co, Cu–Fe, or Ag–Cu, which can nevertheless be obtained as thermodynamically unstable solid solutions over wide composition ranges by HEMA [105-107]. Additionally, HEMA has been reported to result in the formation of either solid solution in Ge–Al [108] and Ag–Bi [109] systems or supersaturated solid solutions between elemental pairs exhibiting positive heat of mixing in Fe–Mg [100], Pb–Al [110, 111], Ni–Ag [112], Fe–Pb [113], and Cu–V [114] systems. Formation of solid solutions rather than amorphous phases in such systems is understandable from a thermodynamic viewpoint, in particular in systems which exhibit immiscibility even in the liquid state.

1.3.3 Formation of an amorphous phase in the immiscible system.

Although amorphous phases are unlikely to occur in alloy systems with positive heat of mixing as outline above in section 1.3.2, there are a minor number of investigations that report on amorphous phase formation is system such as Ag-Fe [115, 116] , Ag-Co [117], Ag-Ni [117], Ag-Cu [118], W-Cu [119, 120] and Ta-Cu [120], some of which are immiscible even in the liquid state. In the classical thermodynamic perspective, the formation of amorphous phases in systems which are immiscible even in the liquid state is exceptional, and is in contrast to the current understanding of the thermodynamics of liquid phases. Recently, non- equilibrium processing of materials, especially HEMA, has been employed to produce a variety of novel and advanced materials, which include amorphous, quasicrystals, metastable intermediate phases, and nano-crystalline materials, among others [121]. The heavy mechanical deformation during HEMA induces particle refinement and consequently decreased diffusion distances. Further, mechanical deformation generates a wide variety of crystal defects, including grain boundaries,

stacking faults, and vacancies, which enhance diffusion. All these effects result in intimate mixing of fine powder particles, and possibly alloying [122]. This has been shown to occur even between difficult to alloy mixtures, which exhibit a positive heat of mixing [109]. Therefore, fully amorphous phases were synthesized by HEMA in elemental pairs such as W-Cu [123], Cu-V [124], Cu-Ta [125, 126], and Nb-Zr [127] which are considered as immiscible system.

The theoretical and experimental precedence of Fe and Fe based alloy for biodegradable medical applications discussed earlier along with the advantages in terms of the physical, chemical and biological properties make Fe alloys suitable for degradable load and non-load bearing bone implants, cardiovascular stents, and other implantable medical devices. This work seeks to optimize a system of alloys featuring elements such as Mg, Mn, Ca, and Zr primarily for biomedical applications. Accordingly, four specific aims have been crafted as discussed henceforth.

1.4 SPECIFIC AIMS

During the past few years significant advances have been made in the development of biodegradable metallic materials for biomedical applications, such as temporary prostheses, cardiovascular stents, and three-dimensional porous structures as scaffolds for tissue engineering. The commonly used stainless steels, titanium and cobalt-chromium based metallic “bio-inert” materials have had a long history of clinical employment as implants in the treatment of temporary clinical problems such as fractured bones, narrowed arteries and congenital cardiovascular defects [11, 12]. However, these permanent implants suffer from some unavoidable short and long term clinical problems such as disease/trauma, permanent physical

irritation, chronic inflammatory discomfort or implant removal/revision surgeries [24-26]. To alleviate these permanent implant related problems, biodegradable materials have received considerable attention in recent years for their unique degradable characteristics [44, 128, 129]. Clinically used degradable biomaterials are typically made of polymer but these polymer-based implants usually possess poor and unsatisfactory mechanical properties [130-134]. As a result, many recent studies have indicated that there is a high demand to design and develop biodegradable metallic materials with controlled degradation rates and suitable mechanical properties for orthopedic, cardiovascular and pediatric applications including bone fixation screws/pins and coronary stents [35].

Up until now, Iron (Fe) and Magnesium (Mg) based alloys are essentially two classes of metals that have been considered for degradable implant applications [1, 7, 22, 53]. Most of the research on Fe and Fe based alloys have reported a very slow degradation rate in physiological environments [26, 54, 76], while Mg and Mg based alloys degrade too rapidly [23, 25]. Fe alloys containing elements such as Mn, C, Si, and Pd show improvement in degradation rates, but their biocompatibility is still unclear especially when alloys contain concentration of the alloying elements [7, 58, 61, 72, 135]. Therefore, it is necessary to develop Fe-based alloys exhibiting improved degradation behavior while also retaining good in vitro and in vivo biocompatibility and cytocompatibility.

The main focus of this thesis is thus to design and develop Fe-based biodegradable alloys employing appropriate alloying techniques displaying tailored corrosion and improved cytocompatible properties using suitable alloying elements. Accordingly, four specific aims have been designed and a summary of the specific aims of this thesis to achieve the work described above are given below:

1.4.1 Specific Aim 1: Synthesis and optimization of the processing parameters for the generation of Fe-Mg binary alloy powders utilizing high energy mechanical alloying (HEMA).

Hypothesis: To date, only two classes of metal alloys have been explored as biodegradable materials for medical devices. They include Fe and Mg-based alloys. However, to the best of our knowledge, there is no study exploring the Fe-Mg binary alloy system as biodegradable metallic materials because of the thermodynamic immiscibility of Fe and Mg under ambient conditions. Thus, synthesis of Fe-Mg binary alloys with high Mg content using HEMA can be very useful. These high magnesium containing alloys may show improved degradation characteristics as well as improved cyto/biocompatibility.

Rationale: Fe is an essential nutrient present in the human body and plays an important role in vital biochemical activities such as oxygen sensing and transport, electron transfer and catalysis [45]. It also exhibits good mechanical properties [58], biocompatibility [42] and hemocompatibility [136]. On the other hand, Mg is a lightweight metal with mechanical properties similar to bone. It is biocompatible and essential to the human metabolism present, as a cofactor for many enzymes [137]. Mg also forms soluble and non-toxic oxides in the body fluid that is harmlessly excreted with the urine [64]. Theoretically, bimetallic (galvanic) corrosion may occur when dissimilar metals, with different potentials, are in contact. Mg is most anodic (less noble) element than Fe, and there is a difference in the electronegative potentials of these two elements. Thus, it can be expected that alloying Fe with high Mg content may result in alloys that are more susceptible to electrochemical corrosion. Although both elements are already known to have high potential for biodegradable materials, there is no report that Fe-Mg alloys have been synthesized and studied for biomedical applications to date. In spite of the

negligible solubility of Fe and Mg, several Fe-rich metastable Fe-Mg solid solutions have been synthesized by HEMA, [100-102] a solid state powder processing technique, known to generate and stabilize thermodynamic non-equilibrium phases and systems [122]. However, these solid solutions (alloys of Fe-Mg system) are formed under very stringent conditions, and further, most studies were focused only on the formation of these rare solid solutions. Additionally, there are very few reports on Fe-Mg binary system over the past few years and the use of Fe-Mg binary system alloys as biodegradable scaffolds is yet to be explored.

1.4.2 Specific Aim 2: Synthesis and optimization of the processing parameters for the deposition of thin layers of Fe-Mg alloys using pulsed laser deposition (PLD) and identification of the potential use of these alloys as biodegradable systems using *in vitro* characterization methods.

Hypothesis: PLD can be used to deposit thin layer or films from any material, starting from pure elements to multi-component compounds, and moreover, a major advantage of this techniques is that the stoichiometry of the target material can be reproduced in entirety in the deposited films [138]. Therefore, it is possible to synthesize thin layers of Fe-Mg alloy from targets formed either using the Fe-Mg alloy powder generated by HEMA (Specific Aim 1) or using blended mixture prepared from the elemental powders of Fe and Mg corresponding to alloy composition in Specific Aim 1 (SA1).

Rationale: There are two approaches for use of PLD in this proposed work. First, PLD is only considered as one of the alloying methods similar to conventional melting or HEMA. In other words, the laser energy provided by the PLD and other related process parameters will be utilized to form alloys in-situ. As mentioned in SA1, Fe and Mg are almost immiscible under

ambient conditions, and it is almost impossible to generate alloys using a conventional method. In the literature, some reports exist on the formation of metastable phases in the immiscible systems using PLD [139-141]. In line with these results, Fe-Mg alloy will be synthesized as a thin layer from targets made of blended mixtures of Fe and Mg elemental powders by PLD, and the generated layers will be evaluated to understand the influence of the processing parameters during PLD. Second, PLD will be used to ablate the Fe-Mg alloy targets to form thin films of the same alloy composition used in the target. However, the phase and structure of the deposited thin layers may vary depending on the deposition conditions. In order to identify the potential use of Fe-Mg alloy as a biodegradable system using *in vitro* characterization methods, it is necessary to form bulk shapes or thin layers from the HEMA derived Fe-Mg alloy powders as described in SA1. Sintering by thermal treatment below the melting temperature of the main constituent material usually transforms a metallic or ceramic powder (or a powder compact) into a bulk solid typically executed in powder metallurgy. However, conventional sintering technique does not permit sintering of Fe-Mg alloy powders as described in SA1 due to the large melting temperature difference between Fe and Mg, namely, 1530°C and 650°C, respectively. Hence, it is impossible to use conventional sintering method to form substrates without inducing any change in composition and structure. Therefore, formation of thin film is one of the solutions to generate dense structures from HEMA derived Fe-Mg powders as part of the next section of the proposed work. There are several possible techniques used to synthesize thin films. Among the different techniques, pulsed laser deposition (PLD) has several characteristics that distinguish it from other film growth methods [138]. We already reported [142] that by controlling optimal deposition parameters in PLD; it is possible to tailor the structural properties of the deposited

thin films in Mg-based amorphous alloys for biomedical applications. These results are also included in this thesis.

1.4.3 Specific Aim 3: Study the effect of addition of manganese (Mn) as an alloying element in the Fe-Mg alloy system and understand the in vitro response to explore the potential of these alloys as novel biodegradable material systems.

Hypothesis: One of the serious limitation of using Fe-based alloy as biodegradable material is its ferromagnetic characteristics that can seriously limit magnetic resonance imaging (MRI) capabilities of Fe based alloys. On the other hand, austenitic Fe-Mn alloys are already known as nonmagnetic and are reported to have higher degradation rates than pure Fe. The degradation rates however can be adjusted further by varying the Mn content [58] in these alloys. Accordingly, it is expected that antiferromagnetic behavior can be achieved by adding Mn to the Fe-Mg alloy as discussed in SA1.

Rationale: Alloying and heat treatment are typically the two possible ways to overcome limitations posed by the ferromagnetic characteristics of pure Fe for biological applications [7]. Austenite, also known as gamma phase iron (γ-Fe), is a metallic, non-magnetic allotropic form of Fe or Fe based alloys [143]. Austenitic Fe–Mn alloys are considered as viable substitutes from the conventional Fe–Cr–Ni austenitic stainless steel alloys, wherein the expensive alloying elements such as chromium (Cr) and nickel (Ni) are replaced by a more inexpensive Mn. Alloying with more than 29 wt-% Mn results in the stabilization of the complete austenitic phase [144, 145] which exhibits antiferromagnetic behavior [146, 147]. Furthermore, Mn is one of the essential trace elements required for the normal development and body function during the life span of all mammals [148]. In addition, Mn contributes to better biological functions than other

austenite stablizing elements such as nickel which is also a suspect carcinogen [149]. Excess Mn is also not reported to be toxic in the cardiovascular system since the extensive plasma protein binding counteracts the effect of Mn toxicity [150, 151]. Therefore, it is hypothesized that adding Mn to Fe-Mg alloy will perform a role that can potentially transform Fe-Mg ferromagnetic alloys into the nonmagnetic form for biological applications.

1.4.4 Specific Aim 4: Study the effect of addition of calcium (Ca) and zirconium (Zr) alloying elements to Fe-Mg or Fe-Mg-Mn alloys and understand the in vitro response to explore the potential of these alloys as novel biodegradable material systems.

Hypothesis: The addition of Ca and Zr to Fe-Mg (Specific Aim1) and Fe-Mg-Mn (Specific Aim3) alloys will improve the bioactivity of these biodegradable alloys in addition to tailoring the biodegradable characteristics. Hence, their alloys can be considered as potentially viable temporary implants.

Rationale: For biomedical applications, the composition of the metal is considered to be extremely crucial since many of the elements that are used in commercially available metals for industrial applications are extremely toxic to the human body. Therefore, in addition to meeting the advanced properties needed for a particular biomedical application, the metal must also be biocompatible. Ideally, a biodegradable medical device should be composed of materials or alloying elements that are nontoxic (bio/cytocompatible) as well as considered non-carcinogenic. It would also be very advantageous if the material is composed of elements and minerals that are already present and known to be compatible within the body. Ca and Zr are considered to be essential trace elements for human life. Ca, in particular, is a major component of the human bone and is essential to the chemical signaling of cells [152]. Also, it is an important element

involved in the muscular action and nerve conduction, and its level in the body is closely monitored and regulated by a process called homeostasis [153]. Therefore, Ca was reported to be the most favorable non-toxic alloying element for biomedical applications [154, 155]. It has also been reported that the addition of Ca significantly enhances the mechanical properties of Mg-based alloy [154]. Zr, on the other hand, is known as a powerful grain refiner and improves the mechanical properties of Mg alloys [156, 157]. More importantly, Zr exhibits low ionic cytotoxicity in vitro, and excellent biocompatibility in vivo with no evidence contributing to any mutagenic or carcinogenic response [158-160]. However, there are only few studies reported on the effect of the addition of Ca and Zr to biodegradable Fe-based alloys in the literature to date. Based on the published literatures it is, therefore anticipated that Ca and Zr will induce positive effects on the degradation rates and cytocompatibility of the Fe-Mg and Fe-Mg-Mn alloys.

2.0 SPECIFIC AIM 1: SYNTHESIS AND OPTIMIZATION OF THE PROCESSING PARAMETERS FOR THE GENERATION OF FE-MG BINARY ALLOY POWDERS UTILIZING HIGH ENERGY MECHANICAL ALLOYING (HEMA)

2.1 INTRODUCTION

Interest in biodegradable metals and metal alloys for use as temporary implant materials in vascular intervention and osteosynthesis has been continuously increasing over the past few years [1-7]. It has been reported that degradable implants in fact, may overcome the disadvantages of permanent devices in certain cases, known to cause prolonged physical irritation and chronic inflammation. At present, Iron (Fe) [7, 53, 72, 75, 78] and magnesium (Mg) [1, 22, 161-164] based alloys are the two prominent classes of metals that have been considered as promising candidates for degradable implantable devices. Mg-based alloys have already been successfully tested in vivo and also pursued for clinical studies [68]. However, the major weakness of theses alloys is the low corrosion resistance [23, 25], especially in electrolytic and aqueous environments, leading to the formation of hydrogen gas pockets [165], hemolysis and alkalization of body fluid which might limit their future biomedical application [25]. In addition, their low strength and hardness also limit clinical application for load bearing bone fixation devices such as screws and plates [166, 167]. On the other hand, superior mechanical properties of pure Fe or Fe-based alloys are more attractive as biodegradable implants compared

to Mg-based alloys. Recent *in vivo* results have showed that pure Fe is a suitable metal for the generation of biodegradable stents without causing stent particle embolization, thrombosis of excess inflammation, fibrin deposition, local or systemic toxicity and significant obstruction of the stented vessel due to inflammation, neointimal proliferation, or short and long term thrombotic effects [21, 42, 54, 168]. However, it has also been shown that iron alloys are ferromagnetic [37, 42, 72] and exhibit very slow degradation rates in physiological environments [26, 54, 76]. Therefore, there is vital need to increase the degradation rate and improve the mechanical properties for each specific application of these Fe-based alloys by modifying the chemical composition and microstructural characteristics.

As outlined above Section 1.2.2, Some researchers have reported possible ways to overcome these limitations by alloying, heat treatment, or surface modification as well as novel fabrication methods [61]. Hermawan et al.[7, 75] developed a Fe-Mn alloy containing 35 wt.% Mn using powder metallurgy. This alloy displayed an increased corrosion rate compared to pure iron [5] and also showed low inhibition of fibroblast cell metabolic activity in cell viability tests. Fe-Mn-Pd alloys were also produced by Schinhammer et al. [72] that reveal a degradation resistance that is one order of magnitude lower than that observed for pure iron. Xu et al. added 1 wt.% of Carbon into a Fe-30Mn (wt.%) alloy resulting in lower magnetic susceptibility and better mechanical properties compared to the Fe-30Mn alloy [74]. Moreover, Schinhammer et al. proposed two criteria for alloying in order to achieve an increased degradation rate [72]: First is the addition of less noble alloying elements within the solubility limit of Fe to make the Fe matrix more susceptible to corrosion. The other is the addition of the noble alloying elements to generate small and finely dispersed intermetallic phases (IMPs) to generate micro galvanic corrosion with Fe matrix. Following these criteria, various different alloying elements (Co, Al,

W, Sn, B, C,S, Si and Pd) have been used but little effect on corrsion was found, and the biocompatibility of alloys with these elements is uncertain, particularly at higher concentrations of the alloying elements [61, 76]. A number of novel fabrication methods such as electroforming [51, 52], powder metallurgy [69], equal channel angular pressing (ECAP) [43] and 3D printing [82] have resulted in pure Fe foil or Fe-based alloys which show faster degradation compard to pure Fe obtained from conventional casting techniques. Recently some researchers reported newly designed biodegradable Fe-X composites (X= W, CNT, Pd, Pt, Bioceramics) prepared by spark plasma sintering (SPS) [70, 77], powder metallurgy [76] and cold drawing [83-85]. As opposed to the above mentioned strategy for development of new Fe based alloys, surface modification has also been used to the increase the degradation rate of Fe as well as improve the biocompatibility. It was found that pure Fe stents maintained a supporting function during the first several weeks or months after implantation for cardiovascular applications because the lower Fe concentration might produce a favorable effect on the metabolic activity of endothelial cells [54] but it started to show signs of in vivo corrosive degradation within a month [53]. In line with this veiwpoint, the Fe-O thin films synthesized on a pure iron surface by plasma immersion, ion implantation and deposition, Lanthanum (La) ion implanted pure Fe, and modified pure Fe by plasma nitriding have been shown in related literatures [78, 79, 81] to effectively improve both the corrosion resistance and biocompatibility.

In spite of these efforts, the degradation rates, and cytocompatibility of Fe based alloys are still far from levels necessary for implementation in clinical applications. An alternative approach is therefore needed to develop Fe-based alloys with improved degradation behavior while maintaining its biocompatibility. In the present studies, one of the motivations is the formation of non-equilibrium alloy phases, particularly in the Fe-Mg binary system, by High

Energy Mechanical Alloying (HEMA). It has been found that HEMA of elemental mixtures can be employed to synthesize various metastable phases, such as supersaturated solid solutions that are immiscible [169]. These include nanostructured, intermetallic[170], quasicrystalline, and amorphous phases [171].

Although Fe and Mg have been studied separately as temporary degradable implants in biological applications, there are no reports on Fe-Mg binary alloys used as biodegradable metallic materials. Mg is a good candidate as an alloying element in Fe due to its lower standard electrode potential (E°) than Fe, making it more anodic and less noble.

The main problem with the synthesis of a Fe-Mg alloy is the immiscibility of Fe and Mg under ambient conditions [96]. Clearly, an even larger thermodynamic driving force is needed for the formation of supersaturated solid solutions between immiscible components since the enthalpy of mixing in such systems is positive [100]. In spite of these process limitations, several Fe-rich metastable Fe-Mg solid solutions have been synthesized by HEMA [100-102, 172], a solid state powder processing technique known to generate and stablize thermodynamic non-equilibrium phases and systems [122, 173]. However, these solid solutions (alloys of Fe-Mg system) are formed under very stringent conditions, and further, most studies were focused only on the formation of these rare solid solutions. It should be noted that this is the first report of Fe-Mg binary alloy systems for bio-degradable metallic materials to the best of the authors' knowledge. The present work therefore reports the new alloying composition of Fe-Mg amorphous systems synthesized by HEMA.

2.2 MATERIALS AND METHODS

2.2.1 Alloy synthesis by high energy mechanical alloying (HEMA)

The alloy powders corresponding to $Fe_{100-x}Mg_x$ (x=1, 5, 10, 20, 30, 40 and 50) atomic % compositions were produced by high energy mechanical alloying (HEMA). Commercial elemental powders of pure Fe (99.9+%, <10 μm, Alfa Aesar) and pure Mg (99.8%, <325 mesh, Alfa Aesar) were chosen as the starting materials. These were weighed corresponding to the desired compositions, mixed and added into stainless steel (SS) vials containing 45 stainless steel balls 2 mm in diameter as the milling media. The ball to powder weight ratio (BPR) was 15 to 1, and the total weight of the starting mixture was 3 g. HEMA was carried out through two sequential process of dry and wet milling. The mixture was subjected to dry milling in a planetary SPEX 8000 high energy Shaker Mill for up to 14 hours with 30 minutes resting intervals after every 1 hour of active milling. After dry milling, 1.5 ml of toluene (anhydrous, 99.8%, Sigma-Aldrich) was loaded in the vial and the as-dry milled powder was subsequently wet milled for a period of up to 17 hours to reduce the adhesion of powders on the balls and the inner surface of the milling vial. Handling of the powders and loading of toluene were conducted inside an argon-filled glove box in which the oxygen concentration was kept below 1.0 ppm.

2.2.2 Characterizations of HEMA derived Fe-Mg binary amorphous powder

The microstructure and qualitative phase analysis of milled powders was examined by conventional X-ray diffraction (XRD; PANalytical X'pert Pro with Cu-Kα radiation). The phase evolution during dry and wet milling was characterized by XRD. The analysis of XRD peaks

was conducted using Pseudo-Voigt shape function to determine the Lorentzian and Gaussian contribution of peak. Lattice parameters were determined with the Nelson-Riley extrapolation method [174, 175]. The International Centre for Diffraction Data's Powder Diffraction File (PDF) database was used for peak identification. The morphology of the powder was observed via scanning electron microscopy (SEM, JEOL, JSM-6610LV) with energy-dispersive X-ray (EDX; EDAX Genesis, Mahwah, NJ) to conduct elemental analysis. A JEOL JEM2000FX operating at 200 kV was used to conduct transmission electron microscopy (TEM) and obtain conventional bright field images. High resolution (HR) TEM observations were carried out using a JEOL JEM-2100F and image processing was carried out using the software package Gatan Digital Micrograph for Fourier transform. TEM samples were obtained by spraying powder onto carbon grids (Ted Pella, USA) using an aerosolizing spray nozzle for the as-milled powder. The thermal properties of the final milled powder were studied by differential scanning calorimetry (DSC, Netzsch STA 409) at a heating rate of 10°C/min under an ultra high purity Ar gas flow.

2.3 RESULTS

2.3.1 Microstructural characterization of Fe-Mg powder after dry milling

Figure 2.1 shows the XRD scans of blended mixtures prepared from the elemental powder of Fe-Mg and as prepared post dry milled powder corresponding to the nominal compositions of $Fe_{100-x}Mg_x$ (x=1, 5, 10, 20, 30, 40 and 50). In Figure 2.1(a), the XRD patterns show only predominant bcc Fe phase up to 20 at.% Mg (x=1~20) and peaks from hcp Mg are observed after Mg composition exceeds 30 at.% (x= 30, 40 and 50). The peak from Mg (101) is faintly visible

around 37° for $Fe_{70}Mg_{30}$ but other peaks from residual Mg emerge and become shaper with increase of intensity for $Fe_{60}Mg_{40}$ and $Fe_{50}Mg_{50}$ in Figure 2.1(a). For all samples, there is an increased broadening of the bcc phase diffraction peaks compared to Fe raw powder and especially they are shifted to smaller diffraction angles between x=5 and 40 powders ($Fe_{95}Mg_5$, $Fe_{90}Mg_{10}$, $Fe_{80}Mg_{20}$, $Fe_{70}Mg_{30}$ and $Fe_{60}Mg_{40}$) in Figure 2.1(b). For the $Fe_{50}Mg_{50}$ powder in Figure 2.1(a) and (b), the bcc phase peaks shift back to the pure α-Fe positions with observation of hcp peaks. This result suggests that Mg dissolves into the Fe bcc lattice for concentration less than 50 at.% [102] but indicates that not all of the Mg have dissolved for $Fe_{70}Mg_{30}$ and $Fe_{60}Mg_{40}$ powders. In the case of $Fe_{50}Mg_{50}$, the microstructure formed after the dry milling for 14 hours consists of two phase mixtures of bcc Fe and hcp Mg without any peak shifting in Figure 2.1(a). Further dry milling does not lead to microstructural changes of all composition compared to Figure 2.1(a) with the increased milling time up to 50 hours (Figure 2.2), indicating that it approaches steady state in this milling conditions.

The structural evolution in the course of post dry milling can be further characterized by the changes in the lattice parameters. Figure 2.3 compares the lattice parameters of the bcc phase determined in this study and those reported in literature [100, 102, 172]. Alloys with Mg concentration below 50 at.% had X-ray peaks which are shifted to lower angles (Figure 2.1(b)), corresponding to an increase in bcc lattice parameter. It shows that the lattice parameter of the bcc phase, initially 0.2866 nm (Iron, PDF# 01-071-4648) as pure α-Fe, is increased with the addition of Mg and reaches a maximum (a = 0.2897 ± 0.0004 nm) at 10 at.% Mg and then it gently decreases as the Mg content of the starting mixture exceeds 20~30 at.%, although it remained larger than for pure α-Fe in Figure 2.3. This trend can be interpreted as the formation of solid solutions of Mg in α-Fe during post dry milling.

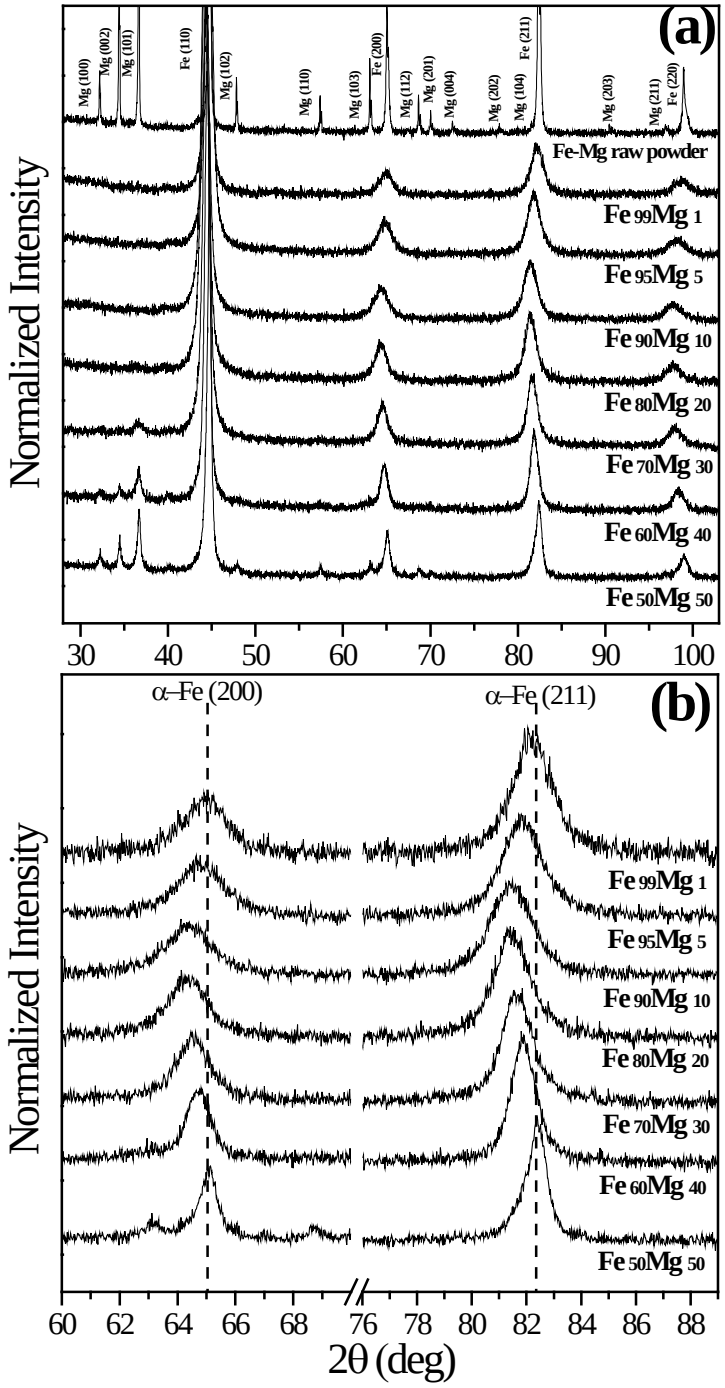

Figure 2.1**.** The X-ray diffraction patterns of (a) raw Fe-Mg blended mixture powder and $Fe_{80-x}Mg_x$ powder (x = 1-50) after post dry milling and (b) enlargement of (200) and (211) profiles from (a); the dash lines indicate the position of the α-Fe (200) and (211) reflection. (PDF# 01-071-4648).

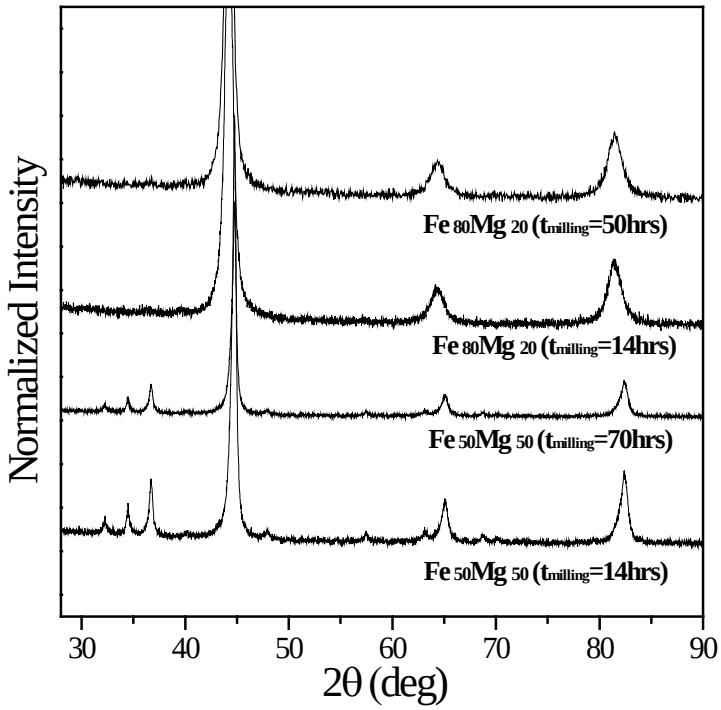

Figure 2.2. The X-ray diffraction patterns of the $Fe_{80-x}Mg_x$ powder (x = 20, 50) with the increased dry milling time up to 50 and 70 hours.

Eventually, it becomes close to the initial lattice parameter at 50 at.% Mg. Notice that the bcc phase lattice parameter continuously decreases with increasing Mg content in as-dry milled powder beyond 10 at.%, as it should if the Mg concentration in the bcc phase were to increase. This means that the Mg supersaturation in solid solution phase decreases with increasing Mg content in this study.

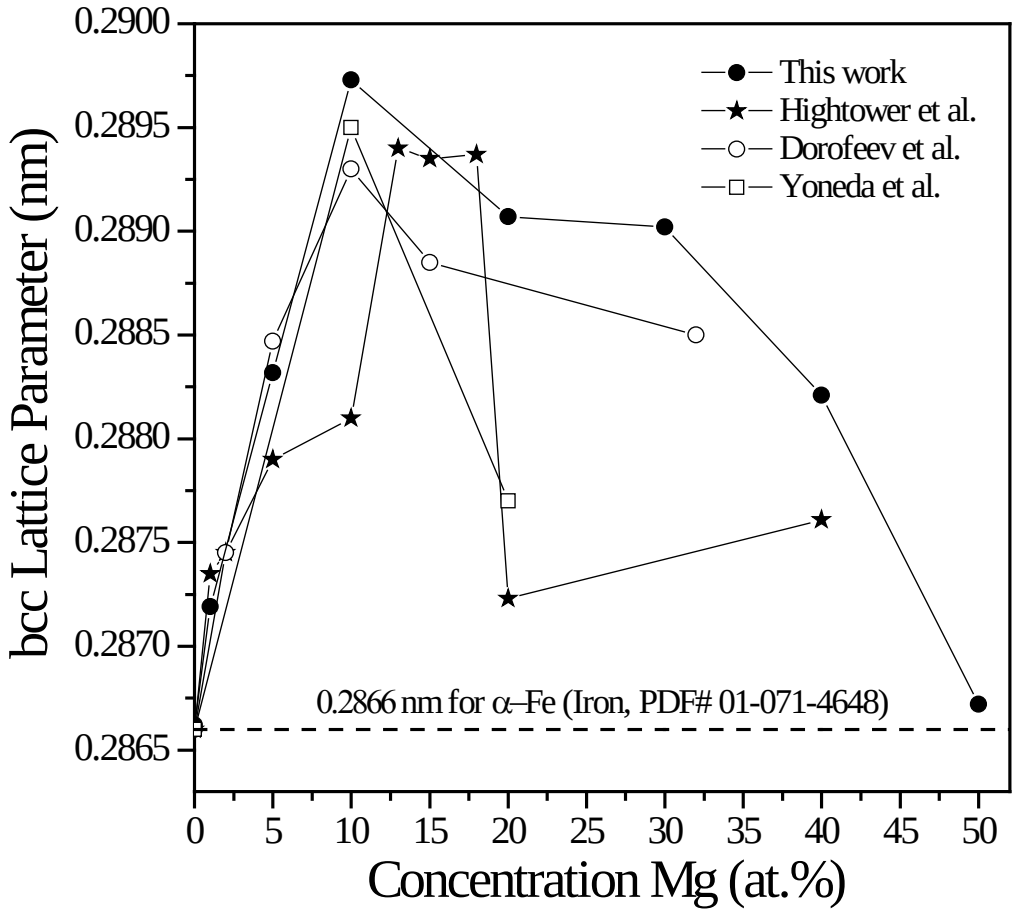

Figure 2.3. Variation of lattice parameter for the bcc phase as a function of nominal composition of the post dry milled powder, with reference data from Hightower et al. [102], Dorofeev et al. [100], Yoneda et al. [172]; the horizontal dash line indicates the lattice parameter of α-Fe. (PDF# 01-071-4648)

2.3.2 Microstructural characterization of Fe-Mg powder after wet milling

Figure 2.4(a) shows the collected XRD patterns of as prepared milled powder after wet milling corresponding to $Fe_{100-x}Mg_x$ along with simulated patterns for bcc-Fe and hcp-Mg. Surprisingly, all of the Bragg peaks due to bcc phase of solid solutions of Mg in α-Fe and hcp-Mg after dry milling have disappeared at x = 10, 20 and 30 ($Fe_{90}Mg_{10}$, $Fe_{80}Mg_{20}$and $Fe_{70}Mg_{30}$) which are shown in Figure 2.1(a) and it exhibits the typical broad diffraction pattern corresponding to the fully amorphous phase with no indication of any residual crystalline phases. This means that it has been completely transformed to a homogeneous amorphous phase and it was observed to be initiated by diffusive mixing mechanism [122, 176]. For x < 10 powders ($Fe_{99}Mg_1$and $Fe_{95}Mg_5$), the intensity of the peak corresponding to bcc (110) is decreased and its width increased due to a reduction in crystallite size and introduction of lattice strain [122, 177] and the peaks from residual bcc (200) and (211) are still faintly visible without amorphization. For $Fe_{60}Mg_{40}$ powder, the XRD pattern also shows the presence of unreacted bcc (110) over the amorphous peak at around 45° and all Mg peaks completely disappear. This unreacted bcc peak becomes significantly sharper with increasing Mg content (x=50) and another three distinct peaks from a crystalline phase which begin to emerge at around 37°, 65° and 82°. These crystalline phases are identified to be Mg (101), α-Fe (200) and (211) phases depending on the composition. Here, it should be noted that diffraction peaks corresponding to unreacted bcc (110) phase are different between x=5, 40 ($Fe_{95}Mg_5$ and $Fe_{60}Mg_{40}$) and x=1, 50 ($Fe_{99}Mg_1$ and $Fe_{50}Mg_{50}$) each other in Figure 2.3(b). The peaks corresponding to bcc (110) of the former composition are shifted to a lower angle indicating lattice expansion and formation of solid solutions of Mg in α-Fe. However, the same peaks from the other (x=1, 50) have same position with pure α-Fe.

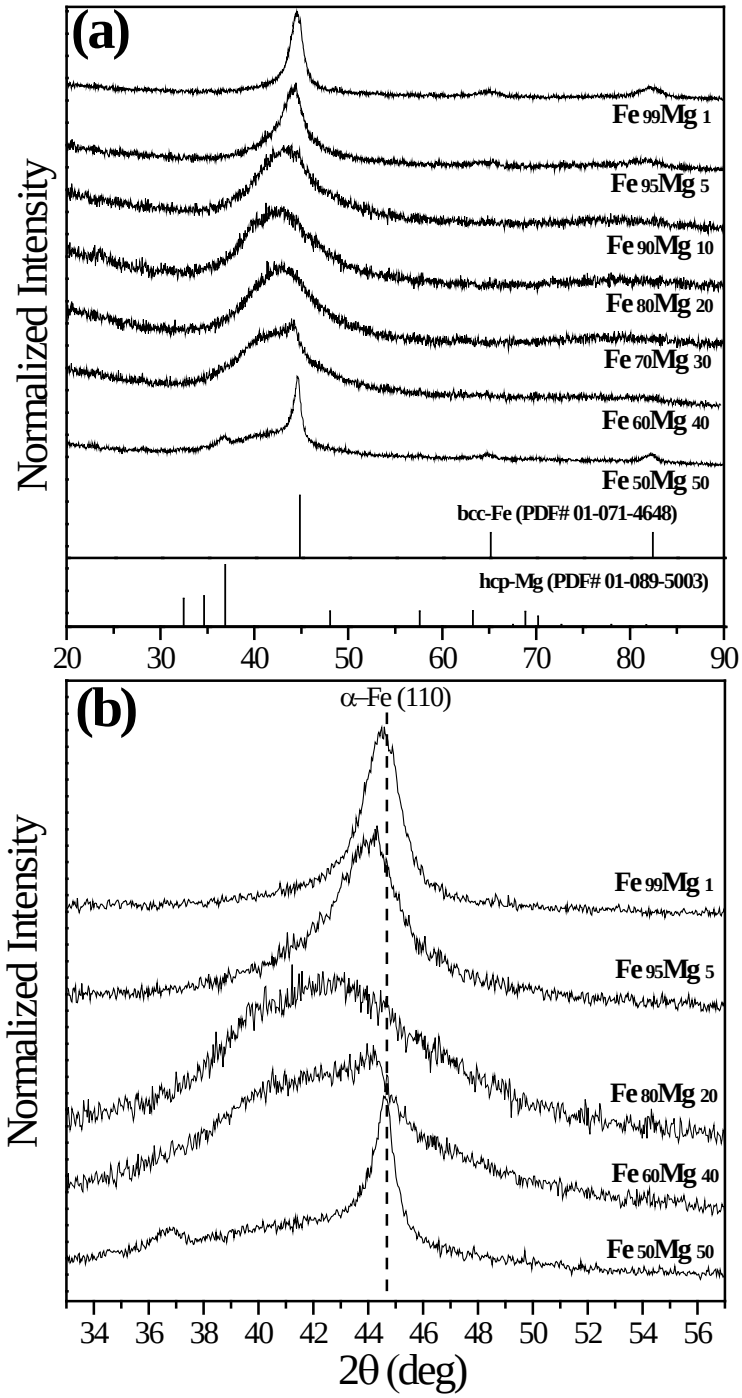

Figure 2.4. The X-ray diffraction patterns of (a) Fe80-xMgx powder (x = 1-50) after subsequent wet milling by HEMA and schematic diffraction patterns of bcc-Fe and hcp Mg. (b) enlargement of (110) profiles from (a); the dashed lines indicate the position of the α-Fe (110) reflection. (PDF# 01-071-4648)

The morphologies of the Fe and Mg raw element powders used in this work as well as the as milled $Fe_{70}Mg_{30}$ powder by HEMA are shown in Figure 2.5 (a-d). The SEM images indicate that the initial Fe and Mg powders consisted of particles below 10μm and 50μm, respectively. These results are in good agreement with the manufacturer's information. During the HEMA process, the powder particles are repeatedly flattened, cold welded, fractured and re-welded such that the final products usually show large changes in shape, size and distribution from their initial state [122]. Particle shapes also varied significantly after HEMA, with both spherical and plate-like morphologies being found in the starting powders. The as-dry milled powder has a relatively broad distribution of particle size from ~2 to ~40 μm and agglomeration of powder particles with formation of tiny flaky structure is observed as shown in Figure 2.5(c). The final $Fe_{70}Mg_{30}$ amorphous powder after wet milling consisted of irregular shaped particles which were smaller than ~5μm with the presence of much finer particles (< 1μm). Some agglomeration of particles was also found but the powder had a relatively homogeneous distribution from the steady-state conditions is achieved, as shown in Figure 2.5(d). EDX analysis in Table 2.1 indicates that the chemical composition of the amorphous powder is very similar to the starting composition. It is also found that the constituent elements are homogeneously distributed at the atomic scales. Figure 2.5(e) and (f) show the bright-field TEM, HRTEM images with corresponding selected-area diffraction (SAD) pattern and the Fourier transform of $Fe_{70}Mg_{30}$ amorphous powder. It can be seen that the particles show a very fine/homogeneous microstructure with amorphous halo SAD pattern in Figure 2.5(e). The HRTEM image and the Fourier transform present a maze like pattern/central halo and diffuse rings which is characteristic of an amorphous structure, also consistent with the XRD results of amorphous powders shown in Figure 2.4(a).

Figure 2.6 shows the corresponding DSC thermograms of the amorphous powder of $Fe_{70}Mg_{30}$ by HEMA. It is apparent from the DSC thermogram that the glass transition temperature (T_g), the crystallization temperature (T_x) and the super-cooled liquid region ($\Delta T=T_x-T_g$) are about 246.5°C, 364.7°C, 118.6°C, respectively. Moreover, one exothermic peak, marked as T_p, is observed in the trace, and is identified as the crystallization reaction peak.

Result from HEMA indicate that an amorphous phase is obtained through a solid solution forms first which upon continued milling becomes amorphous. In the literature, it has been also reported that a solid solution forms first which upon continued milling becomes amorphous [178-180].

Table 2.1**.** Chemical composition the as milled Fe70Mg30 amorphous powder by HEMA.

Element	Chemical composition
Fe K (at%)	70.94 ± 1.88
Mg K (at%)	29.06 ± 1.88

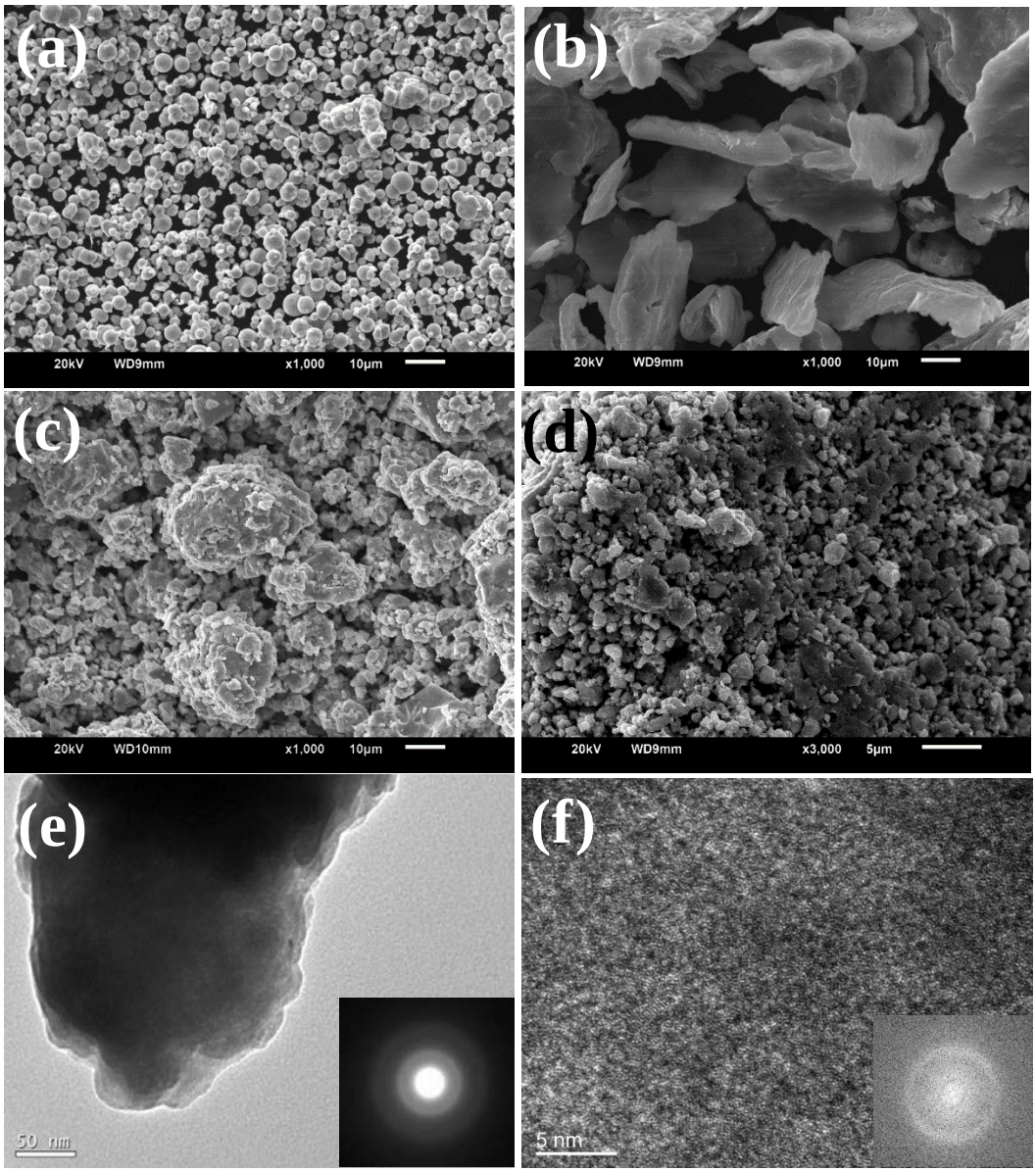

Figure 2.5**.** SEM images of powder precursors to fabricate Fe-Mg amorphous powder. (a) Pure Fe <10μm, (b) Pure Mg <325 mesh, SEM image of as milled $Fe_{70}Mg_{30}$ powder (c) by post dry HEMA, (d) by sequential wet HEMA with overall chemical composition, (e) Bright field TEM image with corresponding SAD pattern and (f) HRTEM image with the Fourier transform of the HRTEM image for HEMA derived amorphous $Fe_{70}Mg_{30}$ powder.

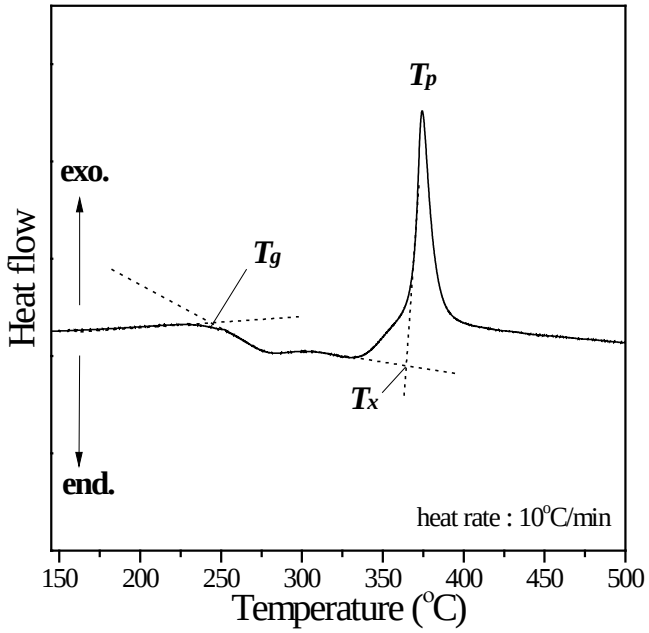

Figure 2.6. DSC thermogram for the $Fe_{70}Mg_{30}$ amorphous powder by HEMA.

2.4 DISCUSSION

2.4.1 Formation of solid solution of Mg in α-Fe during HEMA

The present results provide conclusive evidence that HEMA of Fe and Mg leads to the formation of fully amorphous phase at the $Fe_{100-x}Mg_x$ (x=10, 20 and 30 at.%) composition through two sequential process which are dry and wet milling. After the dry milling process, XRD showed that the samples were entirely bcc phase for Mg concentrations less than 30 at. % in Figure 2.1(a). This suggests solubility of Mg in α-Fe phase , as do the two observations that (1) there is a increased broadening and shift of the bcc diffraction peaks to small angle which are shown in Figure 2.1(b), and (2) the single phase bcc alloy shows an increase in lattice parameter in Figure

2.3 indicating lattice expansion and formation of a solid solution. It can be interpreted that Mg atoms subsitituted for the Fe atoms in the bcc lattice and the lattice parameter of this alloy was larger than that of a pure Fe bcc lattice due to the larger atomic radius of Mg [172]. The formation of supersaturated solid solutions is one of the important metastable constitutional effects observed in alloys by HEMA.

There have been many reports on the extension of solid solubility limits but the reasons are not yet clear [122, 181]. In the literature for Fe-Mg system, HEMA has led to the generation of substitutional solid solutions with up to 20 at. % Mg within the bcc of α-Fe [102]. Later, Dorofeev et al. found that about 5~7 at. % Mg in α-Fe forms in supersaturated solid solution [100, 101, 182] and a single phase bcc alloy was produced using Mg concentration up to about 15 at. % by Yoneda *et al* [172]. These are consistent with present results even though there is a slight difference in the observed solubility limit. Above the solubility limit observed in this study (>~20 at.% Mg), the as-dry milled powders comprised two-phase (solid solution of Mg in α-Fe and hcp-Mg) mixtures which are shown on XRD results of $Fe_{70}Mg_{30}$ and $Fe_{60}Mg_{40}$ in Figure 2.1. These results can be rationalized in terms of the Hume-Rothery rules that was previously proposed for a planetary SPEX 8000 high energy shaker mill [183] and it is reported for limits of solubility of the Fe-Mg system [102]. This rule states that ~25 at.% solubility is achievable for powders prepared by mechanical alloying when the radii of metallic elements differs by <15%, and the electronegativity difference between the two elements is not too large, typically within a range of ± 0.4. Here, the metallic radii of Fe and Mg atoms are 0.126 and 0.16 nm [184], respectively, and their electronegativities are 1.83 and 1.31 [91], respectively. They differ by ~21% in metallic radius and 0.52 in electronegativity. Therefore, the dissolution of Mg in α-Fe alloys was expected to be low in this study and accords closely with predictions.

2.4.2 Formation of amorphous powder by HEMA in Fe-Mg system

It appears from these results that in the post dry milling process that no pronounced amorphous phase formation was achieved using these milling conditions, suggesting that they were not intense enough to destabilize the crystalline phase and allow the formation of an amorphous phase. This is due to the fact that severe plastic deformation, in general, facilitates the formation of an amorphous phase due to the introduction of fresh interfaces that raise the free energy of the system [127], but true alloying among ductile powder particles can occur only when a balance is maintained between cold welding from heavy plastic deformation and fracturing of particles [122, 173]. This balance is controlled mostly by the addition of a process control agent (PCA) [122, 181]. During HEMA, the PCA is absorbed on the surface of the particles and invariably lowers the surface tension of solid materials. In this Fe-Mg system, Mg elemental powder is too ductile to minimize the effect of cold welding and it becomes the dominant factor during post dry milling. Thus, it appears that the increase in free energy of the crystalline phase was not sufficient to exceed that of the hypothetical amorphous phase.

By post dry milling in the absence of the PCA, only solid solution was formed for concentrations less than 50 at.% Mg with an enlarged lattice parameter as shown in Figure 2.1 and the particles appearing as elongated into flake-shaped morphology with large agglomeration observed in Figure 2.5(c). For the sequent wet milling, toluene is added to the as-dry milled powders, as PCA, to reduce the effect of cold welding, thereby inhibiting agglomeration and welding on the vial wall. In this case, the supersaturated α-Fe solid solution becomes unstable and transforms to an amorphous phase, as seen in Figure 2.4(a) from the complete disappearance of the Bragg peaks.

Thus, it can be concluded that the addition of PCS achieves the appropriate balance between cold welding and fracture rate and thus the milling energy reaches a critical value to form the amorphous phase. Increased milling energy is normally expected to introduce more strain and increase the free energy in crystalline powder in HEMA and thus make amorphization easier [122]. This observation clearly confirms that it has been possilbe to produce an amorphous phase in this immiscible Fe-Mg system. One of the interesting results in the present study is the formation of solid solution of Mg in α-Fe at $Fe_{95}Mg_5$, which is formed in dry milling but also observed after wet milling wihtout transfromation to amorphous phase. As summarized earlier, starting from blended $Fe_{100-x}Mg_x$ (x=10, 20, 30 and 40) elemental powders, an amorphous phase can be formed through the formation of supersaturated solid solution, as seen in Figure 2.1 and 2.4. However, it doesn't form any amorphous phase at $Fe_{95}Mg_5$ though HEMA conducted through two sequential process of the dry and wet milling. This can be rationalized in terms of known mechanisms of amorphous phase formation. Amorphization is also facilitated by the strain energy induced into the alloy system due to the size differences between the solvent and solute elements in a binary system. It achieves the critical amount of distortion in lattice which destabilizes the crystal lattice resulting in the formation of the amorphous phase [185-187]. Egami et al. [188] have proposed the criteria (Equation 1) from empirical results to determine the concentration range of binary system where amophrization will occurs. It was originally developed for rapid quenching processing but can be applied to amorphization by HEMA [186]. Some researchers have shown that this criteria is applicable to the immisicle Nb-Zr system which forms amorphous phase by HEMA [109, 127]. The minimum solute concentration, C_B^{min}, necessary to form amorphous phase is inversely related to atomic size mismatch:

$$C_B^{min} = 0.1 \times \left[\left(\frac{r_B}{r_A}\right)^3 - 1\right]^{-1} \quad (1)$$

Where r_B and r_A represent the atomic radius of the solute (B) and solvent (A), respectively. In the case of the Fe-Mg system, the radii of the Fe and Mg atoms are 0.126 and 0.16 nm. Thus the theoretical minimum concentration of Mg for the formation of the amorphous phase is calculated to be 9.54 at. % Mg. Thus, it is worth noticing that this value is very close the composition range of 10~40 at.% Mg for the formation of amorphous phase and it is not surprising that no amorphous phase was obtained at $Fe_{95}Mg_5$ by HEMA (Figure 2.4).

2.5 CONCLUSIONS

This work is the first to demonstrate the formation of an amorphous Fe-Mg alloy, through the process of HEMA from the immiscible Fe-Mg system that show a positive heat of mixing between the constituent elements. It is obtained through the sequential process of dry and then wet milling under the milling conditions described for this study. The formation of the amorphous phase is verified and confirmed by XRD and TEM analysis. Therefore, we can summarize the amorphization process at the $Fe_{100-x}Mg_x$ (x=10, 20, 30 and 40 at.%) composition as follows :

Mixture of elemental powders → solid solution → amorphous

3.0 SPECIFIC AIM 2: SYNTHESIS AND OPTIMIZATION OF THE PROCESSING PARAMETERS FOR THE DEPOSITION OF THIN LAYERS OF IRON-MAGNESIUM ALLOYS USING PULSED LASER DEPOSITION (PLD) AND IDENTIFICATION OF THE POTENTIAL USE OF THESE ALLOYS AS BIODEGRADABLE SYSTEMS USING IN VITRO CHARACTERIZATION METHODS

3.1 INTRODUCTION

Following the synthesis and materials characterization experiments for amorphous $Fe_{70}Mg_{30}$ powder reported in Section 2, amorphous thin layers were prepared by PLD from HEMA derived amorphous powder in order to identify the potential use of Fe-Mg alloy as a biodegradable system using in vitro characterization methods. As shown by the extensive studies over the last three decades [122], HEMA using elemental metals is an efficient way for creating metastable states in particular, supersaturated solid solutions or amorphous structures of immiscible components. However, the approach has one major limitation; to form bulk material from the as synthesized ball milled powders, additional processes such as sintering are necessary. As mentioned in the Section 1.3.2, a major impediment to the use of sintering in the Fe-Mg system is the large temperature difference in the melting points of Fe and Mg. Therefore, formation of thin layer can be one of the solutions that can be explored to overcome this limitation.

There are several possible techniques that can be used to prepare amorphous thin films. Among the different techniques, pulsed laser deposition (PLD) has several characteristics that distinguish it from other film growth methods [138]. These include: (a) attainment of near stoichiometric composition of the target in the deposited film; (b) flexibility and fast response; (c) higher deposition rate; (d) lower synthesis temperature and highly oriented growth of films; (e) *in-situ* deposition of multilayer films; and (f) ease of control of the film thickness. For obtaining metallurgical thin films, other deposition techniques are competitive, but PLD can be used to deposit thin films from any material, from pure elements to multi-component compounds and moreover, a major advantage is that the stoichiometry of the target material can be reproduced in its entirety in the deposited films [138]. PLD has recently been used to direct the plume of material ablated from a biocompatible ceramic target onto substrate materials to form a thin biocompatible coating that may be used for dental or orthopedic implant applications [189]. In particular, PLD has been demonstrated to be an effective method for producing thin films of crystalline calcium hydroxylapatite (HA), the primary mineral constituent of natural bone and one of the most ubiquitous biocompatible materials known [190-192]. Therefore, PLD is especially well suited for metal/ceramic thin films deposition.

Accordingly, in this dissertation, two-pronged approaches employing PLD will be used for biological applications. In the first case, PLD will be used for the synthesis of thin films from the metastable alloys generated by HEMA. In the second approach, PLD will be employed to synthesize the alloy utilizing a mixture of the pure elements. The former technique to generate thin films is one way to solve the limitation of the sintering process for HEMA derived Fe-Mg alloy powders described in Section 1.3.2. In the second, thin film alloying using PLD is one of the preferred paths exploited to synthesize metastable alloys involving immiscible elements

[193-196]. The thermalization rate of the deposited material in PLD is extremely high and lies between $\langle\varepsilon\rangle/\tau = 10^{11}\sim10^{18}$ K/s, where $\langle\varepsilon\rangle$ ~100eV is the mean ion energy and τ the is relaxation time. Under such extremely non-equilibrium formation conditions, the kinetic factors (diffusion rates) rather than thermodynamic driving force (potential barrier heights) play a major role in the formation and stablization of the physical form and structure of the growing films. It thus makes the formation of metastable phases in PLD highly probable [139]. The following examples support this inference. Krebs and Bremert [140] reported on the formation of $Fe_{50}M_{50}$ (M=Zr, Nb, Ti, Hf), $Cu_{50}Zr_{50}$ and $Pd_{80}Si_{20}$ amorphous alloys deposited by PLD. Instead of the decomposition of the immiscible materials systems such as Fe-Nb, Fe-Ag, and Fe-Cu, a continuous series of polycrystalline supersaturated solid solutions were formed. A homogeneous non-equilibrium crystalline alloy with a super-saturation of > 44 at.% Ag in Ag-Ni system on PLD deposited Ag-Ni was reported by van Ingen et al. [141]. It is remarkable that this material system though possessing such a high driving force for decomposition despite the constituents being insoluble in both the solid and the liquid equilibrium states, it is possible to generate the alloys without inducing any precipitation or second phase formation. In line with these reports, it was hypotheseized that the synthesis of Fe-Mg alloying films is possible either by using PLD from a Fe-Mg alloy target derived by powder made by HEMA or from the targets prepared by blending a mixture of the elemental powder of Fe and Mg corresponding to the alloy composition. The present work therefore reports the results of a study conducted to explore the influence of processing parameters/ target on the microstructures of the Fe-Mg amorphous thin film layers by PLD and accordingly, evaluate these layers using preliminary in vitro cytocompatibility and corrosion experiments for biomedical applications. Prior to conducting the PLD studies to generate amorphous films corresponding to the Fe-Mg alloys studied in the previous chapter,

attempts were made to explore the efficacy of the PLD approach by conducting pilot studies on the Mg-Ca-Zn system. These studies were conducted to explore and validate the use of the PLD approach to generate amorphous films mimicking the structure and composition of the amorphous targets. The studies then paved the way for generating the various classes of materials and systems described and outlined in the various four specific aims.

3.2 MATERIALS AND METHODS

3.2.1 Pilot and main PLD studies

In this section, we first performed pilot studies to confirm the suitability of the experimental setup using the Mg-Zn-Ca based systems; these served as a basis for the subsequent main studies for the Fe-Mg system. The Mg-Zn-Ca based systems are one of the representative system with good glass forming ability (GFA) and are ideal candidates for controlling the degradation of metal implants [164, 197].

3.2.2 Alloy synthesis by HEMA

The targets corresponding to $Mg_{60}Zn_{35-x}Ca_x$ (x=1, 3, 5) composition have been produced by high energy mechanical alloying (HEMA) and compaction although powders corresponding to $Mg_{60}Zn_{35-x}Ca_x$ (x =0~20) have been generated. Commercial elemental powders of pure Mg (99.8%, <325 mesh, Alfa Aesar), Zn (97.5%, 6-9 μm, Alfa Aesar) and Ca (99.5%, <16 mesh, Alfa Aesar) were chosen as the starting materials which were accurately weighed corresponding

to the desired compositions. The mixture of elemental powders was loaded into stainless steel (SS) vials containing 2 mm diameter SS balls as the milling media. The ball to powder weight ratio (BPR) was 15 to 1, and the total weight of the starting mixture was 4g. The mixture was subjected to dry milling in a SPEX 8000 high energy Shaker Mill for up to 3h. Post dry milling, 2ml of toluene (anhydrous, 99.8%, Sigma-Aldrich) was loaded into the vial and the mixture was subsequently wet milled for an additional period of up to 3 h to reduce the adhesion of powders on the balls and the inner surface of the milling vial. Handling of the powders and loading of toluene were conducted inside an argon-filled glove box in which the oxygen concentration was kept below 1.0 ppm. The $Fe_{70}Mg_{30}$ amorphous powder were synthesized by similar methods in Section 2.2.1. Post ball milled Mg and Fe based powders were dried and then compacted at a pressure of 60 kpsi using a Flow Autoclave System cold isostatic compaction press to produce 25.0 mm diameter discs to be used as targets for subsequent PLD deposition.

3.2.3 PLD system and thin films production

All the thin films were produced by PLD utilizing a 248 nm KrF excimer laser (Lambda Physik EMG 201) irradiation pulsed at 25 ns FWHM in a high vacuum chamber with a base pressure of 10^{-6} Torr. In all depositions the spot size was approximately 1×3 mm, the fluence was 8.3~9.6 J/cm^2, the laser pulse frequency was maintained at 10 Hz and the deposition rate was approximately 2.3 Å/s determined as a mean value. The cold stage, which was supplied with liquid nitrogen, was installed for deposition of films at low substrate temperatures. The target to substrate distance was maintained that substrate was placed opposite to the target at a distance of 58 and 80 mm, with targets rotated during deposition. The 25 mtorr of Argon partial pressure was introduced to the vacuum system with initial base pressure of 2×10^{-7} torr using a needle

valve gas controller. Films were deposited at -90 °C for a deposition time of 30min on Si wafer and at room temperature for a deposition time of 5, 10 and 30 minutes on three different substrates. The first was amorphous SiO_2 thermally grown on Si wafer for use in glancing angle X-ray diffraction (XRD). The second substrate was a regular cell culture dish for cytocompatibility tests, and the third substrate was fused silica glass for bio-corrosion tests.

3.2.4 Characterization of powders and films

The microstructure and phase assemblage of thin films and milled powders were examined by glancing angle (Philips PW 1830 with Cu-Kα radiation) and conventional X-ray diffraction (PANalytical X'pert Pro with Cu-Kα radiation). The thickness of the deposited films was measured by surface profile measuring system (Veeco Dektak^{3}ST). A JEOL JEM2000FX operating at 200kV was used for conducting transmission electron microscopy (TEM) and obtaining conventional bright field images. High resolution (HR) TEM observations were carried out using a JEOL JEM-2100F equipped with attachments for X-ray energy dispersive spectroscopy (XEDS) analysis from Oxford Instruments (Inca platform). The Gatan Digital Micrograph (Gatan software, USA) and the Image-pro plus (Media Cybernetics, Inc., USA) were used to analyze TEM images. TEM samples were obtained by directly depositing the film by PLD on silicon nitride supported window grids (Ted Pella, USA) for observation under the TEM. Additionally, samples were made by depositing the films on oxidized silicon wafer containing a photo-resist following the above method. Films were lifted off from the substrate by stripping the photo-resist and transferring onto standard TEM copper membrane grid (Ted Pella, USA) for observation under the TEM. The thermal properties of the final milled powder and thin layer

were studied by differential scanning calorimetry (DSC, Netzsch STA 409) at a heating rate of 10°C/min under an ultra high purity Ar gas flow.

3.2.5 Electrochemical bio-corrosion study

Potentiodynamic polarization was used to test the electrochemical corrosion of the Fe-Mg alloy thin layer compared to the film and bulk (99.8+%, 1 mm foil, Goodfellow) of pure Fe. All alloy and pure Fe thin film samples were deposited on fused silica glass for 30 minutes by PLD, with thickness in the range of ~1.3 μm. These films were connected to a Cu lead wire with silver paste and then electrically insulated with epoxy resin leaving an exposed working area of 2 cm^2, so that only one side was exposed for conducting the electrochemical tests. Samples of bulk pure Fe were also prepared by connection to a copper wire lead, mounting in epoxy resin, and one side mechanically polished down to 1 μm flatness. This surface, ~2.25 cm^2, was cleaned with isopropyl alcohol, then immediately exposed to the electrolyte and tested. Testing was carried out utilizing a three-neck jacketed flask (ACE Glassware) filled with the electrolyte of 125 ml DMEM growth media containing 1% penicilin/strepomycin (P/S) and 10% fetal bovine serum (FBS), equilibrated to 37°C. It should be noted that there are some reports that higher corrosion rate may be attributed to higher L-glutamine, which varies depending on cell culture media, since it can form complexes with Mg ions [198, 199] but no similar study has been completed with Fe ions. Ag/AgCl reference electrodes (4.0M KCl, Accument) and a platinum wire counter electrode were employed. All samples were immersed in the electrolyte to reach a stable open circuit potential (OCP) for 40 minutes, before initiating the potentiodynamic polarization at a scanning rate of 0.3 mV/s using a CH instruments potentiostat (CHI 604A). The Tafel plots were extrapolated to determine the corrosion current density, i_{corr}, at the intersection point with the

corrosion potential, E_{corr}. Corroded samples were rinsed with DI water and ethanol and air dried, and subsequently characterized using glancing angle XRD and EDX to assess the formation of corrosion products.

3.2.6 Cytocompatiability tests

In order to explore the cell cytocompatibility of the alloy systems, each alloy system was deposited on the cell culture dish and silica glass by PLD, then cell viability tests were conducted.

3.2.6.1 Cell culture

Murine pre-osteoblast cells (MC3TC-E1, American Type Culture Collection, Rockville, MD), human mesenchymal stem cells (hMSCs, Lonza, USA), human umbilical vein endothelial cells (HUVECs, Linza, USA) and murine fibroblast cells (NIH3T3, American Type Culture Collection, Rockville, MD) were utilized for cell culture studies. Cells were cultured under 37 °C, 5% CO_2, and 95% relative humidity in α-MEM (Gibco, Grand Island, NY) growth media containing 1% P/S (Gibco, Grand Island, NY) and either 10% FBS (Atlanta Biologicals, Lawrenceville, GA), for MC3TC-E1, or 20% FBS for hMSCs, EBM-2 bullet kit (Lonza, USA) for HUVEC and DMEM (Cellgro, Manassas, VA) growth media containing 1% P/S and 10% FBS for NIH3T3. The MC3T3 and NIH3T3 cells cultured at third to seventh passage, and hMSCs and HUVECs cultured at second to third passage were used in this experiment.

3.2.6.2 Direct cell viability and adhesion test (Live/dead assay)

For direct cytocompatibility and cell adhesion testing, MC3TC-E1, hMSC, HUVEC and NIH3T3 cells were cultured directly on the surface of Fe-Mg alloy thin layer deposited by PLD. Fe-Mg

alloys were deposited on fused silica glass by PLD with the film area approximately 9mm x 9mm. The samples were sterilized on all sides by UV for 60 minutes and incubated in cell culture media for 10 minutes, after which time cells were seeded on the samples directly at a density of 80,000 cells per well. Live and dead cells were stained using live/dead staining kit (Life Technologies, Grand Island, NY) on days 1 and 3 post seeding following the manufacturer's protocol. Cells were then imaged by an inverted microscope with the fluorescence illuminator (CKX41, Olympus, Olympus America Inc.). For each substrate images were taken from three to six different locations to obtain an overview of cell attachment. After fluorescence imaging, cells on the samples were fixed by 2.5% glutaraldehyde then subjected to alcohol dehydration. Fixed cells on samples were air-dried, after which they were imaged by SEM.

3.2.6.3 Indirect cell viability test (MTT assay)

Indirect cell viability test was assessed using the MTT activity assay (Vybrant MTT Cell Proliferation Assay Kit). Extraction medium was prepared using each cell growth media supplemented with serum in a surface area/extraction medium ratio 6 cm^2 ml^{-1}, in accordance with ISO 10993-12 [200], at 37 °C in a humid atmosphere with 5% CO_2 for 72 hours. The extracted medium was stored at 4°C until the cytocompatibility testing. This extraction was designated as 100% extract solution. The control groups involved the use of media without extract as a negative control and media containing 10% dimethyl sulfoxide (DMSO) as a positive control. The cells were seeded in 96-well plates at 6000 cells/well with 200µl media in each well and incubated for 24 hours to allow for attachment. After pre-cell culture, the media was then replaced with 100µl of 100% extract medium and incubated for 1, 3 and 7 days. After that, media and extracts were replaced with fresh cell culture media and 10µl of MTT were added to

each well. The samples were incubated with MTT for 4 hours at 37°C and then 100µl of formazansolubilization solution (10% sodium dodecyl sulfate in 0.01M HCl) were added to each well for 12 hours in the incubator under the cell culture atmosphere. The spectrophotometrical absorbance of the samples was measured with the Synergy 2 Multi-Mode Microplate Reader (Bio-Tek Instruments, Winooski, VT) at 570 nm, with a reference wavelength of 630 nm.

3.2.6.4 Ion release

The thin layer samples of $Fe_{70}Mg_{30}$ and pure Fe on glass were immersed in each cell growth media containing serum, equilibrated to 37°C for 72 hours. All conditions for immersion test are same with cell viability test including the surface area/extraction medium ratio (according to the ISO 10993-12 [200]). After immersion for 72 hours, the media was collected and then diluted in 0.03 M Tris buffer solution to be analyzed using inductively coupled plasma optical emission spectroscopy (ICP-OES, iCAP duo 6500, Thermo Fisher). The Fe and Mg ion concentrations in solution were compared to media and each other. Samples were prepared in triplicate for each condition.

3.2.6.5 Statistical analysis

The experimental values were analyzed using the Student's t-test and one-way analysis of variance (ANOVA). They were expressed by mean values ± standard deviation (SD) and statistical significance was considered as $P < 0.05$.

3.3 RESULTS

3.3.1 Mg-Zn-Ca system; HEMA and processing parameter for PLD (Pilot study)

Figure 3.1 shows the XRD patterns of as prepared milled powder corresponding to $Mg_{60}Zn_{40-x}Ca_x$ and the targets generated from the milled powders. The XRD patterns of the powder for x=5 shows the typical broad diffraction pattern corresponding to the fully amorphous phase but x=0, 1, 3 and 10 powders show a few narrow peaks that begin to emerge over the amorphous peak at around 20° and 40°. This result indicates that the HEMA process can generate phases that are fully (or mostly) amorphous from these compositions. Also it is found that the constituent elements are homogeneously distributed at atomic scales, from the result of a XEDS (not shown here). However, at other compositions, X-ray diffraction patterns exhibit low-intensity sharp peaks from a crystalline phase which were found together with a broad diffraction peak from an amorphous phase. These crystalline phases are identified to be an inter-metallic phase of Mg-Zn, Ca-Zn, pure Mg, Zn and Ca depending on the composition (Fig. 3.1). The amorphous phase formation by HEMA is known to be critically dependent on the milling conditions, the detailed history of the starting materials, milling container, grinding medium, and finally the BPR [122]. Results from HEMA indicate that a fully amorphous phase is obtained from only the $Mg_{60}Zn_{35}Ca_5$ composition using the milling condition described for this study, and the formation of the amorphous phase is verified and confirmed by XRD analysis.

Details of the target, including crystal structure, distribution of elements, surface roughness, or optical properties can affect the quality of amorphous films, particularly when the formation of the amorphous phase depends on the deposition rate or kinetics of the flux.

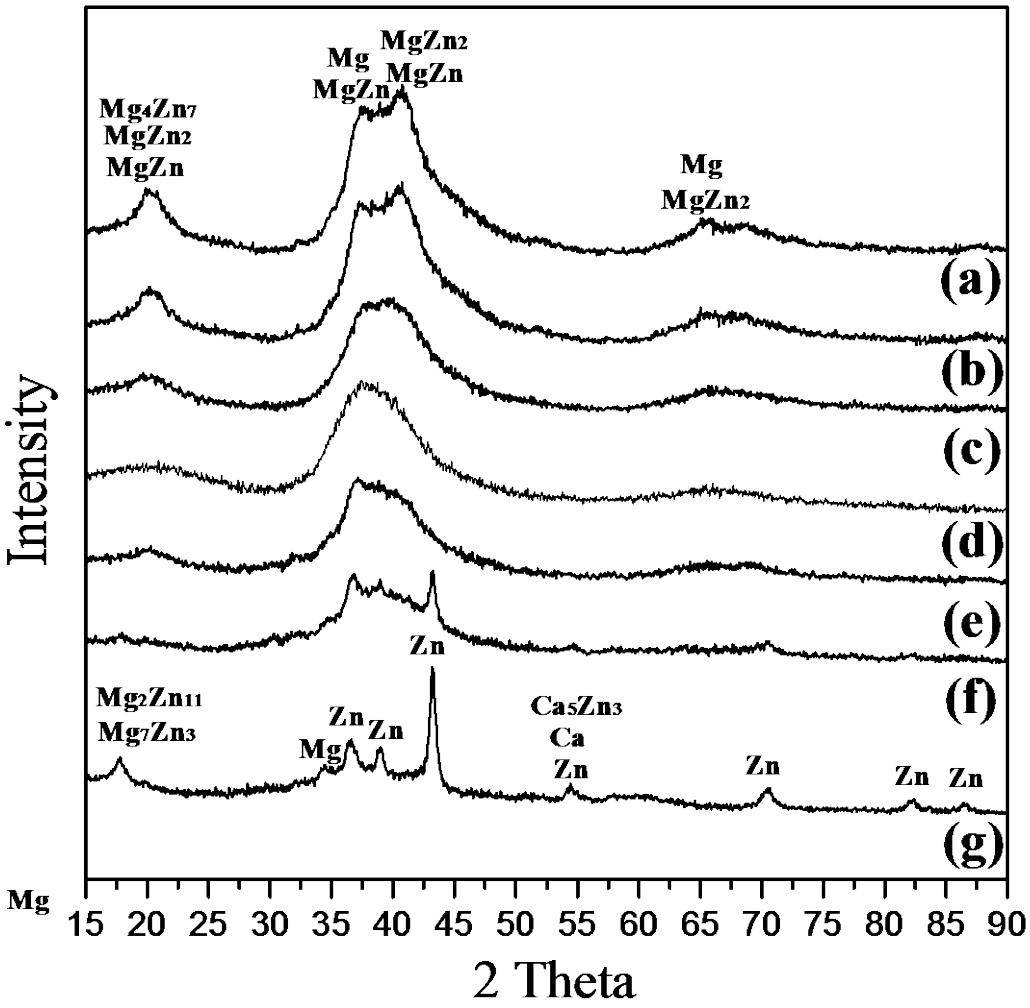

Figure 3.1. The X-ray diffraction patterns of $Mg_{60}Zn_{40-x}Ca_x$ (x=0~20) powder obtained following 6 h of milling time that were used to generate the targets: (a) x=0, (b) x=1, (c) x=3, (d) x=5, (e) x=10, (f) x=15 and (g) x=20, respectively.

In addition, clusters delivered to the deposited film in the form of a) ejected solid fragments [201], or b) molten droplets can also result in unwanted crystalline phases [140]. In the pilot study, the PLD of $Mg_{60}Zn_{35}Ca_5$ film was carried out by varying the crystal structure of the target, as well as varying the deposition time and controlling the substrate temperature.

Figure 3.2 shows the influence of the properties of the target on the characteristics of the deposited Mg-Zn-Ca films. All the thin films were deposited by PLD for 5 minutes from fully amorphous targets as well as targets comprising low and highly crystalline compositions. The thickness of the deposited film is ~ 500 nm corresponding to 5 minutes of deposition time shown in Figure 3.2(d). XRD patterns of all deposited films are shown in Figure 3.2(a). This figure shows broad amorphous diffraction patterns even though the HEMA powders corresponding to x=1 and 3 exhibit a few narrow crystalline peaks according to the XRD profile as shown in Figure 3.1 (b) and (c). These results imply that the amorphous phase is readily formed by PLD from a fully amorphous target in this composition range. Further studies were therefore focused on the $Mg_{60}Zn_{35}Ca_5$ composition since the starting powder, target, and the deposited films as shown in Figures 3.1(d) and Figure 3.2(a) corresponding to this composition was confirmed to be amorphous. In order to evaluate the influence of the structure of the target on the synthesis of amorphous thin films, the amorphous HEMA derived $Mg_{60}Zn_{35}Ca_5$ target was annealed at 200 °C for 20 hours in Ar atmosphere to form crystalline phase(s) of pure Mg, Zn, Ca and Mg-Zn intermetallic as shown by the XRD pattern (#2) in Figure 3.2(b).

In addition, a target comprising a blended mixture prepared from the elemental powder of Mg, Zn and Ca corresponding to $Mg_{60}Zn_{35}Ca_5$ was also prepared, and the corresponding XRD pattern (#3) is shown in Figure 3.2(b). In comparison to Figure 3.2(a), the XRD profiles of deposited thin films from highly crystalline target as shown in Figure 3.2(b) are displayed in

Figure 3.2(c). Sharp crystalline peaks appear over the broad background peaks even though the peak intensities were decreased compared to Figure 3.2(b) for both targets #2 and #3. These sharp peaks are distinctively identified as pure Zn, Ca and Ca-Zn intermetallic in the XRD pattern of the thin film obtained from target #2. In addition to pure Zn and Ca, an inter-metallic phase of Mg-Zn are observed in the XRD pattern of the thin film from target #3. The chemical composition of each thin film was measured by XEDS and shown in Figure 3.2(c). Each chemical composition is very similar to the target composition.

Figure 3.3(a) and (b) show the XRD patterns of PLD derived films for different deposition time and substrate temperature, respectively. For the deposited film corresponding to a PLD time of 10 minutes at 22 ^{o}C (room temperature) shown in Figure 3.3(a), a few narrow peaks start to emerge at around 40°. These narrow peaks become significantly sharper with increasing deposition time (or film thickness), indicating the formation of a greater amount of crystalline phase. This behavior can be due to the diffusional processes leading to nucleation and growth of crystalline regions in the otherwise amorphous film during deposition. Additionally, this can be due to the solid particulates or molten droplets which are ejected from the target and accumulate on the top of the amorphous films. Formation and accumulation of these particulates and droplets are well known in PLD processes and have been reported for other systems [138].

The targets used in this study are made by powder compaction and the roughness of the target surface is higher than the targets made by melting, casting and sintering of the elemental metals. This roughness may lead to the ejection of solid particulates or liquid droplets from the surfaces, which are then deposited on the substrate. Nonetheless, it is important to determine whether these crystalline phases result from these direct transport mechanisms, or were formed on substrate surface after deposition.

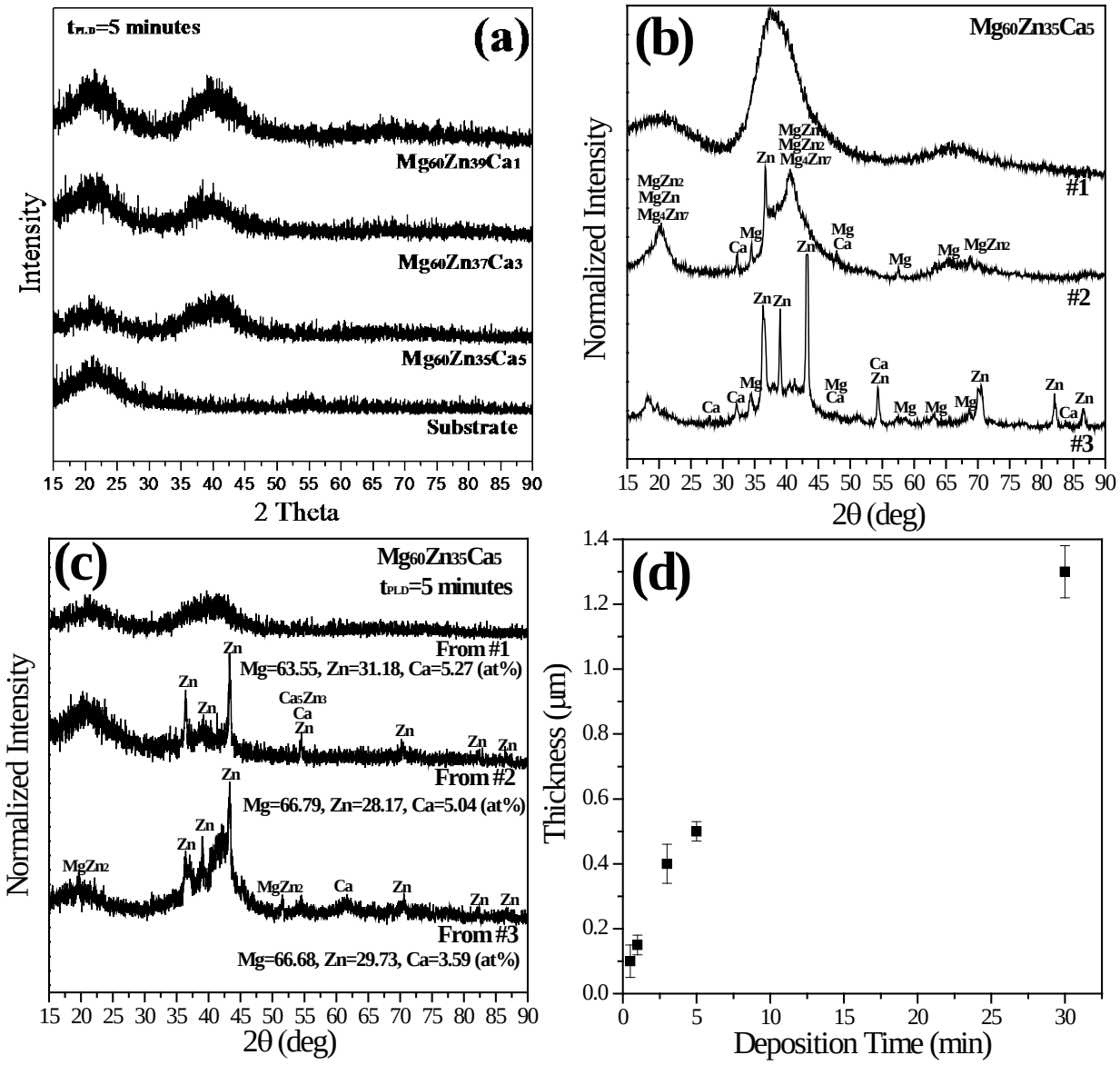

Figure 3.2. The X-ray diffraction patterns of (a) $Mg_{60}Zn_{40-x}Ca_x$ (x=1, 3 and 5) films deposited for 5min by PLD and of bare substrate, (b) different crystal structure targets in $Mg_{60}Zn_{35}Ca_5$ composition; as-milled amorphous target (#1), 200 ^oC annealed target from #1 (#2) and blended mixture starting precursors powders (#3), (c) deposited thin films for 5min by PLD from #1, 2 and 3 target and chemical composition of each films and (d) thickness of the films on normal stage for various time from as-milled amorphous target (#1).

Therefore, if an amorphous film instead of the crystalline film is grown on cold substrate, then it could be expected that the film morphology would reflect to a greater extent the conditions of the plume. Moreover, assuming that solid particulates are indeed ejected directly from the target, they should retain the same properties of the target after being incident on the cold substrate.

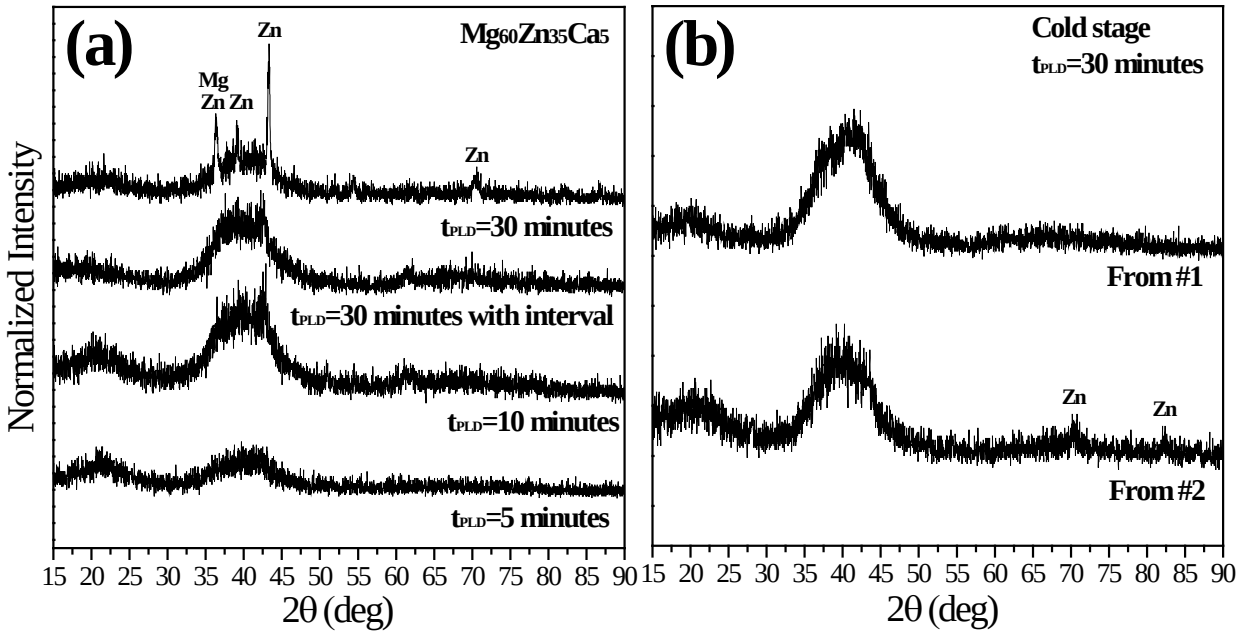

Figure 3.3. The X-ray diffraction patterns of $Mg_{60}Zn_{35}Ca_5$ (a) PLD deposited films on normal stage for various time from as-milled amorphous target (#1) and (b) PLD derived films for 30 minutes on cold stage from target #1 and target #2 (see text for details).

A dramatic influence of the substrate temperature on the deposited films is shown in Figure 3.3(b). Figure 3.3(b) shows the XRD patterns of the films deposited from targets #1 and #2 at a low temperature (-90 ^{o}C) using a cold stage for 30 minutes by PLD. In both cases, the intensity of pure Zn peaks are found to have disappeared or reduced compared to the XRD patterns of room temperature deposited films as shown in Figure 3.2(c) and 3.3(a), respectively.

These results suggest that crystalline phase formation in the deposited film was kinetically suppressed when the substrate temperate is lowered. The crystalline peaks are identified to be pure Zn as shown in Figure 3.3. It seems that Zn can form coarse particles easily on thin films because it has a relatively high vapor pressure and low melting temperature compared to Mg and Ca. This result thus indicates that the substrate temperature is the dominant parameter for formation of amorphous thin films corresponding to $Mg_{60}Zn_{35}Ca_5$ composition.

3.3.2 Fe-Mg system; processing parameter to synthesize amorphous films by PLD

The pilot studies revealed that the substrate temperature during deposition is a dominant parameter contributing to the formation of amorphous thin films of $Mg_{60}Zn_{35}Ca_5$ composition when the substrate is cooled to -90 °C. As mentioned in the section 3.3.1, many experimental parameters can be changed, which then have a strong influence on film properties during PLD.

In order to evaluate the influence of the structure of the target on the synthesis of amorphous thin films, the amorphous HEMA derived Fe70Mg30 target (#1) and a target comprising a blended mixture prepared from elemental powder of Fe and Mg corresponding to same composition (#2) were prepared, with XRD patterns are shown in Figure 3.4(a). Deposited films from amorphous target (#1) in Figure 3.4(b) shows broad amorphous diffraction patterns.

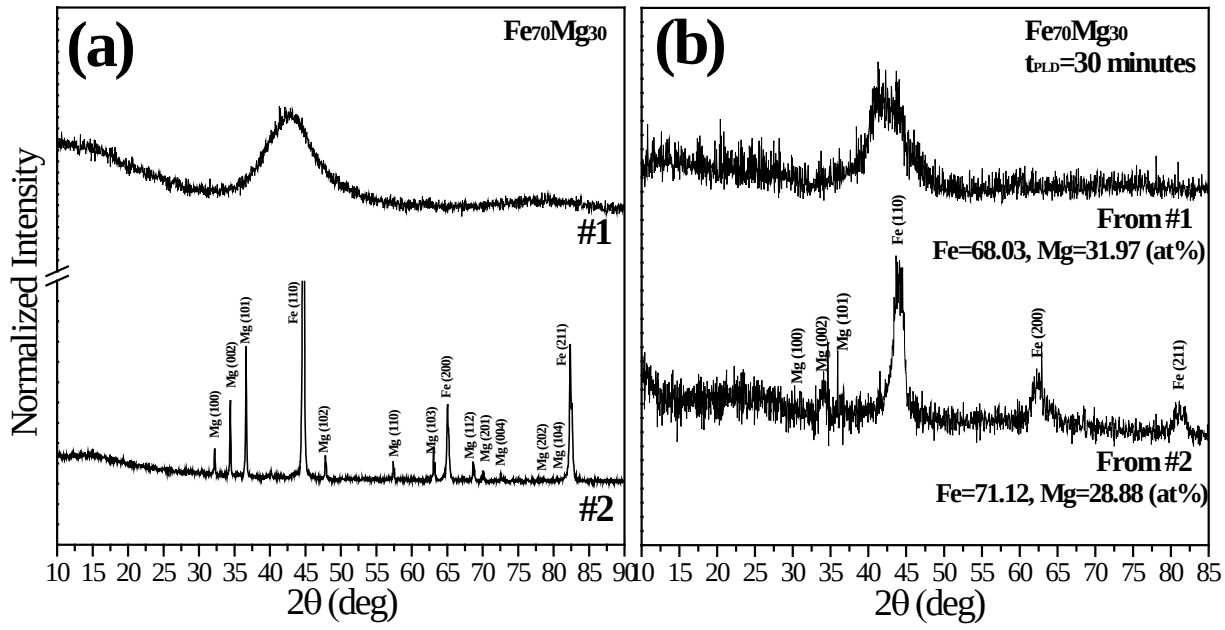

Figure 3.4. The X-ray diffraction patterns of (a) different crystal structure targets in $Fe_{70}Mg_{30}$ composition; as-milled amorphous target (#1) and blended mixture starting precursors powders (#2), (b) deposited thin films for 30min by PLD from #1 and 2 target and chemical composition of each films.

This result imply that the amorphous phase is readily formed by PLD from a fully amorphous target in $Fe_{70}Mg_{30}$ composition. It is good agreement with those obtained from the Mg-Zn-Ca system in pilot study. In comparison to amorphous film from target #1, the XRD profiles of deposited thin film from highly crystalline target (#2) as shown in Figure 3.4(a) is displayed in Figure 3.4(b). The sharp crystalline peaks appear over the broad background peaks even though some Mg peaks were disappeared and peak intensities were decreased compared to Figure 3.4(a) for the targets #2. These sharp peaks are distinctively identified as pure Fe and Mg in the XRD pattern of the thin film from target #2. The chemical composition of each thin film was measured by XEDS in Figure 3.4(b). Each chemical composition is close to the target composition.

These experimental results suggest that amorphous thin films cannot be produced by PLD from highly crystalline targets corresponding to $Fe_{70}Mg_{30}$ composition. However, it must be emphasized that there is no evidence that correlates any direct influence of the crystal structure of the targets on the characteristics of the deposited Fe-Mg films. This is due to the difficulty in separating the effect of target crystallinity from the other strongly coupled effects of the PLD process, including: physics of the plasma plume, flux kinetics at the substrate surface, geometrical relations, surface roughness, non-uniformity in the deposition rate, density of the target, and non-uniformity in the crystallinity of fabricated target, etc [138].

Figure 3.5 shows the XRD patterns of PLD derived films for different deposition time (t_{PLD}) and target/substrate distance (d_{tsd}), back ground pressure and substrate temperature, respectively. The intensity of broaden amorphous peaks was increased with increasing deposition time and there is no emergence of crystalline peak in Figure 3.5(a). Additionally, no significant difference was found for the sample deposited with change of d_{tds} between 58 and 80 mm as shown in Figure 3.5(b).

For the deposited film under the 25 mtorr of Ar partial pressure shown in Figure 3.5(c), some narrow peaks were observed at around 45° and broaden peak became sharper than those under the vacuum atmosphere indicating the formation of small amount of crystalline phase. In contrast to dramatic influence of substrate temperature from pilot studies, we find no significant difference of deposited films between the normal and cold stage. Figure 3.5(d) shows the XRD patterns of the films deposited from #1 and #2 targets at a low temperature (-90^{o}C) using a cold stage for 30 minutes by PLD, respectively. In both case, overall peak shape became more broaden compare to Figure 3.4(b) but the XRD pattern of the film deposited from target #2 still shows shape Fe phased even though all Mg peaks completely disappear. This result suggests that

substrate temperature during deposition is not a dominant parameter contributing to the formation of amorphous thin film of $Fe_{70}Mg_{30}$ composition when the substrate is cooled to -90^{o}C.

Through the pilot and main study conducted to find the optimum process parameters for PLD, it is observed that different results are obtained from each sample systems. As outline above, PLD is a relatively simple experimental deposition technique. However, the deposition process is in fact rather complex and in order to deposit films of optimum quality, the process parameters must be controlled in an adequate manner.

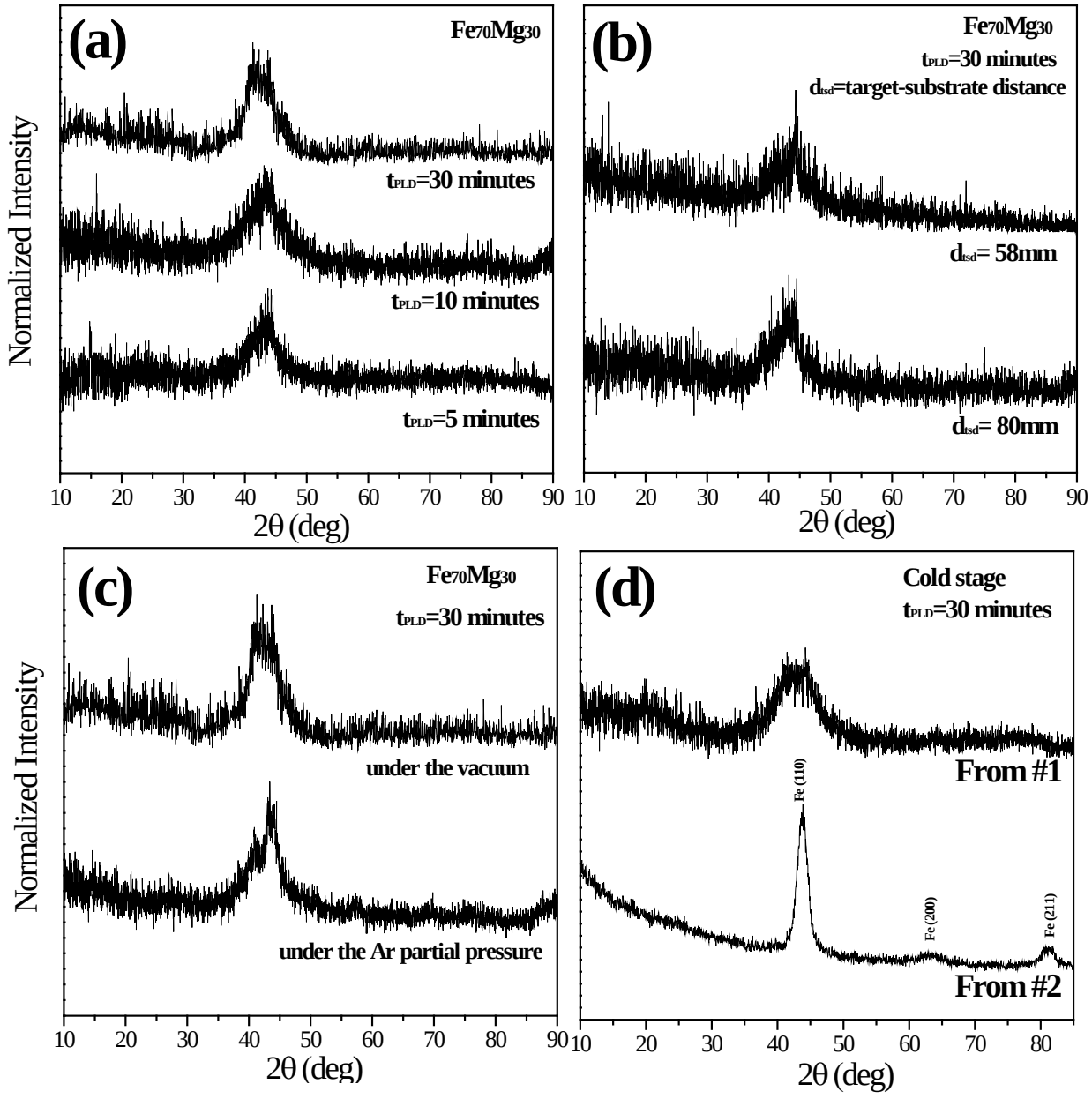

Figure 3.5. The X-ray diffraction patterns of PLD deposited films under normal stage for (a) various deposition times and (b) target-substrate distance from the as-milled amorphous target (#1). (c) PLD derived films deposited for 30 minutes under the Ar and vacuum chamber atmosphere from amorphous target #1 and (d) PLD derived films deposited for 30 minutes using a cold stage from amorphous target #1 and blended mixture starting precursors powder target #2

Theoretical process parameters such as the deposition rate, the kinetic energy of ablated particles and the mobility of adsorbed particles may be controlled by experimental parameters such as the influence of target properties, the background gas pressure and the substrate temperature. In this study, an empirical approach was therefore adopted to find it. The optimum process parameters, however, vary from one material to another. For the formation of $Fe_{70}Mg_{30}$ amorphous thin film layer derived by PLD, optimum process parameters are summarized as follow: The target to substrate distance is constant at 58mm and films is deposited at room temperature for a deposition time of 30 minutes. All further deposition of Fe based alloy in next aims will be follow these parameter conditions. Other specific conditions of PLD system are same which are described in previous section.

3.3.3 Characterization of $Fe_{70}Mg_{30}$ amorphous thin layer by PLD

Thin layer samples were prepared by PLD on glass for 30 minutes from the $Fe_{70}Mg_{30}$ fully amorphous target. Glancing angle XRD analysis was performed on this deposited layer, shown in Figure 3.6(a). This figure also shows a broad amorphous diffraction pattern. Figure 3.6(b) shows the TEM bright-field image and corresponding SAD pattern of the thin layer of $Fe_{70}Mg_{30}$ deposited by PLD. The bright field image shows the presence of large agglomerates or particles (droplets) embedded in the continuous thin layer. This is a typical surface morphology of layers deposited by PLD. There is a diffusive halo typical of an amorphous phase in the corresponding overall SAD pattern even though it consists of few droplets on a thin layer in the TEM bright-field image. In order to investigate the chemical composition of the thin layer, EDX measurement was also performed and results are given in the Table 3.1. The chemical composition of the amorphous thin layer is very similar to the target composition but some

deviation is seen for the particle composition. It is likely due to the varying diffusional kinetics of each element of the target during the PLD process [142].

Table 3.1. Chemical composition the continuous matrix and the particle from $Fe_{70}Mg_{30}$ films deposited for 30 minutes by PLD.

Element	Chemical composition	
	Matrix	Particle
Fe K (at%)	72.56 ± 5.78	48.14 ± 5.37
Mg K (at%)	27.44 ± 5.78	51.86 ± 5.37

Figure 3.7 shows the corresponding DSC thermograms of the thin layer of $Fe_{70}Mg_{30}$. It is apparent from the DSC thermogram that the glass transition temperature (T_g), the crystallization temperature (T_x) and the super-cooled liquid region ($\Delta T=T_x-T_g$) are about 231.5°C, 356.6°C, 125.1°C, respectively. Moreover, one exothermic peak, marked as T_p, is observed in the trace, and is identified as the crystallization reaction peak.

Table 3.2. Corrosion potential (E_{corr}) and current density (i_{corr}) values for $Fe_{70}Mg_{30}$ layer, both bulk and thin layer of pure iron. The corrosion current density is significantly higher for $Fe_{70}Mg_{30}$ than both pure iron samples *(P<0.05)*.

Element	Corrosion potential, E_{corr}(V)	Corrosion current density. I_{corr}(μAcm^{-2})
$Fe_{70}Mg_{30}$ amorphous thin layer	-0.642	98.76±11.08
Pure Fe (thin layer)	-0.616	12.46±2.3
Pure Fe (bulk)	-0.592	14.14±4.35

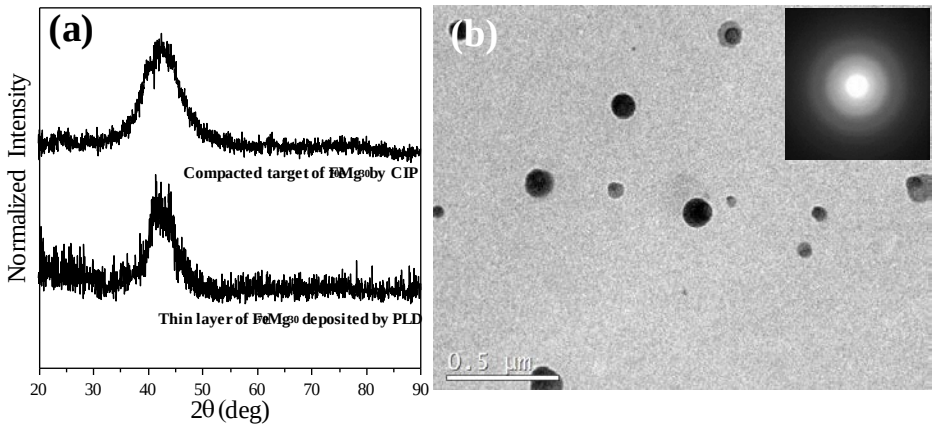

Figure 3.6. Thin layer of $Fe_{70}Mg_{30}$ on glass deposited for 30min by PLD. (a) The X-ray diffraction pattern, (b) Bright field TEM image and corresponding overall SAD pattern with chemical composition.

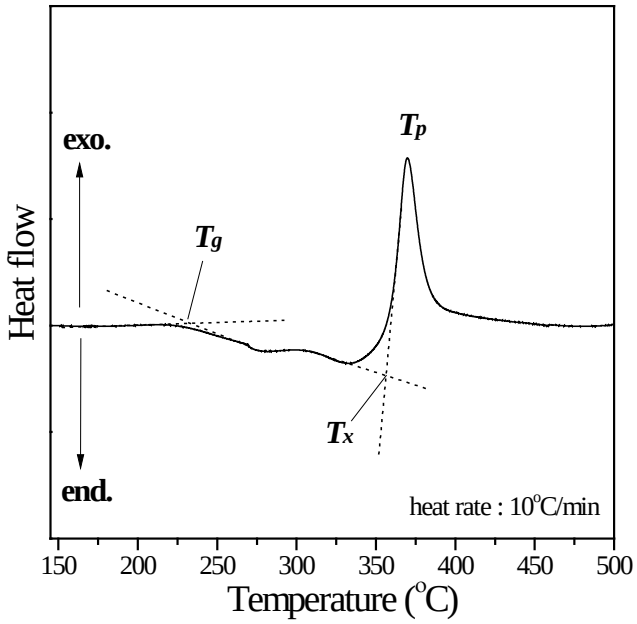

Figure 3.7. DSC thermogram for the $Fe_{70}Mg_{30}$ amorphous thin layer by HEMA.

3.3.4 Corrosion characterization of $Fe_{70}Mg_{30}$ amorphous thin layer by PLD

Potentio-dynamic polarization curves for the thin layer of $Fe_{70}Mg_{30}$ and pure iron on glass and polished bulk pure iron can be seen in Figure 3.8 as a representation of the multiple samples tested. Table 3.2 gives a summary of the corrosion potential and corrosion current densities as calculated from extrapolation of the Tafel plots. The $Fe_{70}Mg_{30}$ amorphous thin layer on glass (a) resulted in an i_{corr} value approximately 8 times higher than both of Fe thin layer of same thickness (b) and bulk (c) samples as well as E_{corr} values that are more cathodic. It can be inferred from the above results that the $Fe_{70}Mg_{30}$ alloy shows improved corrosion rates compared to the pure Fe sample. The $Fe_{70}Mg_{30}$ alloy caused a large increase in corrosion current density over the pure iron samples, which were measured at 14.14 ± 4.35 μA cm^{-2} for bulk and 12.46 ± 2.3 μA cm^{-2} for thin layer, respectively. There is no statistically difference in the value of i_{corr} values between bulk and thin layer for pure iron.

In order to identify the phases formed on $Fe_{70}Mg_{30}$ amorphous layer after the electro-chemical corrosion tests, XRD analysis was performed, and is shown in Figure 3.9. Some oxide and hydroxide phases, likely representing the corrosion products, are observed. These crystalline peaks appear over the broad amorphous peaks, and are specifically identified as $Mg(OH)_2$ (Magnesium Hydroxide, Brucite, PDF# 01-084-2163), $Fe_{+3}(OH)_3$ (Iron Hydroxide, Bernalite, PDF# 00-046-1436), Fe_2O_3 (Iron(III) oxide, PDF# 01-076-1821) and FeO (Iron(II) oxide, Wustite, PDF# 01-079-2179).

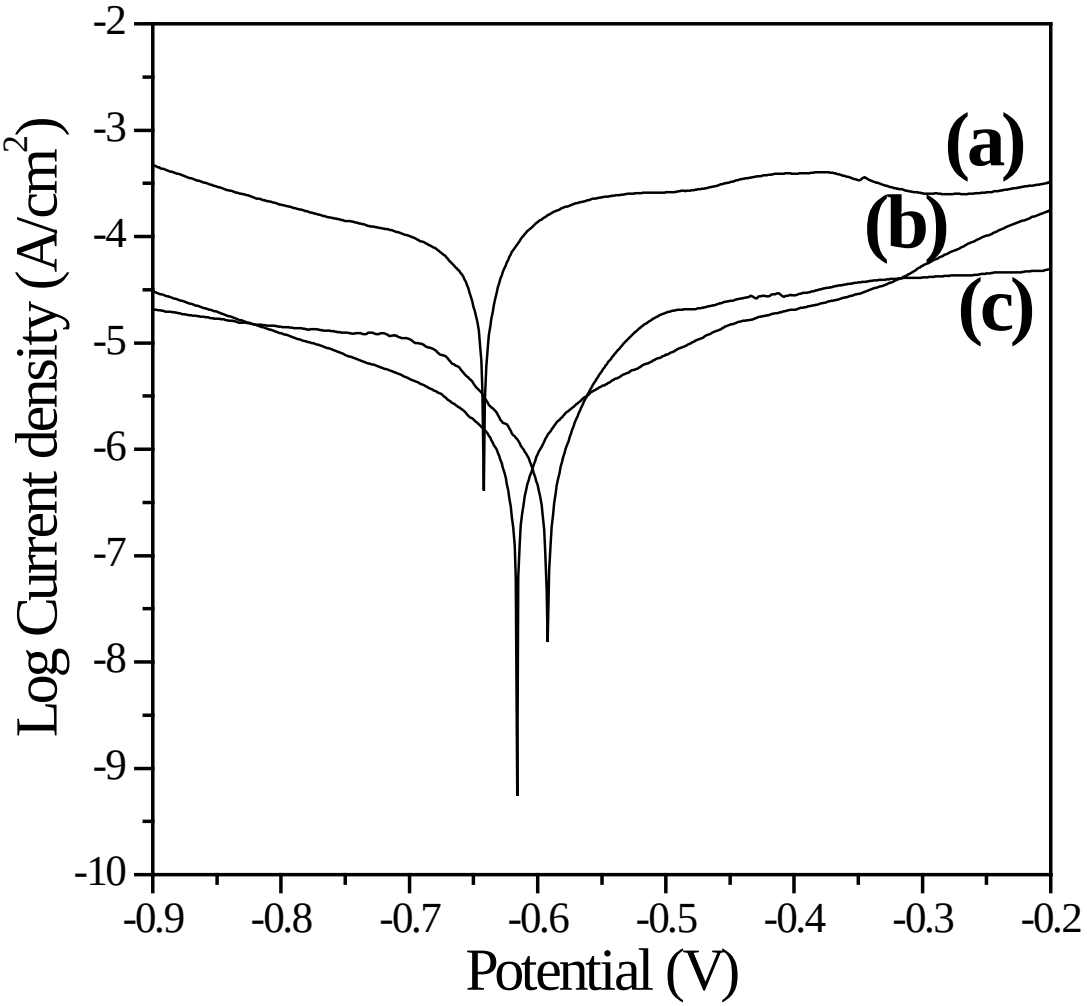

Figure 3.8. Polarization curves of (a) $Fe_{70}Mg_{30}$ amorphous thin layer, (b) Pure iron thin layer on glass derived by PLD and (c) bulk pure iron.

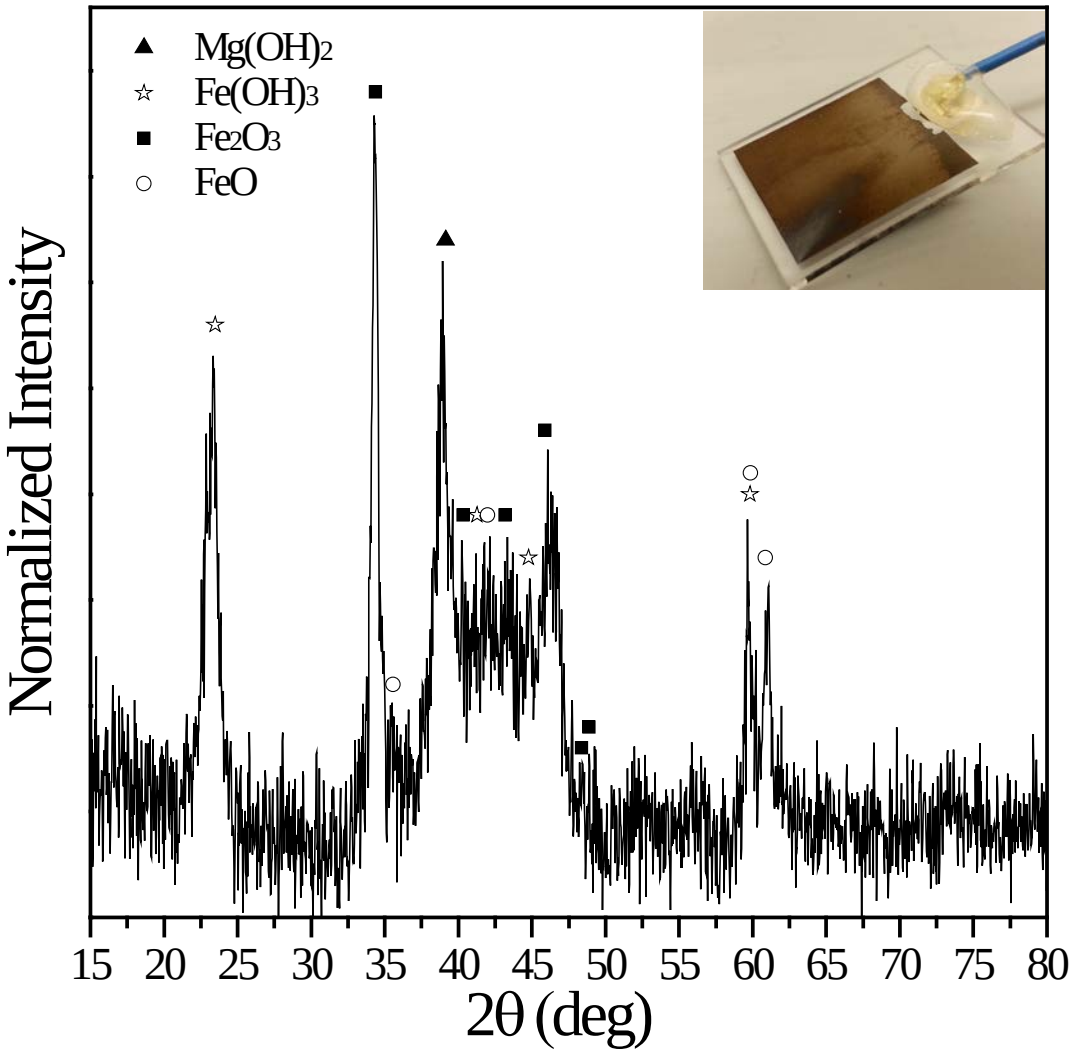

Figure 3.9. The glancing angle X-ray diffraction patterns of the $Fe_{70}Mg_{30}$ thin layer sample after electrochemical corrosion test in DMEM with photo of corrosion sample

3.3.5 *In vitro* cytocompitability measurement of $Fe_{70}Mg_{30}$ amorphous thin layer by PLD

Live/dead staining of MC3T3-E1, hMSCs, HUVECs and NIH3T3 after 1 and 3 days of post seeding on the $Fe_{70}Mg_{30}$ amorphous thin layer and plastic tissue culture surface (control) can be seen in Figure 3.10 and 3.11, respectively. After 1 day, for all cell cultures, fluorescence microscopy from the live/dead assay shows similar live cells (green) attachment with few dead (red) cells on the surface of $Fe_{70}Mg_{30}$ except HUVEC and NIH3T3 cells which show less live cell attachment compared to the control. After 3 days of culture (Figure 3.11), $Fe_{70}Mg_{30}$ amorphous thin films, which were seeded with MC3T3-E1 and hMSCs, still again displayed a similar level of living cell attachment, comparable to the tissue culture plastic as control, with a higher cell density than day 1. Fewer HUVEC live cells attachment compared to tissue culture plastic was still observed after 3 days but the relative cell density was higher than day 1. At day 3, improved cell viability was observed for NIH3T3 when compared with day 1 as the cell density was higher and the cells were more evenly distributed. The live/dead staining indicates good cell viability and proliferation on $Fe_{70}Mg_{30}$ amorphous thin layer.

SEM images of all cells attached to the surface of the $Fe_{70}Mg_{30}$ amorphous thin layer (Figure. 3.12) confirmed the live/dead assay results, with a high attached cell density on the surfaces. All cell types studied were able to attach on the $Fe_{70}Mg_{30}$ amorphous thin layer, and it was also evident that the cells had begun to proliferate on the surfaces. The cell spreading was uniform with filopodia formation, suggesting that $Fe_{70}Mg_{30}$ amorphous thin layer was stable in the physiological environment and was conducive for cell growth and proliferation.

Figure 3.13 illustrates the cell viabilities of MC3TC-E1, hMSCs, HUVECs and NIH3T3 expressed as a percentage of the viability of cell cultured in the negative control after 1, 3, and 7days incubation in extraction mediums after 72 hours using the MTT assay.

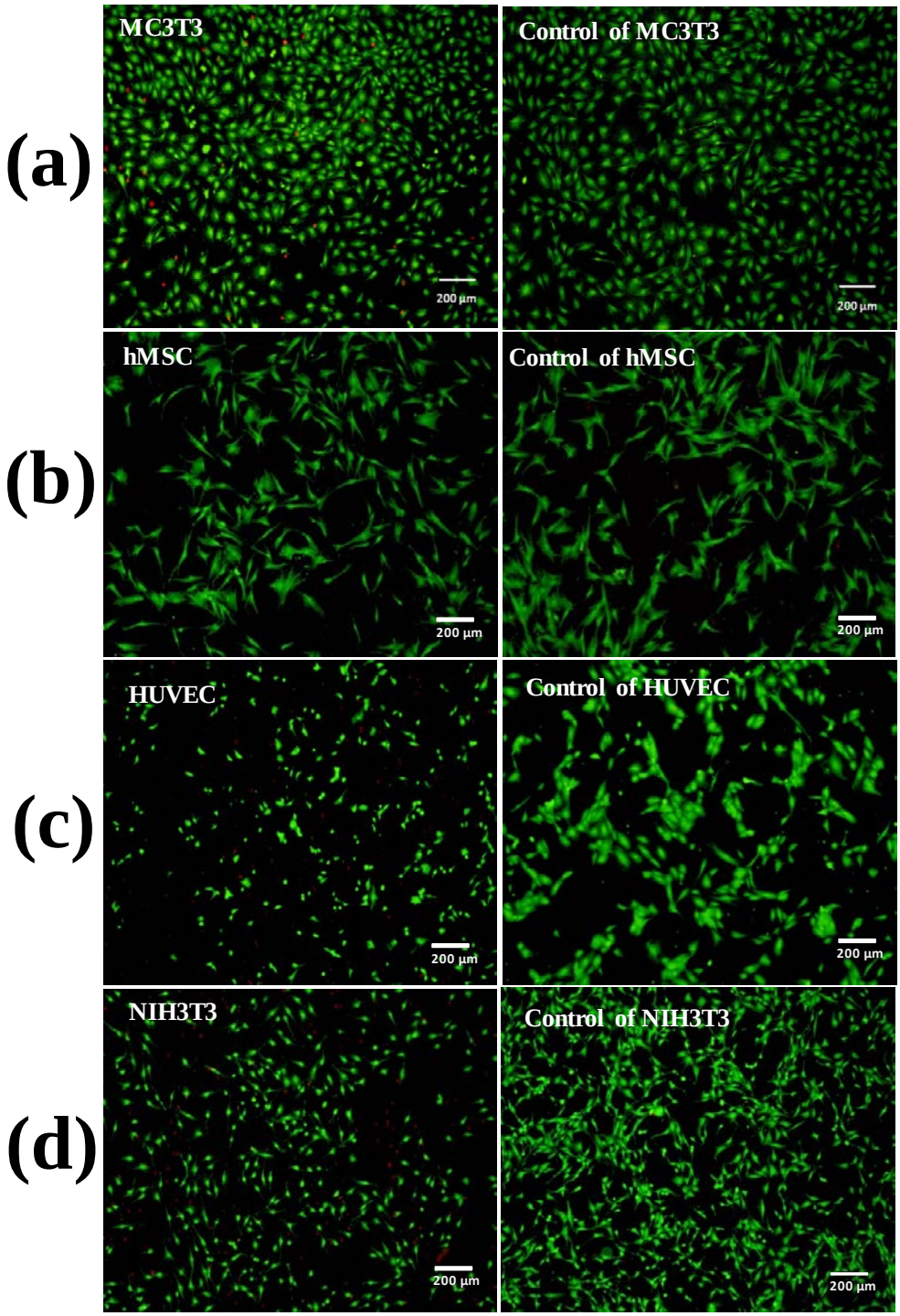

Figure 3.10**.** Live/Dead staining of (a) MC3T3 osteoblasts, (b) hMSCs, (c) HUVECs and (d) NIH3T3 fibroblasts on day 1 of culture post seeding on the thin layer of $Fe_{70}Mg_{30}$ on glass and tissue culture plastics as control.

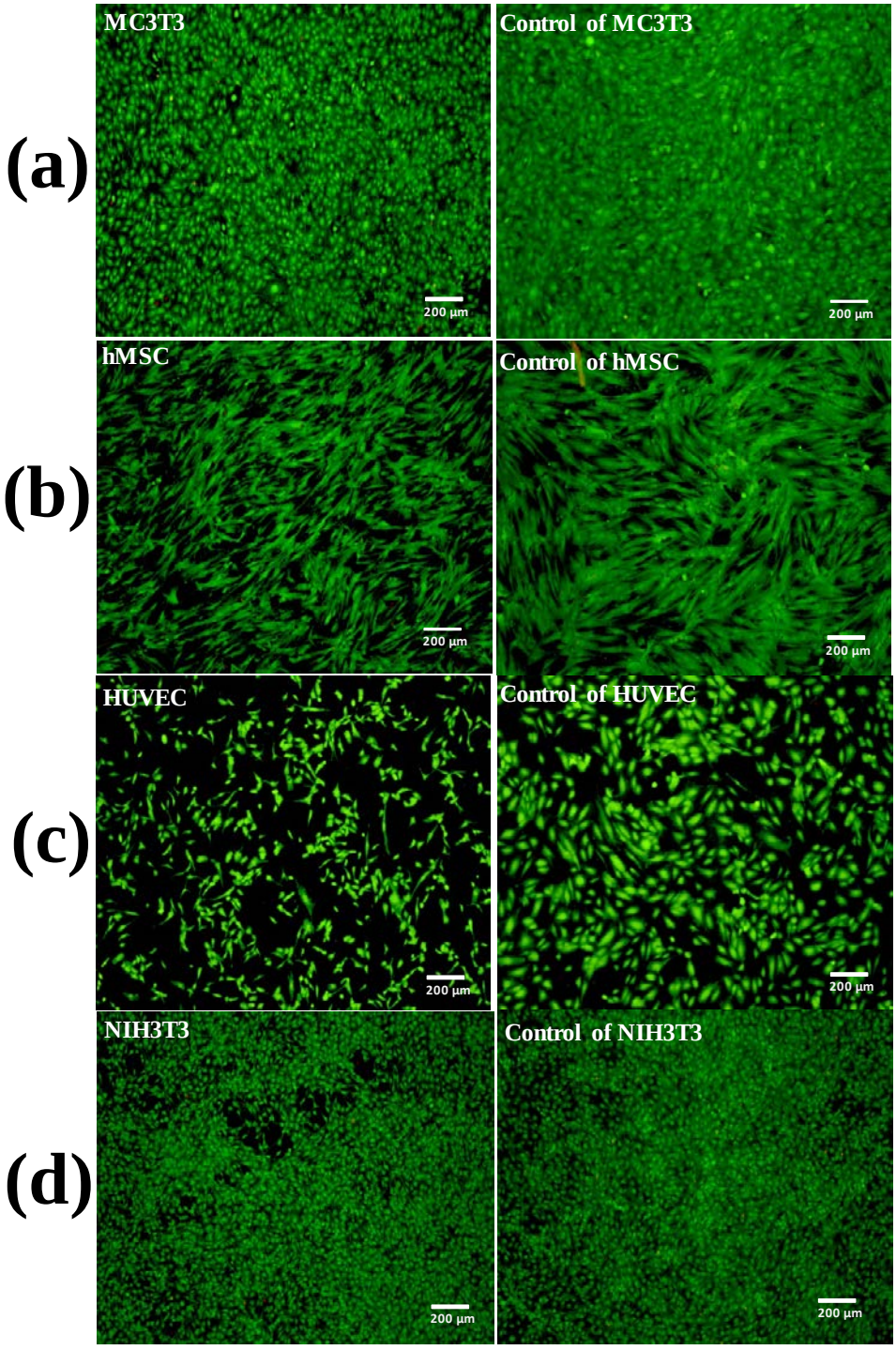

Figure 3.11. Live/Dead staining of (a) MC3T3 osteoblasts, (b) hMSCs, (c) HUVECs and (d) NIH3T3 fibroblasts on day 3 of culture post seeding on the thin layer of $Fe_{70}Mg_{30}$ on glass and tissue culture plastics as control.

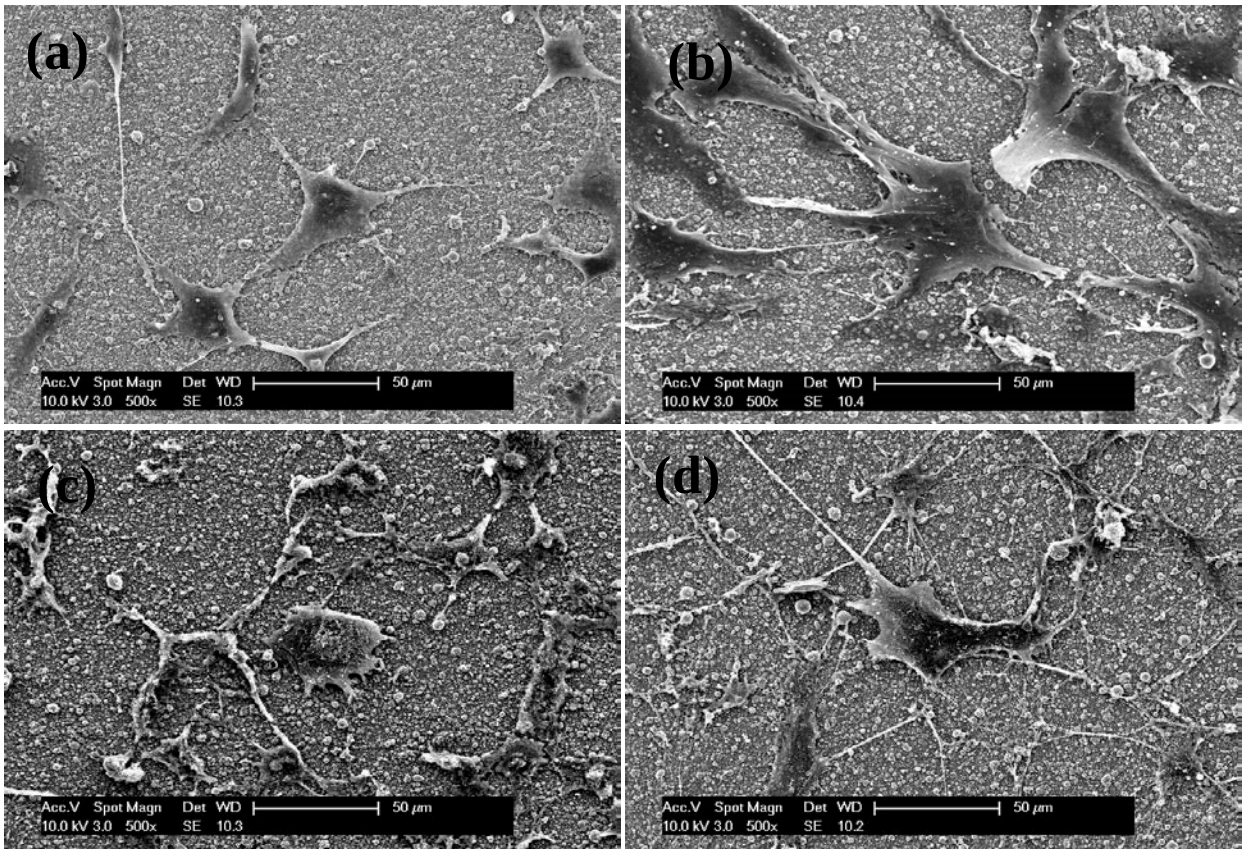

Figure 3.12. SEM morphology of fixed (a) MC3T3 osteoblasts, (b) hMSCs, (c) HUVECs and (d) NIH3T3 fibroblast at 24hrs post-seeding on $Fe_{70}Mg_{30}$ thin layer on glass.

These quantitative results of indirect cell viability support what was seen qualitatively in the live/dead staining, indicating good cell viability and proliferation on $Fe_{70}Mg_{30}$ amorphous thin layers. For 1, 3 and 7 days of culture periods, most cell viabilities of $Fe_{70}Mg_{30}$ were slightly lower but similar to that of pure Fe. There was no significant difference ($P>0.05$) between them except the viability values after 3days incubation in Figure 3.13(a) and the viability values after 3 and 7days incubation in Figure 3.13(c). Several groups exhibited decreased cell viability compared to the negative control. This may be related to the ion concentration of the leaching solution as higher Fe ion concentration led to lower cell viability value. Based on Figure 3.13(a) and (b), values of cell viability for MC3T3 osteoblasts and hMSCs in amorphous $Fe_{70}Mg_{30}$ extracts were nearly 100% after 1 day of exposure. However, viabilities decreased to around 90% compared with that of negative control after 3 and 7 days' incubation. For HUVEC cells, cell viability was about 90% after 1day incubation but also decreased then it was just about 70% compared to negative control after 7day's incubation in Figure 3.13(c). The NIH3T3 cells displayed ~80% viability after 1 day of exposure and conversely exhibited increased viability up to ~85% of the negative control after 7days.

Figure 3.14 shows the release of Fe and Mg ions after 72 hours immersion in αMEM, DMEM and EBM-2 growth media for the thin layer samples of $Fe_{70}Mg_{30}$ and pure Fe on glass by PLD. It can be seen that after 72 hours of immersion corrosion, the average released Fe ion concentrations from $Fe_{70}Mg_{30}$ sample were at most ~4 fold higher than that from pure Fe samples. According to the Figure 3.14, the mean amount of ion released from the $Fe_{70}Mg_{30}$ sample is 48.84 ± 7.13, 51.31 ± 7.23 and 45.03 ± 6.06 ppm for Fe and 18.11 ± 3.56, 25.03 ± 4.53 and 21.1 ± 2.84 ppm for Mg in αMEM, DMEM and EBM-2, respectively.

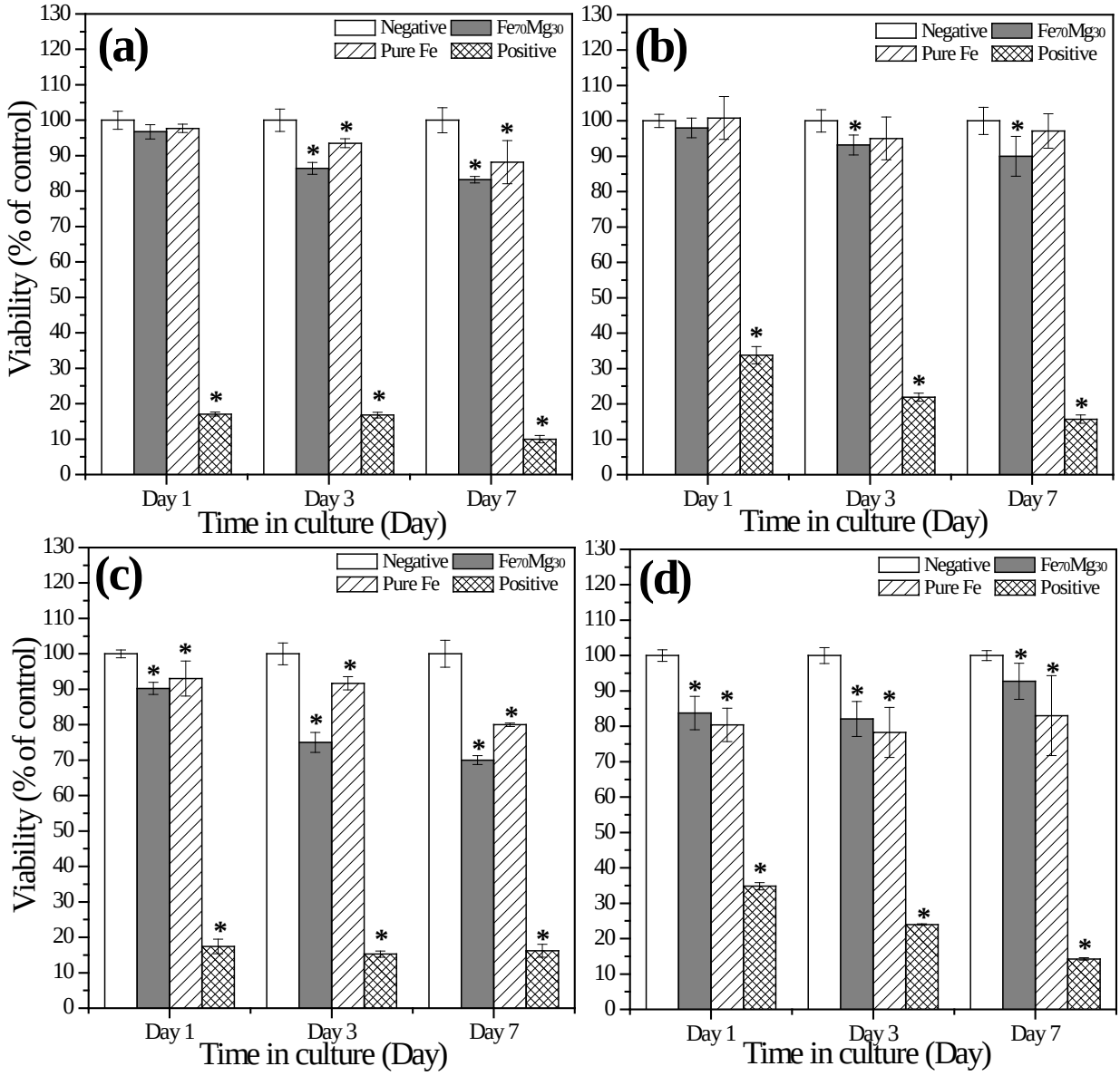

Figure 3.13. Cell viability of (a) MC3T3 osteoblasts, (b) hMSCs, (c) HUVECs and (d) NIH3T3 after 1, 3 and 7 days incubation in extract medium collected after 72 hours from $Fe_{70}Mg_{30}$ and pure Fe thin layer of ~1.3μm thickness on glass. * Significant difference compared to cell viability of the negative control group ($P<0.05$).

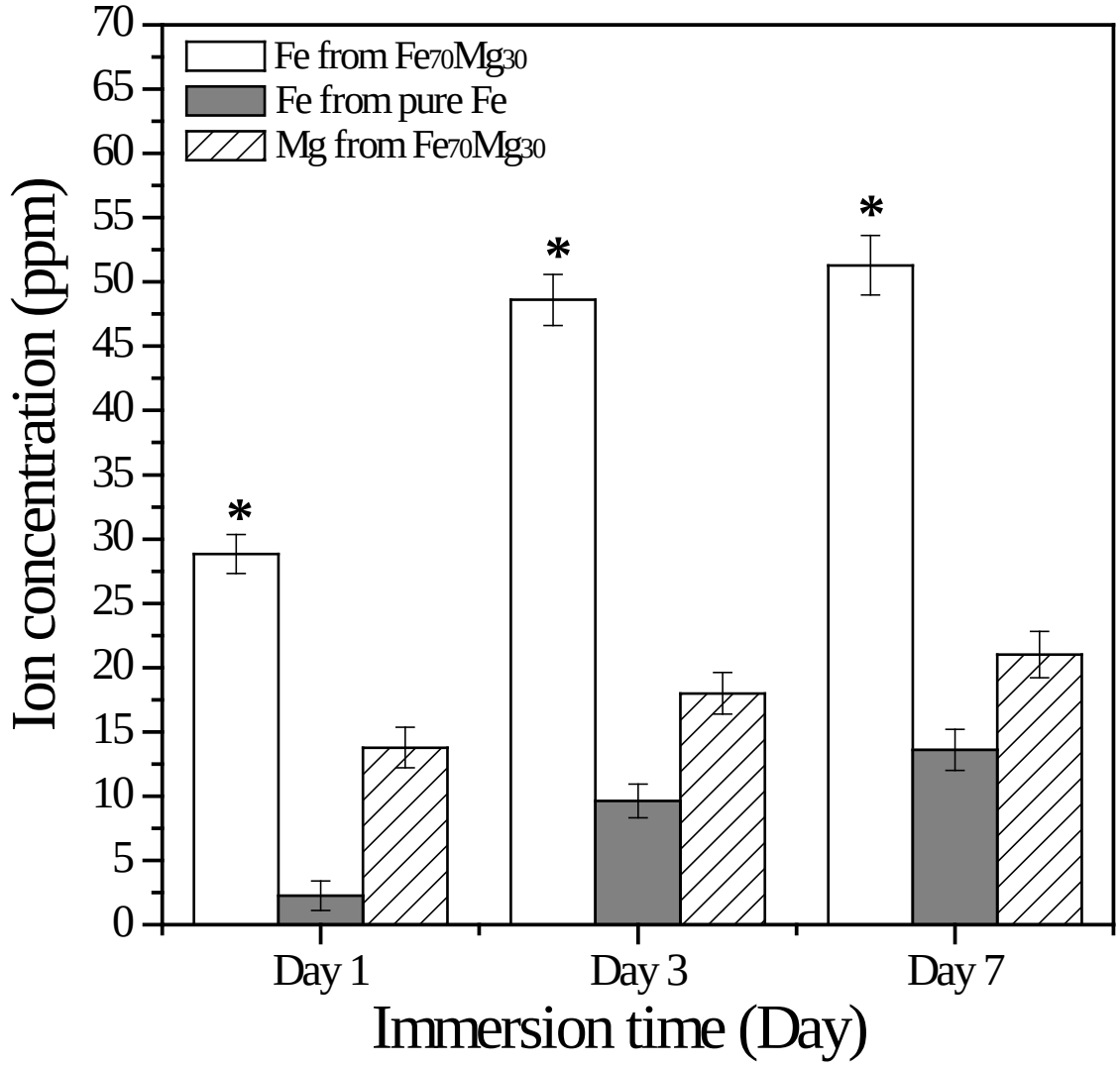

Figure 3.14**.** Ion concentration of Fe and Mg after immersion of the amorphous $Fe_{70}Mg_{30}$ and pure Fe thin layer of ~1.3 μm thickness on glass in cell culture media for each cell line for 72 hours. The $Fe_{70}Mg_{30}$ sample shows statistically higher Fe ion concentrations ($P<0.05$) than pure Fe sample, indicated by asterisk (∗).

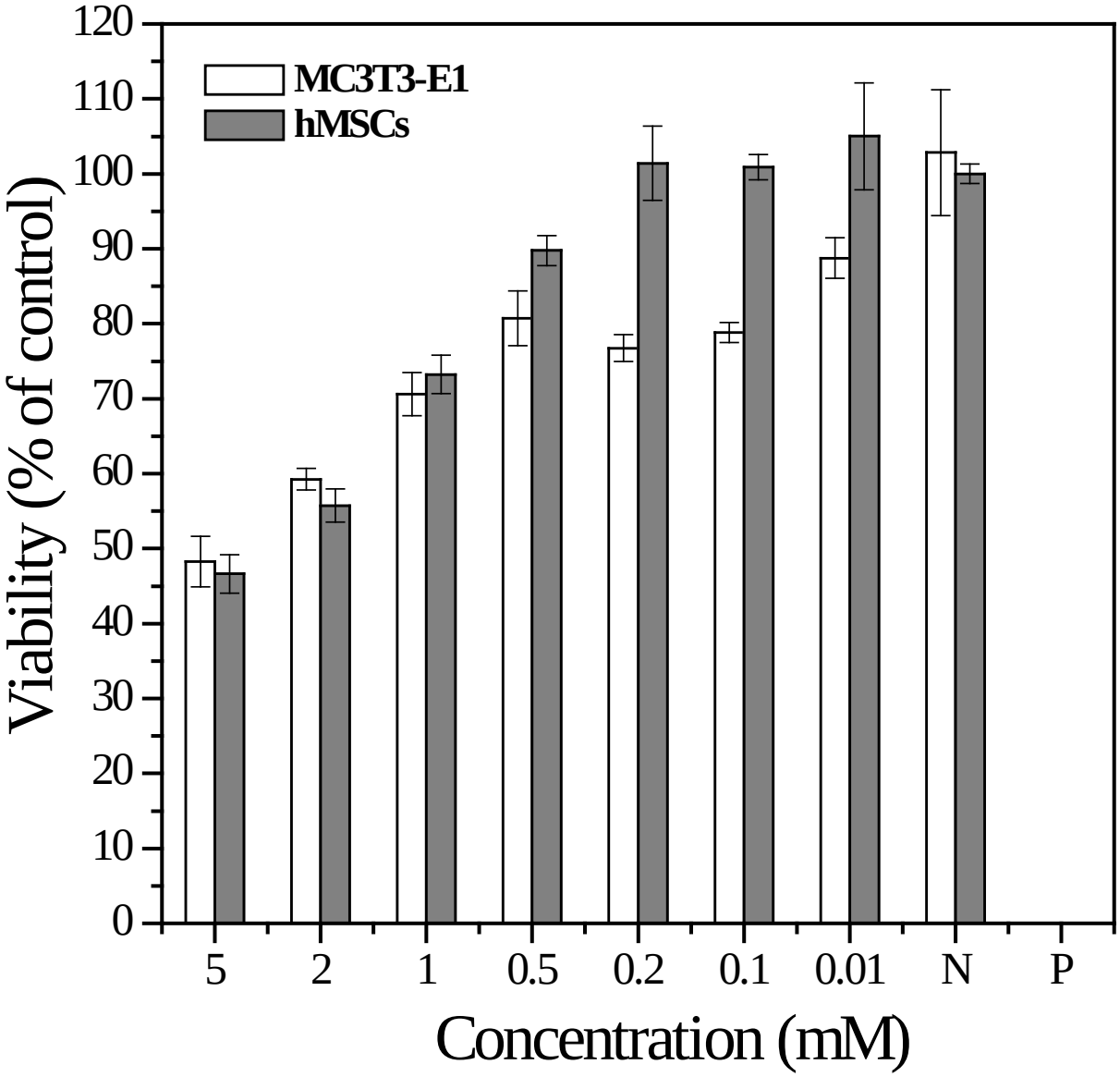

Figure 3.15. Dose-response cell viability of MC3T3-E1 and hMSCs for increasing concentration of Fe^{2+} ions after 3 days of culture.

3.4 DISCUSSION

In this specific aim, it is a preliminary study aimed to investigate the feasility of Fe-Mg binary alloy for biodegradable implant device applications. It focused on the formation of an amorphous thin layer from HEMA derived amorphous $Fe_{70}Mg_{30}$ powder as target and assessed these alloys in terms of *in vitro* corrosion and cytocompatibility. In the conclusions, we provide the basis and direction for future study to develop this amphous Fe-Mg system as novel biodegradable material systems.

3.4.1 Synthesis of amorphous thin layer by PLD in Fe-Mg system

In order to identify the potential use of Fe-Mg alloy as a biodegradable system using *in vitro* characterization methods in this study, it was necessary to form bulk shapes or thin layers from the HEMA derived Fe-Mg amorphous powders. Sintering by thermal treatment below the melting temperature of the main constituent material usually transforms a metallic powder into a bulk solid and is typically executed in powder metallurgy. However, a conventional sintering technique does not permit sintering of Fe-Mg amorphous powders due to the large melting temperature difference between Fe and Mg, which melt at 1530°C and 650°C, respectively. Hence, it is impossible to use a conventional sintering method to form substrates without inducing changes in composition and structure. Therefore, formation of thin layer is one of the solutions to generate dense structures from HEMA derived Fe-Mg amorphous powders shown in previously studies [202-205]. Studies have shown that this amorphous thin layer, while it is prepared by thermal co-evaporation, is focused for only specific field such as studies of atomic vibrational dynamics or Mössbauer spectroscopy [202-205]. However, amorphous Fe–Mg alloy

films may be formed over a narrow composition range under very severe conditions such as the limit of starting elemental material (Fe isotope, ^{57}Fe), ultrahigh vacuum (lower than 1x 10^{-9} mbar), stringent deposition rate (0.1~0.4 Å/s) and extremely low substrate temperature (-140°C) [204].

PLD was chosen to overcome the limitation of the sintering process for HEMA derived Fe-Mg amorphous powder. It expects that while the PLD process is controlled by optimal deposition parameters, amorphous $Fe_{70}Mg_{30}$ thin layers were successfully generated though still had embedded particles (droplets) in the continuous thin layer shown in Figure 3.6. As previously discussed for the deposited thin films in Mg-based amorphous alloys in pilot study, by controlling optimal deposition parameters in PLD, it is possible to tailor the structural properties of the deposited thin films in Fe-Mg amorphous alloys. The amount of unwanted liquid droplets, as seen in Figure 3.6(b), can be reduced by decreasing the laser energy density to the threshold of ablation, and increasing the target-substrate distance [206] or using other approaches such as utilization of dual laser, off-axis laser deposition, cross-flux method and implementation of velocity selection method [138]. Some of these approaches will be adopted in the future.

3.4.2 Degradation rate of $Fe_{70}Mg_{30}$ amorphous thin layer by PLD

The potentiodynamic polarization results in Table 3.2 of $Fe_{70}Mg_{30}$ amorphous thin layer show that corrosion current density significantly increased and corrosion potential is more negative compared to both bulk and thin layerd pure iron. Here, it should be noted that there is some limitation to preparing samples as thin layer by PLD for study of bio corrosion in this work because they are difficult or even impossible to make by conventional sintering or other

technologies in the Fe-Mg system. However, it indicates the benefical accelerated corrosion obtained from the $Fe_{70}Mg_{30}$ amorphous thin layer compared to pure Fe, though these results are indirect estimates from the potentiodynamic polarization results using the Tafel plotting (Figure 3.8) and do not measure the actual corrosion values. These limitation of sample preparation in this study may be solved using new techniques, such as spark plasma sintering (SPS) [207, 208], selective laser sintering [209] or viscous sintering [210] in order to measure more accurate information for corrosion that we will explore in future work.

Within the aforementioned two alloying criteria for high degradation rate which were proposed by Schinhammeret al. [72] state, Mg is considered as a suitable alloying element to pursue based on the first criterion in this study where it can make the Fe matrix more susceptible to corrosion because the standard electrode potential of the reaction $Fe(s) \leftrightarrow Fe^{2+}+2e^{-}$ is E_1= −0.440V [211], whereas that of $Mg(s) \leftrightarrow Mg^{2+}+2e^{-}$ is E_2= −2.372V [212]and then Mg is less noble element than Fe. Thus, the standard potential of Fe-Mg alloy is expected to decrease with increasing Mg content. Atoms in amorphous structures are thermodynamically unstable and should induce a higher dissolution rate compared to crystalline materials of same composition. Additionally, amorphous alloy compositions are not constrained by solubility limits and one can add higher concetrations of less noble alloying elements [213]. Accordingly, the $Fe_{70}Mg_{30}$ amorphous thin layer presents more accelerated corrosion than pure Fe, as seen in Figure 3.8 and Table 3.2. This could be related to the contained high Mg concentration with extension of solid solubility limit, an approach described by Hermawan et al. [7, 75] in the Fe-Mn system which causes accelerated corrosion through the formation of a solid solution.

Under visual observation on the Fe-Mg samples after the corrosion test, it appears that red-brown and black color layers (in Figure 3.9) were formed, believed to be due to released Fe^{2+}

and Mg^{2+} ions from the anodic reaction reacting with the hydroxyl ion (OH^-) relased from the cathodic reaction to form insoluble hydroxides (hydrous metal oxides) such as $Fe_{+3}(OH)_3$, Fe_2O_3, FeO and $Mg(OH)_2$ [75, 90, 214] which matched well with the results in Figure 3.9. It was found that the alloying elements not only increase the degradation rate of Fe-based alloys, but also affect their cytocompatibility [35]. This may be caused either by the amount of released substances from the samples, or cytocompatibility of the added alloying elements. Therefore, these corrosion products and released metal ions may be strongly related to the cell toxicity.

3.4.3 *In vitro* cytotoxicity of $Fe_{70}Mg_{30}$ amorphous thin layer by PLD

Past studies have widely used cytotoxicity assays to determine the response of cells to different substances. Various biocompability tests must be completed prior to the approval of alloys for in vivo use, and secondary cell lines MC3TC-E1, murine fibroblast cells 3T3 and L-929, rodent vascular smooth muscle cells (VSMC) as well as primary cells such as HUVECs, hMSCs and murine bone marow stem cells and have demonstrated positive biocompatibility and cytocompatibility of Fe and Fe based alloys [43, 54, 61, 75, 82, 158, 215, 216]. As a result from *in vitro* cell viability tests in the current study, $Fe_{70}Mg_{30}$ amorphous thin layer by PLD had no adverse effects on cell viability, proliferation and morphology. In the case of direct cell viability and adhesion test as seen in Figure 3.10-3.12, the $Fe_{70}Mg_{30}$ amorphous thin layer demonstrated good cell viability, with well adhered cells on the samples after 1 and 3 days of culture compared to control as well as 0~1 cytotoxicity grades by ISO 10993-5 [217]. The higher cell density observed after 3 days implied that the cell proliferation on $Fe_{70}Mg_{30}$ amorphous thin layer was not inhibited by the substrate, changes in local chemical concentrations in culture media or the corrosion products.

The good morphological features and attachment ability of MC3T3-E1, hMSC, HUVEC and NIH3T3 cells was shown in Figure 3.12 and thus confirmed the cytocompabilitible nature of the materials. Since a great deal of research on Fe and Fe based alloys have been focused on cardiovascular biodegradable stents [2, 5, 218], the endothelialization process on these materials is very important. Thrombogenicity decreases as the stent surface is covered by regrowth of endothelium [77, 219] and thus the morphology of HUVECs on Fe alloys is very important. HUVECs spread out and grew on the thin layers with filopodia extending from the cell edges, forming physical contact with each other to create a dense cell layer a seen in Figure 3.12(c). This indicates that the $Fe_{70}Mg_{30}$ amorphous thin layer exhibited no inhibition on the vascular endothelialization process. The results of the indirect cytotoxicity tests using MTT assay show similar cytotoxicity as the investigated direct test for the $Fe_{70}Mg_{30}$ amorphous thin layer. When cells were exposed to the degradation products in 100% extraction solution, relatively high cell viabilities were still demonstrated after 7 days of cell culture in Figure 3.13 for all tested cell lines even though they were decreased compared to 1 and 3 days of cell culture periods.

According to ISO 10993-5 [217], higher viability after longer cell culture time of more than ~70% compared to that of negative control indicated that cell metabolic activity was uninhibited by corrosion products and proves a material's biosafety for further biomedical applications. In this study, despite cell viabilities being reduced compared to the negative control, their viability remained above 70% to indicate good cytotoxicity grades by ISO 19003-5. The reduction may be related to the concentration of material leaching into solution as higher metal ion concentrations may led to lower cell viability. In most cases, toxicity is provoked by metal elements derived from reactions between metal and body fluids acting as electrolytes. The metal ions, which formed by anodic reaction as $M(s) \leftrightarrow M^{2+}+2e^{-}$, where M is a metal, readily catalyze

the generation of toxic effects [220] with higher concentration of metal ions exerting harmful behaviour. It has been generally found that Fe and Mg show acceptable to good cytocompatibility and the average concentrations of Fe and Mg ions in each collected extract used for indirect cell viability tests were shown in Figure 3.14. The total Mg^{2+} concentration range for mammalian cells is about 340ppm - 486ppm [221] and previous studies provided some information on the concentration of Mg ions after degradation of the alloys *in vitro*. For example, the critical Mg^{2+} ion concentrations were reported as ~245ppm for murine fibroblast cells [41], ~231ppm for HUVECs [222] and Zhao et al. [223] reported that viability was not significantly affected when Mg^{2+} is less than ~730 ppm for human coronary aorta endothelial cells (HCAECs).

As the corrosion extract concentration for Mg was found to be far below critical values from literature, without the concern of releasing other alloying elements, Mg seems not to be responsible for the decrease in cell viability which then may be attributed to Fe ion concentration. Fe is an essential element for fundamental metabolic processes in cells and organism with a high toxic level in serum. Extracellular Fe is exclusively bound to transferrin as the plasma iron carrier, which maintains Fe solubility and nontoxicity, binding to specific receptor on the cell surface to be transported across the endosomal membrane [45]. This internalized Fe is utilized for metabolic purposes but excess is detoxified by sequestration into ferritin [45]. These cellular Fe metabolism mechanisms explained the low inhibition of cell activity when cells were exposed to the range of Fe ion concentration in extraction solution [75]. The critical concentration of Fe ion for each cell line used in this study were found in the literatures and given as the half maximal inhibitory concentration (IC_{50}) values corresponding to the concentrations of substances required to induce a 50% reduction in cellular response in comparison to untreated cells [216].

Generally, the IC_{50} levels strongly depend on the cell type and experimental conditions. Therefore it only shows general trends and cannot be treated as absolute values [135].

For HUVECs, the collected extraction from EBM-2 contained an average concentration of 45.03 ± 6.06 ppm for Fe (Figure 3.14) compared to 335 ppm [135] and 61 ppm [54]. For NIH3T3 fibroblast cells, Fe concentration in extract from DMEM was 51.31 ± 7.23, compared to 389 ppm [158], 380 ppm [215] and 112 ppm [216]. Because the measured corrosion extract concentration of Fe for HUVECs and NIH3T3 were below these IC_{50} values found in literature, the cell viabilities of HUVECs and NIH3T3 for $Fe_{70}Mg_{30}$ sample was expected to be maintained as they were above 70% up to 7 days of incubation, indicating no cytotoxicity from the amorphous thin layer samples of $Fe_{70}Mg_{30}$. Additionally, for MC3T3-E1 and hMSCs, values of cell viability in our expermental materials extracts from αMEM were nearly 100% after cultured for 1 day and decreased to around 80% for MC3T3-E1 and 90% for hMSCs after 3 or 7 days incubation in Figure 3.13 (a) and (b). For hMSCs, there are few such studies for Fe based biodegradable materials in literature. Thus, we performed dose response experiments with soluble $FeCl_2$ (Figure 3.15) revealing that Fe concentrations higher than ~112 ppm (2mM) had adverse effects on the metabolic activity and resulted in a reduced viability of hMSCs. The mean amount of Fe ion released from the $Fe_{70}Mg_{30}$ sample in αMEM was 48.84 ± 7.13 ppm. In this context, the high cell viability was observed due to the Fe ion concentration being lower than the critical concentration to cause toxicity in the extraction solution in this study. Yamamoto et al. [158] also studied MC3T3-E1 and determined an IC_{50} level of ~33 ppm for Fe, which is slightly lower than that of this study but in contrast, we found that high cell viability was demonstrated up to 7 days of cell culture as shown in Figure 3.13(a). These results seem counter-intuitive but recently, Hong et al. [224] performed dose response with soluble $FeCl_3$ revealing that Fe

concentrations less than ~56 ppm had no adverse effects on the cell viability of MC3T3-E1 cells, which suggests that it is in good agreement with those obtained from the $Fe_{70}Mg_{30}$ sample in αMEM. Furthermore, the presence of $Mg(OH)_2$ as a corrosion product (Figure 3.9) can enhance osteoblast activity [225] and may facilitate high cell viability of MC3T3-E1 cells. The actual ion values was difficult to measure due to the complexity of extraction medium, variability with pH and temperature, and potential presence of undissolved corrosion products [41]. Thus for future experiments, we will consider concentrations of metal ions from extracts to be much higher level than would be observed in vivo due to exchange of permanent body fluids. These in vitro results suggest that the corrosion products are well tolerated by the cells, and that the newly developed Fe-Mg alloys show great promise as cytocompatible materials within the framework of the demanding conditions given in present work.

3.5 CONCLUSIONS

Thin films of this novel material demonstrated accelerated corrosion compared to pure Fe which is necessary for biodegradable medical applications. Furthermore, extensive *in vitro* cell studies conducted using cell lines relevant for cardiovascular and orthopedic applications demonstrated high cell viability in direct contact with these materials and in the presence of their degradation products. The combination of the degradation behavior and cytocompatibility of this novel amorphous $Fe_{70}Mg_{30}$ material make it a promising biodegradable material for cardiovascular, orthopedic, and other medical devices. Future work will pursue additional processing methods to produce different forms of the $Fe_{70}Mg_{30}$ alloy such as spark plasma sintering, selective laser sintering, or viscous sintering.

4.0 SPECIFIC AIM 3: STUDY THE EFFECT OF ADDITION OF MANGANESE (MN) AS AN ALLOYING ELEMENT IN THE FE-MG ALLOY SYSTEM AND UNDERSTAND THE IN VITRO RESPONSE TO EXPLORE THE POTENTIAL OF THESE ALLOYS AS NOVEL BIODEGRADABLE MATERIAL SYSTEMS.

4.1 INTRODUCTION

Recent years have seen increasing applications of biodegradable materials as a surgical implant or stent [14]. As outlined above, especially Mg alloys and Fe have been proposed for biodegradable materials. A number of Mg alloys have been proposed, including AE21 [22], AM60B [226], AZ91 [68], and WE43 [23]. The suitability of Fe as a degradable implant material has been studied in various *in vitro* and *in vivo* settings using variety of cells and animal models [13, 21, 26, 42, 43, 51-54]. However, the degradation rates were considered too rapid for Mg alloys and too slow for pure iron for biomedical application. From a structural point of view, the mechanical properties of iron are more attractive than those of magnesium alloys, if compared with stainless steel. Moreover, the properties of Fe alloys could be further improved by targeted alloying and by applying specific thermomechanical treatment. A careful selection of potential alloying elements could also result in non-ferromagnetic properties, thus increasing the compatibility of the resulting alloy with Magnetic Resonance Imaging (MRI), which is the default non–invasive imaging modality ubiquitously employed for coronary investigation and

screening of other of disease conditions. MRI is already quite used but is expected to rapidly become in the next decade a key diagnostic tool the post implantation monitoring of medical devices. With the growing importance of MRI, the MRI compatibility is becoming essential or at least desirable [58]. As discussed above for Fe alloy category in introduction, Fe is a ferromagnetic metal, an important magnetic characteristic which can influence its interaction with MRI technique. Accordingly, in order to overcome this impediment, extensive materials analysis, and toxicological review were carried out to select the optimal alloying elements for iron. Industrials and clinicians agree to state that three main characteristics should be owned by biodegradable implant and stents [58]: (1) mechanical properties approaching those of SS316L alloy; (2) controlled degradation process beginning after the stented vessel is healed and remodeled (6–12 months [227]) but completed within a reasonable period (12–24 months [67]) and (3) during the degradation process, the stent material should not release substances having toxic effects. To approach the characteristics of SS316L, extensive materials analysis and toxicological review were carried out to select the optimum alloying elements for iron. The choice was narrowed to the selection of Ni and Mn that can enable conversion of ferromagnetic iron to its nonmagnetic alloy form (austenite–forming elements) [228, 229]. Ni is known to form compounds classified by the International Agency for Research on Cancer (IARC) as carcinogenic to humans [149, 230]. On the contrary, Mn is an essential trace element needed for the body function of all mammals, specifically for bone formation, calcium absorption, blood sugar regulation, and fat and carbohydrate metabolism [231]. Mn was finally selected for the following reasons.

The present study is thus exploring the use of Mn as additional alloying element in the parent Fe-Mg alloy discussed in Chapter 2 and 3. Therefore reports the new alloying

composition of Fe-Mg amorphous systems synthesized by HEMA and accordingly, experiments were performed to synthesize thin film layers by PLD and evaluate these films using preliminary *in vitro* cytocompatibility and corrosion experiments for biomedical applications.

4.2 MATERIALS AND METHODS

4.2.1 Alloy powder preparation and synthesis of thin films

Powders of elemental Fe (99.9+%, <10 μm, Alfa Aesar), Mg (99.8%, <325 mesh, Alfa Aesar) and Mn (99.3%, <325 mesh, Alfa Aesar) corresponding to $Fe_{60}Mg_{40-x}Mn_x$ (x=0~40) atomic % compositions were milled in a planetary SPEX 8000 high energy Shaker Mill through a sequential process of dry and wet milling in this study. The ball to powder weight ratio (BPR) was 15 to 1, and the total weight of the starting mixture was 4g as powder. After dry milling, 1.5ml of toluene (anhydrous, 99.8%, Sigma-Aldrich) was loaded in the vial and the as-dry milled powder was subsequently wet milled for a period of up to 17 hours to reduce the adhesion of powders on the balls and the inner surface of the milling vial. The post ball milled powders were dried and then compacted at a pressure of 60 kpsi using a Flow Autoclave System cold isostatic compaction press to produce 25.0 mm diameter discs to be employed as targets for PLD. All the thin films were produced by PLD utilizing a 248 nm KrF excimer laser (Lambda Physik EMG 201) irradiation pulsed at 25 ns FWHM in a high vacuum chamber with a base pressure of 10^{-6} Torr. In all depositions the spot size was approximately 1×3 mm, the fluence was 8.3~9.6 J/cm^2, the laser pulse frequency was maintained at 10 Hz and the deposition rate was approximately 2.3 Å/s determined as a mean value. The target to substrate distance was maintained constant at 58

mm, with targets rotated during deposition. Films were deposited at room temperature for a deposition time of 30 minutes on three different substrates corresponding to film thicknesses of ~1.3 microns. The first was amorphous SiO_2 thermally grown on Si wafer for use in glancing angle X-ray diffraction (XRD). The second substrate was a regular cell culture dish for cytocompatibility tests, and the third substrate was fused silica glass for bio-corrosion tests.

4.2.2 Characterization of the synthesized powder and thin films

X-ray diffraction (XRD) phase analysis was performed using PANalytical X'Pert Pro system employing the Cu K_α (λ=1.54056 Å) radiation source with a Si-detector for glancing and conventional measurements. X-ray generator was operated at 45 kV and 40 mA at a 2θ range of 10-90°. PANalytical HighScore Plush version 3.5 software was used to identify the XRD patterns comparing to ICSD database. Morphological studies along with elemental compositional analysis were performed using a Jeol JSM-6610LV SEM equipped with an energy dispersive x-ray spectroscopy (EDAX) analyzer.

TEM was performed using a JEOL JEM 2000FX TEM (operated at 200 kV) to study additional morphological characteristics such as particle size, shape and distribution for conventional bright field images. High resolution (HR) TEM observations were carried out using a JEOL JEM-2100F and image processing was carried out using the software package Gatan Digital Micrograph for Fourier transform. ICP-OES used to perform elemental analysis (ICP, iCAP duo 6500, Thermo Scientific) of the extracted solution from immersion test. Magnetic hysteresis loops were measured at room temperature with vibration sample magnetometer (VSM, Lakeshore 7400) with a maximum magnetic field of 2 T. The thermal properties of the final

milled powder and thin layer films were studied by differential scanning calorimetry (DSC, Netzsch STA 409) at a heating rate of 10°C/min under an ultra high purity Ar gas flow.

4.2.3 Corrosion test of Fe-Mg-Mn alloy thin films

The potentiodynamic polarization technique was used to test corrosion of the PLD derived Fe-Mg-Mn amorphous thin layer compared to the film/bulk (99.8+%, 1mm foil, Good fellow) of pure Fe and Fe-Mg amorphous films which were studied and reported in Chapter 3. It was performed using a CH604A (CH Instruments Inc.) electrochemical work station. Following sample preparation as described in previous chapter in detail, length and width were measured and then one side of each sample was connected to a wire with silver epoxy and then electrically insulated with polymeric epoxy, such that only one side is exposed for electrochemical testing. Ag/AgCl reference electrode (4.0 M KCl, Accument) and a platinum wire counter electrode were employed. The test was performed in Dulbecco's Modified Eagle Medium (DMEM, with 4.5 g/l glucose, L-glutamine, and sodium pyruvate, Cellgro, Manassas, VA) supplemented with 10% fetal bovine serum (FBS), 1% penicillin/streptomycin at pH 7.2 ± 0.2 and held at 37 °C. Before each measurement, the sample was immersed in the corrosion media to provide stability for 40 minutes. The cathodic and anodic portions of the generated Tafel plots were fit linearly to allow calculation of corrosion potential, E_{corr}, and corrosion current density, i_{corr}.

4.2.4 Cell culture for cytocompatibility test

Murine pre-osteoblast cells (MC3TC-E1, American Type Culture Collection, Rockville, MD), Human Mesenchymal Stem Cells (hMSCs, Lonza, USA), human umbilical vein endothelial cells

(HUVECs, Linza, USA) and Murine fibroblast cells (NIH3T3, American Type Culture Collection, Rockville, MD) were utilized for cell culture studies. Cells were cultured under 37 °C, 5% CO2, and 95% relative humidity in α-MEM (Gibco, Grand Island, NY) growth media containing 1% P/S (Gibco, Grand Island, NY) and either 10% FBS (Atlanta Biologicals, Lawrenceville, GA), for MC3TC-E1, or 20% FBS for hMSCs, EBM-2 bullet kit (Lonza, USA) for HUVEC and DMEM (Cellgro, Manassas, VA) growth media containg 1% P/S and 10% FBS for NIH3T3. The MC3T3 and NIH3T3 at third to seventh passage, hMSCs and HUVECs at second to third passage were used in this experiment.

4.2.5 Direct Live/dead assay

For direct cytocompatibility and cell adhesion testing, MC3TC-E1, hMSCs, HUVECs and NIH3T3 were cultured directly on the surface of Fe-Mg alloy thin layer by PLD. Fe-Mg alloys were deposited on fused silica glass by PLD with the film area approximately 9mm x 9mm. The samples were sterilized on all sides by UV for 60 minutes and incubated in cell culture media for 10 minutes, after which time cells were seeded on the samples at a density of 80,000 cells per well. Live and dead cells were stained using live/dead staining kit (Life technologies, Grand Island, NY) on days 1 and 3 post seeding following the manufacturer's protocol. Cells were then imaged by an inverted microscope with the fluorescence illuminator (CKX41, Olympus, Olympus America Inc.). For each substrate images were taken from three to six different locations to obtain an overview of the cell attachment. After fluorescence imaging, cells on the samples were fixed by 2.5% glutaraldehyde then subjected to alcohol dehydration. Fixed cells on samples were air-dried, after which they were imaged by SEM.

4.2.6 Indirect MTT assay

Indirect cell viability test was assessed using the MTT activity assay (Vybrant MTT Cell Proliferation Assay Kit). Extraction medium was prepared using each cell growth media supplemented with serum in a surface area/extraction medium ratio 6 cm^2ml^{-1}, in accordance with the ISO 10993-12 [200], at 37 °C in a humid atmosphere with 5% CO_2 for 72 hours. The extracted medium was stored at 4°C until cytocompatibility testing. This extraction was designated as 100% extract solution. The control groups involved the use of media without extract as a negative control and media containing 10% dimethyl sulfoxide (DMSO) as a positive control. The cells were seeded in 96-well plates at 6000 cells/well with 200μl media in each well and incubated for 24 hours to allow for attachment. After pre-cell culture, the media was then replaced with 100 μl of extract medium and incubated for 1, 3 and 7 days. After that, media and extracts were replaced with fresh cell culture media and 10 μl of MTT were added to each well. The samples were incubated with MTT for 4 hours at 37°C and then 100 μl of formazansolubilization solution (10% sodium dodecyl sulfate in 0.01M HCl) were added to each well for 12 hours in the incubator under the cell culture atmosphere. The spectrophotometrical absorbance of the samples was measured with the Synergy 2 Multi-Mode Microplate Reader (Bio-Tek Instruments, Winooski, VT) at 570 nm, with a reference wavelength of 630 nm.

4.2.7 Ion release

The thin layer samples of $Fe_{60}Mg_{20}Mn_{20}$ and pure Fe on glass were immersed in each cell growth media containing serum, equilibrated to 37°C for 72 hours. All conditions for immersion test are same with cell viability test including the surface area/extraction medium ratio

(according to ISO 10993-12 [200]). After immersion for 72 hours, the media was collected and then diluted in 0.03 M Tris buffer solution to be analyzed using inductively coupled plasma optical emission spectroscopy (ICP-OES, iCAP duo 6500 Thermo Fisher).The Fe and Mg ion concentrations in solution were compared to media and each other. Samples were prepared in triplicate for each condition.

4.2.8 Statistical analysis

The experimental values were analyzed using the Student's t-test and one-way analysis of variance (ANOVA) and then expressed by mean values ± standard deviation (SD) and statistical significance was considered at $P < 0.05$.

4.3 RESULTS AND DISCUSSION

4.3.1 Microstructural characterization of Fe-Mg-Mn amorphous powder and thin layer

The XRD traces presented in Figure 4.1 follow the structural evolution of as prepared post dry milled powder corresponding to the nominal compositions of $Fe_{60}Mg_{40-x}Mn_x$ (x=0, 5, 10, 15, 20, 25, 30, 35, 40 and 50). The sharp crystalline diffraction peaks of the blended raw mixture powder broadened progressively during HEMA associated with accumulated internal strain and refinement of grain size. For $Fe_{40}Mg_{60}$ (x=0) in Figure 4.1(a), The XRD patterns show a predominant α Fe phase up to x=20 ($Fe_{60}Mg_{20}Mn_{20}$) and peak from hcp Mg is faintly observed around 37° for $Fe_{60}Mg_{40}$, $Fe_{60}Mg_{35}Mn_5$ and $Fe_{60}Mg_{30}Mn_{10}$. The dash lines in Figure 4.1(a)

indicate the position of the Fe (100), Fe (200) and (211) reflection. (PDF# 01-071-4648). For all samples in Figure 4.1(a), the crystalline α peaks displaced towards lower angles, compared to the dash lines indicating positions of pure α Fe, suggesting that Fe lattice expanded as Mg atoms diffuse substitutionally into the Fe lattice which was previously discussed in Section 2.

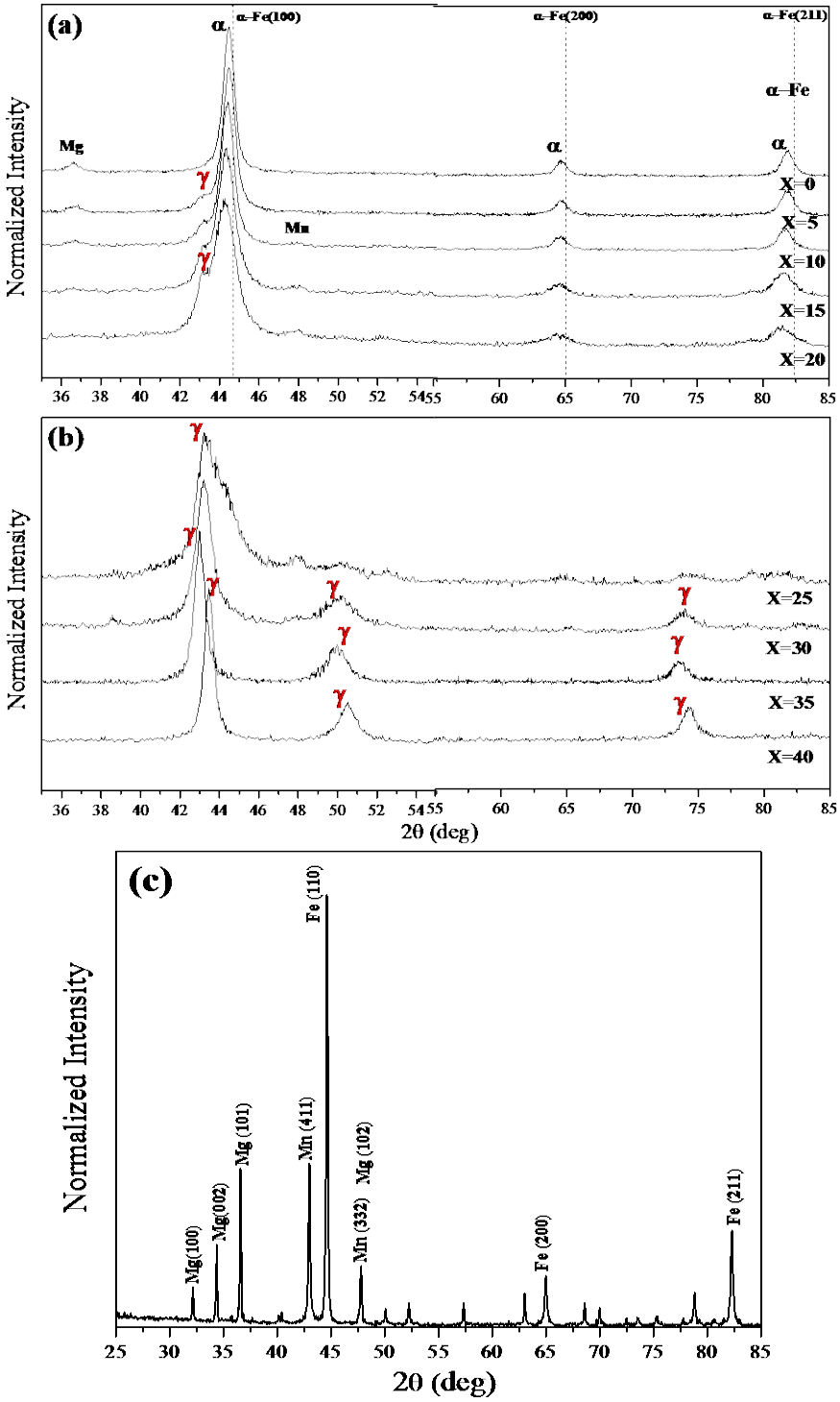

Figure 4.1. The X-ray diffraction patterns of $Fe_{60}Mg_{40-x}Mn_x$ powder (a) x= 0~20, (b) x= 25~40 after post dry milling and (c) the blended raw mixture Fe-Mg-Mn powder.

With increasing Mn content up to 20 at.% (relatively decreased Mg content), the peak from γ phase emerges which is faintly visible around 43° and it yields γ phase (austenite) coexisting with the solid solutions of Mg in α-Fe. This result indicates that α phase is partially transferred to the γ phase with increasing Mn contents up to 20 at.% during post dry-milling.

Interestingly, all of the supersaturated α-Fe solid solution transforms to the γ phase after Mn composition exceeds 25 at.%, as seen in Figure 4.1(b) from the complete disappearance of the Bragg peaks. The α→γ transformation is due to the higher content of austenite forming element, Mn, and the structure became completely austenite between x=25 amd 40 powders ($Fe_{60}Mg_{15}Mn_{25}$, $Fe_{60}Mg_{10}Mn_{30,}$ $Fe_{60}Mg_{5}Mn_{35}$ and $Fe_{60}Mn_{40}$ in Figure 4.1(b). These γ phases are specifically identified as γ Fe (PDF# 01-089-4185 and 03-065-4150). The discrepancies in the α and γ stability are likely caused by the energy stored in HEMA [122, 232]. HEMA is characterized by intensive plastic deformation of powder particles at extremely high strain rate and therefore, creation of a high density of lattice defects such as vacancies, interstitials, dislocations, stacking faults and grain boundaries. The energy associated with these defects can influence the thermodynamics of the phase transition during HEMA by raising the free energy of α and γ crystalline phases and thus changes the stability range of α and γ phases with respect to the equilibrium state. There is still much uncertainty regarding which defects play a major role in raising the free energy of the crystalline state. Nano-crystalline grain boundaries are more likely sources of energy storage in HEMA materials.

Figure 4.2 shows the collected XRD patterns of as prepared milled powder after wet milling corresponding to $Fe_{60}Mg_{40-x}Mn_{x}$. Surprisingly, all of the Bragg peaks due to the solid solutions of Mg in α-Fe, γ phase and bcc- Mn after dry milling have disappeared at x= 20 and 25 ($Fe_{60}Mg_{20}$ Mn_{20} and $Fe_{60}Mg_{15}$ Mn_{25}) which are shown in Figure 4.1 and these formulations

exhibit the typical broad diffraction pattern corresponding to the fully amorphous phase with no indication of any residual crystalline phases. This implies that it has been completely transformed to a homogeneous amorphous phase and it was observed to be initiated by diffusive mixing mechanism [122, 176]. For x < 20 powders ($Fe_{60}Mg_{40,}$ $Fe_{60}Mg_{35}Mn_{5,}$ $Fe_{60}Mg_{30}$ Mn_{10} and $Fe_{60}Mg_{25}$ Mn_{15}), XRD patterns exhibit low intensity sharp peaks from a crystalline phase which were found together with a broad diffraction peak from an amorphous phase. These crystalline phases are identified as γ Fe (PDF# 03-065-4150) and γ Mn (COD# 96-900-8591) for $Fe_{60}Mg_{25}Mn_{15}$, γ Mn and α Fe (COD# 96-901-2709) for $Fe_{60}Mg_{30}Mn_{10}$ and $Fe_{60}Mg_{35}Mn_{5}$, and the solid solutions of Mg in α-Fe. For $Fe_{60}Mg_{10}Mn_{30,}$ the XRD pattern also show the presence of γ (111) and γ Mn over the amorphous peak at around 45° and the peaks from residual γ (200) and (220) as seen in Figure 4.1(b) completely disappear. These unreacted peaks become sharper with increasing Mn content (x=35) and finally transform to the $Fe_{95}Mn_{5}$ (Iron Manganese, PDF# 01-071-8287) for $Fe_{60}Mg_{40}$. However, some unexpected peaks were found for $Fe_{60}Mn_{40}$ and identified as Fe_3C (Iron Carbide, ICSD# 98-011-6089) around 38° and 49° which were introduced by a process control agent (PCA) [233, 234].

As outlined above, HEMA is a solid state process capable of obtaining metastable structures like amorphous and nano crystalline materials. During HEMA, powder particles are subjected to high-energy collisions, which causes the powder particles to be cold-welded together and fractured [122, 173]. It appears from the results following dry milling processing in Figure 4.1 that no pronounced amorphous phase formation was achieved at these milling conditions, suggesting that the current milling conditions were not intense enough to destabilize the crystalline phase and allow the formation of an amorphous phase because of the severe plastic deformation and welding of very ductile powders. There are two methods to prevent the

severe welding: one is to lower the temperature of the milling vial and the other is to add PCA to the powders [233]. Usually, the latter is more favored, thus, toluene was loaded in the vial after dry milling. As shown in Figure 4.1, only α and γ solid solution were formed by dry milling without PCA. However, PCA can reduce the effect of cold welding, thereby inhibiting agglomeration and welding on the vial wall during the seqent wet milling. In this case, supersaturated α-Fe solid solution and γ phase become unstable and transform to an amorphous phase for $Fe_{60}Mg_{20}$ Mn_{20} and $Fe_{60}Mg_{15}$ Mn_{25}, as seen in Figure 4.2. In spite of the important role and multiple influences of PCA in HEMA of ductile materials, it could introduce contaminants. Organic PCA containing atoms such as O, C, H, etc. may affect the process of HEMA [235] and sometimes the atoms exist as impurities after consolidation of mechanically alloyed powders. In this study, Fe_3C was found as a contaminant in Figure 4.2. Therefore, it is important to select an appropriate PCA and its amount in order to avoid complications. Some of these approaches will be adopted in the future.

The morphologies of the as milled $Fe_{60}Mg_{20}Mn_{20}$ powder by HEMA are shown in Figure 4.3 (a). During the HEMA process, the powder particles are repeatedly flattened, cold welded, fractured and re-welded such that the final products usually show large changes in shape, size and distribution from their initial state [122]. Particle shapes also varied significantly after HEMA, with both spherical and plate-like particles being found in the starting powders in Figure 2.4(a) and (b). The final $Fe_{60}Mg_{20}Mn_{20}$ amorphous powder after wet milling consisted of irregular shaped particles which were smaller than ~5 μm with the presence of much finer particles (< 1 μm). Some agglomeration of particles was also found but the powder had a relatively homogeneous distribution due to the reachable in steady-state conditions is achieved, as shown in Figure 4.3(a). EDX analysis in Table 4.1 indicates that the chemical composition of

the amorphous powder is very similar to the starting composition. It is also found that the constituent elements are homogeneously distributed at the atomic scale.

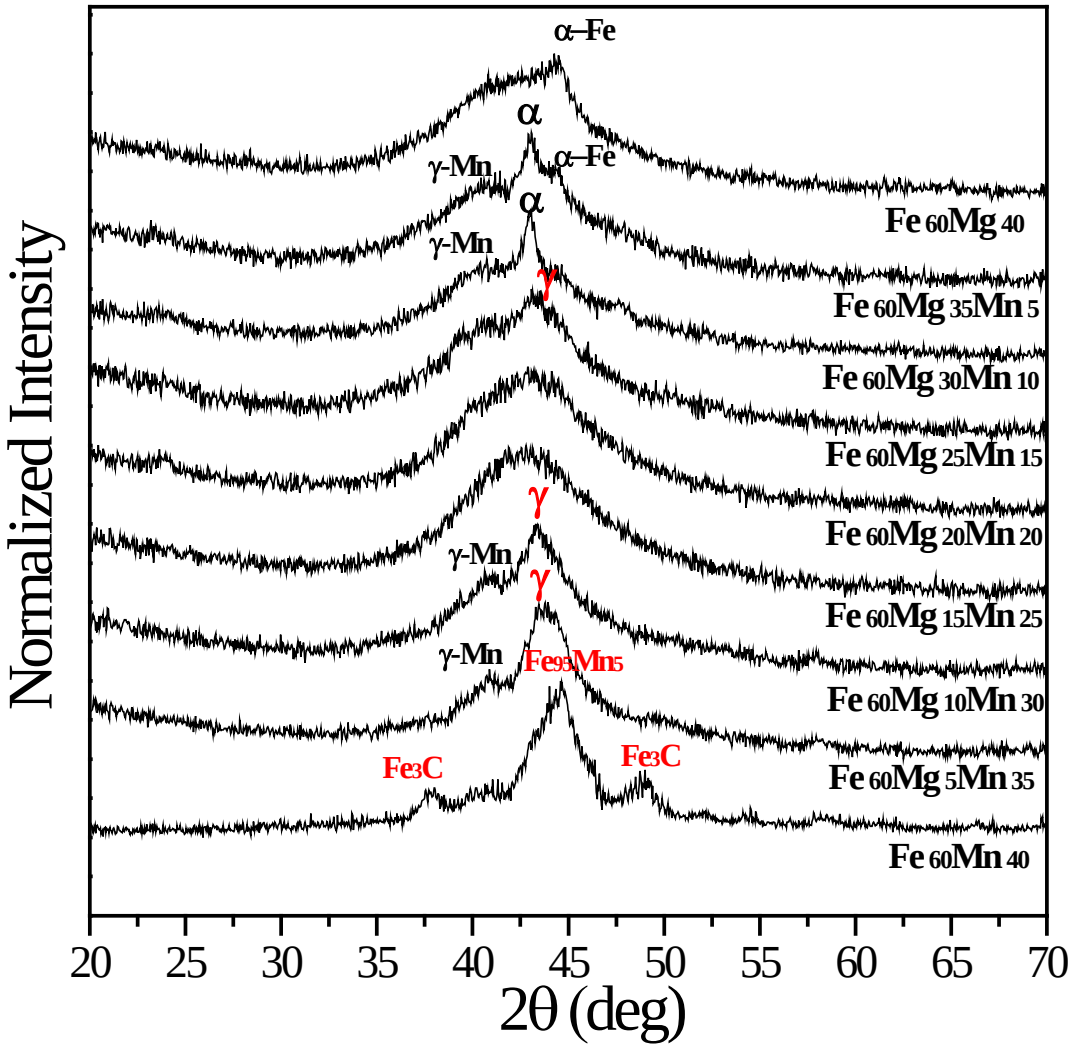

Figure 4.2. The X-ray diffraction patterns of $Fe_{60}Mg_{40-x}Mn_x$ powder (x = 0~40) after subsequent wet milling by HEMA

Table 4.1. Chemical composition the as milled $Fe_{60}Mg_{20}Mn_{20}$ amorphous powder by HEMA and PLD derived $Fe_{60}Mg_{20}Mn_{20}$ amorphous thin layer for 30 minutes of deposition time.

Element	Chemical composition		
	Powder by HEMA	Thin layer by PLD	
		Film	Droplet
Fe K (at%)	60.24 ± 1.32	62.33 ± 4.11	63.81 ± 3.01
Mg K (at%)	20.03 ± 1.32	16.71 ± 4.11	18.21 ± 3.01
Mn K (at%)	19.73 ± 1.32	20.96 ± 4.11	17.98 ± 3.01

Figure 4.3(b) show the HRTEM image with the Fourier transform of the HRTEM image of $Fe_{60}Mg_{20}Mn_{20}$ amorphous powder. The HRTEM image and the Fourier transform present a maze-like pattern/central halo and diffuse rings which is characteristic of an amorphous structure, also consistent with the XRD results of amorphous powders shown in Figure 4.2. Result from HEMA indicate that an amorphous phase is obtained through the sequential process of dry and then wet milling under the milling condition described for this study. The formation of the amorphous phase is verified and confirmed by XRD and TEM analysis. Therefore, we can summarize the amorphization process at the $Fe_{60}Mg_{40-x}Mn_x$ (x= 20 and 25).

Mixture of elemental powders → solid solution → amorphous

In some instances, it has been reported that a solid solution forms first which on continued milling becomes amorphous [178-180]. Thin layer samples were prepared by PLD on glass for 30 minutes from the $Fe_{60}Mg_{20}Mn_{20}$ fully amorphous target. Glancing angle XRD analysis was performed on this deposited layer, shown in Figure 4.4(a). This figure also shows a broad amorphous diffraction pattern.

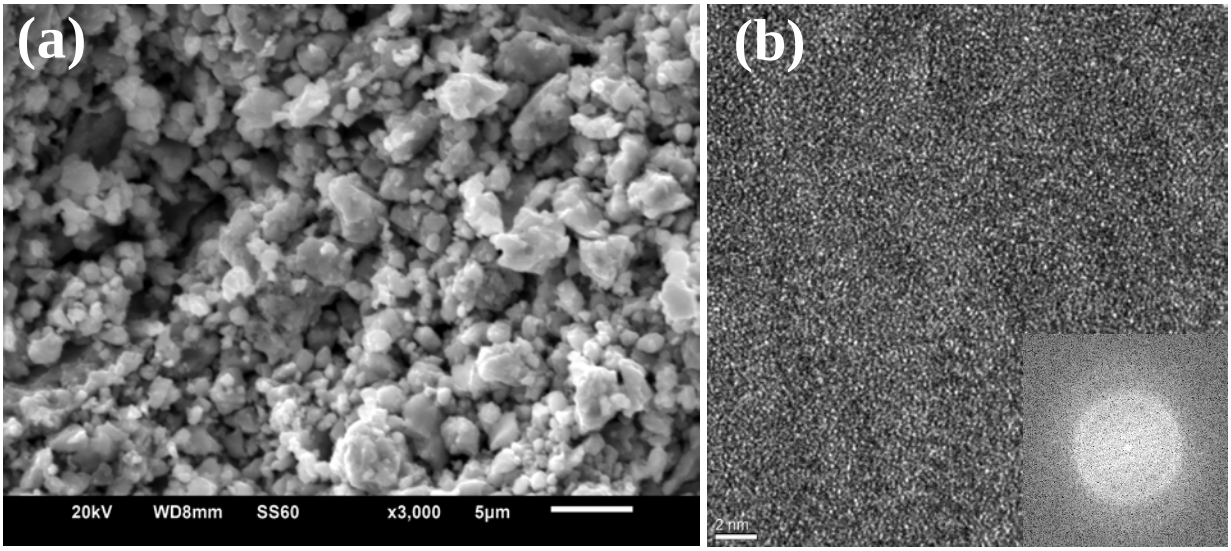

Figure 4.3. (a) The SEM image of $Fe_{60}Mg_{20}Mn_{20}$ following wet milling by HEMA; (b) bright field TEM image and FFT diffraction pattern showing the amorphous nature of the composition.

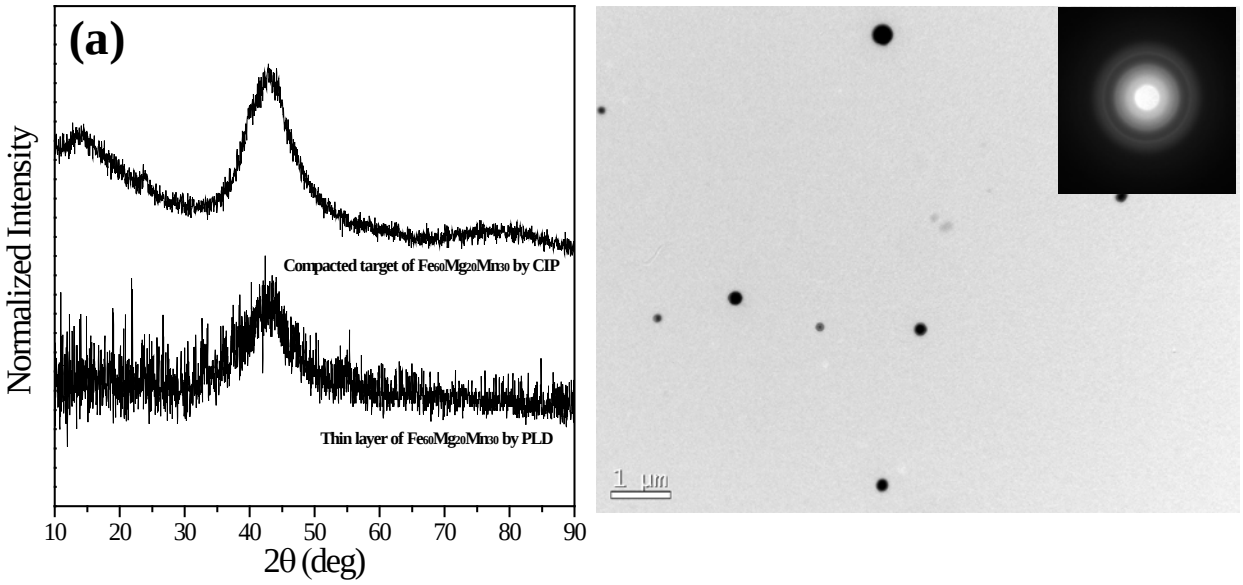

Figure 4.4. Thin layer of $Fe_{60}Mg_{20}Mn_{20}$ on glass deposited for 30min by PLD (a) The X-ray diffraction pattern, (b) Bright field TEM image and corresponding overall SAD pattern.

Figure 4.4(b) shows the TEM bright-field image and corresponding SAD pattern of the thin layer of $Fe_{60}Mg_{20}Mn_{20}$ deposited by PLD. The bright field image shows the presence of large agglomerates or particles (droplets) embedded in the continuous thin layer. This is a typical surface morphology of layers deposited by PLD as seen for the other compositions in the Fe-Mg and Mg-Zn-Ca systems discussed earlier. There is a diffusive halo typical of an amorphous phase in the corresponding overall SAD pattern even though it consists of few droplets on thin layer in the TEM bright-field image. In order to investigate the chemical composition of the thin layer, EDX measurement was also performed and results are given in the Table 4.1. The chemical composition of the amorphous thin layer is very similar to the target composition but some deviation is seen for the particle composition. It is likely due to the varying diffusional kinetics of each elements of target during PLD process [142].

Figure 4.5 shows the corresponding DSC thermograms of the amorphous powder and thin layer of the $Fe_{60}Mg_{20}Mn_{20}$. It is apparent from the DSC thermogram that the glass transition temperature (T_g), the crystallization temperature (T_x) and the super-cooled liquid region ($\Delta T=T_x-T_g$) are about 276.06°C, 399°C, 112.94°C for powder and 261.63°C, 382.23°C, 120.6°C for the thin layer, respectively. Moreover, one exothermic peak, marked as T_p is observed in the trace, and is identified to be the peak corresponding to crystallization of the amorphous phase.

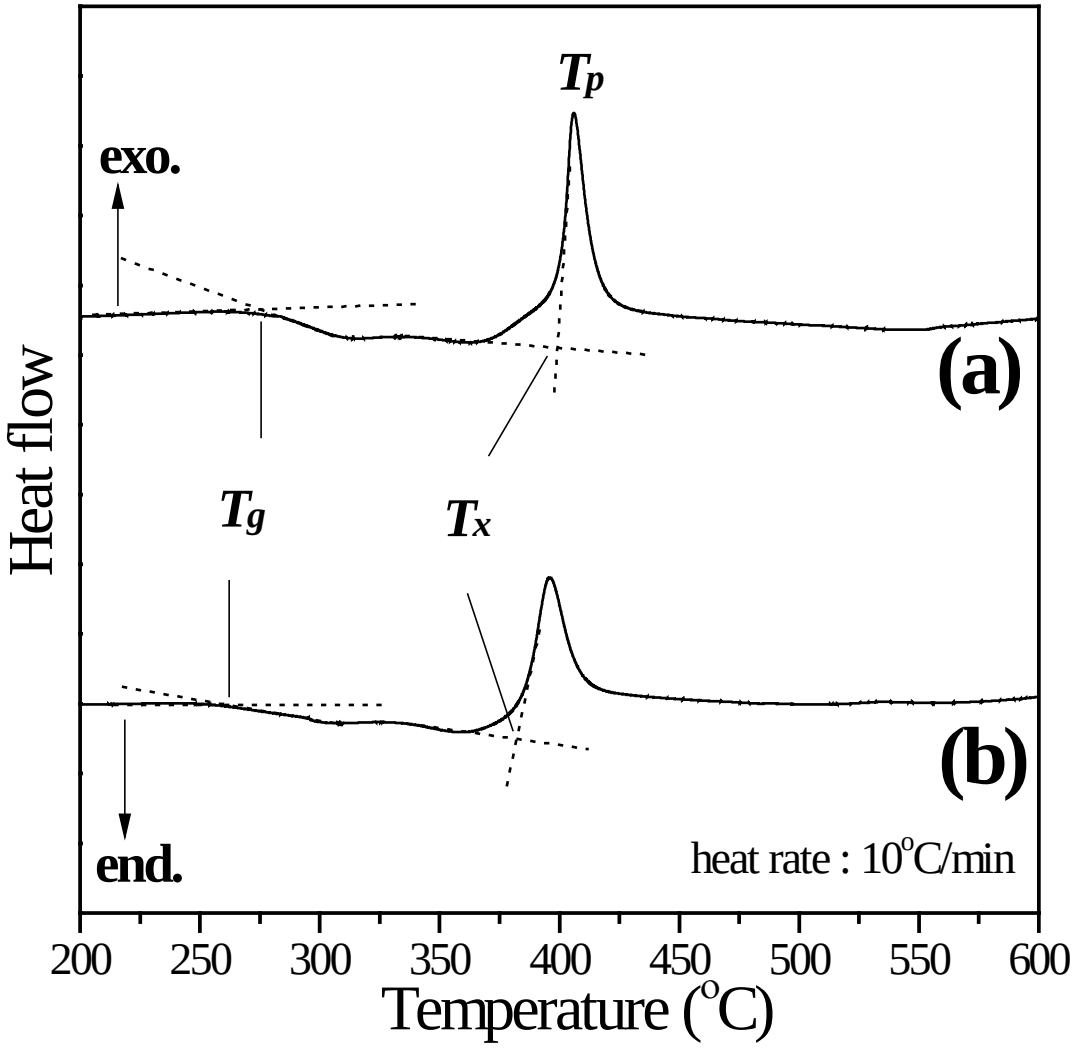

Figure 4.5. DSC thermogram for the $Fe_{60}Mg_{20}Mn_{20}$ (a) amorphous powder by HEMA, (b) amorphous thin layer by PLD.

4.3.2 Magnetic properties of Fe-Mg-Mn powder by HEMA.

Figure 4.6 presented the Magnetization (hysteresis) curves of as prepared post dry milled powder corresponding to the nominal composition of $Fe_{60}Mg_{40-x}Mn_x$ (x= 5 and 35) with pure Fe and SS316L alloy. These two compositions are representative of Mg and Mn rich compositions, repetitively. Compared with SS316L alloy, the as dry milled $Fe_{60}Mg_{35}Mn_5$ shows a higher value of M/H slopes with relatively larger hysteresis loop area but $Fe_{60}Mg_5Mn_{35}$ composition exhibits a much lower and smaller area than those shown in Figure 4.6(a) which can be linked to the XRD patterns and the phase evolution shown in Figure 4.1.

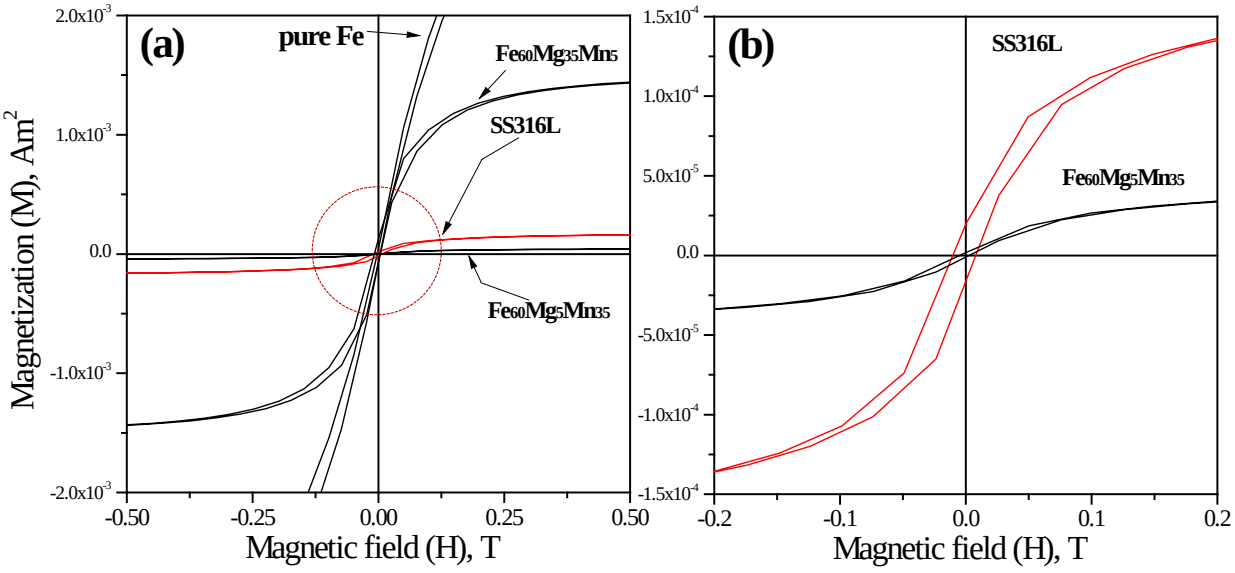

Figure 4.6. (a) M-H curves of Pure Fe, SS316L alloy and $Fe_{60}Mg_{40-x}Mn_x$ powder (x = 5 and 35) after dry milling by HEMA and (b) enlargement of the circled region of the M-H curve in (a).

For as dry milled $Fe_{60}Mg_{35}Mn_5$, it exhibited a typical ferromagnetic behavior with saturation magnetization (M_s) of 138.9 Am^2/kg. It is inferred that the XRD pattern of

$Fe_{60}Mg_{35}Mn_5$ shows a predominant α Fe phase in Figure 4.1(a). The α Fe, ferrite, is one of allotropes of Fe with bcc structure and the classic example of a ferromagnetic material which gives Fe based alloys their magnetic properties [236]. In this context, its ferromagnetic behavior was observed due to the formation of supersaturated solid solutions of Mg in α-Fe. For the $Fe_{60}Mg_5Mn_{35,}$ it has lower M/H slope and M_s value, 1.36 Am^2/kg, compared to SS316L alloy (8.09 Am^2/kg). It is likely due to the $\alpha \rightarrow \gamma$ transformation during dry HEMA in Figure 4.1(b). The γ Fe, austenite, is a nonmagnetic allotrope of Fe with an alloying element [236]. It known that γ phase in Fe-Mn alloys a antiferromagnetic [146, 147], meanwhile the γ phase in SS316L is paramagnetic. Ferrite or ferritic steels are usually classified as magnetic materials, whereas austenite or austenitic steels are often described as non-magnetic, paramagnetic materials [237]. Following dry milling, the material consists of the major crystalline ferrite phase, α Fe phase as shown in Figure 4.1(a), providing a high saturation magnetization. With progressive mechanical alloying (MA), the ferrite phase disappears and the austenite phase, γ phase in Figure 4.1(b), begins to dominate and the saturation magnetization correspondingly decreases.

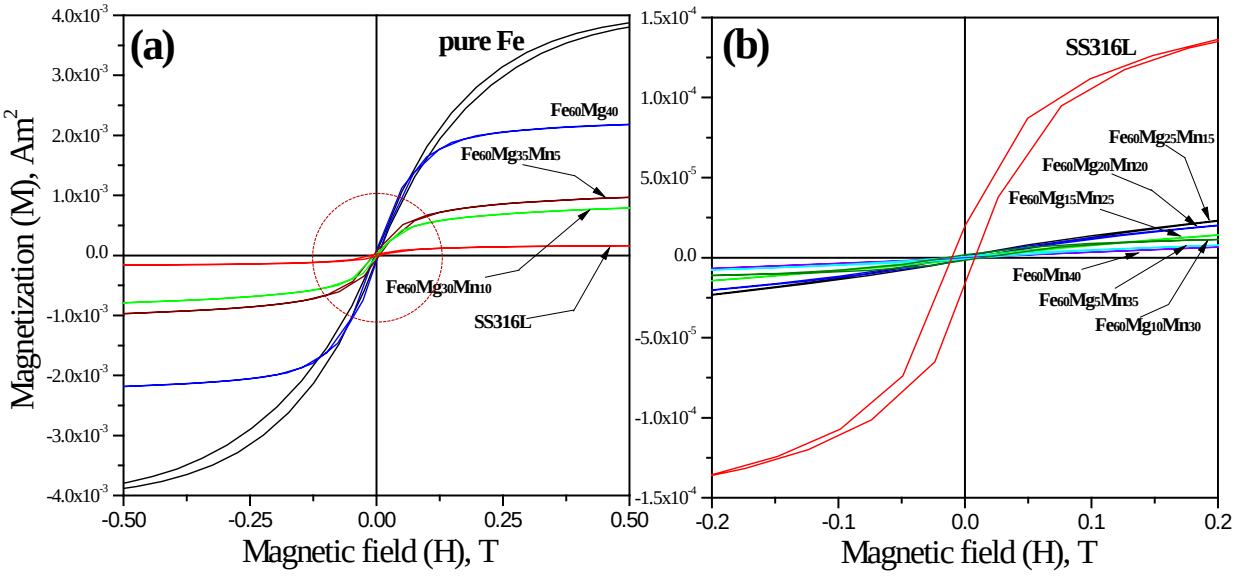

Figure 4.7. (a) M-H curves of Pure Fe, SS316L alloy and $Fe_{60}Mg_{40-x}Mn_x$ powder (x = 0~40) after subsequent wet milling by HEMA and (b) enlargement of red circle on (a) M-H curve.

The hysteresis loop for Fe-Mg-Mn alloy powder after subsequent wet milling is shown in Figure 4.7. As shown in Figure 4.2, their XRD patterns exhibit low intensity sharp peaks from α Fe, γFe and γMn phases which were found together with a broad diffraction peak from an amorphous phase up to 10 at.% Mn (x=0, 5 and 10). Due to the presence of unreacted α Fe phases within the amorphous phase, all the samples with Mn concentration below 10 at.% still exhibit the ferromagnetic behavior but with much reduced saturation magnetization compared with that of $Fe_{60}Mg_{35}Mn_5$ after dry milling shown in Figure 4.6(a). The M_s values were reduced to 83.82, 46.31 and 39.87 Am^2/kg for $Fe_{60}Mg_{40}$, $Fe_{60}Mg_{35}Mn_5$ and $Fe_{60}Mg_{30}Mn_{10}$, respectively. Primary magnetic properties derived from the magnetization loops shown in Figure 4.6 and Figure 4.7 are summarized in Table 4.2.

A dramatic change in the magnetic properties of the $Fe_{60}Mg_{40-x}Mn_x$ powder (x = 15~40) after subsequent wet milling by HEMA is shown in Figure 4.7(b). All the samples exhibit almost no

hysteresis loop and no area of loop compared to SS316L. Primary magnetic properties derived from the magnetization loops show that compared to SS316L, they have lower M_s, lower remnant magnetization (M_r), lower initial susceptibility (χ_o) and coercivity (H_c). It can also be seen that as the Mn content increases the slopes and the area of hysteresis loops decrease. Notice that the magnetic properties also continuously decrease with increasing Mn content in the as milled powder up to 40 at.% Mn as it should if the α phases were decreased. These observations therefore implies that most of the α-ferrite phase is transferred to the amorphous phase or γ phase during wet milling which is in good agreement with XRD patterns after wet HEMA as shown in Figure 4.2. The decrease in the magnetization of the Fe-Mg-Mn alloys can result from the amorphous structure produced during the high-energy milling process. Amini et al, reported a similar behavior in Fe-Cr-Mn-N alloy system [237]. With continued progression of the MA process, an amorphous phase is created growing along grain boundaries and consumes the crystalline lattice. With sufficient and extended milling, the amorphization process is thus completed and consequently, the saturation magnetization decreased.

Table 4.2. Magnetic properties of the as milled $Fe_{60}Mg_{40-x}Mn_x$ powder (x = 0~40) powder derived by HEMA and SS316L.

Materials	Hc (10^{-3}T)	Mr (10^{-2}A m²/kg)	Ms (A m²/kg)	Mr/Ms	χ_o (A m²/(kg T))
$Fe_{60}Mg_{35}Mn_5$ (dry milling)	6.02	905.88	138.39	0.065	6.76
SS316L	9.09	77.87	8.09	0.096	2.18
$Fe_{60}Mg_{40}$	3.69	314	83.82	0.037	5.15
$Fe_{60}Mg_{35}Mn_5$	5.95	262	46.31	0.056	4.99
$Fe_{60}Mg_{30}Mn_{10}$	2.76	105	39.87	0.026	5.09
$Fe_{60}Mg_{25}Mn_{15}$	7	4.84	5.96	0.008	1.31
$Fe_{60}Mg_{20}Mn_{20}$	4.77	2.07	5.59	0.004	1.03
$Fe_{60}Mg_{15}Mn_{25}$	7.43	3.03	4.51	0.006	0.93
$Fe_{60}Mg_{10}Mn_{30}$	4.87	1.27	2.1	0.006	0.9
$Fe_{60}Mg_5Mn_{35}$	1.35	1.08	1.73	0.006	0.71
$Fe_{60}Mn_{40}$	1.47	1.01	1.14	0.008	0.38

H_c: coercivity. M_r: remanent magnetization. Ms: saturation magnetization χ_o: initial suscepitibility

4.3.3 Corrosion characterization of $Fe_{60}Mg_{20}Mn_{20}$ amorphous thin layer by PLD.

Potentio-dynamic polarization (PDP) curves obtained for the thin films of $Fe_{60}Mg_{20}Mn_{20}$ and pure iron on glass and polished bulk pure iron can be seen in Figure 4.8 as a representative scan of the multiple samples tested. Table 4.3 gives a summary of the corrosion potential and the corrosion current densities as calculated from extrapolation of the Tafel plots. The $Fe_{60}Mg_{20}Mn_{20}$ amorphous thin film on glass (a) resulted in an i_{corr} value approximately 2 fold higher than that of both Fe thin layer of same thickness (c) and bulk (d) samples as well as E_{corr} values that are more cathodic. It can be inferred from the above results that the $Fe_{60}Mg_{20}Mn_{20}$ alloy shows improved corrosion rates compared to that of pure Fe samples. However, E_{corr} of the $Fe_{60}Mg_{20}Mn_{20}$ amorphous sample is still less negative compared to that of $Fe_{70}Mg_{30}$ from Chapter 3, indicating that it has relatively slower degradation rate compared to $Fe_{70}Mg_{30}$ amorphous alloy. The $Fe_{60}Mg_{20}Mn_{20}$ alloy exhibits an increase in corrosion current density over that of pure iron samples, which were measured at 14.14±4.35µA cm^{-2} for bulk and 12.46±2.3µA cm^{-2} for thin layer, respectively. There is however, no statistical difference in the value of i_{corr} value between bulk and thin layers of pure iron.

Table 4.3. Corrosion potential (E_{corr}) and current density (i_{corr}) values for $Fe_{60}Mg_{20}Mn_{20}$ layer, both bulk and thin layer of pure iron. The corrosion current density is significantly higher for $Fe_{60}Mg_{20}Mn_{20}$ than both pure iron samples *(P<0.05)*.

Element	Corrosion potential, E_{corr}(V)	Corrosion current density. I_{corr}(μAcm^{-2})
$Fe_{60}Mg_{20}Mn_{20}$ amorphous thin layer	-0.621	27.07±3.3
$Fe_{70}Mg_{30}$ amorphous thin layer	-0.642	98.76±11.08
Pure Fe (thin layer)	-0.616	12.46±2.3
Pure Fe (bulk)	-0.592	14.14±4.35

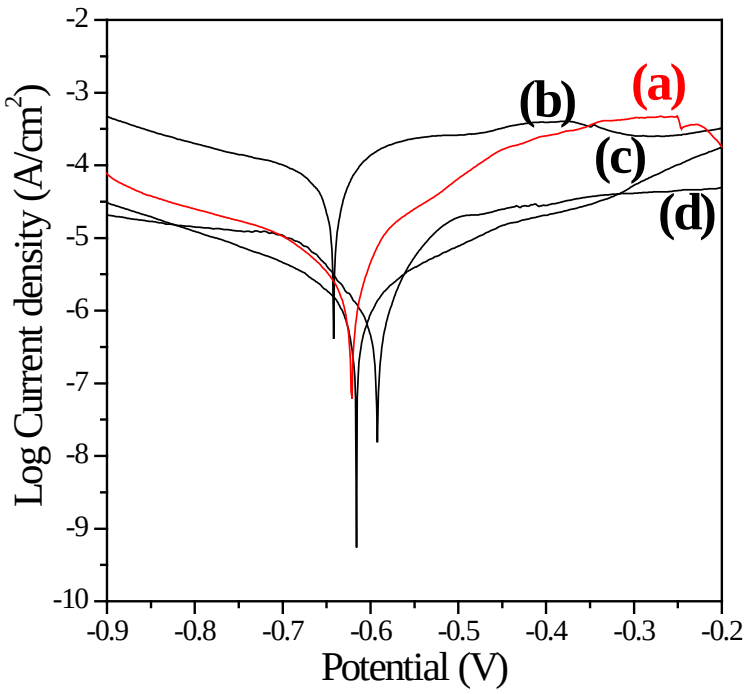

Figure 4.8. Polarization curves of (a) $Fe_{60}Mg_{20}Mn_{20}$ amorphous thin layer, (b) $Fe_{70}Mg_{30}$ amorphous thin layer, (c) pure iron thin layer on glass derived by PLD and (d) mounted bulk pure iron.

4.3.4 In vitro cytocompitability measurement of $Fe_{60}Mg_{20}Mn_{20}$ amorphous thin layer by PLD.

Live/Dead staining of MC3T3-E1, hMSCs, HUVECs and NIH3T3 on day 1 and day 3 of post seeding can be seen in Figure 4.9 and 4.10, respectively. Figure 4.9 shows the fluorescence microscopy images of live/dead assay conducted on the amorphous thin layer and plastic tissue culture surface (control) after 1 day. For all the cell cultures, fluorescence microscopy from the live/dead assay shows similar live cells (green) attachment with few dead cells (red) on the surface of $Fe_{60}Mg_{20}Mn_{20}$ layer except NIH3T3 which shows less live cell attachment and unususal shapes which are shrunk compared to the control. After 3 days of culture (Figure 4.10), the $Fe_{60}Mg_{20}Mn_{20}$ amorphous thin films, seeded with MC3T3-E1, hMSCs and HUVEC still again displayed a similar or a slightly less level of living cell attached comparable to the tissue culture plastic as control, with a higher cell density than day 1 and cells more evenly distributed. NIH3T3 still however, showed fewer live cells attached than the tissue culture plastic. The live/dead staining overall indicates good cell viability and proliferation on $Fe_{60}Mg_{20}Mn_{20}$ amorphous thin layer for MC3T3-E1, hMSCs and HUVECs although showing some cytotoxicity for NIH3T3 fibroblasts cells.

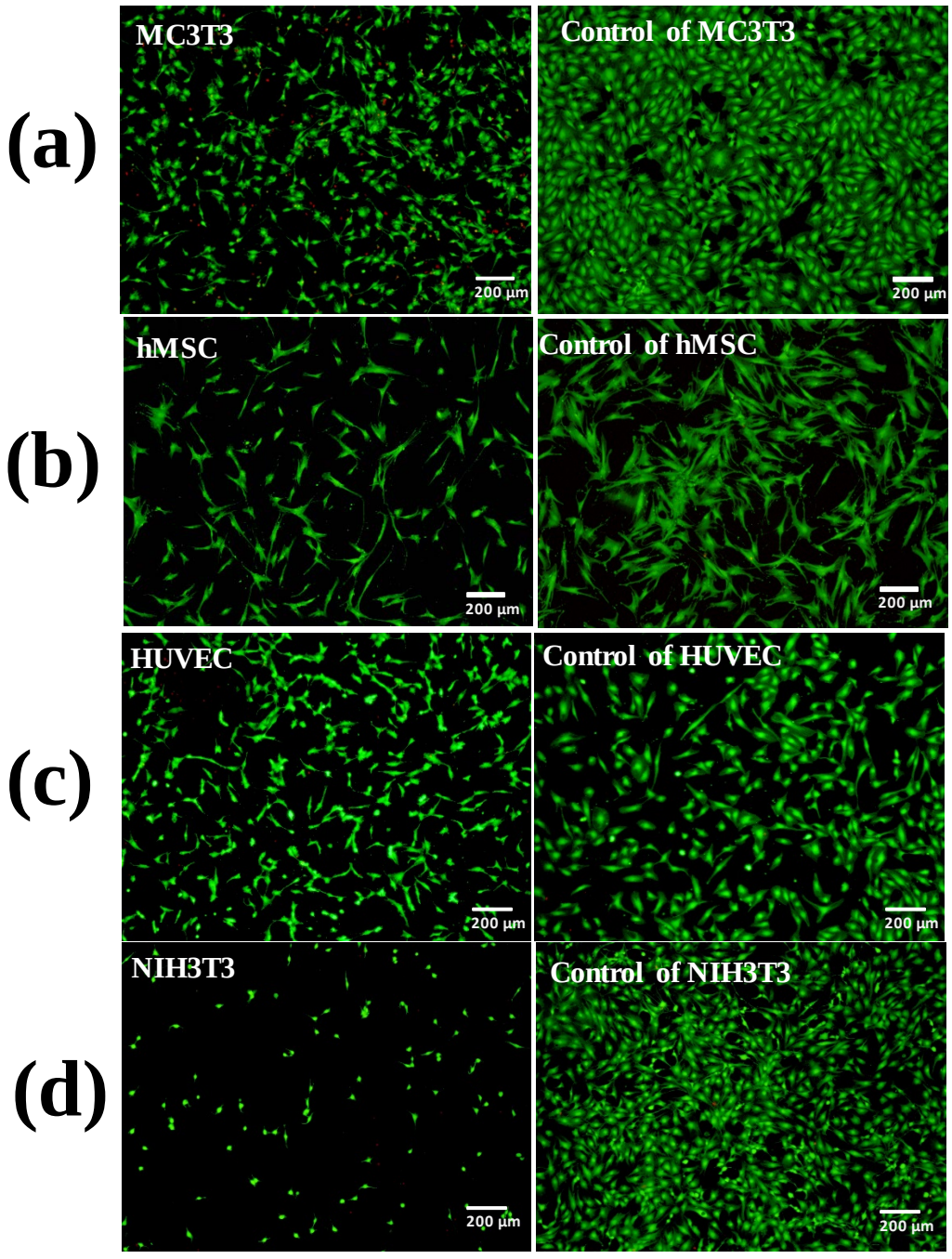

Figure 4.9**.** Live/Dead staining of (a) MC3T3 osteoblasts, (b) hMSCs, (c) HUVECs and (d) NIH3T3 fibroblasts on day 1 of culture post seeding on the thin layer of $Fe_{60}Mg_{20}Mn_{20}$ on glass and tissue culture plastic as control.

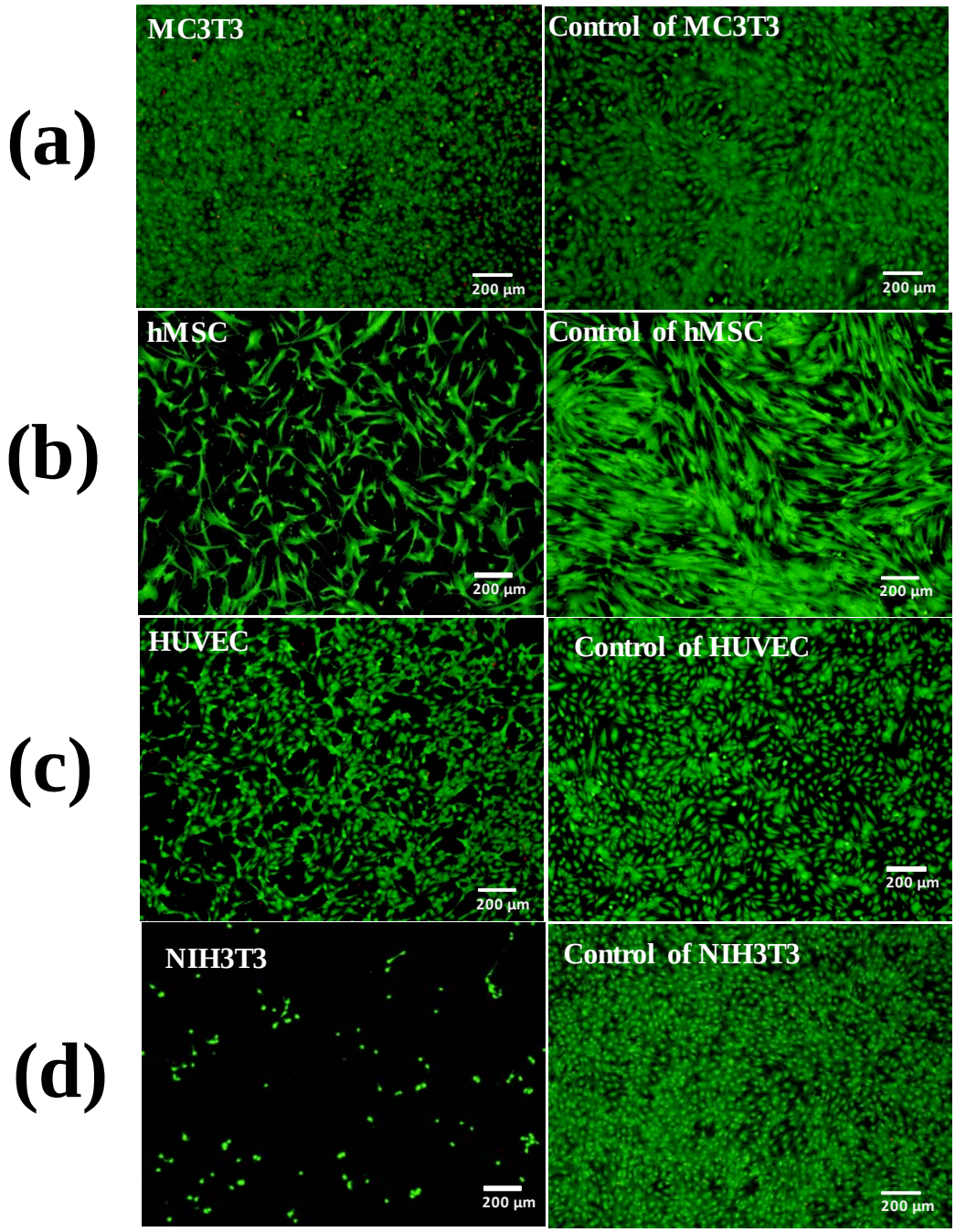

Figure 4.10. Live/Dead staining of (a) MC3T3 osteoblasts, (b) hMSCs, (c) HUVECs and (d) NIH3T3 fibroblasts on day 3 of culture post seeding on the thin layer of $Fe_{60}Mg_{20}Mn_{20}$ on glass and tissue culture plastic as control.

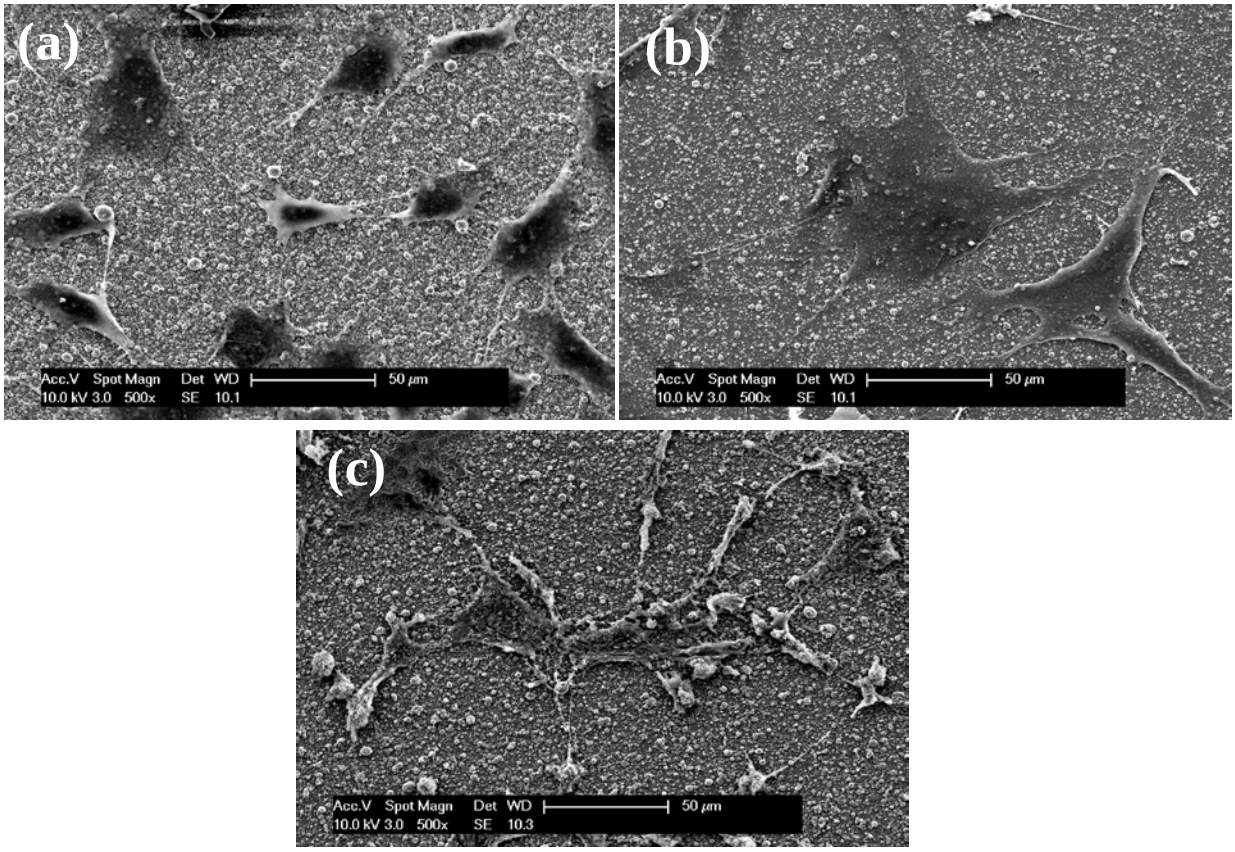

Figure 4.11. SEM morphology of fixed (a) MC3TC-E1, (b) hMSCs and (c) HUVECs at 24h post-seeding on $Fe_{60}Mg_{20}Mn_{20}$ thin layer deposited on glass.

SEM images of all the cells except NIH3T3 fibroblast cell attached to the surface of the $Fe_{60}Mg_{20}Mn_{20}$ amorphous thin layer (Figure. 4.11) confirms the live/dead assay results, with a high attached cell density on the surface. MC3T3-E1, hMSCs and HUVECs also exhibit good cell attachment on the $Fe_{60}Mg_{20}Mn_{20}$ amorphous thin layer, and it was also evident that the cells started to proliferate on the surface. The cell spreading was uniform with filopodia formation, suggesting that $Fe_{60}Mg_{20}Mn_{20}$ amorphous thin layer is stable under the physiological environment and is conducive for cell growth and proliferation.

Figure 4.12 illustrates the cell viabilities of MC3TC-E1, hMSCs, HUVECs and NIH3T3 expressed as a percentage of the viability of cell cultured in the negative control after 1, 3, and 7 days' incubation in the extraction mediums after 72 hours using the MTT assay. These quantitative results of indirect cell viability support what was seen qualitatively in the live/dead staining, indicating good cell viability and proliferation on $Fe_{60}Mg_{20}Mn_{20}$ amorphous thin layers. For all the 1, 3 and 7 days of culture periods, the cell viabilities for MC3TC-E1 and HUVECs on $Fe_{60}Mg_{20}Mn_{20}$ was only slightly lower than the control but similar to that of pure Fe while the viability of the other two cell lines (hMSCs and NIH3T3) were lower than that of pure Fe. There was also significant difference ($P<0.05$) between the results shown in Figure 4.12(b) and (d). Several groups have also reported decreased cell viability compared to the negative control. This may be related to concentration of specific ions leaching out into the solution as higher Mn ion concentration are known to lead to lower cell viability. Based on Figure 4.11(a), values of cell viability for MC3T3 osteoblasts in amorphous $Fe_{60}Mg_{20}Mn_{20}$ extracts was nearly 100% after 1 day of exposure. However, viabilities decreased to ~ 90% compared with that of negative control after 3 and 7 days' incubation. For NIH3T3 cells, the cell viability was however lowered to about 40% after 1day incubation which is in good agreement with live/dead result on day 1 shown in Figure 4.9(d). The viability was also finally just below half the value compared to the negative control after 7day's incubation shown in Figure 4.11 (d). The hMSCs and HUVEC cells displayed ~70% and ~80% viability after 1 day of exposure and continuously exhibited similar viability ~75% and ~85 of the negative control after 7days, respectively.

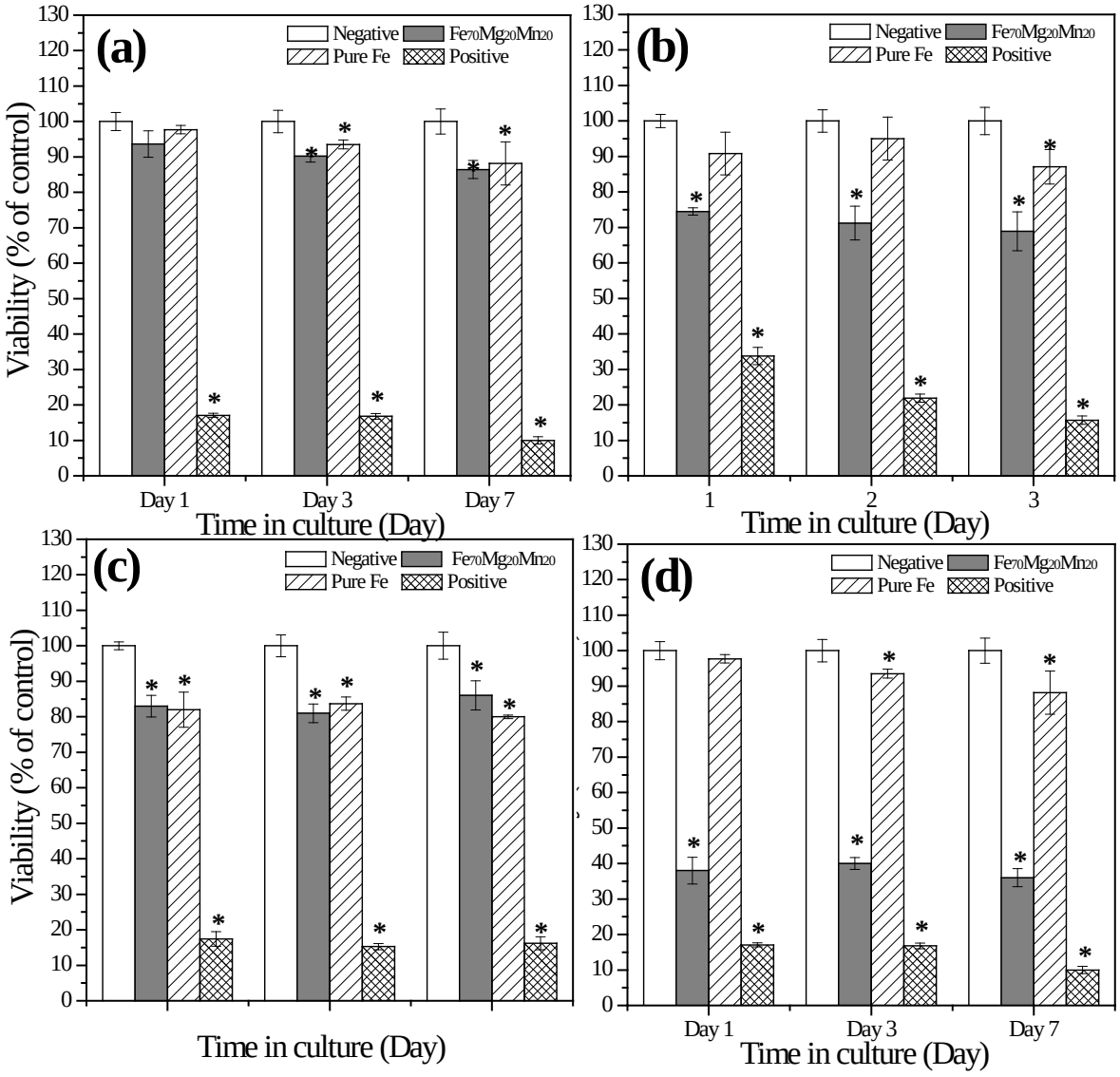

Figure 4.12. Cell viability of (a) MC3T3 osteoblasts, (b) hMSCs, (c) HUVECs and (d) NIH3T3 after 1, 3 and 7 days incubation in extract medium collected after 72 hours from $Fe_{60}Mg_{20}Mn_{20}$ and pure Fe thin layer of ~1.3μm thickness on glass. * Significant difference compared to cell viability of the negative control group ($P<0.05$).

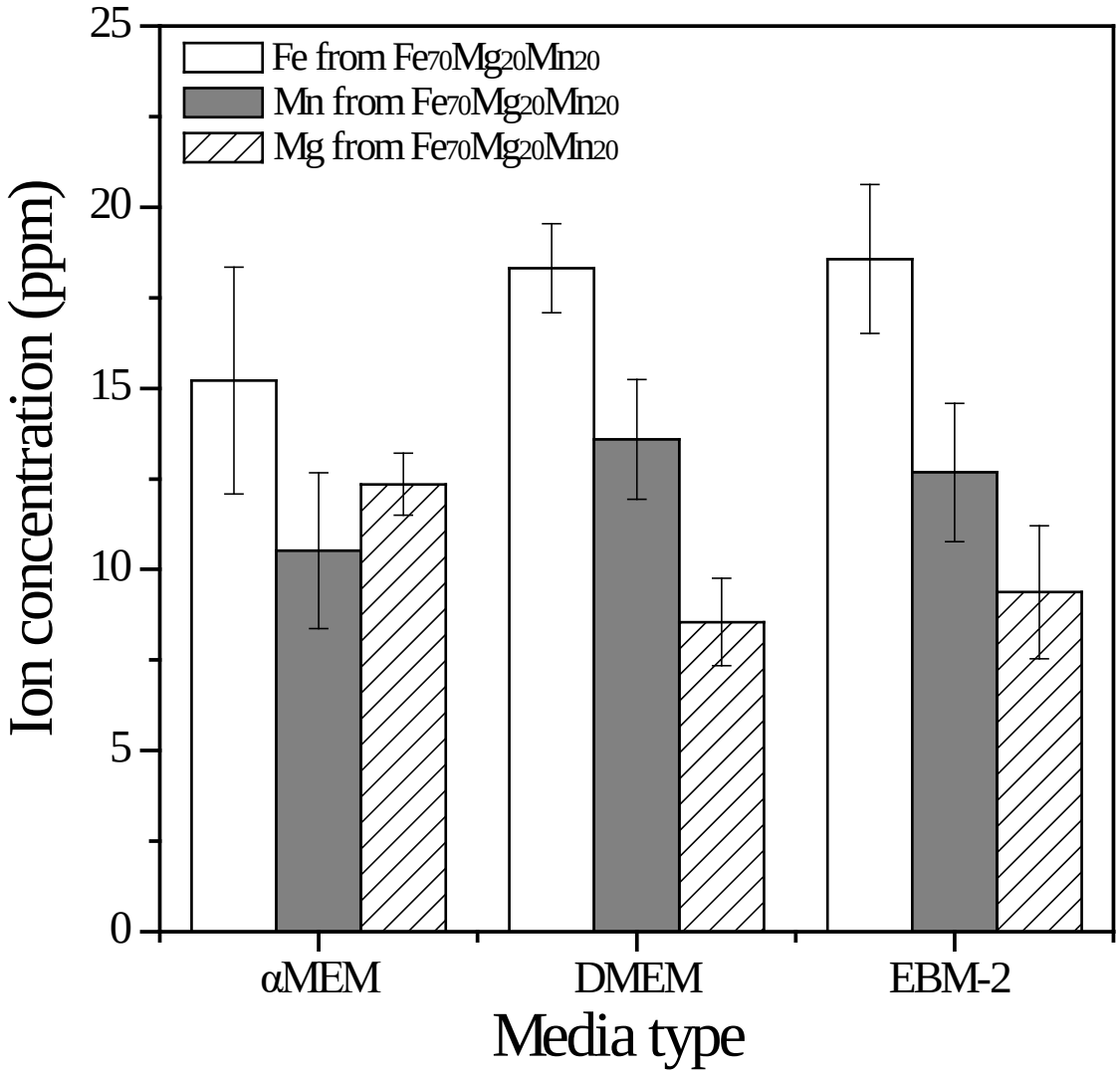

Figure 4.13. Ion concentration of Fe, Mn and Mg after immersion of the amorphous $Fe_{60}Mg_{20}Mn_{20}$ thin layer of ~1.3 μm thickness on glass in cell culture media for each cell line for 72 hours.

As can be seen, based on the *in vitro* cell viability tests conducted in the current study, $Fe_{60}Mg_{20}Mn_{20}$ amorphous thin film layers derived by PLD seemed to exhibit very good viability, proliferation and morphology for MC3T3-E1 cells. There was also no adverse effects on cell cell viability, proliferation and morphology for all the other cell lines except for NIH3T3 cells. In the case of the direct cell viability and adhesion test for MC3TC-E1, hMSCs and HUVECs as seen in Figure 4.9-4.11, the $Fe_{60}Mg_{20}Mn_{20}$ amorphous thin films demonstrated good cell viability, with well adhered cells on the samples after 1 and 3 days of culture compared to control as well as 0~1 cytotoxicity grades by ISO 10993-5 [217]. However, the $Fe_{60}Mg_{20}Mn_{20}$ amorphous thin layer indicates much reduced cytocompatibility effect for NIH3T3 cells indicating a grade 3 level of cytoxicity with not more than 70% growth inhibition observable and only ~40% cell viabiity for all three, day 1, day 3 and day 7 of the indirect MTT cell viability assay [217].

As discussed earlier, toxicity of metal elements is provoked from reactions between metal and body fluids acting as electrolytes. The metal ions, which are formed by anodic reaction as $M(s) \leftrightarrow M^{2+}+2e^{-}$, readily catalyze the generation of toxic reactions [220]. This depends on the character of the metal ions itself against cell metabolic activities. Hence, the toxicity of metal elements in this study, indicating low cell viability, is usually explained by higher concentration of metal ions that may exert harmful behavior. It has been generally found that pure Fe and pure Mg show acceptable to good cytocompatibility and this has already been evaluated based on the cytocompatibility of Fe and Mg using the average concentations of their ions in each collected extract used in indirect cell viability test for $Fe_{70}Mg_{30}$ alloy in previous chapter. In this chapter, similar experiments were conducted to measure the effects of $Fe_{60}Mg_{20}Mn_{20}$ alloy and the results

are shown in Figure 4.13. Compared to the results from $Fe_{70}Mg_{30}$, the alloy exhibited lower concnetration of Fe and Mg ions in each growth media in this study. However, the $Fe_{60}Mg_{20}Mn_{20}$ amorphous thin layer exhibited cytotoxic effect for NIH3T3 fibroblasts cells even though they have lower concentration value of Fe and Mg ions in media compard to previous results in Figure 3.14. As the corrosion extract concentration for Fe and Mg (Figure 4.12) was found to be much lower than the critical values from literature, with no other alloying elements being released, it appears that the decrease in cell viability is mainly due to the Mn ion concentration in extract solution in this study.

Mn is also an element essential for development and body functions, specifically for bone formation, calcium absorption, blood sugar regulation, and fat and carbohydrate metabolism [135, 238]. It forms part of several enzymes, glutamine synthetase and superoxide dismutase [238]. Manganese, like Fe, is a redox active species and can switch between Mn^{2+} and Mn^{3+}. In addition, due to transport mechanisms that favor influx over efflux, intracellular Mn^{2+} is sequestered in the mitochondria and these are therefore the primary pool of Mn in the cells [238, 239]. The role of Mn is hence ambivalent as regards to the generation and attenuation of oxidative stress [239, 240]. Finally, Mn is expected to show toxicity via oxidation of biological molecules, and by the influencing Ca and Fe homeostasis [241, 242]. These arguments therefore likely explain the limited cytocompatibility observed for Mn. Past studies have demonstrated positive biocompatibility and cytocompatibility of Fe and Fe-Mn, with iron degradation products shown to be cleared by macrophages without inducing any local toxic effects [42], and Mn appears to have the highest inhibition effect to the NIH3T3 fibroblast cells [75]. The critical concentration of Mn ion for each cell line used in this study were found in the literatures and given as the half maximal inhibitory concentration (IC_{50}) values for compatibility corresponding

to the concentrations of substances required to induce a 50% reduction in cellular response in comparison to untreated cells [216]. Generally, the IC_{50} levels strongly depend on the cell type and experimental conditions [135].

For HUVECs, the collected extraction from EBM-2 contained average concentration of 12.68±1.91 ppm for Mn after 72 hours immersion (Figure 4.13) and the IC_{50s} of Mn for HUVECs were found to be ~60 ppm [135]. For NIH3T3 fibroblast cells, the Mn concentration in extraction from DMEM was 13.59±1.65 ppm, while for Mn the IC_{50s} is about 2.52 ppm [158] and 5.5 ppm [75]. The cell viability of HUVEC for $Fe_{60}Mg_{20}Mn_{20}$ sample is more than ~85% compared with that of negative control up to 7 days of incubation, indicating no cytotoxicity following the ISO 10993-5 [217] protocol. It can be interpreted that the measured Mn ion value is below the IC_{50s} of Mn for HUVECs. In contrast with HUVECs, the $Fe_{60}Mg_{20}Mn_{20}$ amorphous thin layer exhibited cytotoxic effect for NIH3T3 fibroblasts cells since the measured corrosion extract concentration of Mn was much higher than the IC_{50} values found in literature. However, it exhibited more than ~75% cell viability for MC3T3-E1 compared with that of negative control even though measured Mn concentration in αMEM (10.52±2.15 ppm) was higher than the IC_{50s} of Mn (2.09 ppm) [158]. Therefore the IC_{50} levels only show general trends and cannot be treated as absolute values [135]. As mentioned in earlier chapters, it was difficult to measure the concentration of corrosion products due to the fact that the extraction medium is a very complex solution and sensitive to pH value and temperature. Therefore, it is difficult to measure the actual ion concentration in solution because of undissolved corrosion product in the solution. Assuming the corrosion products to be well tolerated by the cells, the newly developed Fe-Mg-Mn alloys can be considered to be cytocompatible within the framework of the demanding conditions given in the present work.

4.4 CONCLUSIONS

In the present studies, the amorphous powder and amorphous thin film of $Fe_{60}Mg_{20}Mn_{20}$ composition have been successfully generated with non magnetic antiferromagnetic property by HEMA and PLD. Based on the results, it can be seen that the amorphization process is summarized for the $Fe_{60}Mg_{40-x}Mn_x$ (x= 20 and 25) composition as follows:

Mixture of elemental powders → solid solution (α,γ) → amorphous

Potentiodymamic polarization test in DMEM + 10% FBS shows that the $Fe_{60}Mg_{20}Mn_{20}$ amorphous thin layer on glass resulted in an i_{corr} value approximately 2 fold higher than both of Fe thin layer of same thickness and bulk samples as well as E_{corr} values that are more cathodic. However, the composition shows relatively slow degradation rate compared to the $Fe_{70}Mg_{30}$ amorphous alloy which was discussed in Chapter 2 and 3. Preliminary *in vitro* cell viability tests also show that the $Fe_{60}Mg_{20}Mn_{20}$ amorphous thin layer demonstrated good cell viability for MC3TC-E1, hMSCs and HUVEC cells as well as 0~1 cytotoxicity grades by ISO 10993-5 with comparatively lower viability and cytocompatibility with a grade 3 cytotoxicity for NIH3T3 cells due to the likely effects of Mn concentration released on the NIH3T3 cells.

5.0 SPECIFIC AIM 4: STUDY THE EFFECT OF ADDITION OF CALCIUM (CA) AND ZIRCONIUM (ZR) ALLOYING ELEMENTS TO FE-MG OR FE-MG-MN ALLOYS AND UNDERSTAND THE IN VITRO RESPONSE TO EXPLORE THE POTENTIAL OF THESE ALLOYS AS NOVEL BIODEGRADABLE MATERIAL SYSTEMS

5.1 INTRODUCTION

As discussed all along in the previous chapters, Fe and Fe based alloys have been widely researched as potential degradable metallic biomaterial with suitable mechanical properties and biocompatibility [14]. In particular, corrosion is the major degradation mechanism of biodegradable Fe alloys which need to be controlled or monitored to achieve the optimal device resorption rates desired by devices to be successfully used for different applications [39, 63]. Corrosion of Fe alloys as outlined in the earlier chapters is controlled by modifying various alloying elements, heat treatment, or surface modification as well as novel fabrication methods [61]. Attempts to accelerate the degradation kinetics of Fe is indeed the major cornerstone ultimately desired requiring proper design of the alloy composition as well as the processing conditions and parameters to achieve and maintain the optimal metal ion release rates to be within the accepted tolerable ranges. Successful achievement of the desired corrosion and

degradation characteristics of Fe based alloys will provide a pathway for using these alloy systems ultimately for various device applications.

In addition to the above, Fe is ferromagnetic in nature and it is therefore essential to identify ideally alloying elements that will alter this property to render Fe alloys compatible with high magnetic field such as that generated by Magnetic Resonance Imaging (MRI) to be widely used for post-implantation monitoring and diagnostic testing as well as universal acceptance as an implant material [58]. Advanced clinical synergy is also anticipated and desired when biodegradable Fe alloys is used as bone fixation devices or cardiovascular stents. Fe alloys are attractive as outlined earlier primarily due to the excellent match in terms of its mechanical properties. Bone fixation devices or implants while being very essential are also not preferred to remain in the body once bone healing and desired remodeling has been achieved. Permanent metallic devices as is the norm today are allowed to remain in the body as permanently implanted systems. In some instances, they are often removed from patients in the event of undesirable corrosion and wear of the devices leading to complications and inflammation. However, such removal surgeries are more prescribed by the clinicians due to complications or rejection of the implanted hardware leaving the patient very much compromised without a proper remedial treatment of the original medical problem.

In most cases, once a solution has been provided and there is healing of the bone with the implanted inert and biocompatible hardware, the hardware is in general kept inside the patient due to the stiffness mismatch with normal bone causing residual stress and stress shielding problems. Removal surgery is more common in pediatric patients to avoid any interference or conflict with growing inherent pediatric bone plates with the implanted hardware causing major complications that run the risk of creating permanent damage. However, such removal surgeries

as outlined earlier have their own share of associated risks of recurring fracture, inflammation and other complications. Hence the option of having a degradable metal with mechanical properties matching natural bone renders the concept very attractive and highly lucrative. Therefore, iron-based materials are considered an interesting option for novel biodegradable medical implants due to their appropriate ductility and strength compared with their counterparts, magnesium alloys. Moreover, the properties of Fe alloys could be further enhanced by purposeful alloying and by applying specific thermo-mechanical treatments [243]. Recently, an alternative approach has been launched to develop Fe-based materials with improved degradation behavior and bioactivity for bone implant applications by incorporating various bioactive bio ceramics such as hydroxyapatite, tricalcium phosphate, biphasic calcium phosphate and calcium phosphate/chitosan [218].

In this regard, Ca and Zr are favorable alloying elements used for biomedical research of Mg-based alloys. In the conventional steel industry, Ca or Zr additions have been used in order to enhance the mechanical and physical properties of steels but there is sparse information in the literature for the bio related applications of these alloys. *In vitro* corrosion test described earlier in Chapters 2 and 3 have shown that $Fe_{70}Mg_{30}$ amorphous film displays faster corrosion rate than pure Fe film (~9 fold). Especially, Ca is one of the elements that possesses a more negative value of the standard electrochemical potential. The electrode potential value for Ca is more negative than Mg and Fe. Usually, the more negative the standard electrode potential, the greater the tendency to form metal cations and hence, a greater propensity for these alloys to undergo rapid corrosion [244]. Therefore, addition of Ca is expected to enhance the corrosion rates of Fe-Mg alloys. As mentioned previously, Zr is an essential trace element in humans and is reported as one of the favorable alloying elements for biological applications. It has been widely used for

biomedical and nephrological applications [245]. Additionally, Zr is a representative element used for generating bulk metallic glasses and also has been widely studied in the materials science community because it usually imparts and facilitates the glass forming ability (GFA) to a very large extent thus leading to the generation of amorphous alloys.

The present study is thus focused at exploring the use of Ca and Zr as additional alloying element in the parent Fe-Mg and Fe-Mg-Mn alloy discussed earlier in Chapter 1, 2 and 3. Accordingly, the Fe-Mg-Ca, Fe-Mg-Zr, Fe-Mg-Mn-Ca and Fe-Mg-Mn-Zr alloys have been synthesized through the process of HEMA followed by PLD to examine the corrosion and magnetic properties with preliminary *in vitro* cytocompatibility for bio applications.

5.2 MATERIALS AND METHODS

5.2.1 Preparation for alloy powders and thin films

The alloys to be considered in this study are divided to two categories basically considering $Fe_{70}Mg_{30}$ and $Fe_{60}Mg_{20}Mn_{20}$ as the parent alloy compositions. The alloy corresponding to $Fe_{70}Mg_{30-x}M_x$ (M=Ca, Zr wherein x= 3, 5, 8 for Ca and x=0.1~30 for Zr) and $Fe_{60}Mg_{20}Mn_{20-x}M_x$ (M=Ca, Zr wherein x= 1, 5 for Ca and x= 0.5~20 for Zr) atomic % compositions were produced as for the parent alloy compositions using the process of HEMA followed by PLD. Accordingly, commercial powders of elemental Fe (99.9+%, <10 μm, Alfa Aesar), Mg (99.8%, <325 mesh, Alfa Aesar), Mn (99.3%, <325 mesh, Alfa Aesar), Ca (99.5%, -16 mesh, Alfa Aesar) and Zr (99.8%, -325 mesh, Alfa Aesar) were chosen. These were weighed corresponding to 4g batch powder for each desired compositions and placed in to SS vials with

SS balls (BPR was 15 to 1). A planetary SPEX 8000 high energy Shaker Mill was used to perform up to 14 h of dry milling followed by 17 h of wet milling cycle with toluene. The post ball milled powders were dried and then compacted at a pressure of 60 kpsi using a Flow Autoclave System cold isostatic compaction press to produce 25.0 mm diameter discs to be used as targets for subsequent PLD. All the thin films will be produced by PLD utilizing a 248 nm KrF excimer laser (Lambda Physik EMG 201) irradiation pulsed at 25 ns FWHM in a high vacuum chamber with a base pressure of 10^{-6} Torr. In all depositions the spot size was approximately 1×3 mm, the fluence was 8.3~9.6 J/cm^2, the laser pulse frequency was maintained at 10 Hz and the deposition rate was approximately 2.3 Å/s determined as a mean value. The target to substrate distance was maintained constant at 58 mm, with targets rotated during deposition. Films were deposited at room temperature for a deposition time of 30 minutes on three different substrates corresponding to film thicknesses of ~1.3 microns. The first was amorphous SiO_2 thermally grown on Si wafer for use in glancing angle X-ray diffraction (XRD). The second substrate was a regular cell culture dish for cytocompatibility tests, and the third substrate was fused silica glass for bio-corrosion tests.

5.2.2 Characterization of the synthesized powder and thin films

X-ray diffraction (XRD) phase analysis was performed using PANalytical X'Pert Pro system employing the Cu K_α (λ=1.54056 Å) radiation source with a Si-detector for glancing and conventional measurements. The x-ray generator was operated at 45 kV and 40 mA at a 2θ range of 10-90°. PANalytical HighScore Plush version 3.5 software was used to identify the peaks in the XRD patterns comparing the data to the ICSD database. Magnetic hysteresis loops were

measured at room temperature with vibration sample magnetometer (VSM, Lakeshore 7400) with a maximum magnetic field of 2 T similar to the alloys as described in Chapter 4.

5.2.3 Electrochemical bio-corrosion study

Electrochemical corrosion characterization studies of the PLD derived Fe-Mg-X and Fe-Mg-Mn-X (X=Ca and Zr) thin layers were performed using CH604A (CH Instruments Inc) electrochemical work station. Following sample preparation as described in the above section and previous chapters, one side of each sample was connected to a copper wire with silver epoxy and then electrically insulated, so that only one side is exposed for conducting the electrochemical tests. The length and width measurements were taken for corrosion current calculations. Ag/AgCl and a platinum wire were employed as the reference and counter electrodes, respectively. Testing was carried out utilizing a 3-neck jacketed flask (ACE Glassware) filled with 125 mL Dulbecco's Modified Eagle's Medium (DMEM) containing 10 % fetal bovine serum (FBS, Atlanta Biologicals, Lawerenceville, GA) and 1 % penicillin/streptomycin antibiotics (P/S, Gibco, Grand Island,NY), equilibrated to at 37 °C. All the specimens were allowed to equilibrate to maintain stability and reach a stable open circuit potential (OCP) for 40 minutes, before initiating the polarization tests at a scan rate of 0.3 mV/s. The corrosion current was determined using the Tafel extrapolation of the polarization curve and normalized by the exposed surface area to yield a measurement of corrosion current density. The software program Origin with a Tafel packet was used to perform the Tafel extrapolation and plot the data.

5.2.4 Cell culture

Murine pre-osteoblast cells (MC3TC-E1, American Type Culture Collection, Rockville, MD), human mesenchymal stem cells (hMSCs, Lonza, USA), human umbilical vein endothelial cells (HUVECs, Linza, USA) and murine fibroblast cells (NIH3T3, American Type Culture Collection, Rockville, MD) were utilized for cell culture studies similar to the earlier studies reported for Fe-Mg alloy films in Chapter 3 and for the Fe-Mg-Mn alloy films in Chapter 4. Cells were cultured under 37 °C, 5% CO_2, and 95% relative humidity in α-MEM (Gibco, Grand Island, NY) growth media containing 1% P/S (Gibco, Grand Island, NY) and either 10% FBS (Atlanta Biologicals, Lawrenceville, GA), for MC3TC-E1, or 20% FBS for hMSCs, EBM-2 bullet kit (Lonza, USA) for HUVEC and DMEM (Cellgro, Manassas, VA) growth media containing 1% P/S and 10% FBS for NIH3T3. The MC3T3 and NIH3T3 cells cultured at third to seventh passage, and hMSCs and HUVECs cultured at second to third passage were used in this experiment as the case for the alloy films described in Chapters 3 and 4.

5.2.5 Direct cell viability and adhesion test (Live/dead assay)

MC3TC-E1, hMSC, HUVEC and NIH3T3 cells were cultured directly on the surface of Fe-Mg-X and Fe-Mg-Mn-X (X=Ca and Zr) thin layers deposited by PLD. These alloys were deposited on fused silica glass by PLD with the film area approximately 9mm x 9mm. The samples were sterilized on all sides by UV for 60 minutes and incubated in cell culture media for 10 minutes, after which time, cells were seeded on the samples directly at a density of 80,000 cells per well. After 24 and 72 h of incubation, the live/dead assay was performed using commercially available LIVE/DEAD viability/cytotoxicity kit (Invitrogen Inc. Karlsruhe, Germany) to stain the live and

dead cells to glow green (ethidium homodimer-1) for live and red (calcein-AM) indicating dead cells, respectively, imaged under a fluorescence microscope at the excitation wavelength of 495 nm. For each substrate, images were taken from three to six different locations to obtain an overview of the cell attachment profiles.

5.2.6 Direct cell viability and adhesion test (Live/dead assay)

Indirect cell viability test was assessed using the MTT activity assay (Vybrant MTT Cell Proliferation Assay Kit). Extraction medium was prepared using each cell growth media supplemented with serum in a surface area/extraction medium ratio 6 cm^2 ml^{-1}, in accordance with ISO 10993-12 [200], at 37 °C in a humid atmosphere with 5% CO_2 for 72 hours. The extracted medium was stored at 4°C until the cytocompatibility testing. This extraction was designated as 100% extract solution. The control groups involved the use of media without extract as a negative control and media containing 10% dimethyl sulfoxide (DMSO) as a positive control. The cells were seeded in 96-well plates at 6000 cells/well with 200µl media in each well and incubated for 24 hours to allow for attachment. After pre-cell culture, the media was then replaced with 100µl of 100% extract medium and incubated for 1, 3 and 7 days. After that, media and extracts were replaced with fresh cell culture media and 10µl of MTT were added to each well. The samples were incubated with MTT for 4 hours at 37°C and then 100µl of formazan solubilization solution (10% sodium dodecyl sulfate in 0.01M HCl) were added to each well for 12 hours in the incubator under the cell culture atmosphere. The spectrophotometer absorbance of the samples was measured with the Synergy 2 Multi-Mode Microplate Reader (Bio-Tek Instruments, Winooski, VT) at 570 nm, with a reference wavelength of 630 nm.

5.3 RESULTS AND DISCUSSION

5.3.1 Fe-Mg-X (X= Ca and Zr)

As reported and discussed in Chapter 2 and 3, uniform corrosion of $Fe_{70}Mg_{30}$ amorphous thin layer was observed and the corrosion current density value was calculated to be approximately 8 fold higher than pure Fe. The direct and indirect cytotoxicity results also indicated that $Fe_{70}Mg_{30}$ amorphous thin layer exhibit no cytotoxicity to MC3T3-E1, hMSCs, HUVECs and NIH3T3 cell lines. Therefore, to further explore the system, Ca and Zr were added into the parent this alloy as additional alloying elements. Table 5.1 tabulates the abbreviated notation and the nominal chemical composition of the thin film systems deposited corresponding to Fe-Mg-X (X=Ca and Zr) alloy systems.

5.3.1.1 Fe-Mg-Ca system

Figure 5.1(a) shows the XRD patterns of as prepared milled powder following dry and wet milling corresponding to $Fe_{70}Mg_{30-x}Ca_x$ powder (x = 0, 3, 5 and 8). The $Fe_{70}Mg_{30}$ powder exhibits the typical broad diffraction pattern corresponding to the fully amorphous phase which was already discussed in chapter 2 previously. However, the XRD patterns show low intensity sharp peaks indicative of crystalline phase which were found together with a broad diffraction peak from the amorphous phase with increasing Ca content (up to 8 at.%). These crystalline phase are identified to be pure Fe and Ca for x=3, 5 while the two peaks characteristic of Ca appear to disappear for the composition corresponding to $Fe_{70}Mg_{22}Ca_8$. These results thus indicate that $Fe_{70}Mg_{30-x}Ca_x$ powders (x =3, 5 and 8) are predominantly amorphous with a small

amount of likely unreacted Ca and Fe remaining in the resulting milled powder under the milling conditions employed.

Table 5.1. Summary of the chemical formula of Fe-Mg-X (X=Ca, Zr) films.

x	Chemical formula	
	$Fe_{70}Mg_{30-x}Ca_x$	$Fe_{70}Mg_{30-x}Zr_x$
0	$Fe_{70}Mg_{30}$	$Fe_{70}Mg_{30}$
0.1, 0.5	--	$Fe_{70}Mg_{29.9}Zr_{0.1}$ $Fe_{70}Mg_{29.5}Zr_{20.5}$
2	--	$Fe_{70}Mg_{28}Zr_2$
3	$Fe_{70}Mg_{27}Ca_3$	--
5	$Fe_{70}Mg_{25}Ca_5$	$Fe_{70}Mg_{25}Zr_5$
8	$Fe_{70}Mg_{22}Ca_8$	--
10, 15	--	$Fe_{70}Mg_{20}Zr_{10}$ $Fe_{70}Mg_{15}Zr_{15}$
20, 25	--	$Fe_{70}Mg_{10}Zr_{20}$ $Fe_{70}Mg_5Zr_{25}$
29	--	$Fe_{70}Mg_1Zr_{29}$
30		$Fe_{70}Zr_{30}$

In order to study the effect of addition of Ca on the Fe-Mg system, further studies were therefore conducted on the $Fe_{70}Mg_{22}Ca_8$ composition. This composition was selected since it represented a larger Ca content and hence, could likely have a stronger propensity towards exhibiting the higher desired degradation under in vitro conditions. The starting powder, target generated for PLD studies, and the deposited films thus corresponded to this composition containing the highest amount of Ca. Thin layer samples of ~1.3 μm thickness were also prepared by PLD on glass substrates for 30 minutes from the milled and cold isostatic pressed (CIP) compact corresponding to $Fe_{70}Mg_{22}Ca_8$ as the target that is largely amorphous with crystalline Fe. Glancing angle XRD analysis was performed on this deposited layer, which is shown in Figure 5.1(b). The figure also shows that the deposited thin layer is predominantly amorphous with a small amount of likely unreacted Fe.

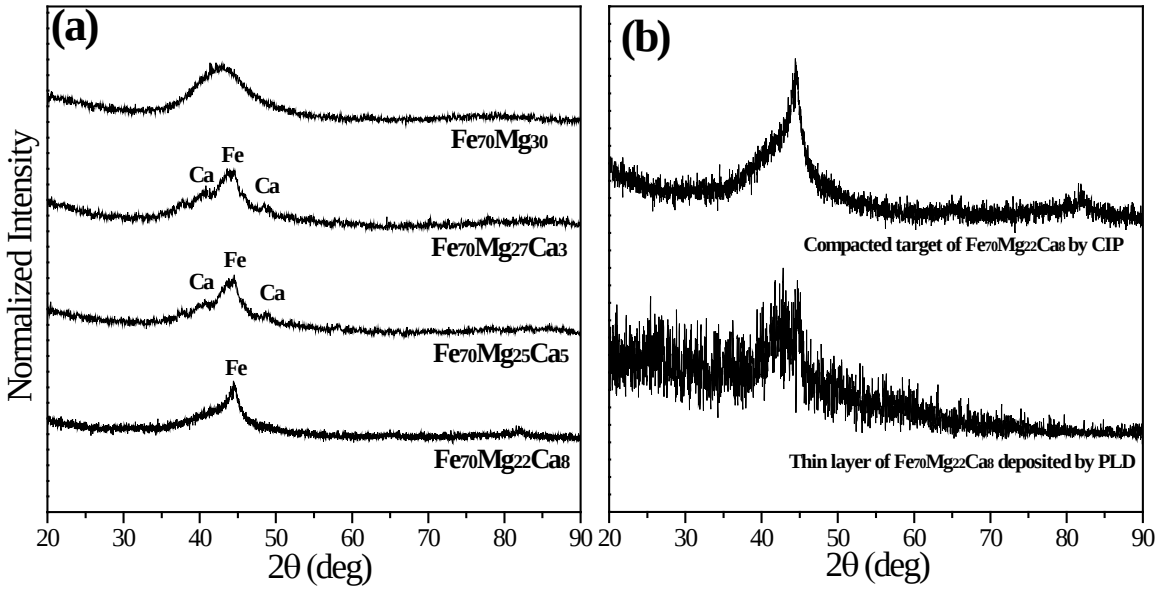

Figure 5.1. The X-ray diffraction patterns of (a) $Fe_{70}Mg_{30-x}Ca_x$ powder (x = 0, 3, 5 and 8) after dry and wet milling by HEMA and (b) thin layer of $Fe_{70}Mg_{22}Ca_8$ (x=8) on glass deposited for 30 minutes by PLD.

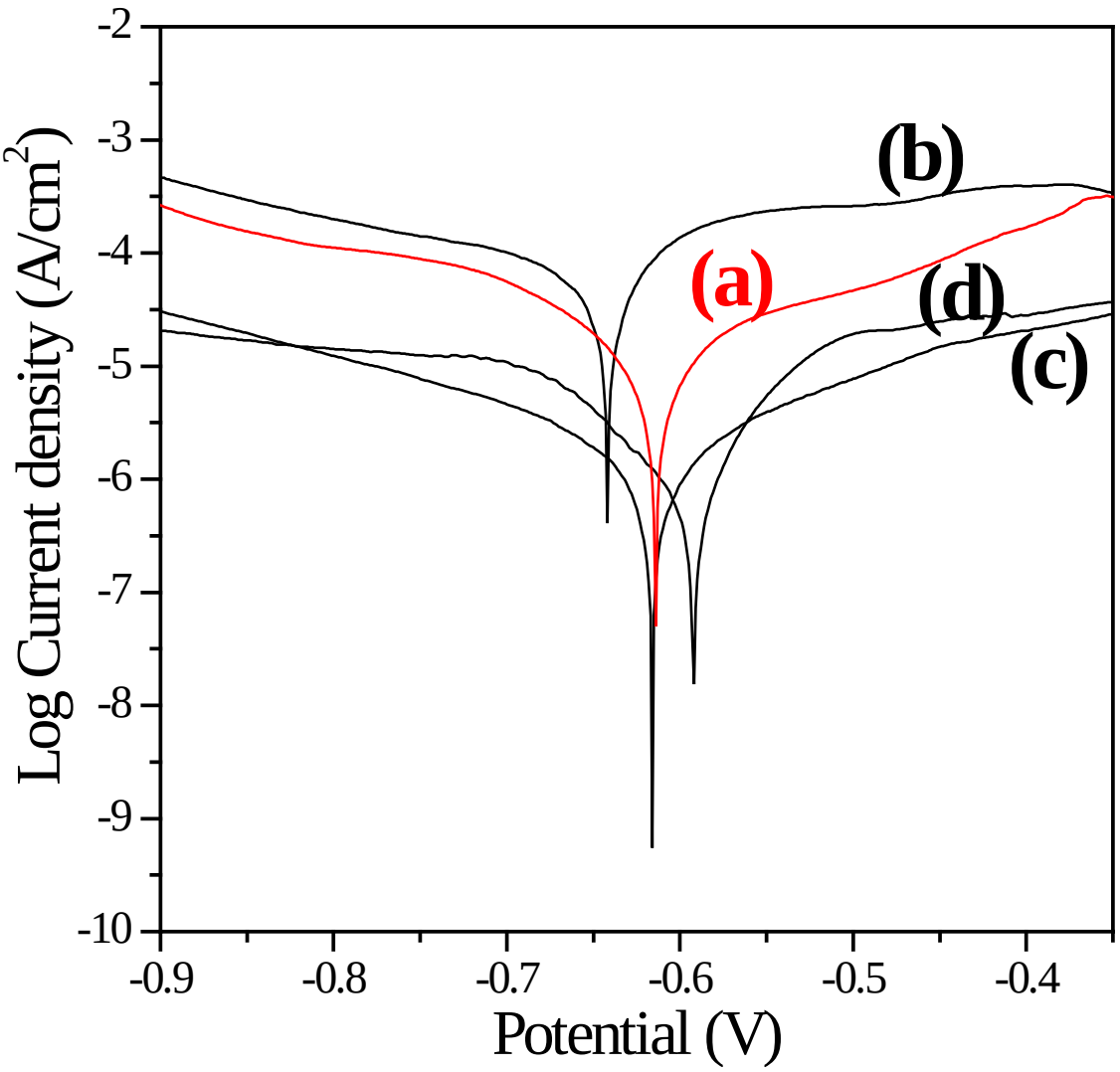

Figure 5.2. Polarization curves of (a) $Fe_{70}Mg_{22}Ca_8$ thin layer, (b) $Fe_{70}Mg_{30}$ amorphous thin layer, (c) pure iron thin layer on glass derived by PLD and (d) mounted bulk pure iron.

The potentio-dynamic polarization (PDP) behavior of the thin layer of $Fe_{70}Mg_{22}Ca_8$ has also been studied and the potentio-dynamic polarization curves (Tafel plot) of the $Fe_{70}Mg_{22}Ca_8$ thin layer, $Fe_{70}Mg_{30}$ amorphous thin layer and both, pure Fe thin layer and bulk Fe sample, recorded at a scan rate of ~1 mV/s are plotted in Figure 5.2. Table 5.2 gives a summary of the corrosion potential and corrosion current densities calculated from extrapolation of the Tafel plots shown in Figure 5.2.

Table 5.2. Corrosion potential (E_{corr}) and current density (i_{corr}) values for $Fe_{70}Mg_{22}Ca_8$ layer, $Fe_{70}Mg_{30}$ amorphous layer, both bulk and thin layer of pure iron.

Element	Corrosion potential, E_{corr}(V)	Corrosion current density. I_{corr}(μAcm^{-2})
$Fe_{70}Mg_{22}Ca_8$ thin layer	**-0.614**	**28.21±3.84**
$Fe_{70}Mg_{30}$ amorphous thin layer	-0.642	98.76±11.08
Pure Fe (thin layer)	-0.616	12.46±2.3
Pure Fe (bulk)	-0.592	14.14±4.35

The $Fe_{70}Mg_{22}Ca_8$ thin layer on glass exhibited E_{corr} value of -0.614V as and a corrosion current density which is ~2 fold higher than that of both pure iron samples of thin film and bulk iron, but is clearly lower than $Fe_{70}Mg_{30}$ amorphous film of similar thickness of ~1.3 μm ($P<0.05$). The addition of Ca thus does not appear to further enhance the positive attributes already induced by the addition of Mg to Fe as illustrated in Chapters 1-3.

The direct live/dead assay was conducted on the PLD derived $Fe_{70}Mg_{22}Ca_8$ thin film of ~1-3-micron thickness on glass (Figure 5.3 and 5.4). Both figures display cell density of attached live MC3T3-E1, hMSCs, HUVECs and NIH3T3 fibroblasts cell on the thin layer after 1 and 3

days of culture. For MC3T3-E1, hMSCs and NIH3T3 fibroblasts cell, relatively few apoptotic cells compared to live cells and normal cell morphology was observed on each alloy, indicating the favorable, high cell viability due to the addition of Mg and Ca to the base Fe alloy.

After 1 day, MC3T3-E1 and hMSC cell density appeared similar to that of the tissue culture plastic (TCP). HUVECs and NIH3T3 fibroblasts cells attached with few dead cells seen on the surface of $Fe_{70}Mg_{22}Ca_8$ showing also less cells attached compared to the control. After 3 days culture, MC3T3-E1, hMSC and NIH3T3 fibroblasts cells seem to attach very well on the $Fe_{70}Mg_{22}Ca_8$ thin layer indicating live cell attachment densities very similar to that of the tissue culture plastic. Comparing the cell density on the alloys from 1 to 3 days, the increased number of cell density clearly indicated healthy cell proliferation. However, fewer HUVEC live cells appeared to attach compared to tissue cultrue plastic observed after 3days. Further, the shape of the cell also seemed to become more spread out with relativly increased cell density compared to 1 day.

Figure 5.5 shows the indirect cytotoxicity results of PLD derived $Fe_{70}Mg_{22}Ca_8$ thin layers deposited on glass conducted using MC3T3-E1, hMSCs, HUVECs and NIH3T3 fibroblasts cell using the MTT assay. The MTT assay conducted on all the cells with the 100% extract taken from the $Fe_{70}Mg_{22}Ca_8$ thin layer displayed low toxicity of the alloy extract, with at least ~80% cell viability observed for all days of culture. Reduction in cell viability by more than 30% is typically considered to be cytotoxic according to ISO 10993-5 [217]. Thus the results presented here seem to indicate that all the alloys could be considered to be non-cytotoxic.

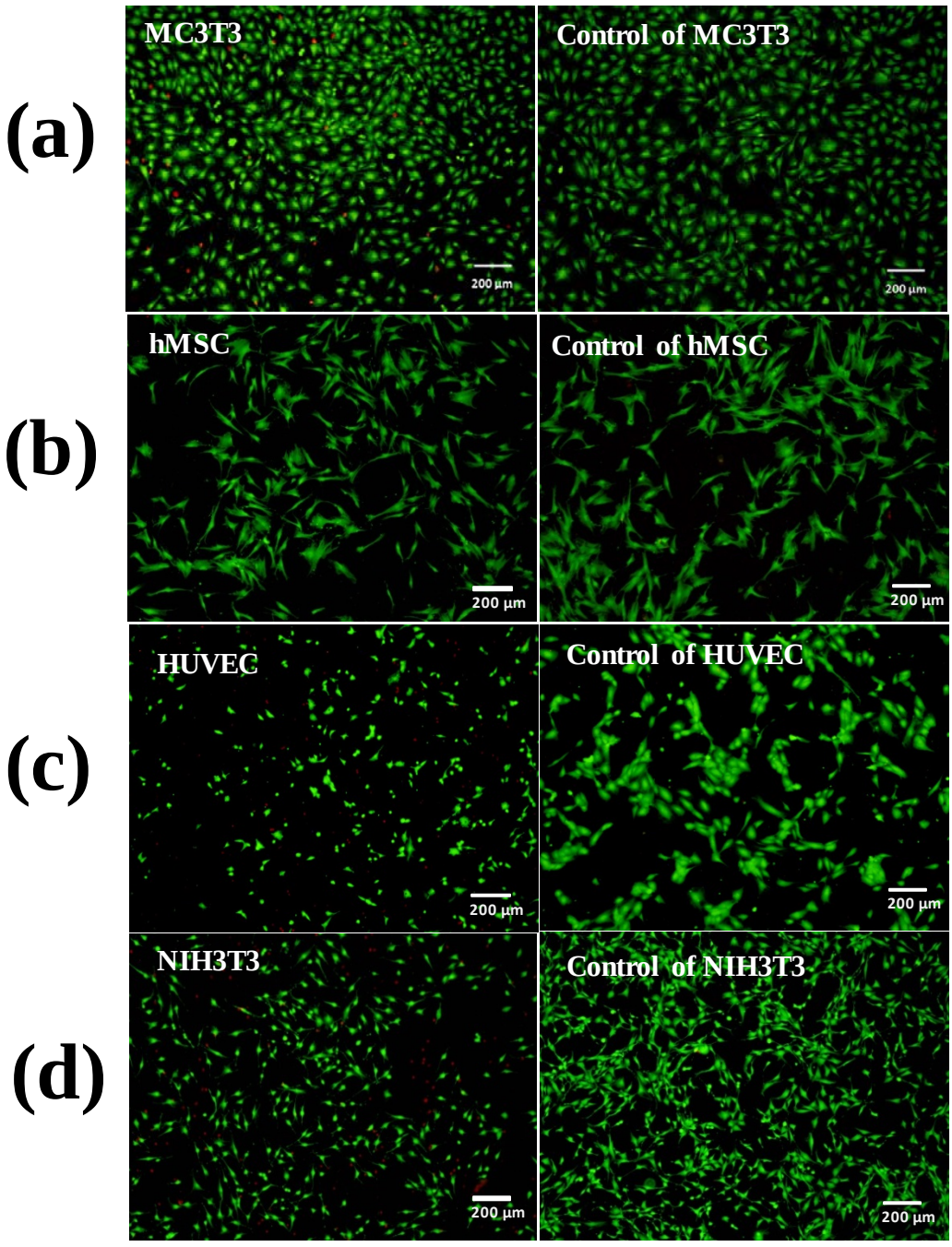

Figure 5.3. Live/Dead staining of MC3T3 osteoblasts, hMSCs, HUVECs and NIH3T3 fibroblast on day 1 of culture post seeding on the thin layer of $Fe_{70}Mg_{22}Ca_8$ on glass and each tissue culture plastics as control.

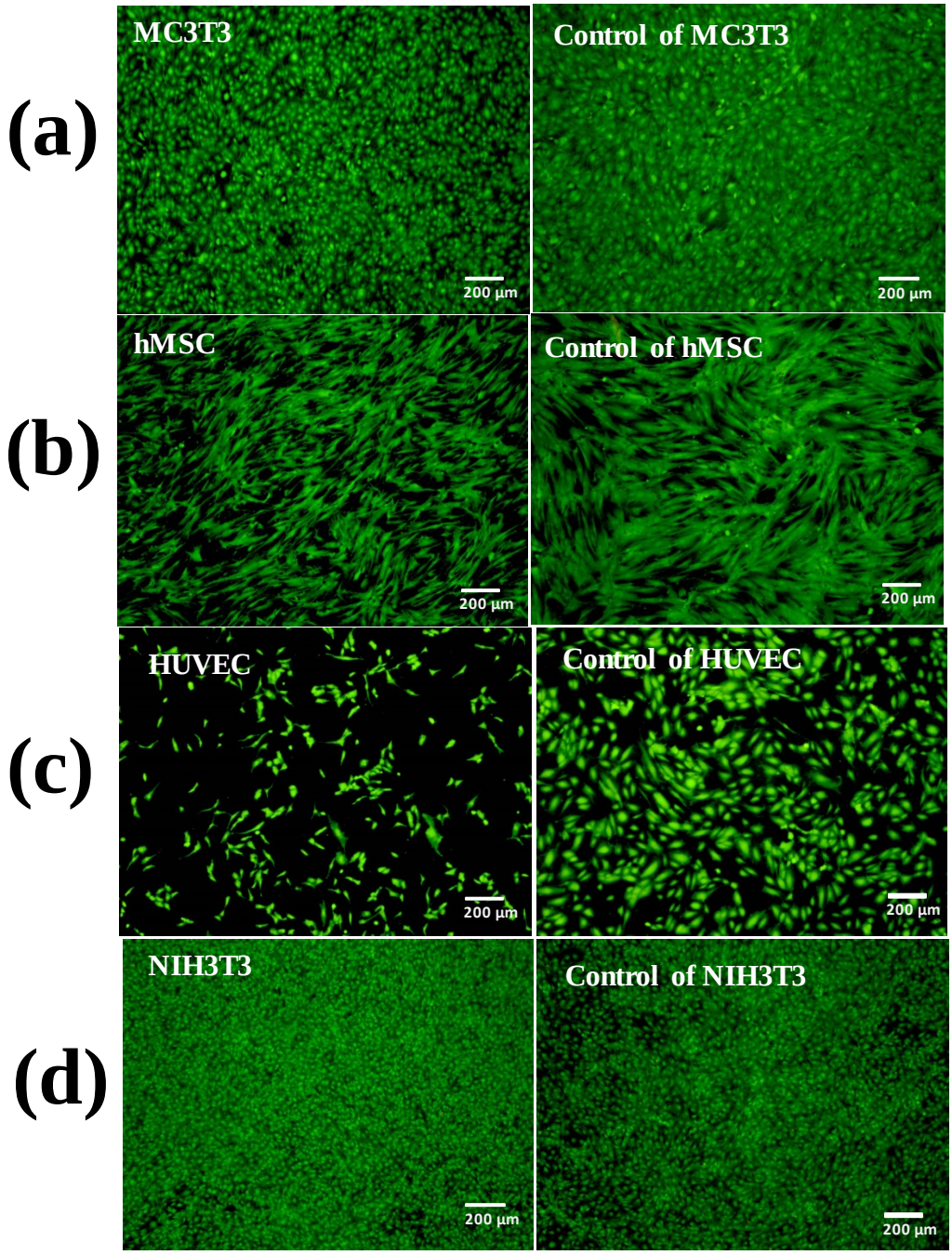

Figure 5.4. Live/Dead staining of MC3T3 osteoblasts, hMSCs, HUVECs and NIH3T3 fibroblast on day 3 of culture post seeding on the thin layer of $Fe_{70}Mg_{22}Ca_8$ on glass and each tissue culture plastics as control.

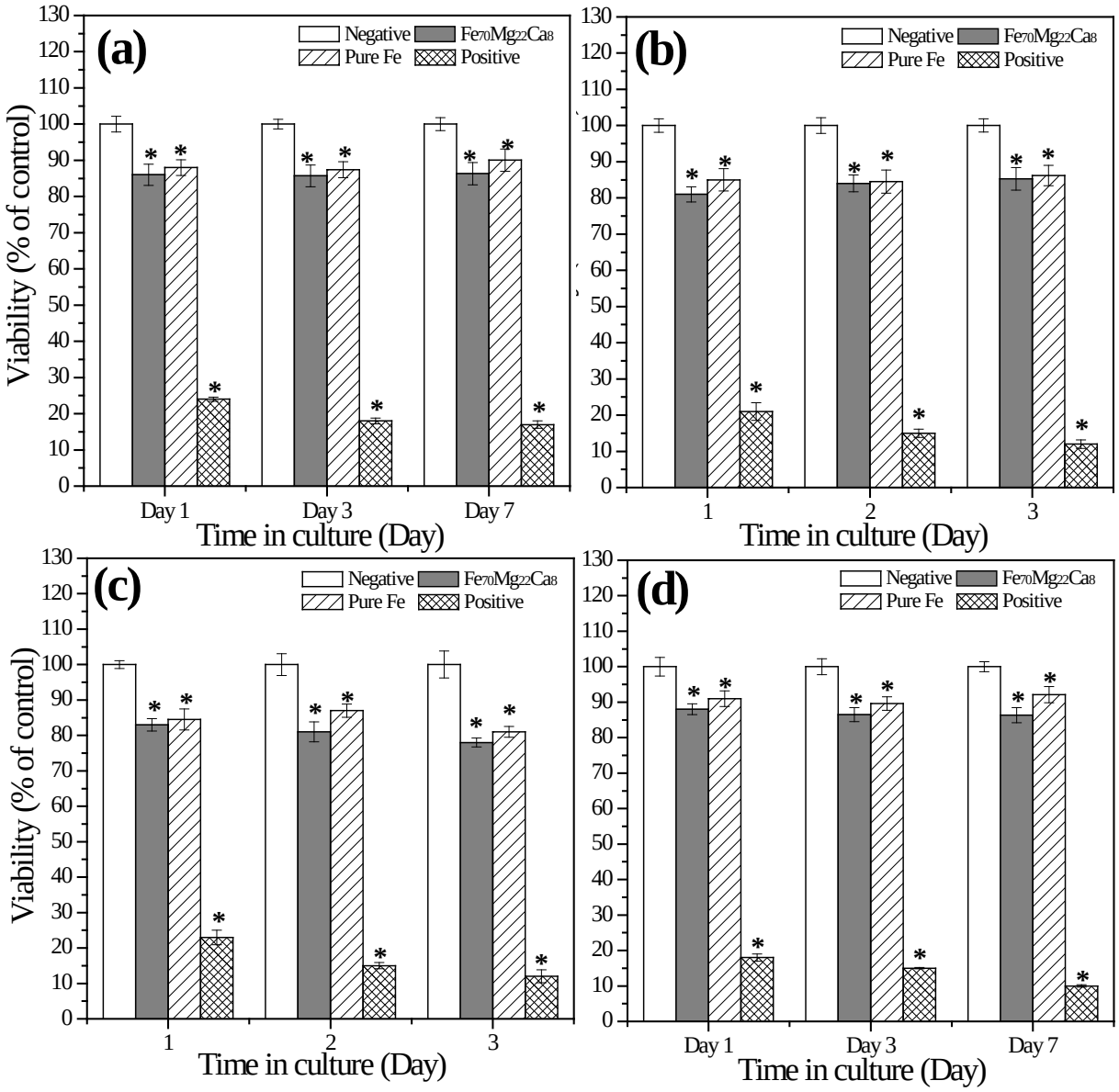

Figure 5.5. Cell viability of (a) MC3T3 osteoblasts, (b) hMSCs, (c) HUVECs and (d) NIH3T3 after 1, 3 and 7days incubation in extract medium collected after 72 hours from $Fe_{70}Mg_{22}Ca_8$ and pure Fe thin layer of ~1.3μm thickness on glass. * Significant difference compared to cell viability of the negative control group ($P<0.05$).

5.3.1.2 Fe-Mg-Zr system

Figure 5.6(a) shows the XRD patterns of the as prepared milled powder corresponding to $Fe_{70}Mg_{30-x}Zr_x$ powder (x = 0~30). The XRD patterns of the powders for x=0, 0.1, 0.5 and 2) show the typical broad diffraction pattern corresponding to the fully amorphous phase although x>2 powders show a few narrow peaks that begin to emerge over the amorphous peaks at around 34°, 40°, and 57°. This result indicates that the HEMA process can generate phases that are fully (or mostly) amorphous for these compositions. However, at other compositions, the x-ray diffraction patterns exhibit low-intensity sharp peaks indicative of a crystalline phase which are found together with a broad diffraction peak from an amorphous phase. These crystalline phases are identified to be an inter-metallic phase of unreacted pure Zr and Fe depending on the composition as indicated in Figure 5.6(a). The corresponding amorphous thin layer was synthesized by PLD on glass substrate for 30 min of deposition time to form films corresponding to the $Fe_{70}Mg_{28}Zr_2$ fully amorphous composition from a corresponding fully amorphous target of the same composition. Glancing angle XRD analysis was performed on this deposited layer, shown in Figure 5.6(b) which exhibits the characteristic broad amorphous diffraction pattern.

Potentio-dynamic polarization (PDP) curves for the thin layer of $Fe_{70}Mg_{28}Zr_2$ and pure iron on glass and polished bulk pure iron can be seen in Figure 5.7 taken from representative samples from the multiple samples tested. Table 5.3 also gives a summary of the corrosion potential and corrosion current densities as calculated from extrapolation of the Tafel plots. The $Fe_{70}Mg_{28}Zr_2$ amorphous thin layer on glass (a) resulted in an i_{corr} value higher than that of both, Fe thin layer of same thickness of ~1.3 μm, (b) as well as bulk Fe (c) samples including, E_{corr} values that are more cathodic and closer to that of amorphous thin layers corresponding to

Table 5.3. Corrosion potential (E_{corr}) and current density (i_{corr}) values for $Fe_{70}Mg_{28}Zr_2$ layer as well as both bulk and thin layer of pure iron.

Element	Corrosion potential, E_{corr}(V)	Corrosion current density. I_{corr}(μAcm^{-2})
$Fe_{70}Mg_{28}Zr_2$ thin layer	**-0.636**	**21.33±2.31**
$Fe_{70}Mg_{22}Ca_8$ thin layer	-0.614	28.21±3.84
$Fe_{70}Mg_{30}$ amorphous thin layer	-0.642	98.76±11.08
Pure Fe (thin layer)	-0.616	12.46±2.3
Pure Fe (bulk)	-0.592	14.14±4.35

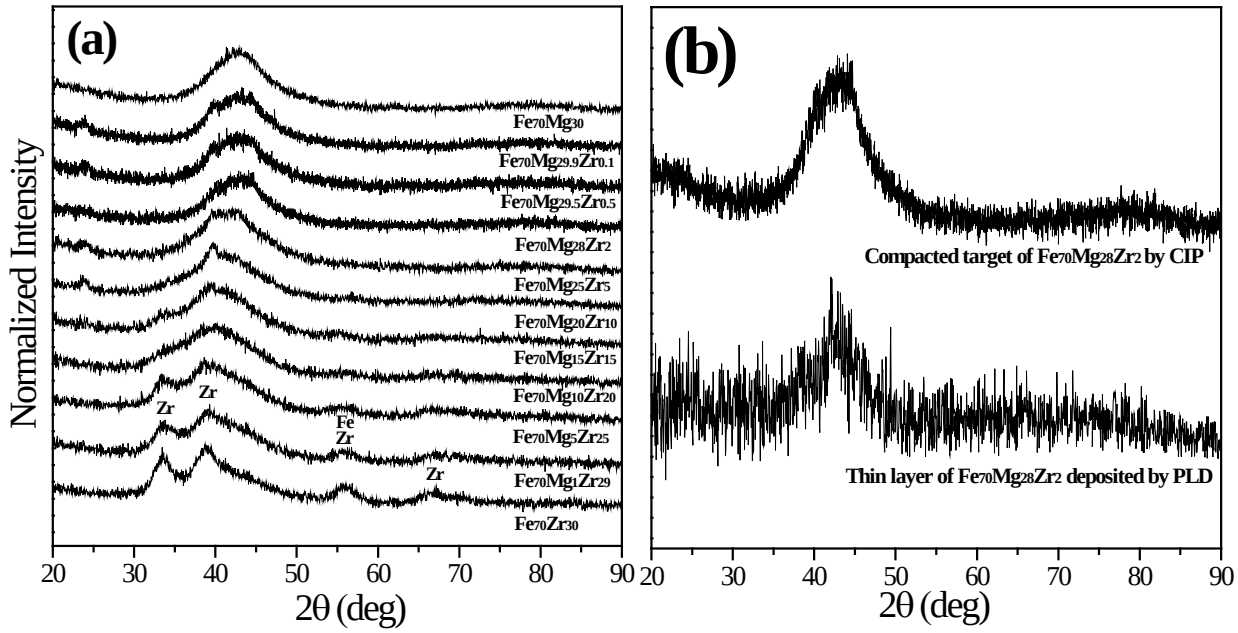

Figure 5.6. The X-ray diffraction patterns of (a) $Fe_{70}Mg_{30-x}Zr_x$ powder (x = 0~30) after dry and wet milling by HEMA and (b) thin layer of $Fe_{70}Mg_{28}Zr_2$ (x=2) on glass deposited for 30 minutes by PLD.

$Fe_{70}Mg_{30}$ composition. It can be inferred from the above results that the $Fe_{70}Mg_{30}$ alloy shows indeed improved corrosion rates compared to pure Fe bulk and thin film samples. The corrosion current density corresponding to the amorphous layer of $Fe_{70}Mg_{28}Zr_2$ is significantly higher than that of both pure iron samples but clearly lower than amorphous $Fe_{70}Mg_{30}$ and $Fe_{70}Mg_{22}Ca_8$ thin layers *($P<0.05$).*

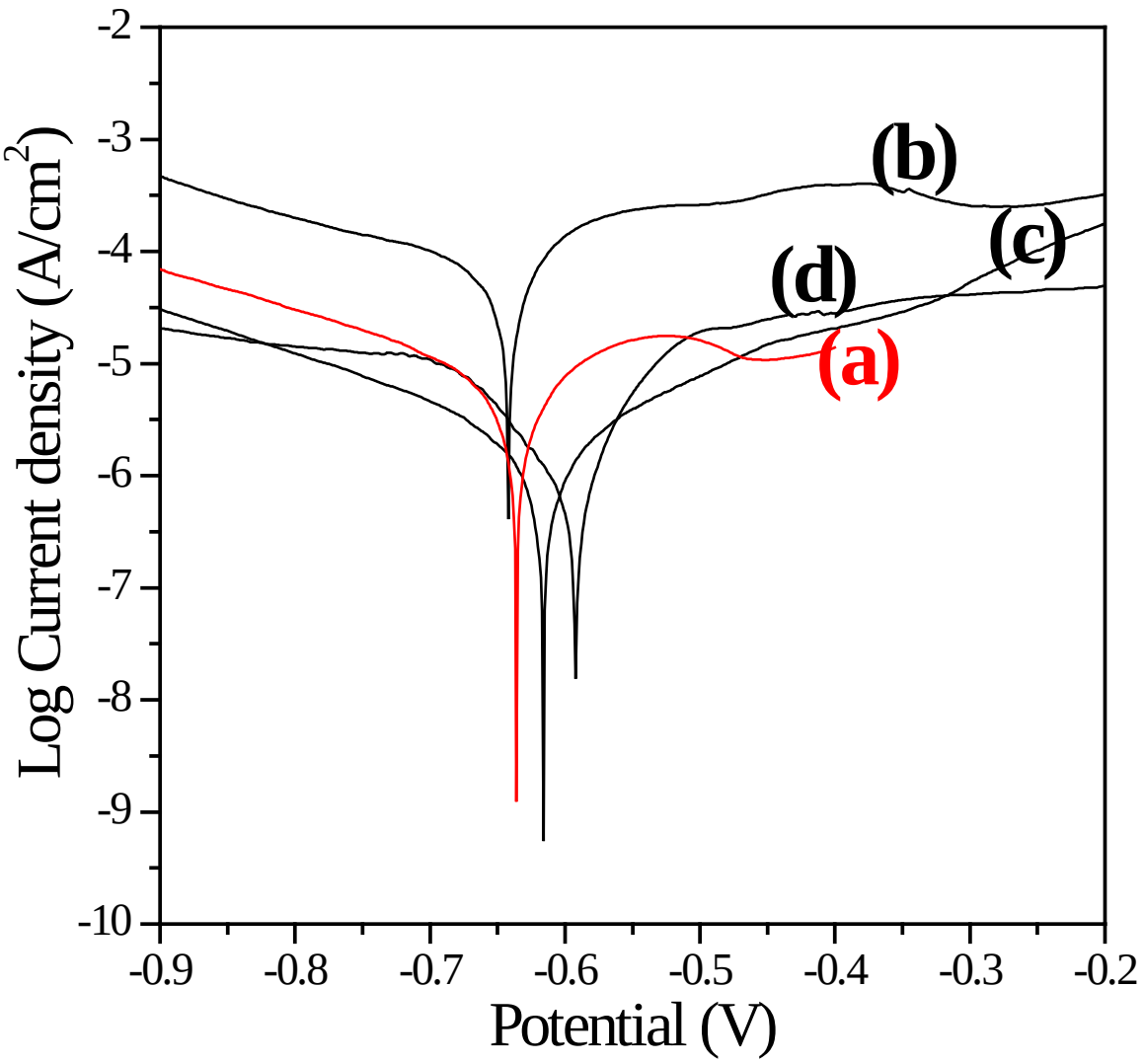

Figure 5.7. Polarization curves of (a) $Fe_{70}Mg_{28}Zr_2$ amorphous thin layer, (b) $Fe_{70}Mg_{30}$ amorphous thin layer, (c) pure iron thin layer on glass derived by PLD and (d) mounted bulk polished pure iron.

Live/dead staining of MC3T3-E1, hMSCs, HUVECs and NIH3T3 after 1 and 3 days of post seeding on the $Fe_{70}Mg_{28}Zr_2$ amorphous thin layer and plastic tissue culture surface (control) can be seen in Figure 5.8 and 5.9, respectively. After 1 day, for all the cell cultures, fluorescence microscopy images collected from the live/dead assay shows similar levels of live cell (green) attached with few dead (red) cells on the surface of $Fe_{70}Mg_{28}Zr_2$ compared to the control. After 3 days of culture (Figure 5.9), amorphous thin films of $Fe_{70}Mg_{28}Zr_2$, which were seeded with all of MC3T3-E1, hMSCs, HUVECs and NIH3T3, still again displayed a similar level of living cells attached comparable to that of the tissue culture plastic used as the control, with a higher cell density than day 1. The live/dead staining indeed indicates good cell viability and proliferation on $Fe_{70}Mg_{28}Zr_2$ amorphous thin layer.

Figure 5.10 illustrates the cell viabilities of MC3TC-E1, hMSCs, HUVECs and NIH3T3 expressed as a percentage of the viability of cells cultured in the negative control after 1, 3, and 7days incubation in 100% extraction mediums after 72 hours using the MTT assay. These quantitative results of indirect cell viability indicate good cell viability and proliferation on $Fe_{70}Mg_{28}Zr_2$ amorphous thin layers. For 1, 3 and 7 days of culture, most of the cell viabilities were slightly higher or lower but by and large, similar to that of pure Fe. There is no significant difference ($P>0.05$) among them with however, a decreased cell viability compared to the negative control. Based on Figure 5.10(a) and (b), values of cell viability for MC3T3 osteoblasts and hMSCs for the amorphous $Fe_{70}Mg_{28}Zr_2$ extracts were nearly 90% after 1day of exposure. The viabilities slightly increased and were again similar ~90% compared to that of the negative control after 3 and 7 days' incubation. For HUVEC cells, the cell viability was about 85% after 1day incubation and remained at this value. The viability also remained just about 85% compared to the negative control after 7day's incubation as shown in Figure 5.10(c). The

NIH3T3 cells displayed ~90% cell viability after 1day of exposure remained in the same range of ~90% of the negative control without extract even after 7days.

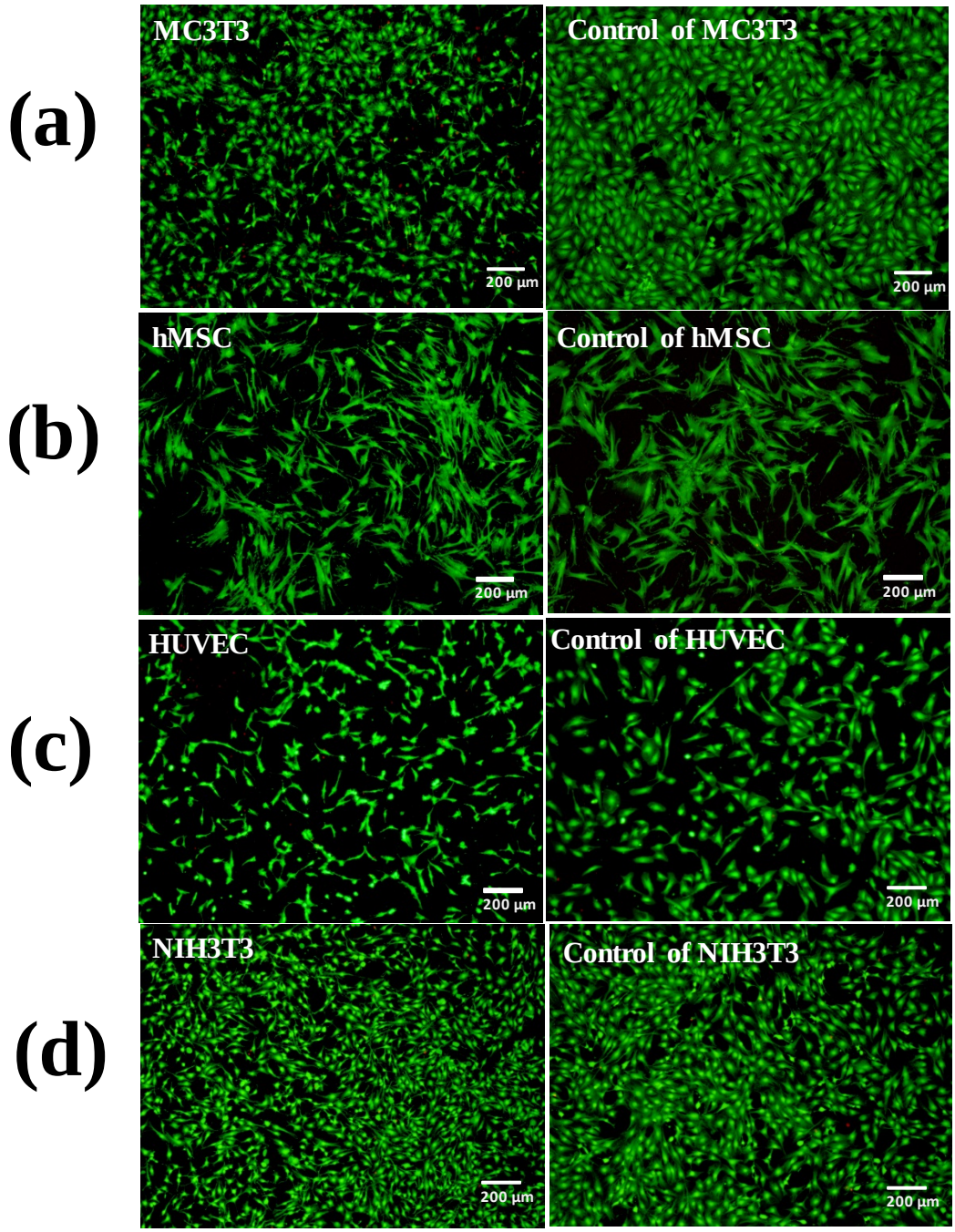

Figure 5.8. Live/Dead staining of MC3T3 osteoblasts, hMSCs, HUVECs and NIH3T3 fibroblast on day 1 of culture post seeding on the thin layer of $Fe_{70}Mg_{28}Zr_2$ on glass and each tissue culture plastic as control.

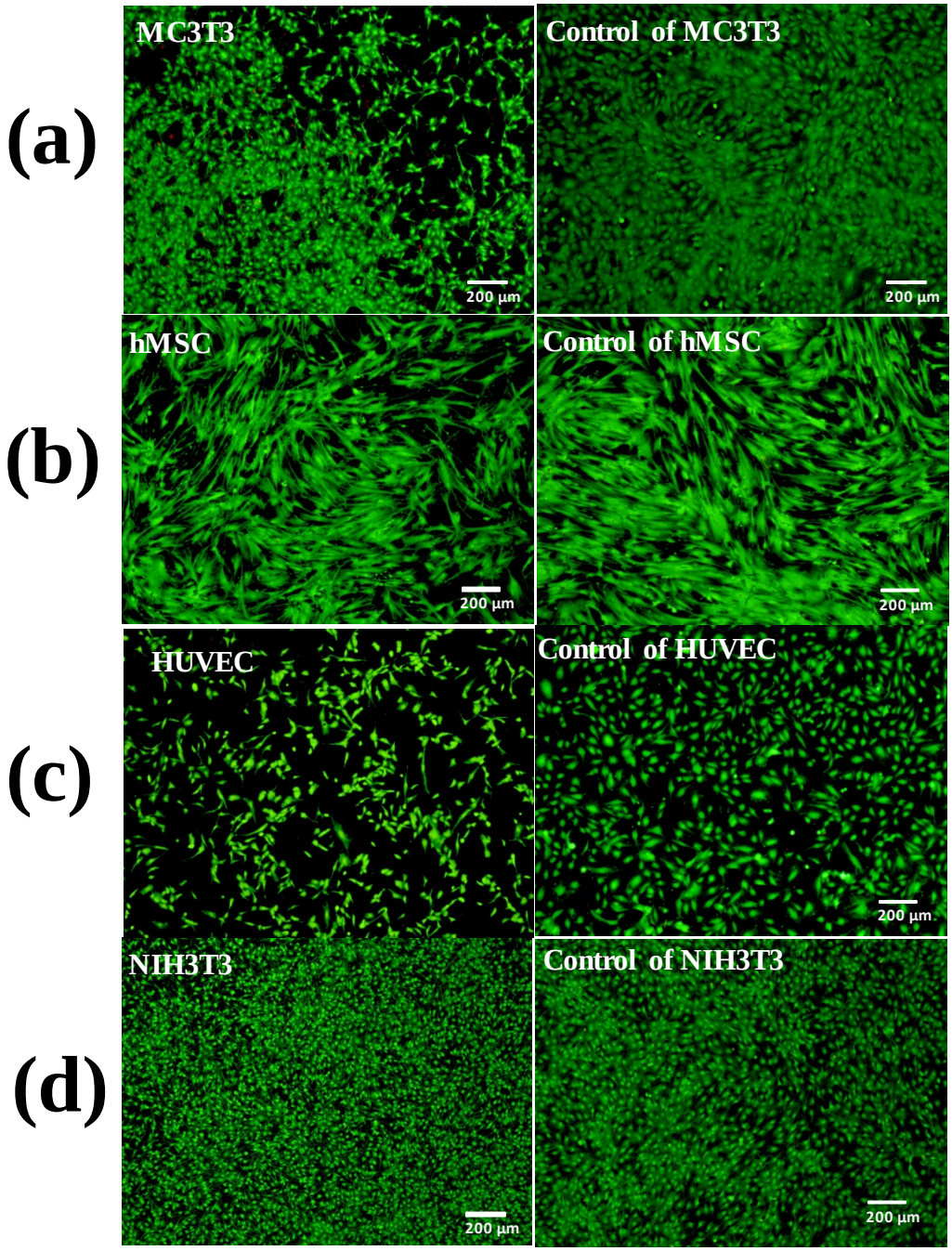

Figure 5.9. Live/Dead staining of MC3T3 osteoblasts, hMSCs, HUVECs and NIH3T3 fibroblast on day 3 of culture post seeding on the thin layer of $Fe_{70}Mg_{28}Zr_2$ on glass and each tissue culture plastic as control.

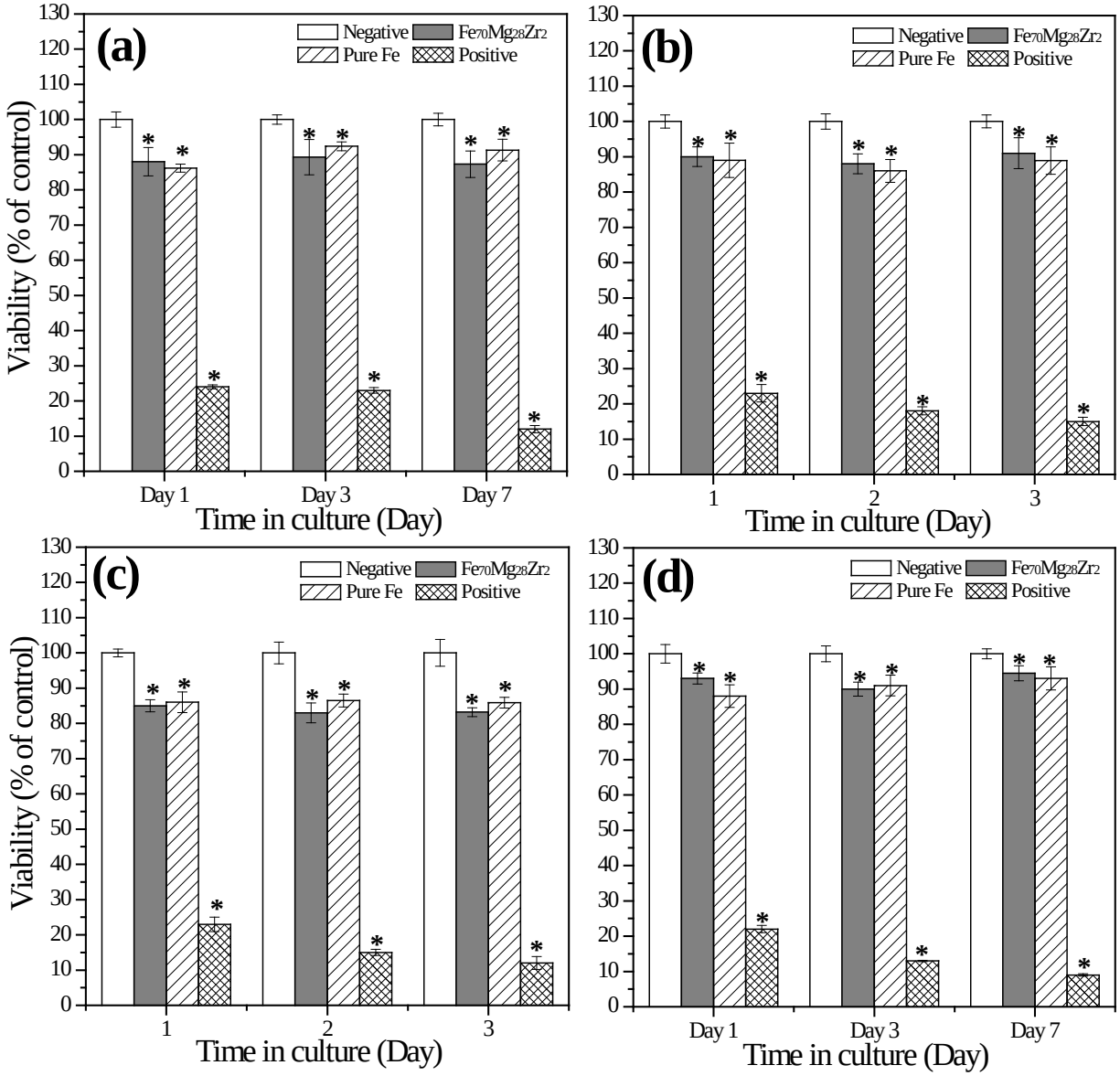

Figure 5.10. Cell viability of (a) MC3T3 osteoblasts, (b) hMSCs, (c) HUVECs and (d) NIH3T3 after 1, 3 and 7days incubation in extract medium collected after 72 hours from $Fe_{70}Mg_{28}Zr_2$ and pure Fe thin layer of ~1.3μm thickness on glass. * Significant difference compared to cell viability of the negative control group ($P<0.05$).

5.3.2 Fe-Mg-Mn-X (X= Ca and Zr)

In Chapter 4 as described, the $Fe_{60}Mg_{20}Mn_{20}$ amorphous powder and amorphous thin film layer have been successfully generated with non magnetic antiferromagnetic property derived by HEMA and PLD. Uniform corrosion behavior was observed and the corrosion current density value was approximately 2 fold higher than that of pure Fe. The direct and indirect cytotoxicity results however, indicated that $Fe_{70}Mg_{30}$ amorphous thin layer has no cytotoxicity to MC3T3-E1, hMSCs and HUVECs. As discussed above, Ca and Zr were added to this parent alloy as additional alloying elements. Table 5.1 tabulated the abbreviated notation and chemical composition of Fe-Mg-Mn-X (X=Ca and Zr) alloys which is also reproduced below in Table 5.4.

Table 5.4. Summary of chemical formula for Fe-Mg-Mn-X (X=Ca, Zr)

x	Chemical formula	
	$Fe_{60}Mg_{20}Mn_{20-x}Ca_x$	$Fe_{60}Mg_{20}Mn_{20-x}Zr_x$
0	$Fe_{60}Mg_{20}Mn_{20}$	$Fe_{60}Mg_{20}Mn_{20}$
0.5	--	$Fe_{60}Mg_{20}Mn_{19.5}Zr_{0.5}$
1	$Fe_{60}Mg_{20}Mn_{19}Ca_1$	--
5	$Fe_{60}Mg_{20}Mn_{15}Ca_5$	$Fe_{60}Mg_{20}Mn_{15}Zr_5$
10	--	$Fe_{60}Mg_{20}Mn_{10}Zr_{10}$
15	--	$Fe_{60}Mg_{20}Mn_5Zr_{15}$
20	--	$Fe_{60}Mg_{20}Zr_{20}$

5.3.2.1 Fe-Mg-Mn-Ca system

Figure 5.11(a) shows the XRD scans of blended mixtures prepared from the elemental powder of Fe, Mg, Mn, and Ca and as prepared milled powder corresponding to the nominal compositions of $Fe_{60}Mg_{20}Mn_{20-x}Ca_x$ powder (x = 0, 1, 5). With increasing Ca of 1 and 5 at.% Ca,), the XRD patterns exhibit low intensity sharp peaks from a crystalline phase which were found together with a broad diffraction peak from the amorphous phase. These crystalline phases are identified γ(PDF# 01-089-4185) for $Fe_{60}Mg_{20}Mn_{19}Ca_1$, Fe_3Mn_7 (PDF# 01-071-8284) and Fe_8Mn_2 (PDF# PDF# 01-071-8284) and pure Fe for the $Fe_{20}Mg_{20}Mn_{15}Ca_5$ alloy powder. Thin layer samples were prepared by PLD on glass for 30 minutes from the $Fe_{20}Mg_{20}Mn_{15}Ca_5$ partially amorphous target. Again, the higher Ca containing composition was selected due to the likely higher expected cytocompatibility and better corrosion characteristics that would be expected similar to the Fe-Mg-Ca system discussed earlier. Glancing angle XRD analysis was performed on this deposited layer, shown in Figure 5.1(b). This figure also shows that the as-deposited thin layer is predominantly amorphous with a small amount of unreacted Fe.

Figure 5.12 presented the Magnetization (hysteresis) curves of as milled powder corresponding to the nominal composition $Fe_{60}Mg_{20}Mn_{20-x}Ca_x$ powder (x = 0, 1, 5) and SS316L alloy. Compared to SS316L alloy, the as dry milled $Fe_{60}Mg_{35}Mn_{15}Ca_5$ shows a higher value of M/H slopes with high M_s value due to the formation of pure Fe as shown in Figure 5.11. This is a typical ferromagnetic behavior. This trend can be interpreted that nonmagnetic phase (x=0 or 1) disappear or transfer to the ferrite phase with increasing Ca content.

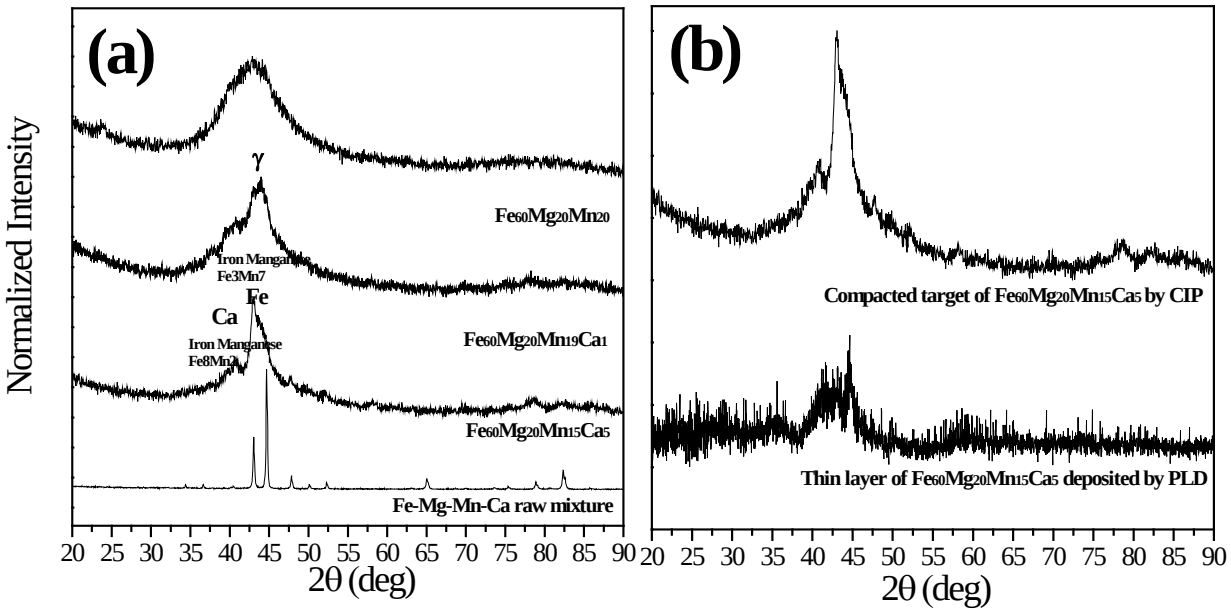

Figure 5.11. The X-ray diffraction patterns of (a) $Fe_{60}Mg_{20}Mn_{20-x}Ca_x$ powder (x = 0, 1, 5) after dry and wet milling by HEMA; γ(PDF# 01-089-4185), Fe_3Mn_7 (PDF# 01-071-8284) and Fe_8Mn_2 (PDF# PDF# 01-071-8284) and (b) thin layer of $Fe_{20}Mg_{20}Mn_{15}Ca_5$ (x=5) on glass deposited for 30 minutes by PLD.

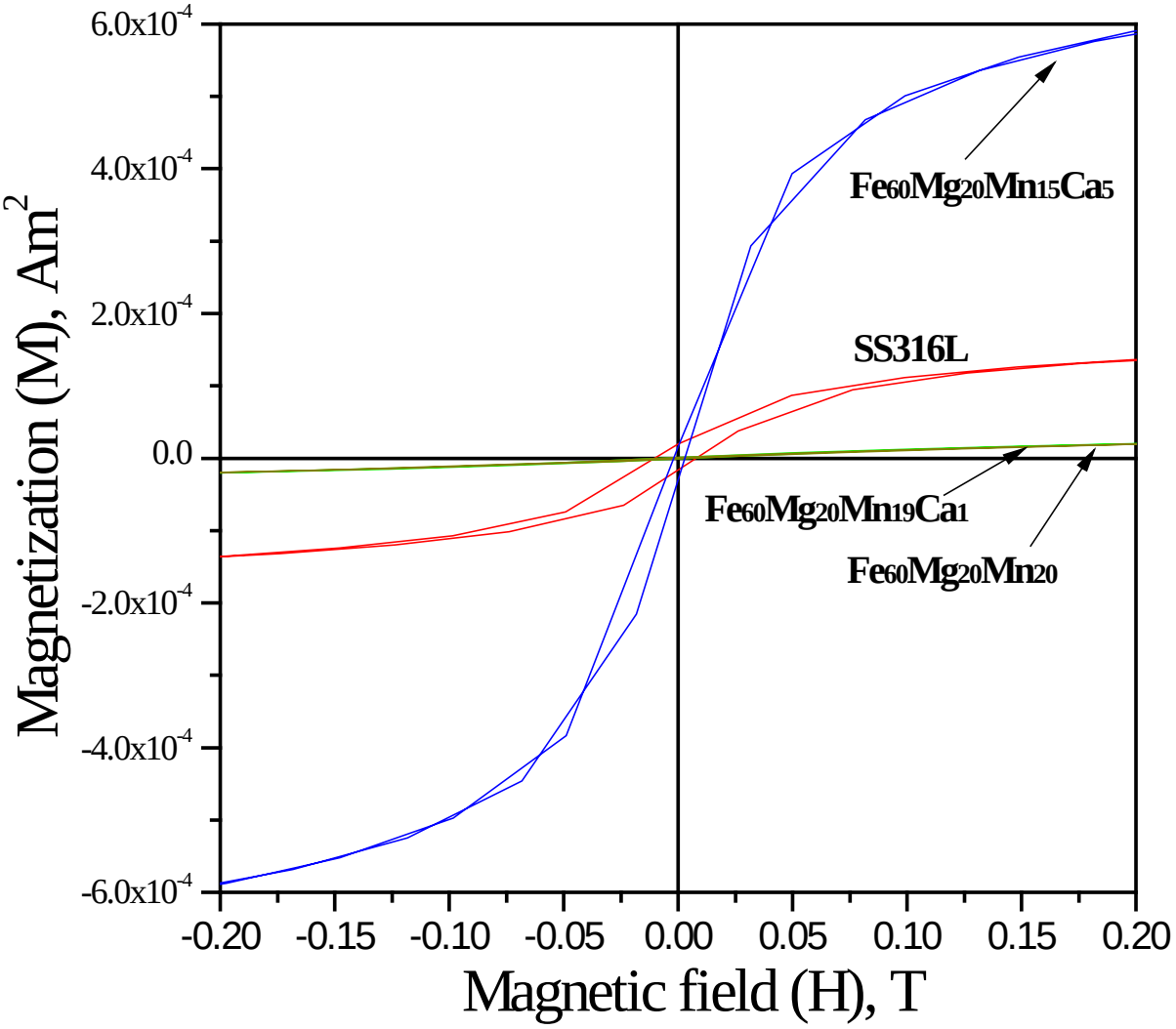

Figure 5.12. (a) M-H curves of SS316L alloy and $Fe_{60}Mg_{20}Mn_{20-x}Ca_x$ powder (x = 0, 1 and 5) after dry and wet milling by HEMA.

Potentio-dynamic polarization (PDP) curves for the thin layer of $Fe_{60}Mg_{20}Mn_{15}Ca_5$, $Fe_{60}Mg_{20}Mn_{20}$ and pure iron on glass and polished bulk pure iron can be seen in Figure 5.13 taken from representative samples of the multiple samples tested. Table 5.5 give a summary of the corrosion potential and corrosion current densities as calculated from extrapolation of the Tafel plots.

Table 5.5. Corrosion potential (E_{corr}) and current density (i_{corr}) values for $Fe_{60}Mg_{20}Mn_{15}Ca_5$ layer, both bulk and thin layer of pure iron. The corrosion current density is significantly higher for $Fe_{60}Mg_{20}Mn_{15}Ca_5$ than pure iron in layer samples *($P<0.05$)*.

Element	Corrosion potential, E_{corr}(V)	Corrosion current density. I_{corr}(μAcm^{-2})
$Fe_{60}Mg_{20}Mn_{15}Ca_5$ thin layer	**-0.599**	**18.27±2.11**
$Fe_{60}Mg_{20}Mn_{20}$ amorphous thin layer	-0.621	27.07±3.3
$Fe_{70}Mg_{30}$ amorphous thin layer	-0.642	98.76±11.08
Pure Fe (thin layer)	-0.616	12.46±2.3
Pure Fe (bulk)	-0.592	14.14±4.35

The $Fe_{60}Mg_{20}Mn_{15}Ca_5$ thin layer on glass (a) resulted in a i_{corr} value higher than both Fe thin layer of same thickness of ~1-3 microns (b) and bulk (c) Fe samples but exhibit E_{corr} values that are more anodic than $Fe_{60}Mg_{20}Mn_{20}$ and $Fe_{70}Mg_{30}$ amorphous thin layer. It can therefore be inferred from the above results that the $Fe_{60}Mg_{20}Mn_{15}Ca_5$ alloy shows no improved corrosion behavior compared to the $Fe_{60}Mg_{20}Mn_{20}$ amorphous thin layer.

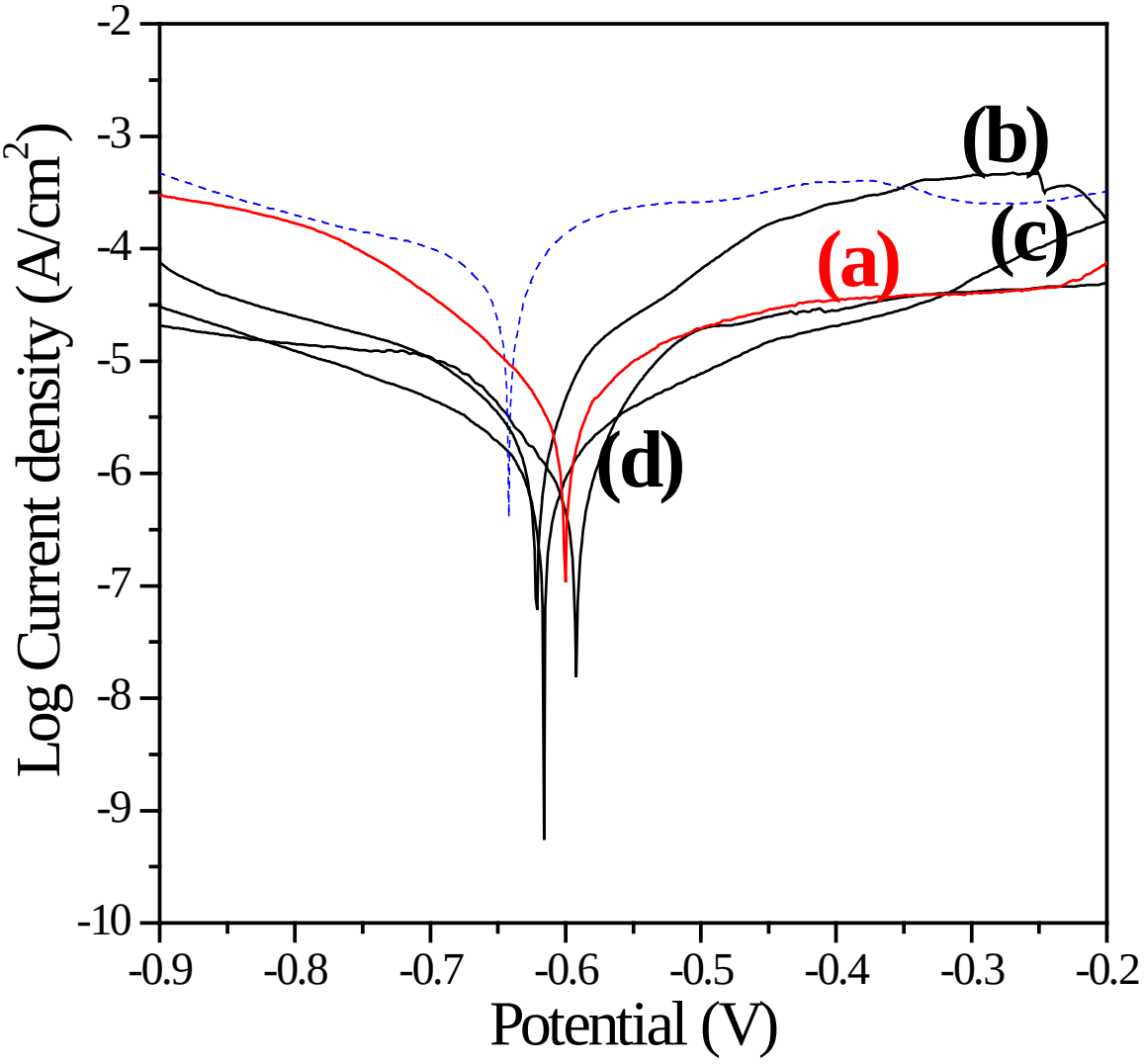

Figure 5.13. Polarization curves of (a) $Fe_{60}Mg_{20}Mn_{15}Ca_5$ amorphous thin layer, (b) $Fe_{60}Mg_{20}Mn_{20}$ amorphous thin layer, (c) pure iron thin layer on glass derived by PLD and (d) mounted bulk polished pure iron; blue dashed lines ($Fe_{70}Mg_{30}$) amorphous thin layer.

Live/Dead staining of MC3T3-E1, hMSCs, HUVECs and NIH3T3 fibroblasts cell on 1 and 3 days of post seeding on the films of $Fe_{60}Mg_{20}Mn_{15}Ca_5$ can be seen in Figure 5.14 and 5.15, respectively. Figure 5.14 shows the fluorescence microscopy images collected following live/dead assay on the amorphous thin layer and plastic tissue culture surface (control) after 1 day. For MC3T3-E1 and hMSCs cell cultures, fluorescence microscopy from the live/dead assay shows similar live cells (green) attachment with few dead cells (red) on the surface of $Fe_{60}Mg_{20}Mn_{15}Ca_5$. After 3 days of culture (Figure 5.15), $Fe_{60}Mg_{20}Mn_{15}Ca_5$ amorphous thin films, which were seeded with MC3T3-E1 and hMSCs still again displayed a similar level of living cells attached that is comparable to the tissue culture plastic used as the control, with a higher cell density than day 1. The cells were also more evenly distributed. The HUVECs also showed good cell attachment with few dead cells on the surface of $Fe_{60}Mg_{20}Mn_{15}Ca_5$ compared to the control after day1. The cells also displayed good cell attachment compared to tissue cultrue plastic even after 3 days of culture. The cells also seem to spread with relativly increased cell density compared to 1 day. NIH3T3 fibroblasts cells on the other hand, showed less live cell attachment with considerable dead cells that were largely shrunk compared to the control of tissue culture plastic after 1day. The result thus indicates inferior cell viability and proliferation on $Fe_{60}Mg_{20}Mn_{15}Ca_5$ thin layer for NIH3T3 fibroblasts cells. This is also discussed in previous Chapter 4 and seems to arise due to Mn which appears to have a high inhibition effect to the NIH3T3 fibroblast cells [75].

Figure 5.16 shows the indirect cytotoxicity results of PLD derived the $Fe_{60}Mg_{20}Mn_{15}Ca_5$ thin layer on glass performed using MC3T3-E1, hMSCs, HUVECs and NIH3T3 fibroblasts cell and the MTT assay. The MTT assay conducted with MC3T3-E1 and hMSCs with extract from

$Fe_{60}Mg_{20}Mn_{15}Ca_5$ thin layer displayed low toxicity of the alloy extract, with at least ~90% cell viability observed for all culture days. In contrast the results for HUVEC are in the range of 60% for day 1 with slight increment reaching ~65% for day 3 and day 7. Reduction in cell viability by more than 30% is considered to be a good indicator of cytotoxicity according to ISO 10993-5 [217]. Thus the alloy film considered here may be construed to be non-cytotoxic based on the response seen for MC3T3-E1 and hMSC with HUVEC indicating acceptable cytocompatibility although more detailed cell culture studies will be desired to understand the response of HUVECs. However, values of cell viability for NIH3T3 fibroblast cell in amorphous $Fe_{60}Mg_{20}Mn_{15}Ca_5$ thin layer extracts was barely below 50% after 1 day of exposure. The viabilities slightly increased for the subsequent culture days of 3 and 7 but nevertheless still remain below ~50% compared with that of the negative control after 3 and 7 days' incubation.

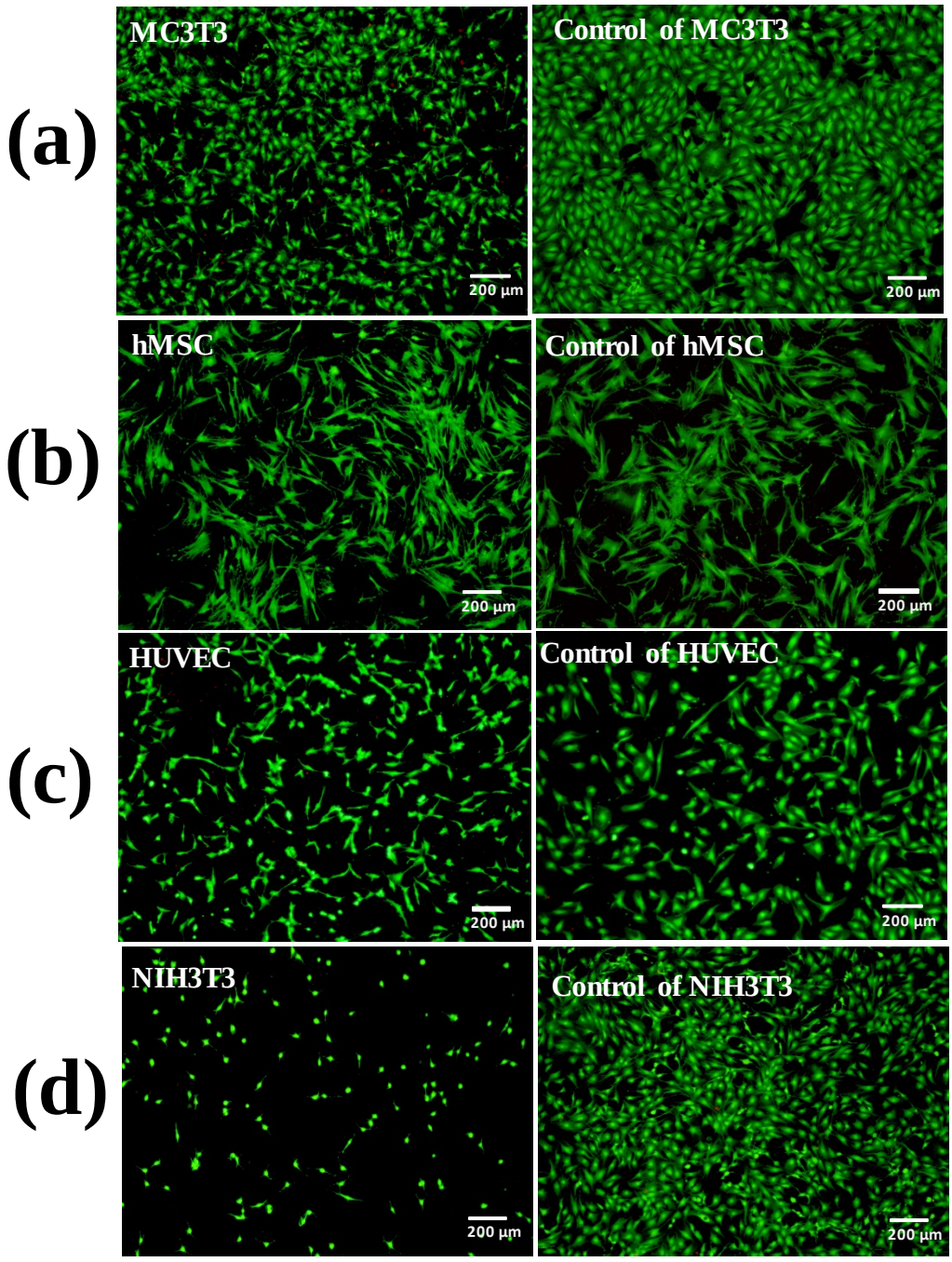

Figure 5.14**.** Live/Dead staining of (a) MC3T3 osteoblasts, (b) hMSCs, (c) HUVECs and (d) NIH3T3 fibroblasts on day 1 of culture post seeding on the thin layer of $Fe_{60}Mg_{20}Mn_{15}Ca_5$ on glass and tissue culture plastic as control.

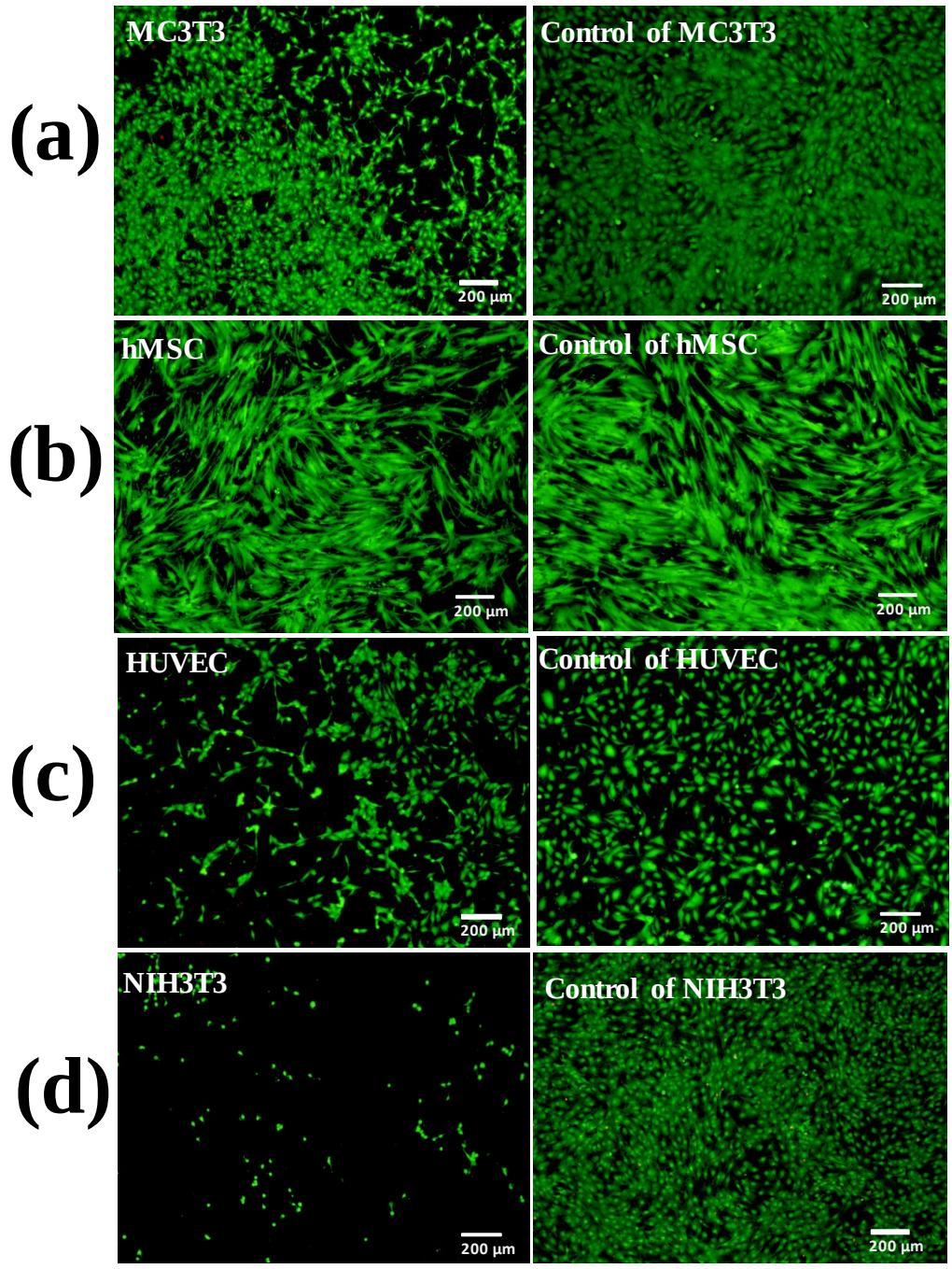

Figure 5.15**.** Live/Dead staining of (a) MC3T3 osteoblasts, (b) hMSCs, (c) HUVECs and (d) NIH3T3 fibroblasts on day 3 of culture post seeding on the thin layer of $Fe_{60}Mg_{20}Mn_{15}Ca_5$ on glass and tissue culture plastic as control.

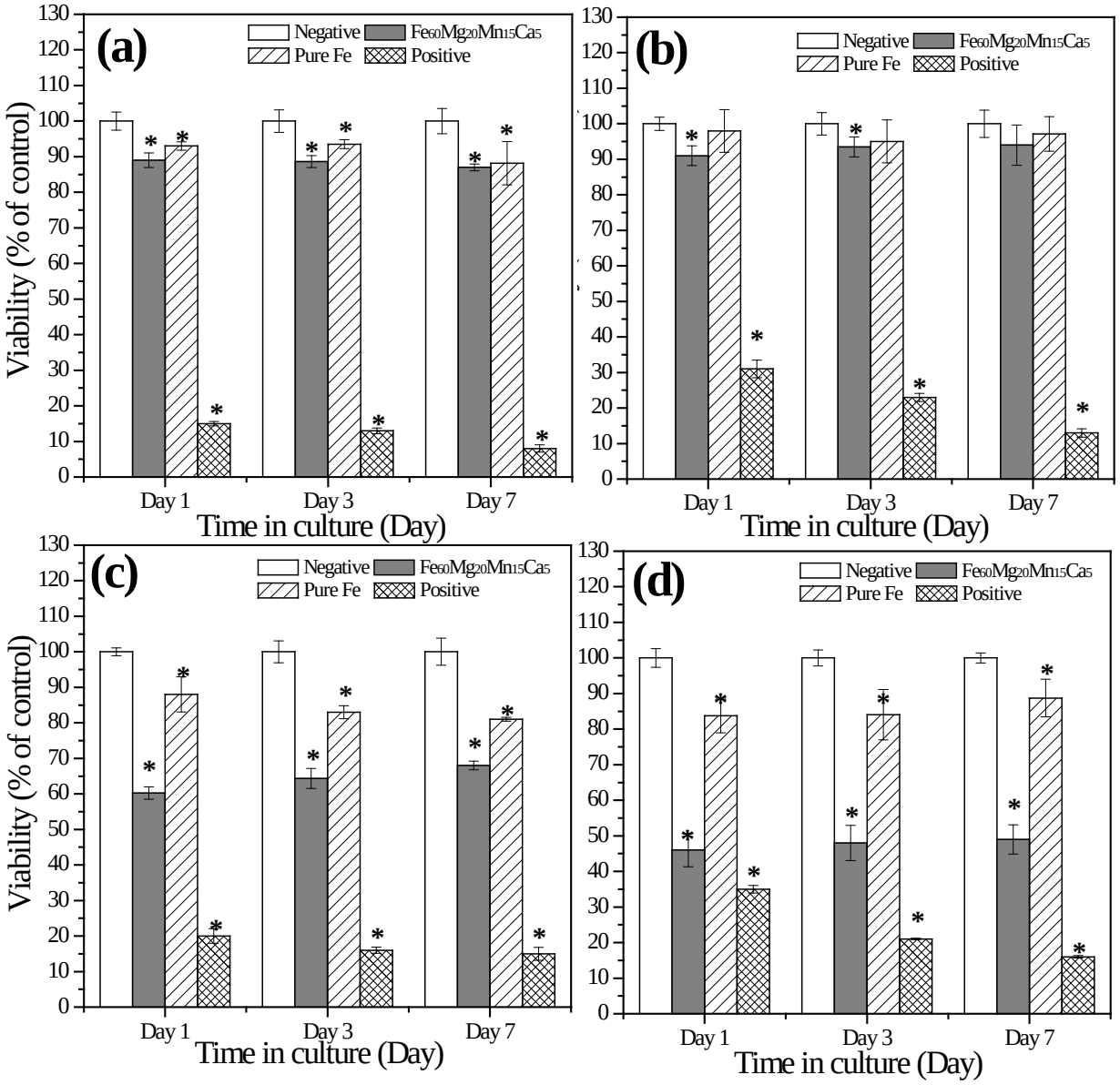

Figure 5.16. Cell viability of (a) MC3T3 osteoblasts, (b) hMSCs, (c) HUVECs and (d) NIH3T3 after 1, 3 and 7days incubation in extract medium collected after 72 hours from $Fe_{60}Mg_{20}Mn_{15}Ca_5$ and pure Fe thin layer of ~1.3μm thickness on glass. * Significant difference compared to cell viability of the negative control group ($P<0.05$).

5.3.2.2 Fe-Mg-Mn-Zr system

Figure 5.17 shows the XRD patterns for the as prepared milled powder corresponding to $Fe_{60}Mg_{20}Mn_{20-x}Zr_x$ compositions (x = 0.5, 5, 10, 15, 20). The XRD patterns of the powder for all ranges of x shows the typical broad diffraction pattern corresponding to the fully amorphous phase. Further studies were therefore focused on the $Fe_{60}Mg_{20}Mn_{10}Zr_{10}$ composition with a median value of x representing an optimal amount of Mn and Zr. Based on the studies presented earlier, it is expected that a reduction in the Mn content for this composition offset by larger amount of the more cytocompatible Zr would likely have a more favorable response to the cell viability without compromising the magnetic behavior. The XRD patterns of the starting powder, target, and the deposited films as shown in Figure 5.17 (a) and (b) corresponding to this composition all confirm the amorphous nature.

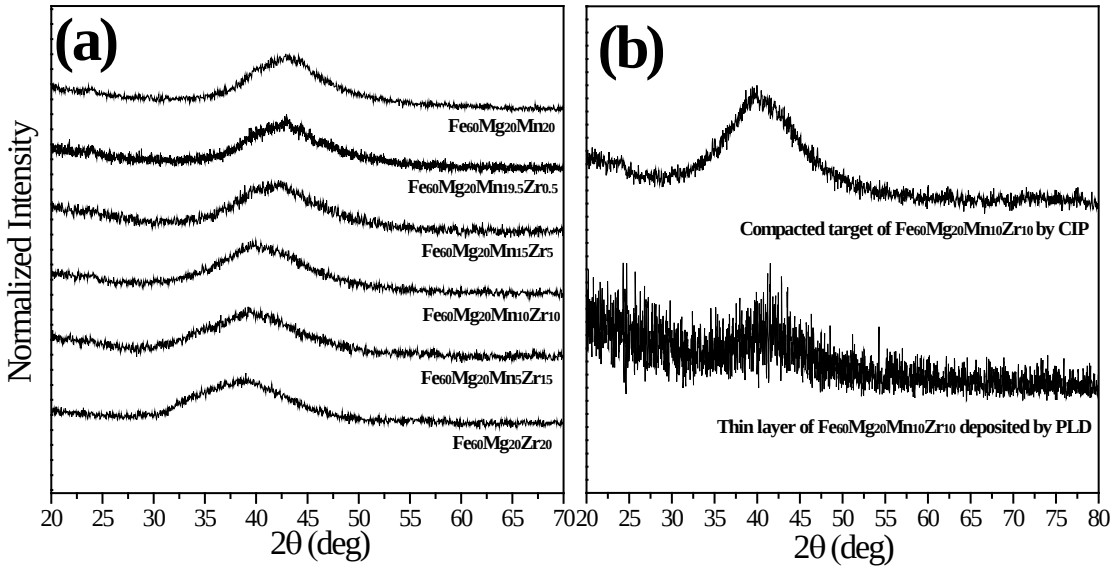

Figure 5.17. The X-ray diffraction patterns of (a) $Fe_{60}Mg_{20}Mn_{20-x}Zr_x$ powder (x = 0 ~ 20) after dry and wet milling by HEMA and (b) thin layer of $Fe_{60}Mg_{20}Mn_{10}Zr_{10}$ (x=10) on glass deposited for 30 minutes by PLD.

The hysteresis loop for $Fe_{60}Mg_{20}Mn_{20-x}Zr_x$ (x = 0 ~ 20) alloy powder after dry and wet milling is shown in Figure 5.18. All the samples exhibit almost no hysteresis compared to SS316L. In contrast to the addition of Ca discussed earlier, all the alloys exhibit non-magnetic properties. An interesting result that can be seen in this study is the formation of nonmagnetic phase without the presence of Mn in the case of $Fe_{60}Mg_{20-x}Zr_x$(x=20) which is known to be the austenite stabilizing element. To the best of the known reported work in the literature, there are few studies reported with the inclusion of Zr and the austenite phase. The few reports on Zr relate to sulfide shape control in carbon steel[246] and as an austenite grain coarsening agent[246]. This interesting result certainly prompt future work to be conducted to further study the effect of Zr as an alloying element and its influence on the magnetic properties of the Fe-Mg system.

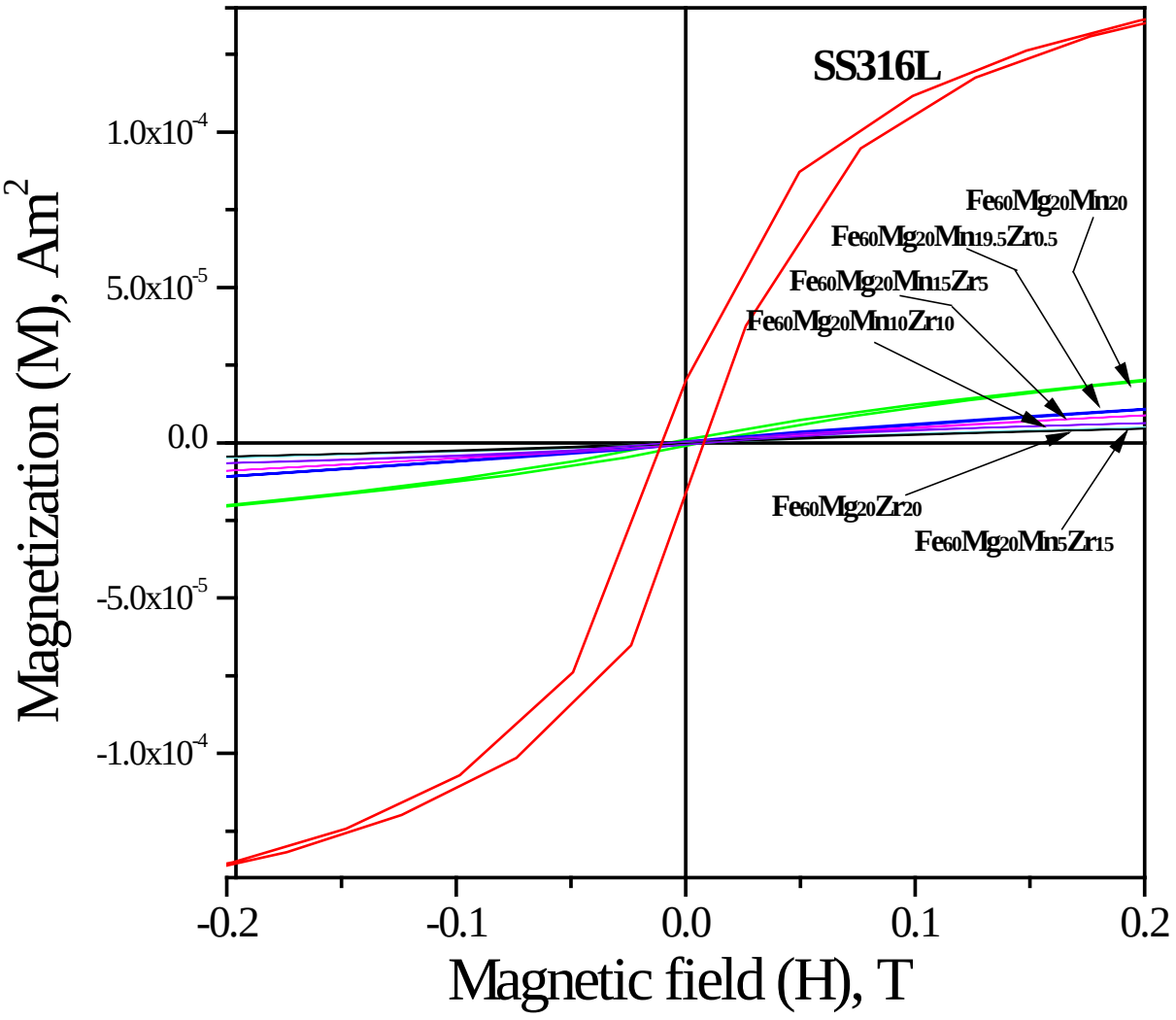

Figure 5.18. (a) M-H curves of SS316L alloy and $Fe_{60}Mg_{20}Mn_{20-x}Zr_x$ powder (x = 0~20) after subsequent wet milling by HEMA and (b) enlargement of red circle on (a) M-H curve.

Potentio-dynamic polarization curves (PDP) for the thin layer of $Fe_{60}Mg_{20}Mn_{10}Zr_{10}$ and pure iron on glass and polished bulk pure iron can be seen in Figure 5.19 as a representation of the multiple samples tested. Table 5.6 gives a summary of the corrosion potential and corrosion current densities as calculated from extrapolation of the Tafel plots. The $Fe_{60}Mg_{20}Mn_{10}Zr_{10}$ amorphous thin layer on glass (a) yields an i_{corr} value similar to that of Fe thin layer of similar thickness (~1-3 micron) (b) and bulk (c) Fe samples as well as E_{corr} values that are more cathodic indicating its lower propensity for undergoing faster degradation compared to bulk Fe and $Fe_{70}Mg_{30}$ composition.

Table 5.6. Corrosion potential (E_{corr}) and current density (i_{corr}) values for $Fe_{60}Mg_{20}Mn_{10}Zr_{10}$ layer, both bulk and thin layer of pure iron.

Element	Corrosion potential, E_{corr}(V)	Corrosion current density. I_{corr}(μAcm^{-2})
$Fe_{60}Mg_{20}Mn_{10}Zr_{10}$ thin layer	**-0.551**	**13.95±4.01**
$Fe_{60}Mg_{20}Mn_{20}$ amorphous thin layer	-0.621	27.07±3.3
Pure Fe (thin layer)	-0.616	12.46±2.3
Pure Fe (bulk)	-0.592	14.14±4.35
$Fe_{70}Mg_{30}$ amorphous thin layer	-0.642	98.76±11.08

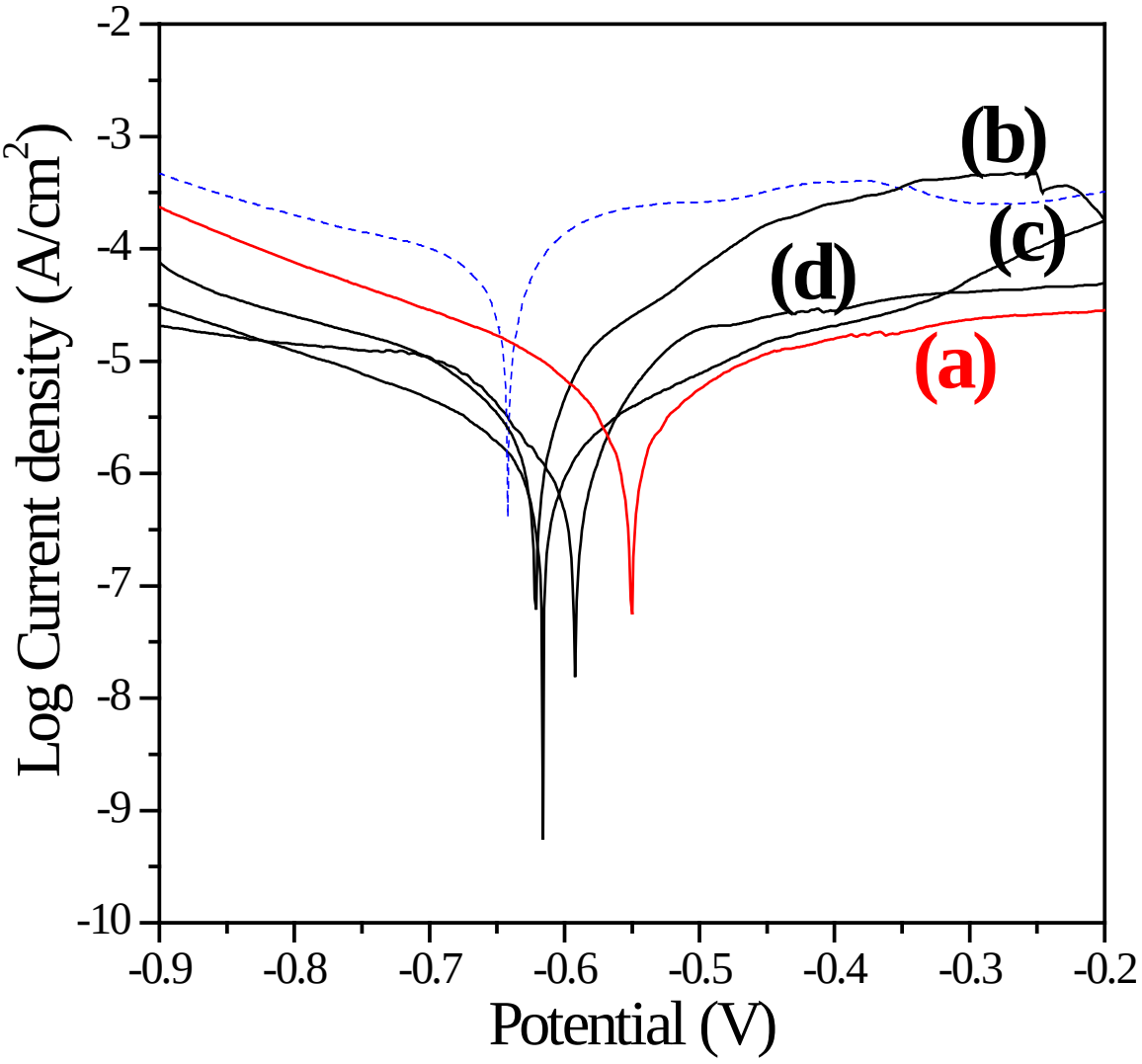

Figure 5.19. Polarization curves of (a) $Fe_{60}Mg_{20}Mn_{10}Zr_{10}$ amorphous thin layer, (b) $Fe_{60}Mg_{20}Mn_{20}$ amorphous thin layer, (c) pure iron thin layer on glass derived by PLD and (d) mounted bulk polished pure iron; blue dashed line ($Fe_{70}Mg_{30}$) amorphous thin layer.

Live/dead staining of MC3T3-E1, hMSCs, HUVECs and NIH3T3 after 1 and 3 days of post seeding on the $Fe_{60}Mg_{20}Mn_{10}Zr_{10}$ amorphous thin layer and plastic tissue culture surface (control) can be seen in Figure 5.20 and 5.21, respectively. After 1 day, for MC3T3-E1, hMSCs and HUVECs cultures, fluorescence microscopy images collected from the live/dead assay shows similar live cells (green) attachment with few dead (red) cells seen on the surface of $Fe_{60}Mg_{20}Mn_{10}Zr_{10}$ films compared to the control. After 3 days of culture (Figure 5.21), $Fe_{60}Mg_{20}Mn_{10}Zr_{10}$ amorphous thin films, which were seeded with all of MC3T3-E1, hMSCs and HUVECs still again displayed a similar level of living cell attachment, comparable to the tissue culture plastic as control, with a higher cell density than day 1. The live/dead staining indicates good cell viability and proliferation on $Fe_{60}Mg_{20}Mn_{10}Zr_{10}$ amorphous thin layer. NIH3T3 fibroblasts cells however, show lower live cell attachment with dead cells and shrunken morphology for the cells compared to the control after 1day with continued indication of reduced number of live cells attached to the thin fiom surface compared to the tissure culture plastic at day3. The live/dead staining results thus indicates relatively good cell viability and proliferationa for MC3T3-E1, hMSCs and HUVECs with some likely cytotoxicity for NIH3T3 fibroblasts cells.

To further corroborate the live/dead assay results, indirect MTT assay studies were conducted. Figure 5.22 illustrates the cell viabilities of MC3TC-E1, hMSCs, HUVECs and NIH3T3 expressed as a percentage of the viability of cell cultured in the negative control after 1, 3, and 7days incubation in 100% extraction mediums after 72 hours using the MTT assay. These quantitative results of indirect cell viability indicate good cell viability and proliferation on $Fe_{60}Mg_{20}Mn_{10}Zr_{10}$ amorphous thin layers. For 1, 3 and 7 days of culture, cell viabilities of MC3TC-E1 indicate slight variations although by and large similar to that of pure Fe. There is no significant difference ($P>0.05$) among them although there is consistently lower cell viability

compared to the negative control. Based on Figure 5.22(b) and (c), values of cell viability for hMSCs and HUVECs on 100% extracts collected over amorphous $Fe_{60}Mg_{20}Mn_{10}Zr_{10}$ show 70% after 1day of exposure. The viabilities however, slightly increased indicating values ~75% compared with that of negative control after 3 and 7 days' incubation for HUVECs and hMSCs while exhibiting ~80% or higher viabilities for HUVECs following day 3 and 7. For NIH3T3 cell however, cell viability was about 60% after 1day incubation and remained in the same range following day 3 and 7 incubation as shown in Figure 5.22(d). The MC3T3-E1 cells on the other hand displayed almost ~80% cell viability after 1day of exposure increasing to above ~90% of the negative control without extract after 7days of incubation. These results therefore indicate that the amorphous layers of $Fe_{60}Mg_{20}Mn_{10}Zr_{10}$ show good cell viability for all cells except for the NIH3T3 fibroblasts cell.

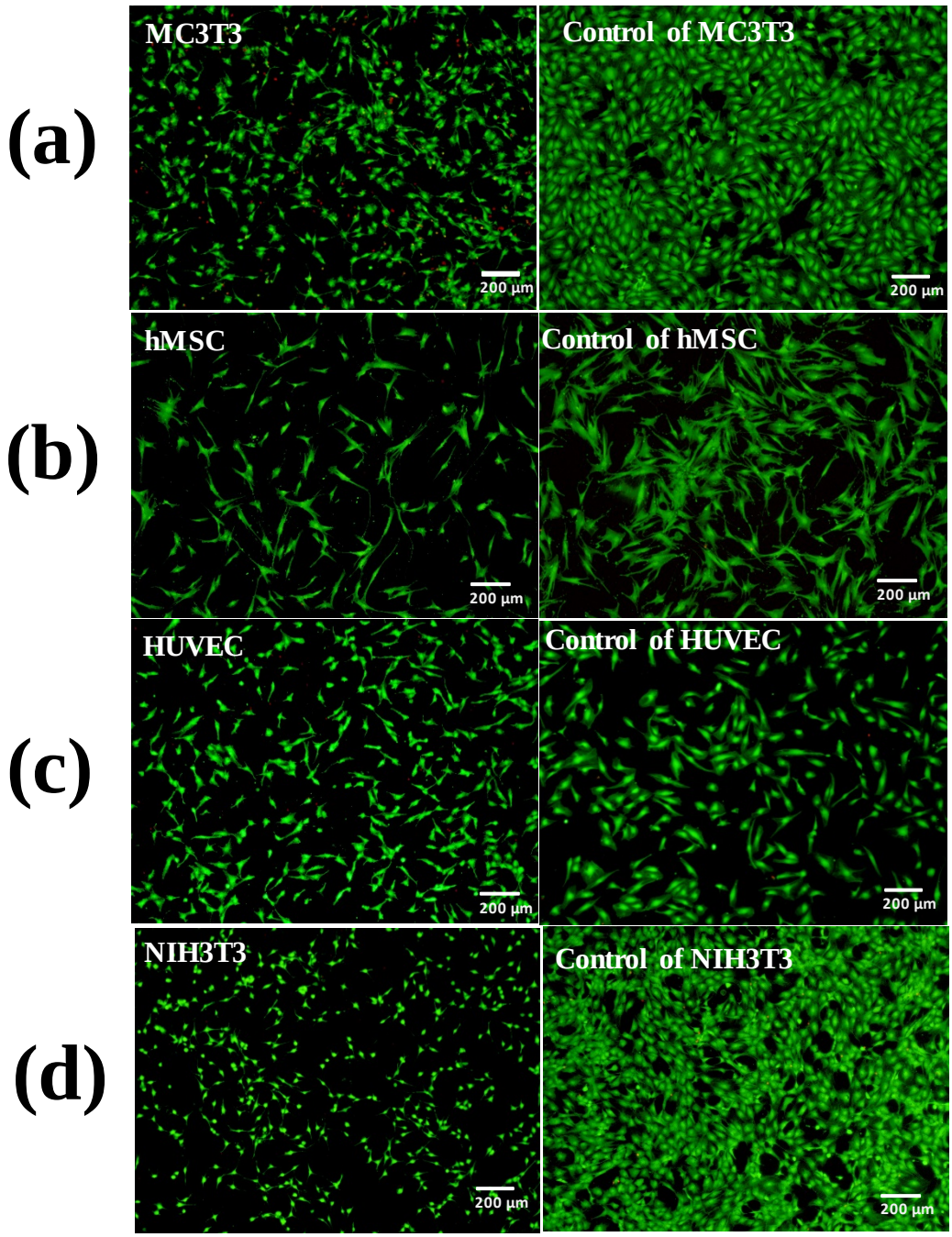

Figure 5.20**.** Live/Dead staining of (a) MC3T3 osteoblasts, (b) hMSCs, (c) HUVECs and (d) NIH3T3 fibroblasts on day 1 of culture post seeding on the thin layer of $Fe_{60}Mg_{20}Mn_{10}Zr_{10}$ on glass and tissue culture plastics as control.

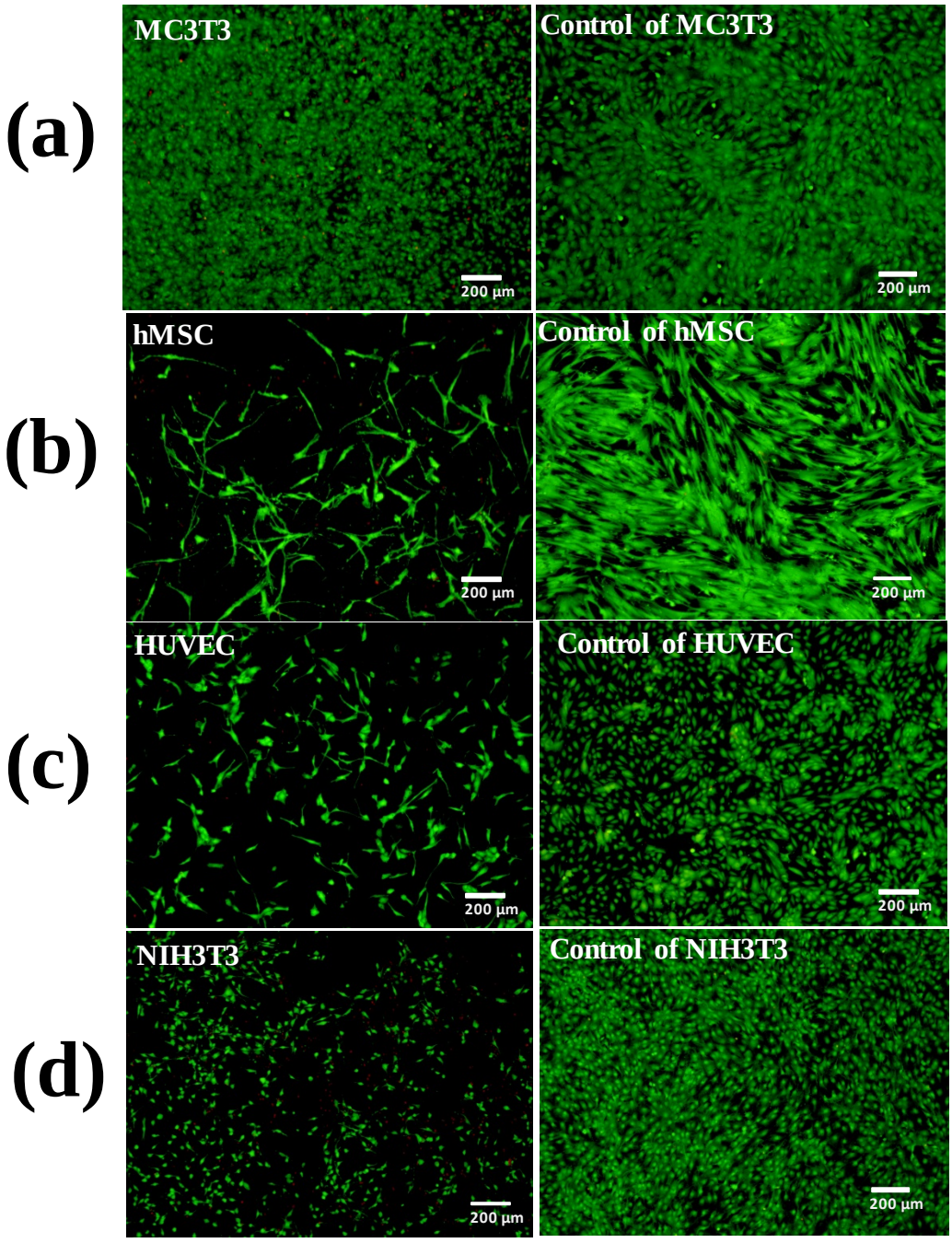

Figure 5.21**.** Live/Dead staining of (a) MC3T3 osteoblasts, (b) hMSCs, (c) HUVECs and (d) NIH3T3 fibroblasts on day 3 of culture post seeding on the thin layer of $Fe_{60}Mg_{20}Mn_{10}Zr_{10}$ on glass and tissue culture plastics as control.

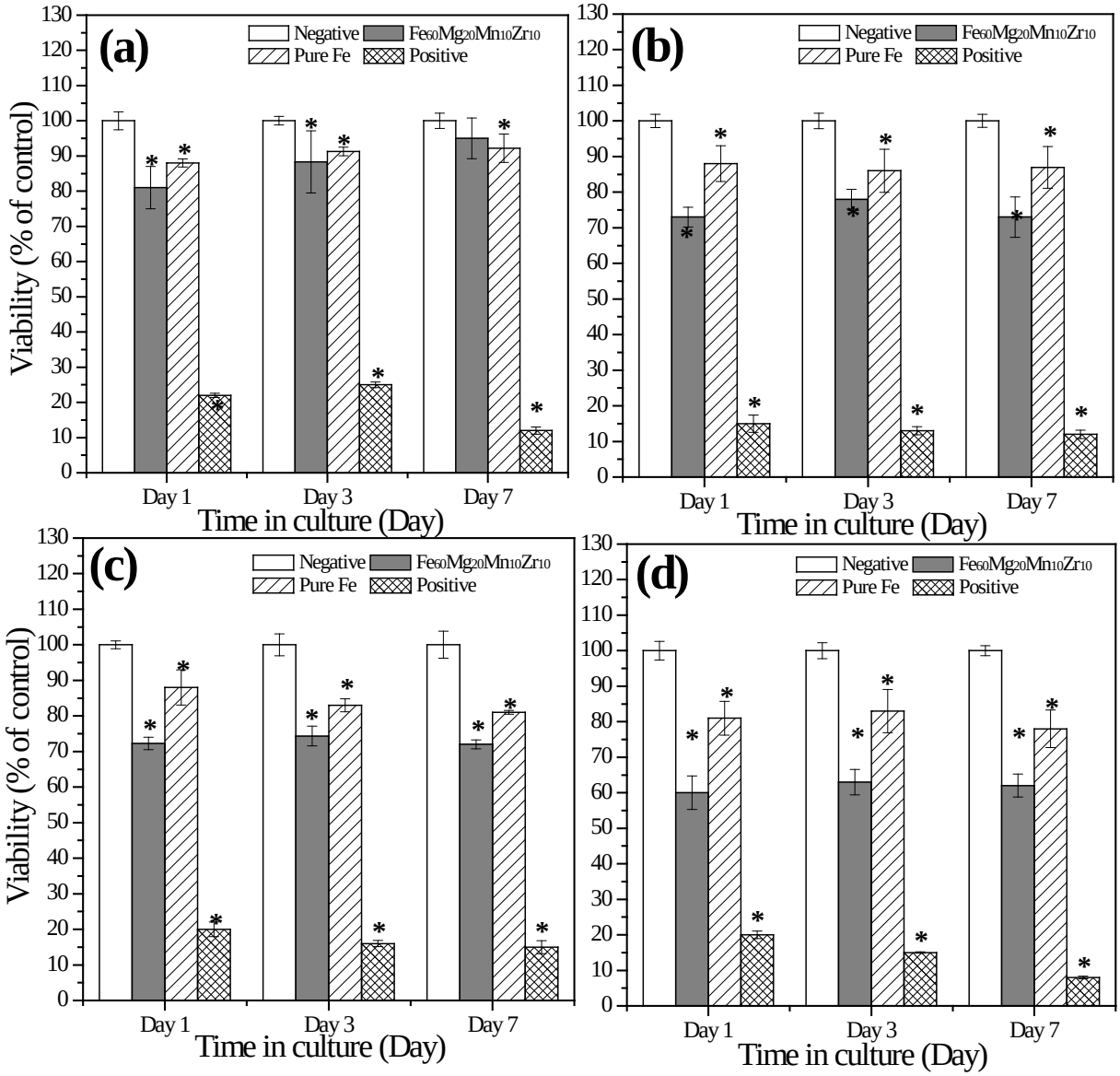

Figure 5.22. Cell viability of (a) MC3T3 osteoblasts, (b) hMSCs, (c) HUVECs and (d) NIH3T3 after 1, 3 and 7days incubation in extract medium collected after 72 hours from $Fe_{60}Mg_{20}Mn_{10}Zr_{10}$ and pure Fe thin layer of ~1.3μm thickness on glass. * Significant difference compared to cell viability of the negative control group ($P<0.05$).

5.4 CONCLUSIONS

Results of the studies discussed above indicate that addition of Ca and Zr to Fe-Mg and Fe-Mg-Mn systems can generate amorphous powders following HEMA as well as amorphous films by PLD. The in vitro effects of the alloying elements Ca and Zr on Fe-Mg and Fe-Mg-Mn alloys were also investigated. The results provide good insights into the future design of new biodegradable Fe-based alloys for use as medical device applications. The systems have been studied in terms of corrosion, magnetic properties as well as cytocompatibility.

The results indicate that by addition of Ca as an alloying element to $Fe_{70}Mg_{30}$ amorphous alloy results in the successful generation of $Fe_{70}Mg_{22}Ca_8$ thin layer by PLD from HEMA derived powders compacted to form targets of the same crystal structure and chemical composition. The powders and the films exhibit partial amorphous structures with unreacted pure Fe. The in vitro corrosion results indicate corrosion current density value was approximately 2 fold higher than pure Fe but slower compared to that of $Fe_{70}Mg_{30}$ amorphous thin layer. The direct and indirect cytotoxicity results also indicated that $Fe_{70}Mg_{22}Ca_8$ thin layer exhibits no cytotoxicity to MC3T3-E1, hMSCs, HUVECs and NIH3T3 cell lines.

Second, by adding the transition elemt, Zr to $Fe_{70}Mg_{30}$ amorphous alloy, the amorphous composition of $Fe_{70}Mg_{28}Zr_2$ thin layer was deposited by PLD. For corrosion behavior, it was determined that the composition exhibits rapid corrosion compared to pure Fe although slower compared to the $Fe_{70}Mg_{30}$ amorphous thin layer. The MTT assay conducted with all the cell lines with 100% extract from $Fe_{70}Mg_{28}Zr_2$ thin layer displayed low toxicity of the alloy extract, with at

least ~80% cell viability observed for all the three cell culture conditions of day 1, day 3 and day 7. Thus the alloys may be considered non-cytotoxic.

Third, for alloying elements Ca on $Fe_{60}Mg_{20}Mn_{20}$ amorphous alloy, $Fe_{60}Mg_{35}Mn_{15}Ca_5$ thin layer was successfully synthesized by PLD from HEMA derived powder compacted targets of the same crystal structure and chemical composition. The films exhibit partial amorphous phase and also exhibit ferromagnetic property in contrast to $Fe_{60}Mg_{20}Mn_{20}$ amorphous alloy. $Fe_{60}Mg_{35}Mn_{15}Ca_5$ thin layer nevertheless, still exhibits rapid corrosion compared to pure Fe but is lower than $Fe_{60}Mg_{20}Mn_{20}$ amorphous thin layer. The films show good cell viability results for all cells except NIH3T3 fibroblasts cell.

Finally, $Fe_{60}Mg_{20}Mn_{10}Zr_{10}$ amorphous thin layer was successfully synthesized by PLD from HEMA derived compacted powders comprising the same crystal structure and chemical composition. All the powders exhibit nonmagnetic characteristics although the corrosion behavior appears to be similar to pure Fe. The direct and indirect cytotoxicity results indicated the $Fe_{60}Mg_{20}Mn_{10}Zr_{10}$ amorphous thin layer may be considered non-cytotoxic for MC3T3-E1, hMSCs and HUVECs except for the NIH3T3 cell lines.

The results discussed above show that addition of Mn is critical to induce antiferromagnetic properties to the amorphous $Fe_{70}Mg_{30}$ system. However, cell viability appears to be variable due to the toxicity associated with Mn particularly, wit NIH3T3 and HUVEC lines. Addition of 20 at% Zr with the absence of Mn however, tends to transfer anti-ferromagnetic characteristics to the amorphous phase of $Fe_{70}Mg_{30}$ showing the potential of this system serving as a viable system that is indeed worthy of further studies.

6.0 OVERALL CONCLUSIONS AND FUTURE WORK

The dissertation study was initiated to explore the concept of generating degradable thin film systems as a means to identify potential classes of materials that could serve as degradable materials systems to be generated in the bulk. As introduced earlier in this dissertation, biodegradable metals have been widely studied. Specifically, to date, iron (Fe) and magnesium (Mg) are the two main classes of metals that have been considered as promising candidates but most of the research on Fe and Fe based alloys have reported very slow degradation rates in physiological environments while Mg and Mg based alloys exhibit rapid degradation. Many research studies have been directed to overcome these limitations as outlined in the various Chapters of this thesis. However, despite these extensive studies, the degradation rates and cytocompatibility of the two main classes of metals are still far from levels necessary for implementation in the clinic for treating various trauma, congenital as well as battlefield injuries sustained by miltary, servicemen, and the common citizens. Although Fe and Mg have been studied separately as degradable implants, there are no reports to date on the Fe-Mg binary alloy system for use as biodegradable metallic materilas due to the inherent thermodynamic immiscibility of Fe and Mg under ambient conditions. The system has therefore not been considered further due to the extremely limited solubility of Mg in Fe [72]. This hypothesis thus formed the first aim of this dissertation.

In the first aim, as described, high energy mechanical alloy(HEMA) was explored as a solution to synthesize Fe-Mg binary alloys with high Mg content. The technique of HEMA, a solid state powder processing technique, known to generate and stabilize thermodynamic non-equilibrium phases and systems was explored to identify alloys in this novel but esoteric system [122]. A variety of process parameters were modified to generate Fe-Mg alloys with varying Fe and Mg amounts, including the addition of a process control agent (PCA), milling containers, grinding media, and finally the ball to powder ratio (BPR). The alloy powders corresponding to $Fe_{100-x}Mg_x$ (x=20, 30, 45 and 50) atomic % compositions were produced by high energy mechanical alloying (HEMA). Through post dry milling and sequent wet HEMA, $Fe_{100-x}Mg_x$ (x=10, 20 and 30 at.%) alloy powders were generated in the fully amorphous state. The study reported for the first time to the best of the reported work to date exhibited the formation of solid solution of Mg in α-Fe during post dry milling which then subsequently underwent complete disorder resulting in solid state transformation to generate the amorphous phase by sequent wet milling. This amorphization process can be summarized as follows:

Mixture of elemental powders → solid solution → amorphous

Further studies were therefore focused on the $Fe_{70}Mg_{30}$ composition due to its highest Mg concentration. However, one limitation was identified to advance the study further into the next stage. In order to identify the potential use of Fe-Mg amorphous powders as possible biodegradable systems using *in vitro* characterization methods, it was deemed necessary to form bulk shapes or thin layers. It was soon realized that it is impossible to use conventional sintering method to form substrates due to the large melting temperature difference between Fe and Mg, namely, 1530°C and 650°C, respectively. Therefore, formation of thin film was considered as one of the solutions to generate dense structures of Fe-Mg alloys from the HEMA generated Fe-

Mg amorphous powders. Therefore, pulsed laser deposition (PLD) was chosen to solve the limitation of the sintering process exploiting the known attribute of PLD to generate identical composition of the target by laser ablation. It was also soon realized that with minimal modification of the PLD parameters, it was also possible to generate the amorphous state of the target in addition to maintaining identical compositions of the target. This therefore formed the theme of the dissertation work leading to the four different aims that have been outlined in the work.

In Specific Aim 2, based on the results from the pilot study conducted in the Mg-Zn-Ca system, optimal processing parameters were identified to synthesize amorphous thin film layers for PLD and applied to the Fe-Mg system to synthesize amorphous layers. Amorphous $Fe_{70}Mg_{30}$ thin layers was successfully deposited by pulsed laser deposition (PLD) from the amorphous powder in aim 1 without inducing any change in the crystal structure and chemical composition compared to target and was then subjected to in vitro assessments to determine the corrosion behavior and cytocompatibility. It was determined that the amorphous alloy films of $Fe_{70}Mg_{30}$ composition exhibited uniform corrosion and the corrosion current density value was approximately 8 fold higher than pure Fe. Furthermore, extensive *in vitro* cell studies conducted using MC3T3-E1, hMSCs, HUVECs and NIH3T3 cell lines relevant for cardiovascular and orthopedic applications demonstrated high cell viability in direct contact with these materials and in the presence of their degradation products. The combination of the degradation behavior and cytocompatibility of this novel amorphous $Fe_{70}Mg_{30}$ material render it a promising biodegradable material for further exploration for use in cardiovascular, orthopedic, and other medical devices. However, the system due to the large amount of Fe exhibits ferromagnetic properties. As introduced earlier chapter in this dissertation, this was therefore another challenge

that needed to be overcome if Fe based alloys were to be considered as biodegradable materials for various medical implant device applications. The ferromagnetic characteristics of these alloys can seriously limit magnetic resonance imaging (MRI) of Fe based alloy. Therefore, ideal alloying elements were needed to be identified to alter this natural magnetic property of Fe based systems to make Fe alloys compatible with high magnetic fields generated by MRI which has become widely used for post implantation monitoring and diagnostic testing [62]. Mn was thus considered finally as an alloying element to stabilize the austenite phase and render the system antiferromagnetic which became the focus of Specific Aim 3

The study explored the use of Mn as additional alloying element in the parent Fe-Mg alloy system following the synthesis procedures outlined in Specific Aims 1 and 2. A variety of parameters were modified to achieve the formation of Fe-Mg-Mn alloys, including the addition of varying amounts of Mn from 0 to 40 at.% and the change in process parameter for HEMA and PLD. Finally, the amorphous powder and amorphous thin film of $Fe_{60}Mg_{20}Mn_{20}$ composition were successfully generated with the desired non-magnetic property by HEMA for synthesizing the powders and PLD for generating the thin films. Based on the results, it can be seen that the amorphization process to form amorphous compositions in the $Fe_{60}Mg_{40-x}Mn_x$ (x= 20 and 25) system can be summarized as under:

Mixture of elemental powders → solid solution (α, γ) → amorphous

The $Fe_{60}Mg_{20}Mn_{20}$ amorphous thin layer on glass resulted in an i_{corr} value approximately 2 fold higher than pure Fe but the composition shows relatively slow degradation rate compared to that of $Fe_{70}Mg_{30}$ amorphous alloy which was discussed in Specific Aim 1 and 2. Preliminary *in vitro* cell viability tests also show that $Fe_{60}Mg_{20}Mn_{20}$ amorphous thin layer demonstrated good cell viability for MC3TC-E1, hMSCs and HUVEC cells with comparatively lower viability and

cytocompatibility for NIH3T3 cells due to the likely effects of higher Mn ion concentrations released when exposed to the NIH3T3 cells.

Addition of Ca and Zr as alloying elements to Fe-Mg and Fe-Mg-Mn alloys were investigated to further improve the corrosion behavior and cell viability in Specific Aim 4. Addition of Ca shows improvement in the corrosion rate compared to pure Fe but relatively slow degradation rate compared to that of $Fe_{70}Mg_{30}$ and $Fe_{60}Mg_{20}Mn_{20}$ amorphous alloy which was discussed in Specific Aim 1 – 3. Further, it was determined that there is no positive effect to alter and eliminate the magnetic properties and all compositions still exhibit the typical ferromagnetic behavior. Direct and indirect cytotoxicity results also indicate that there is no significant effect upon addition of Ca compared to the parent alloys. In the case of Zr when used as an alloying element, it was found to exhibit no deleterious effect on the cell viability compared to $Fe_{70}Mg_{30}$ and $Fe_{60}Mg_{20}Mn_{20}$ amorphous alloys. In contrast to addition of Ca, however, Fe-Mg-Mn-Zr alloys still displayed nonmagnetic behavior. Especially, an interesting result that was seen herein is the formation of nonmagnetic phase corresponding to $Fe_{60}Mg_{20}Zr_{20}$ without the presence of Mn which is known as an austenite stabilizing elements. Based on the reported literature thus far, there are few studies reported on alloys containing Zr and the austenite phase. It has been studied largely for determining and controlling sulfide shape in carbon steels[246], austenite grain coarsening [246]. Future work will be conducted to determine the specific effects of Zr as an alloying element for studying the magnetic properties.

Based on the studies conducted in this dissertation, this is the first report to demonstrate the formation of an amorphous Fe-Mg alloy, through the process of HEMA followed by PLD in order to overcome the limitations of the thermodynamic immiscibility of Fe-Mg. Through addition of Mn element, the nonmagnetic state has been achieved. Thin films of this novel

material demonstrated accelerated corrosion compared to pure Fe which is necessary for biodegradable medical applications. Furthermore, *in vitro* cell studies conducted using cell lines relevant for cardiovascular and orthopedic applications demonstrated high cell viability in direct contact with these materials and in the presence of their degradation products. However, there is still the problem to produce bulk shape eventhough thin film layer was synthesized PLD.

Future work will thus focus on pursuing additional processing methods to produce different forms of these alloys exploiting techniques such as spark plasma sintering, selective laser sintering, or viscous sintering to generate amorphous alloys. At the same time, attempts will be made to combine heat treatment following the non-conventional sintering techniques to generate biphasic or multiphasic alloys as discussed in the various Chapters 2-4 to form fast degrading systems while also exhibiting good cytocompatibility. Additionally, work will focus on generating thin coating layers on the surfaces of various materials to generate smart structures for embedding carriers to deliver growth factors, antibiotics as well as signaling molecules since surface modification is one of possible approach to overcome limitations of achieving controlled release of these various agents. Lastly, based on the studies conducted herein, attempts will be made to identify the specific effects of Zr as an alloying element for exploring the ability to impart non-magnetic properties. Generally, Mn is known to have the highest inhibition effect on NIH 3T3 fibroblast cells [75] but it is also considered an essential alloying element to remove ferromagnetic property for Fe alloys. If Zr can be added for creating and imparting antiferromagnetic properties, it can certainly create a wider alloy design space for generating degradable Fe based alloys. These studies will be hopefully conducted in the near future.

APPENDIX A

PERMISSIONS

This dissertation has text, figures and tables reprinted / reproduced with permission from a publishing company and society. The journal paper listed here has been published in print and electronic form, wherein I (Sung Jae Chung) am a co-author.

The journal paper listed below has been used in Chapter 3:

1. Chung SJ, Roy A, Hong D, Leonard JP, Kumta PN. Microstructure of Mg–Zn–Ca thin film derived by pulsed laser deposition. Materials Science and Engineering: B. 2011;176:1690-4.

BIBLIOGRAPHY

[1] Staiger MP, Pietak AM, Huadmai J, Dias G. Magnesium and its alloys as orthopedic biomaterials: A review. Biomaterials. 2006;27:1728-34.

[2] Mani G, Feldman MD, Patel D, Agrawal CM. Coronary stents: A materials perspective. Biomaterials. 2007;28:1689-710.

[3] O'Brien B, Carroll W. The evolution of cardiovascular stent materials and surfaces in response to clinical drivers: A review. Acta Biomater. 2009;5:945-58.

[4] Hänzi AC, Gunde P, Schinhammer M, Uggowitzer PJ. On the biodegradation performance of an Mg–Y–RE alloy with various surface conditions in simulated body fluid. Acta Biomater. 2009;5:162-71.

[5] Hermawan H, Moravej M, Dubé D, Fiset M, Mantovani D. Degradation behaviour of metallic biomaterials for degradable stents. Advanced Materials Research2007. p. 113-8.

[6] Hermawan H, Dubé D, Mantovani D. Development of degradable Fe-35Mn alloy for biomedical application. Advanced Materials Research2007. p. 107-12.

[7] Hermawan H, Alamdari H, Mantovani D, Dubé D. Iron-manganese: new class of metallic degradable biomaterials prepared by powder metallurgy. Powder Metallurgy. 2008;51:38-45.

[8] Ratner BD. Biomaterials science : an introduction to materials in medicine. 2nd ed. Amsterdam ; Boston: Elsevier Academic Press; 2004.

[9] Wong JY, Bronzino JD. Biomaterials. Boca Raton: CRC Press; 2007.

[10] Bruck SD. Properties of biomaterials in the physiological environment. Boca Raton, Fla.: CRC Press; 1980.

[11] Niinomi M. Recent metallic materials for biomedical applications. Metall and Mat Trans A. 2002;33:477-86.

[12] Hermawan H, Mantovani D. Degradable metallic biomaterials: the concept, current developments and future directions. Minerva Biotecnol. 2009;21:207-16.

[13] Moravej M, Mantovani D. Biodegradable Metals for Cardiovascular Stent Application: Interests and New Opportunities. International Journal of Molecular Sciences. 2011;12:4250.

[14] Nasution AK, Hermawan H. Degradable Biomaterials for Temporary Medical Implants. In: Mahyudin F, Hermawan H, editors. Biomaterials and Medical Devices: A Perspective from an Emerging Country. Cham: Springer International Publishing; 2016. p. 127-60.

[15] Habibovic P, Barrère F, Van Blitterswijk CA, de Groot K, Layrolle P. Biomimetic Hydroxyapatite Coating on Metal Implants. Journal of the American Ceramic Society. 2002;85:517-22.

[16] Lahann J, Klee D, Thelen H, Bienert H, Vorwerk D, Ho¨cker H. Improvement of haemocompatibility of metallic stents by polymer coating. J Mater Sci: Mater Med. 1999;10:443-8.

[17] Yang K, Ren Y. Nickel-free austenitic stainless steels for medical applications. Science and Technology of Advanced Materials. 2010;11:014105.

[18] Jenkins M. Biomedical Polymers: Elsevier Science; 2007.

[19] Kokubo T. Bioceramics and their Clinical Applications: Elsevier Science; 2008.

[20] Davim JP. Biomedical Composites: Materials, Manufacturing and Engineering: De Gruyter; 2014.

[21] Peuster M, Wohlsein P, Brugmann M, Ehlerding M, Seidler K, Fink C, et al. A novel approach to temporary stenting: degradable cardiovascular stents produced from corrodible metal-results 6-18 months after implantation into New Zealand white rabbits. Heart (British Cardiac Society). 2001;86:563-9.

[22] Heublein B, Rohde R, Kaese V, Niemeyer M, Hartung W, Haverich A. Biocorrosion of magnesium alloys: a new principle in cardiovascular implant technology? Heart. 2003;89:651-6.

[23] Di Mario C, Griffiths HUW, Goktekin O, Peeters N, Verbist JAN, Bosiers M, et al. Drug-Eluting Bioabsorbable Magnesium Stent. Journal of interventional cardiology. 2004;17:391-5.

[24] Gristina A. Biomaterial-centered infection: microbial adhesion versus tissue integration. Science. 1987;237:1588-95.

[25] Song G, Song S. A Possible Biodegradable Magnesium Implant Material. Adv Eng Mater. 2007;9:298-302.

[26] Zhang EL, Chen HY, Shen F. Biocorrosion properties and blood and cell compatibility of pure iron as a biodegradable biomaterial. J Mater Sci-Mater M. 2010;21:2151-63.

[27] Kirchhoff C, Braunstein V, Kirchhoff S, Sprecher CM, Ockert B, Fischer F, et al. Outcome analysis following removal of locking plate fixation of the proximal humerus. BMC Musculoskeletal Disorders. 2008;9:1-8.

[28] Chaturvedi TP. Allergy related to dental implant and its clinical significance. Clinical, Cosmetic and Investigational Dentistry. 2013;5:57-61.

[29] Sigwart U, Puel J, Mirkovitch V, Joffre F, Kappenberger L. Intravascular Stents to Prevent Occlusion and Re-Stenosis after Transluminal Angioplasty. New England Journal of Medicine. 1987;316:701-6.

[30] Arjomand H, Turi ZG, McCormick D, Goldberg S. Percutaneous coronary intervention: historical perspectives, current status, and future directions. American Heart Journal. 2003;146:787-96.

[31] Bavry AA, Kumbhani DJ, Helton TJ, Borek PP, Mood GR, Bhatt DL. Late Thrombosis of Drug-Eluting Stents: A Meta-Analysis of Randomized Clinical Trials. The American Journal of Medicine. 2006;119:1056-61.

[32] Grewe PH, Thomas D, Machraoui A, Barmeyer J, Müller KM. Coronary morphologic findings after stent implantation. American Journal of Cardiology. 2000;85:554-8.

[33] Willfort-Ehringer A, Ahmadi R, Gruber D, Gschwandtner ME, Haumer A, Haumer M, et al. Arterial remodeling and hemodynamics in carotid stents: a prospective duplex ultrasound study over 2 years. Journal of Vascular Surgery. 2004;39:728-34.

[34] Black J. Biological Performance of Materials: Fundamentals of Biocompatibility, Fourth Edition: CRC Press; 2005.

[35] Zheng YF, Gu XN, Witte F. Biodegradable metals. Materials Science and Engineering: R: Reports. 2014;77:1-34.

[36] Witte F, Hort N, Vogt C, Cohen S, Kainer KU, Willumeit R, et al. Degradable biomaterials based on magnesium corrosion. Current Opinion in Solid State and Materials Science. 2008;12:63-72.

[37] Hermawan H, Dubé D, Mantovani D. Developments in metallic biodegradable stents. Acta Biomaterialia. 2010;6:1693-7.

[38] Waizy H, Seitz J-M, Reifenrath J, Weizbauer A, Bach F-W, Meyer-Lindenberg A, et al. Biodegradable magnesium implants for orthopedic applications. J Mater Sci. 2013;48:39-50.

[39] Hermawan H. Biodegradable metals : from concept to applications. Heidelberg ; New York: Springer; 2012.

[40] Windhagen H, Radtke K, Weizbauer A, Diekmann J, Noll Y, Kreimeyer U, et al. Biodegradable magnesium-based screw clinically equivalent to titanium screw in hallux valgus surgery: short term results of the first prospective, randomized, controlled clinical pilot study. BioMedical Engineering OnLine. 2013;12:1-10.

[41] Hänzi AC, Gerber I, Schinhammer M, Löffler JF, Uggowitzer PJ. On the in vitro and in vivo degradation performance and biological response of new biodegradable Mg–Y–Zn alloys. Acta Biomater. 2010;6:1824-33.

[42] Peuster M, Hesse C, Schloo T, Fink C, Beerbaum P, von Schnakenburg C. Long-term biocompatibility of a corrodible peripheral iron stent in the porcine descending aorta. Biomaterials. 2006;27:4955-62.

[43] Nie FL, Zheng YF, Wei SC, Hu C, Yang G. In vitro corrosion, cytotoxicity and hemocompatibility of bulk nanocrystalline pure iron. Biomed Mater. 2010;5:065015.

[44] Tan L, Yu X, Wan P, Yang K. Biodegradable Materials for Bone Repairs: A Review. J Mater Sci Technol. 2013;29:503-13.

[45] Papanikolaou G, Pantopoulos K. Iron metabolism and toxicity. Toxicology and Applied Pharmacology. 2005;202:199-211.

[46] von Drygalski A, Adamson JW. Iron metabolism in man. JPEN J Parenter Enteral Nutr. 2013;37:599-606.

[47] Stubbe J, Ge J, Yee CS. The evolution of ribonucleotide reduction revisited. Trends in Biochemical Sciences. 2001;26:93-9.

[48] Fenton HJH. LXXIII.-Oxidation of tartaric acid in presence of iron. Journal of the Chemical Society, Transactions. 1894;65:899-910.

[49] Bezkorovainy A. Biochemistry of nonheme iron in man. I. Iron proteins and cellular iron metabolism. Clin Physiol Biochem. 1989;7:1-17.

[50] Ponka P, Schulman HM, Woodworth RC, Richter GW. Iron Transport and Storage: Taylor & Francis; 1990.

[51] Moravej M, Purnama A, Fiset M, Couet J, Mantovani D. Electroformed pure iron as a new biomaterial for degradable stents: In vitro degradation and preliminary cell viability studies. Acta Biomater. 2010;6:1843-51.

[52] Moravej M, Prima F, Fiset M, Mantovani D. Electroformed iron as new biomaterial for degradable stents: Development process and structure-properties relationship. Acta Biomater. 2010;6:1726-35.

[53] Waksman RON, Pakala R, Baffour R, Seabron R, Hellinga D, Tio FO. Short-Term Effects of Biocorrodible Iron Stents in Porcine Coronary Arteries. Journal of interventional cardiology. 2008;21:15-20.

[54] Zhu S, Huang N, Xu L, Zhang Y, Liu H, Sun H, et al. Biocompatibility of pure iron: In vitro assessment of degradation kinetics and cytotoxicity on endothelial cells. Materials Science and Engineering: C. 2009;29:1589-92.

[55] Siah CW, Trinder D, Olynyk JK. Iron overload. Clinica Chimica Acta. 2005;358:24-36.

[56] Kraus T, Moszner F, Fischerauer S, Fiedler M, Martinelli E, Eichler J, et al. Biodegradable Fe-based alloys for use in osteosynthesis: Outcome of an in vivo study after 52 weeks. Acta Biomater. 2014;10:3346-53.

[57] Schinhammer M, Steiger P, Moszner F, Löffler JF, Uggowitzer PJ. Degradation performance of biodegradable FeMnC(Pd) alloys. Materials Science and Engineering: C. 2013;33:1882-93.

[58] Hermawan H, Dubé D, Mantovani D. Degradable metallic biomaterials: Design and development of Fe–Mn alloys for stents. J Biomed Mater Res A. 2010;93A:1-11.

[59] Drynda A, Hassel T, Bach FW, Peuster M. In vitro and in vivo corrosion properties of new iron–manganese alloys designed for cardiovascular applications. Journal of Biomedical Materials Research Part B: Applied Biomaterials. 2015;103:649-60.

[60] Chen H, Zhang E, Yang K. Microstructure, corrosion properties and bio-compatibility of calcium zinc phosphate coating on pure iron for biomedical application. Materials Science and Engineering: C. 2014;34:201-6.

[61] Liu B, Zheng YF. Effects of alloying elements (Mn, Co, Al, W, Sn, B, C and S) on biodegradability and in vitro biocompatibility of pure iron. Acta Biomater. 2011;7:1407-20.

[62] Hermawan H, Dube D, Mantovani D. Degradable metallic biomaterials: Design and development of Fe-Mn alloys for stents. J Biomed Mater Res A. 2010;93A:1-11.

[63] Eliaz N. Degradation of Implant Materials: Springer New York; 2012.

[64] Saris N-EL, Mervaala E, Karppanen H, Khawaja JA, Lewenstam A. Magnesium: An update on physiological, clinical and analytical aspects. Clinica Chimica Acta. 2000;294:1-26.

[65] Waksman R, Erbel R, Di Mario C, Bartunek J, de Bruyne B, Eberli FR, et al. Early- and Long-Term Intravascular Ultrasound and Angiographic Findings After Bioabsorbable Magnesium Stent Implantation in Human Coronary Arteries. JACC: Cardiovascular Interventions. 2009;2:312-20.

[66] Haude M, Erbel R, Erne P, Verheye S, Degen H, Böse D, et al. Safety and performance of the drug-eluting absorbable metal scaffold (DREAMS) in patients with de-novo coronary lesions: 12 month results of the prospective, multicentre, first-in-man BIOSOLVE-I trial. The Lancet.381:836-44.

[67] Campos C, Muramatsu T, Iqbal J, Zhang Y-J, Onuma Y, Garcia-Garcia H, et al. Bioresorbable Drug-Eluting Magnesium-Alloy Scaffold for Treatment of Coronary Artery Disease. International Journal of Molecular Sciences. 2013;14:24492.

[68] Witte F, Kaese V, Haferkamp H, Switzer E, Meyer-Lindenberg A, Wirth CJ, et al. In vivo corrosion of four magnesium alloys and the associated bone response. Biomaterials. 2005;26:3557-63.

[69] Wegener B, Sievers B, Utzschneider S, Müller P, Jansson V, Rößler S, et al. Microstructure, cytotoxicity and corrosion of powder-metallurgical iron alloys for biodegradable bone replacement materials. Materials Science and Engineering: B. 2011;176:1789-96.

[70] Cheng J, Zheng YF. In vitro study on newly designed biodegradable Fe-X composites (X = W, CNT) prepared by spark plasma sintering. Journal of Biomedical Materials Research Part B: Applied Biomaterials. 2013;101B:485-97.

[71] Feng Q, Zhang D, Xin C, Liu X, Lin W, Zhang W, et al. Characterization and in vivo evaluation of a bio-corrodible nitrided iron stent. J Mater Sci: Mater Med. 2013;24:713-24.

[72] Schinhammer M, Hänzi AC, Löffler JF, Uggowitzer PJ. Design strategy for biodegradable Fe-based alloys for medical applications. Acta Biomater. 2010;6:1705-13.

[73] Liu B, Zheng YF, Ruan L. In vitro investigation of Fe30Mn6Si shape memory alloy as potential biodegradable metallic material. Mater Lett. 2011;65:540-3.

[74] Xu W, Lu X, Tan L, Yang K. Study on properties of a novel biodegradable Fe-30Mn-1C alloy. Jinshu Xuebao/Acta Metallurgica Sinica. 2011;47:1342-7.

[75] Hermawan H, Purnama A, Dube D, Couet J, Mantovani D. Fe–Mn alloys for metallic biodegradable stents: Degradation and cell viability studies. Acta Biomater. 2010;6:1852-60.

[76] Ulum MF, Arafat A, Noviana D, Yusop AH, Nasution AK, Abdul Kadir MR, et al. In vitro and in vivo degradation evaluation of novel iron-bioceramic composites for bone implant applications. Materials Science and Engineering: C. 2014;36:336-44.

[77] Huang T, Cheng J, Zheng YF. In vitro degradation and biocompatibility of Fe–Pd and Fe–Pt composites fabricated by spark plasma sintering. Materials Science and Engineering: C. 2014;35:43-53.

[78] Zhu S, Huang N, Xu L, Zhang Y, Liu H, Lei Y, et al. Biocompatibility of Fe–O films synthesized by plasma immersion ion implantation and deposition. Surface and Coatings Technology. 2009;203:1523-9.

[79] Zhu S, Huang N, Shu H, Wu Y, Xu L. Corrosion resistance and blood compatibility of lanthanum ion implanted pure iron by MEVVA. Applied Surface Science. 2009;256:99-104.

[80] Cheng J, Huang T, Zheng YF. Relatively uniform and accelerated degradation of pure iron coated with micro-patterned Au disc arrays. Materials Science and Engineering: C. 2015;48:679-87.

[81] Chen C-Z, Shi X-H, Zhang P-C, Bai B, Leng Y-X, Huang N. The microstructure and properties of commercial pure iron modified by plasma nitriding. Solid State Ionics. 2008;179:971-4.

[82] Chou D-T, Wells D, Hong D, Lee B, Kuhn H, Kumta PN. Novel processing of iron–manganese alloy-based biomaterials by inkjet 3-D printing. Acta Biomater. 2013;9:8593-603.

[83] Schaffer JE, Nauman EA, Stanciu LA. Cold-Drawn Bioabsorbable Ferrous and Ferrous Composite Wires: An Evaluation of Mechanical Strength and Fatigue Durability. Metall Mater Trans B. 2012;43:984-94.

[84] Schaffer JE, Nauman EA, Stanciu LA. Cold drawn bioabsorbable ferrous and ferrous composite wires: An evaluation of in vitro vascular cytocompatibility. Acta Biomater. 2013;9:8574-84.

[85] Walker EK, Nauman EA, Allain JP, Stanciu LA. An in vitro model for preclinical testing of thrombogenicity of resorbable metallic stents. J Biomed Mater Res A. 2014:n/a-n/a.

[86] Cheng J, Huang T, Zheng YF. Microstructure, mechanical property, biodegradation behavior, and biocompatibility of biodegradable Fe–Fe2O3 composites. J Biomed Mater Res A. 2014;102:2277-87.

[87] Schinhammer M, Pecnik CM, Rechberger F, Hänzi AC, Löffler JF, Uggowitzer PJ. Recrystallization behavior, microstructure evolution and mechanical properties of biodegradable Fe–Mn–C(–Pd) TWIP alloys. Acta Materialia. 2012;60:2746-56.

[88] Wang YB, Li HF, Zheng YF, Li M. Corrosion performances in simulated body fluids and cytotoxicity evaluation of Fe-based bulk metallic glasses. Materials Science and Engineering: C. 2012;32:599-606.

[89] Mohd Daud N, Sing NB, Yusop AH, Abdul Majid FA, Hermawan H. Degradation and in vitro cell–material interaction studies on hydroxyapatite-coated biodegradable porous iron for hard tissue scaffolds. Journal of Orthopaedic Translation. 2014;2:177-84.

[90] Huang T, Cheng J, Bian D, Zheng Y. Fe–Au and Fe–Ag composites as candidates for biodegradable stent materials. Journal of Biomedical Materials Research Part B: Applied Biomaterials. 2015:n/a-n/a.

[91] Haynes WM. CRC Handbook of Chemistry and Physics, 96th Edition: CRC Press; 2015.

[92] Revie RW, Uhlig HH. Corrosion and corrosion control : an introduction to corrosion science and engineering. 4th ed. Hoboken, N.J.: Wiley-Interscience; 2008.

[93] Kawashima A, Asami K, Hashimoto K. EFFECT OF MANGANESE ON THE CORROSION BEHAVIOR OF CHROMIUM-BEARING AMORPHOUS METAL-METALLOID ALLOYS. Science Reports of the Research Institutes, Tohoku University, Series A: Physics, Chemistry and Metallurgy. 1981;29:276-83.

[94] Vargel C. Corrosion of aluminium. 1st ed. Amsterdam ; Boston: Elsevier; 2004.

[95] Haynes WM. CRC Handbook of Chemistry and Physics, 93rd Edition: Taylor & Francis; 2012.

[96] Nayeb-Hashemi AA, Clark JB, Swartzendruber LJ. The Fe−Mg (Iron-Magnesium) system. Bulletin of Alloy Phase Diagrams. 1985;6:235-8.

[97] Haitani T, Tamura Y, Motegi T, Kono N, Tamehiro H. Solubility of iron in pure magnesium and cast structure of Mg - Fe alloy. Materials Science Forum2003. p. 697-702.

[98] Boer FRd. Cohesion in metals : transition metal alloys. Amsterdam ; New York

New York, N.Y., U.S.A.: North-Holland ;

Sole distributors for the U.S.A. and Canada, Elsevier Scientific Pub. Co.; 1988.

[99] Cahn RW, Haasen P. Physical metallurgy. 4th, rev. and enhanced ed. Amsterdam ; New York: North-Holland; 1996.

[100] Dorofeev GA, Elsukov EP, Ul'yanov AL. Mechanical alloying of immiscible elements in the Fe-Mg system. Inorganic Materials. 2004;40:690-9.

[101] Yelsukov EP, Dorofeev GA, Ulyanov AL. Mechanism and kinetics of mechanical alloying in an immiscible Fe-Mg system. Czechoslovak Journal of Physics. 2005;55:913-21.

[102] Hightower A, Fultz B, Bowman Jr RC. Mechanical alloying of Fe and Mg. Journal of Alloys and Compounds. 1997;252:238-44.

[103] Dubrovinskaia N, Dubrovinsky L, McCammon C. Iron-magnesium alloying at high pressures and temperatures. Journal of Physics Condensed Matter. 2004;16:S1143-S50.

[104] Michaelsen C, Gente C, Bormann R. The thermodynamics of amorphous phases in immiscible systems: The example of sputter-deposited Nb–Cu alloys. Journal of Applied Physics. 1997;81:6024-30.

[105] Gente C, Oehring M, Bormann R. Formation of thermodynamically unstable solid solutions in the Cu-Co system by mechanical alloying. Physical Review B. 1993;48:13244-52.

[106] Xu J, Herr U, Klassen T, Averback RS. Formation of supersaturated solid solutions in the immiscible Ni–Ag system by mechanical alloying. Journal of Applied Physics. 1996;79:3935-45.

[107] Ma E, Atzmon M. Phase transformations induced by mechanical alloying in binary systems. Materials Chemistry & Physics. 1995;39:249-67.

[108] Shaikh MA, Iqbal M, Akhter JI, Ahmad M, Zaman Q, Akhtar M, et al. Alloying of immiscible Ge with Al by ball milling. Mater Lett. 2003;57:3681-5.

[109] Al-Aqeeli N, Hussein MA, Suryanarayana C. Phase evolution during high energy ball milling of immiscible Nb–Zr alloys. Advanced Powder Technology. 2015;26:385-91.

[110] Zhu M, Che XZ, Li ZX, Lai JKL, Qi M. Mechanical alloying of immiscible Pb-Al binary system by high energy ball milling. J Mater Sci. 1998;33:5873-81.

[111] Zhu M, Li BL, Gao Y, Li L, Luo KC, Sui HX, et al. Microstructure characteristics of nanophase composite synthesized by mechanical alloying of immiscible Pb-Al and Fe-Cu systems. Scripta Materialia. 1997;36:447-53.

[112] Xu J, Herr U, Klassen T, Averback RS. Formation of supersaturated solid solutions in the immiscible Ni-Ag system by mechanical alloying. Journal of Applied Physics. 1996;79:3935-45.

[113] Dorofeev GA, Elsukov EP. Mechanical alloying of the Fe-Pb system immiscible in the equilibrium state. Phys Metals Metallogr. 2007;103:593-9.

[114] Sakurai K, Lee CH, Kuroda N, Fukunaga T, Mizutani U. Nitrogen effect in mechanical alloying of immiscible Cu-V: Extended x-ray absorption fine structure study. Journal of Applied Physics. 1994;75:7752-5.

[115] Chien CL, Unruh KM. Magnetic properties and hyperfine interactions in concentrated Fe-Ag alloys. Physical Review B. 1983;28:1214-8.

[116] Takao M, Senno H. Insoluble binary system thin film. Journal of Magnetism and Magnetic Materials. 1983;31:949-50.

[117] Hauser JJ. Amorphous ferromagnetic Ag-X (X=Ni,Co,Gd) alloys. Physical Review B. 1975;12:5160-5.

[118] Mader S, Widmer H, apos, Heurle FM, Nowick AS. METASTABLE ALLOYS OF Cu–Co AND Cu–Ag THIN FILMS DEPOSITED IN VACUUM. Applied Physics Letters. 1963;3:201-3.

[119] Rizzo HF, Massalski TB, Nastasi M. Metastable crystalline and amorphous structures formed in the Cu-W system by vapor deposition. Metallurgical Transactions A. 1993;24:1027-37.

[120] Nastasi M, Saris FW, Hung LS, Mayer JW. Stability of amorphous Cu/Ta and Cu/W alloys. Journal of Applied Physics. 1985;58:3052-8.

[121] Suryanarayana C, Al-Aqeeli N. Mechanically alloyed nanocomposites. Progress in Materials Science. 2013;58:383-502.

[122] Suryanarayana C. Mechanical alloying and milling. Progress in Materials Science. 2001;46:1-184.

[123] Aboud T, Weiss BZ, Chaim R. Mechanical alloying of the immiscible system W-Cu. Nanostructured Materials. 1995;6:405-8.

[124] Fukunaga T, Mori M, Inou K, Mizutani U. Amorphization in an immiscible Cu-V system by mechanical alloying and structure observed by neutron diffraction. Materials Science and Engineering: A. 1991;134:863-6.

[125] Fukunaga T, Nakamura K, Suzuki K, Mizutani U. Amorphization of immiscible Cu-Ta system by mechanical alloying and its structure observation. J Non-Cryst Solids. 1990;117–118, Part 2:700-3.

[126] Lee CH, Fukunaga T, Yamada Y, Mizutani U, Okamoto H. Amorphization process induced by mechanical alloying in the immiscible Cu-Ta system. JPE. 1993;14:167-71.

[127] Al-Aqeeli N, Suryanarayana C, Hussein MA. Formation of an amorphous phase and its crystallization in the immiscible Nb–Zr system by mechanical alloying. Journal of Applied Physics. 2013;114:153512.

[128] Ashammakhi N, Rokkanen P. Absorbable polyglycolide devices in trauma and bone surgery. Biomaterials. 1997;18:3-9.

[129] Wong HM, Yeung KWK, Lam KO, Tam V, Chu PK, Luk KDK, et al. A biodegradable polymer-based coating to control the performance of magnesium alloy orthopaedic implants. Biomaterials. 2010;31:2084-96.

[130] Yang S-l, Wu Z-H, Yang W, Yang M-B. Thermal and mechanical properties of chemical crosslinked polylactide (PLA). Polymer Testing. 2008;27:957-63.

[131] Paragkumar N T, Edith D, Six J-L. Surface characteristics of PLA and PLGA films. Applied Surface Science. 2006;253:2758-64.

[132] Cai K, Yao K, Yang Z, Li X. Surface modification of three-dimensional poly(d,l-lactic acid) scaffolds with baicalin: A histological study. Acta Biomater. 2007;3:597-605.

[133] Lee CH, Singla A, Lee Y. Biomedical applications of collagen. International Journal of Pharmaceutics. 2001;221:1-22.

[134] Liu S-J, Chi P-S, Lin S-S, Ueng SW-N, Chan E-C, Chen J-K. Novel solvent-free fabrication of biodegradable poly-lactic-glycolic acid (PLGA) capsules for antibiotics and rhBMP-2 delivery. International Journal of Pharmaceutics. 2007;330:45-53.

[135] Schinhammer M, Gerber I, Hänzi AC, Uggowitzer PJ. On the cytocompatibility of biodegradable Fe-based alloys. Materials Science and Engineering: C. 2013;33:782-9.

[136] Song M-M, Song W-J, Bi H, Wang J, Wu W-L, Sun J, et al. Cytotoxicity and cellular uptake of iron nanowires. Biomaterials. 2010;31:1509-17.

[137] Wolf FI, Cittadini A. Chemistry and biochemistry of magnesium. Molecular Aspects of Medicine. 2003;24:3-9.

[138] Chrisey DB, Hubler GK. Pulsed laser deposition of thin films. New York: J. Wiley; 1994.

[139] Eason R. Pulsed laser deposition of thin films : applications-led growth of functional materials. Hoboken, N.J.: Wiley-Interscience; 2007.

[140] Krebs HU, Bremert O. Pulsed laser deposition of thin metallic alloys. Applied Physics Letters. 1993;62:2341-3.

[141] van Ingen R, Fastenau R, Mittemeijer E. Formation of crystalline AgxNi1-x solid solutions of unusually high supersaturation by laser ablation deposition. Physical Review Letters. 1994;72:3116-9.

[142] Chung SJ, Roy A, Hong D, Leonard JP, Kumta PN. Microstructure of Mg–Zn–Ca thin film derived by pulsed laser deposition. Materials Science and Engineering: B. 2011;176:1690-4.

[143] Reed-Hill RE, Abbaschian R. Physical metallurgy principles. 3rd ed. Boston: PWS-Kent Pub.; 1992.

[144] Brandes EA, Brook GB, Smithells CJ. Smithells metals reference book. 7th ed / edited by E.A. Brandes and G.B. Brook. ed. Oxford ; Boston: Butterworth-Heinemann,; 1998. p. 1 v.

[145] Schumann H. Effect of Mechanical Stresses on the Microstructure of Alloys Undergoing the Martensitic Transformation. Praktische Metallographie/Practical Metallography. 1975;12:511-25.

[146] Ishikawa Y, Endoh Y. Antiferromagnetism of γ-FeMn Alloys. Journal of Applied Physics. 1968;39:1318-9.

[147] Rabinkin A. On magnetic contributions to γ→ε phase transformations in Fe-Mn alloys. Calphad. 1979;3:77-84.

[148] Sigel A, Sigel H. Manganese and its role in biological processes. New York: Marcel Dekker; 2000.

[149] McGregor DB, Baan RA, Partensky C, Rice JM, Wilbourn JD. Evaluation of the carcinogenic risks to humans associated with surgical implants and other foreign bodies — a report of an IARC Monographs Programme Meeting. Eur J Cancer. 2000;36:307-13.

[150] Jynge P, Brurok H, Asplund A, Towart R, Refsum H, Karlsson JOG. Cardiovascular safety of MnDPDP and MnCl2. Acta Radiologica. 1997;38:740-9.

[151] Crossgrove J, Zheng W. Manganese toxicity upon overexposure. NMR in Biomedicine. 2004;17:544-53.

[152] Ilich JZ, Kerstetter JE. Nutrition in Bone Health Revisited: A Story Beyond Calcium. Journal of the American College of Nutrition. 2000;19:715-37.

[153] Rodan GA. Bone homeostasis. Proceedings of the National Academy of Sciences of the United States of America. 1998;95:13361-2.

[154] Wu A-r, Xia C-q. Study of the microstructure and mechanical properties of Mg-rare earth alloys. Materials & Design. 2007;28:1963-7.

[155] Li Y, Wen C, Mushahary D, Sravanthi R, Harishankar N, Pande G, et al. Mg–Zr–Sr alloys as biodegradable implant materials. Acta Biomater. 2012;8:3177-88.

[156] Qian M, Das A. Grain refinement of magnesium alloys by zirconium: Formation of equiaxed grains. Scripta Materialia. 2006;54:881-6.

[157] Ghali E. Corrosion Resistance of Aluminum and Magnesium Alloys: Wiley; 2010.

[158] Yamamoto A, Honma R, Sumita M. Cytotoxicity evaluation of 43 metal salts using murine fibroblasts and osteoblastic cells. Journal of Biomedical Materials Research. 1998;39:331-40.

[159] Eisenbarth E, Velten D, Müller M, Thull R, Breme J. Biocompatibility of β-stabilizing elements of titanium alloys. Biomaterials. 2004;25:5705-13.

[160] Matsuno H, Yokoyama A, Watari F, Uo M, Kawasaki T. Biocompatibility and osteogenesis of refractory metal implants, titanium, hafnium, niobium, tantalum and rhenium. Biomaterials. 2001;22:1253-62.

[161] Witte F, Fischer J, Nellesen J, Crostack H-A, Kaese V, Pisch A, et al. In vitro and in vivo corrosion measurements of magnesium alloys. Biomaterials. 2006;27:1013-8.

[162] Kannan MB, Raman RKS. In vitro degradation and mechanical integrity of calcium-containing magnesium alloys in modified-simulated body fluid. Biomaterials. 2008;29:2306-14.

[163] Gu X, Zheng Y, Cheng Y, Zhong S, Xi T. In vitro corrosion and biocompatibility of binary magnesium alloys. Biomaterials. 2009;30:484-98.

[164] Gu X, Zheng Y, Zhong S, Xi T, Wang J, Wang W. Corrosion of, and cellular responses to Mg–Zn–Ca bulk metallic glasses. Biomaterials. 2010;31:1093-103.

[165] Song GL, Atrens A. Understanding magnesium corrosion - A framework for improved alloy performance. Adv Eng Mater. 2003;5:837-58.

[166] Seelig MG. A study of magnesium wire as an absorbable suture and ligature material. Archives of Surgery. 1924;8:669-80.

[167] Witte F. The history of biodegradable magnesium implants: A review. Acta Biomaterialia. 2010;6:1680-92.

[168] Waksman R, Pakala R, Baffour R, Seabron R, Hellinga D, Tio FO. Short-term effects of biocorrodible iron stents in porcine coronary arteries. Journal of interventional cardiology. 2008;21:15-20.

[169] Louidi S, Bentayeb FZ, Tebib W, Suñol JJ, Mercier AM, Grenèche JM. Amorphisation of Cr–10Co mixture by mechanical alloying. J Non-Cryst Solids. 2010;356:1052-6.

[170] Crivello JC, Nobuki T, Kuji T. Limits of the Mg–Al γ-phase range by ball-milling. Intermetallics. 2007;15:1432-7.

[171] Pabi SK, Manna I, Murty BS. Alloying behaviour in nanocrystalline materials during mechanical alloying. Bull Mater Sci. 1999;22:321-7.

[172] Yoneda Y, Abe H, Ohshima T, Uchida H. Phase transformation of Mg–Fe alloys. Journal of Applied Physics. 2010;107:-.

[173] Lü L, Lai MO. Mechanical Alloying: Springer US; 2013.

[174] Cullity BD, Stock SR. Elements of X-ray Diffraction: Prentice Hall; 2001.

[175] Klug HP, Alexander LE. X-Ray Diffraction Procedures: For Polycrystalline and Amorphous Materials: Wiley; 1974.

[176] Novel materials synthesis by mechanical alloying/milling. International Materials Reviews. 1998;43:101-41.

[177] Suryanarayana C. Mechanical Alloying And Milling: CRC Press; 2004.

[178] El-Eskandarany MS. Thermally assisted and mechanically driven solid-state reactions for formation of amorphous AI33Ta67 alloy powders. Metall and Mat Trans A. 1996;27:3267-78.

[179] Suryanarayana C, Chen G-H, Frefer A, Froes FH. Structural evolution of mechanically alloyed Ti-Al alloys. Materials Science and Engineering: A. 1992;158:93-101.

[180] Fecht HJ, Han G, Fu Z, Johnson WL. Metastable phase formation in the Zr-Al binary system induced by mechanical alloying. Journal of Applied Physics. 1990;67:1744-8.

[181] P S Gilman a, Benjamin JS. Mechanical Alloying. Annual Review of Materials Science. 1983;13:279-300.

[182] Dorofeev GA, Yelsukov EP, Ulyanov AL, Konygin GN. Thermodynamic simulation of mechanically alloyed solid solution formation in Fe-Sn system. Mater Sci Forum. 2000;343-3:585-90.

[183] Bansal C, Gao ZQ, Hong LB, Fultz B. Phases and phase stabilities of Fe3X alloys (X=Al, As, Ge, In, Sb, Si, Sn, Zn) prepared by mechanical alloying. Journal of Applied Physics. 1994;76:5961-6.

[184] Greenwood NN, Earnshaw A. Chemistry of the Elements: Elsevier Science; 2012.

[185] Egami T. The atomic structure of aluminum based metallic glasses and universal criterion for glass formation. J Non-Cryst Solids. 1996;205–207, Part 2:575-82.

[186] Chakk Y, Berger S, Weiss BZ, Brook-Levinson E. Solid state amorphization by mechanical alloying-An atomistic model. Acta Metallurgica et Materialia. 1994;42:3679-85.

[187] Miracle DB, Senkov ON. Topological criterion for metallic glass formation. Materials Science and Engineering: A. 2003;347:50-8.

[188] Egami T, Waseda Y. Atomic size effect on the formability of metallic glasses. J Non-Cryst Solids. 1984;64:113-34.

[189] Cotell CM, Chrisey DB, Grabowski KS, Sprague JA, Gossett CR. Pulsed laser deposition of hydroxylapatite thin films on Ti-6Al-4V. J Appl Biomater. 1992;3:87-93.

[190] Baeri P, Torrisi L, Marino N, Foti G. Ablation of hydroxyapatite by pulsed laser irradiation. Applied Surface Science. 1992;54:210-4.

[191] Zeng H, Lacefield WR. XPS, EDX and FTIR analysis of pulsed laser deposited calcium phosphate bioceramic coatings: the effects of various process parameters. Biomaterials. 2000;21:23-30.

[192] Combes C, Rey C. Amorphous calcium phosphates: Synthesis, properties and uses in biomaterials. Acta Biomater. 2010;6:3362-78.

[193] Stevens J, Hwang R. Strain Stabilized Alloying of Immiscible Metals in Thin Films. Physical Review Letters. 1995;74:2078-81.

[194] Nag S, Mahdak K, Devaraj A, Gohil S, Ayyub P, Banerjee R. Phase separation in immiscible silver–copper alloy thin films. J Mater Sci. 2009;44:3393-401.

[195] Dotsenko FF, Bashev VF, Ryabtsev SI, Korchak AS. Emission properties of thin-film alloys of immiscible components. Phys Metals Metallogr. 2010;110:223-8.

[196] Zhou L-p, Wang M-p, Peng K, Zhu J-j, Fu Z, Li Z. Structure characteristic and its evolution of Cu-W films prepared by dual-target magnetron sputtering deposition. Transactions of Nonferrous Metals Society of China. 2012;22:2700-6.

[197] Zberg B, Uggowitzer PJ, Loffler JF. MgZnCa glasses without clinically observable hydrogen evolution for biodegradable implants. Nat Mater. 2009;8:887-91.

[198] Bobe K, Willbold E, Morgenthal I, Andersen O, Studnitzky T, Nellesen J, et al. In vitro and in vivo evaluation of biodegradable, open-porous scaffolds made of sintered magnesium W4 short fibres. Acta Biomater. 2013;9:8611-23.

[199] Hong D, Saha P, Chou D-T, Lee B, Collins BE, Tan Z, et al. In vitro degradation and cytotoxicity response of Mg–4% Zn–0.5% Zr (ZK40) alloy as a potential biodegradable material. Acta Biomaterialia. 2013;9:8534-47.

[200] Standardization IOf. Biological Evaluation of Medical Devices- Part 12: Sample preparation and reference materials (ISO 10993-12:2012): ISO; 2012.

[201] Okunev VD, Samoilenko ZA, Svistunov VM, Abal'oshev A, Dynowska E, Gierłowski P, et al. Amorphous state and pulsed laser deposition of YBa2Cu3O7−δ thin films. Journal of Applied Physics. 1999;85:7282-90.

[202] van der Kraan AM, Buschow KHJ. 57 Mössbauer effect and magnetic properties in amorphous Fe-based alloys. Physical Review B. 1982;25:3311-8.

[203] van der Kraan AM, Buschow KHJ. Fe Mössbauer effect and magnetic properties in amorphous Fe-based alloys. Physical Review B. 1982;25:3311-8.

[204] Sahoo B, Keune W, Sturhahn W, Toellner TS, Alp EE. Atomic vibrational dynamics of amorphous Fe–Mg alloy thin films. Journal of Physics and Chemistry of Solids. 2005;66:2263-70.

[205] Sahoo B, Keune W, Schuster E, Sturhahn W, Toellner TS, Alp EE. Amorphous Fe–Mg alloy thin films: magnetic properties and atomic vibrational dynamics. Hyperfine Interact. 2006;168:1185-90.

[206] Yano T, Ooze T, Yoneda M, Katsumura M. Amorphous alloy films deposited by excimer laser ablation using sintered Ta-Ni targets. J Mater Sci Lett. 1996;15:1994-6.

[207] Munir ZA, Anselmi-Tamburini U, Ohyanagi M. The effect of electric field and pressure on the synthesis and consolidation of materials: A review of the spark plasma sintering method. J Mater Sci. 2006;41:763-77.

[208] Singh A, Harimkar SP. Spark plasma sintering of in situ and ex situ iron-based amorphous matrix composites. Journal of Alloys and Compounds. 2010;497:121-6.

[209] Fischer P, Blatter A, Romano V, Weber HP. Selective laser sintering of amorphous metal powder. Applied Physics A. 2005;80:489-92.

[210] Scherer GW. Viscous Sintering under a Uniaxial Load. Journal of the American Ceramic Society. 1986;69:C-206-C-7.

[211] Atkins P, de Paula J. Atkins' Physical Chemistry: OUP Oxford; 2010.

[212] Haynes WM. CRC Handbook of Chemistry and Physics, 94th Edition: CRC Press; 2016.

[213] Landolt D. Corrosion and Surface Chemistry of Metals: EFPL Press; 2007.

[214] Shaw BA. Corrosion Resistance of Magnesium Alloys. ASM International. 2003;13A.

[215] Contreras RG, Vilchis JRS, Sakagami H, Nakamura Y, Nakamura Y, Hibino Y, et al. Type of cell death induced by seven metals in cultured mouse osteoblastic cells. In Vivo. 2010;24:507-12.

[216] Sauvant MP, Pepin D, Bohatier J, Groliere CA, Guillot J. Toxicity Assessment of 16 Inorganic Environmental Pollutants by Six Bioassays. Ecotoxicology and Environmental Safety. 1997;37:131-40.

[217] Standardization IOf. Biological Evaluation of Medical Devices - Part 5: Tests for in Vitro Cytotoxicity (ISO 10993-5:2009): ISO; 2009.

[218] Francis A, Yang Y, Virtanen S, Boccaccini AR. Iron and iron-based alloys for temporary cardiovascular applications. J Mater Sci: Mater Med. 2015;26:1-16.

[219] Dichek DA, Neville RF, Zwiebel JA, Freeman SM, Leon MB, Anderson WF. Seeding of intravascular stents with genetically engineered endothelial cells. Circulation. 1989;80:1347-53.

[220] Flint GN. A metallurgical approach to metal contact dermatitis. Contact Dermatitis. 1998;39:213-21.

[221] Romani A. Regulation of magnesium homeostasis and transport in mammalian cells. Archives of Biochemistry and Biophysics. 2007;458:90-102.

[222] Zhang J, Kong N, Shi Y, Niu J, Mao L, Li H, et al. Influence of proteins and cells on in vitro corrosion of Mg–Nd–Zn–Zr alloy. Corrosion Science. 2014;85:477-81.

[223] Zhao N, Zhu D. Endothelial responses of magnesium and other alloying elements in magnesium-based stent materials. Metallomics. 2015;7:118-28.

[224] Daeho Hong, Da-Tren Chou, Oleg I. Velikokhatnyi, Abhijit Roy, Boeun Lee, Isaac Swink, et al. Binder-jetting 3D printing and alloy development of biodegradable Fe-Mn-Ca/Mg alloys for patient-specific cranio-maxillofacial scaffolds. Acta Biomater. 2016;Under the review.

[225] Janning C, Willbold E, Vogt C, Nellesen J, Meyer-Lindenberg A, Windhagen H, et al. Magnesium hydroxide temporarily enhancing osteoblast activity and decreasing the osteoclast number in peri-implant bone remodelling. Acta Biomater. 2010;6:1861-8.

[226] Levesque J, Hermawan H, Dube D, Mantovani D. Design of a pseudo-physiological test bench specific to the development of biodegradable metallic biomaterials. Acta Biomater. 2008;4:284-95.

[227] Schömig A, Kastrati A, Mudra H, Blasini R, Schühlen H, Klauss V, et al. Four-year experience with Palmaz-Schatz stenting in coronary angioplasty complicated by dissection with threatened or present vessel closure. Circulation. 1994;90:2716-24.

[228] Hansen M, Anderko K. Constitution of binary alloys. 2d ed. New York: McGraw-Hill; 1958.

[229] Huang WM. An Assessment of the Fe-Mn System. Calphad. 1989;13:243-52.

[230] Boffetta P. Carcinogenicity of Trace-Elements with Reference to Evaluations Made by the International-Agency-for-Research-on-Cancer. Scand J Work Env Hea. 1993;19:67-70.

[231] Keen CL, Ensunsa JL, Clegg MS. Manganese metabolism in animals and humans including the toxicity of manganese. Metal ions in biological systems. 2000;37:89-121.

[232] Enayati MH, Bafandeh MR. Phase transitions in nanostructured Fe–Cr–Ni alloys prepared by mechanical alloying. Journal of Alloys and Compounds. 2008;454:228-32.

[233] Lee W, Kwun SI. The effects of process control agents on mechanical alloying mechanisms in the Ti-Al system. Journal of Alloys and Compounds. 1996;240:193-9.

[234] Shaw L, Villegas J, Luo H, Zawrah M, Miracle D. Effects of process-control agents on mechanical alloying of nanostructured aluminum alloys. Metall and Mat Trans A. 2003;34:159-70.

[235] Wang KY, Shen TD, Wang JT, Quan MX. Amorphization reaction during mechanical alloying: Influence of the milling atmospheres. Scripta Metallurgica et Materialia. 1991;25:2227-31.

[236] Maranian P. Reducing Brittle and Fatigue Failures in Steel Structures: American Society of Civil Engineers; 2010.

[237] Amini R, Shokrollahi H, Salahinejad E, Hadianfard MJ, Marasi M, Sritharan T. Microstructural, thermal and magnetic properties of amorphous/nanocrystalline FeCrMnN alloys prepared by mechanical alloying and subsequent heat treatment. Journal of Alloys and Compounds. 2009;480:617-24.

[238] Bowman AB, Kwakye GF, Herrero Hernández E, Aschner M. Role of manganese in neurodegenerative diseases. Journal of Trace Elements in Medicine and Biology. 2011;25:191-203.

[239] HaMai D, Bondy SC. Oxidative basis of manganese neurotoxicity. Annals of the New York Academy of Sciences2004. p. 129-41.

[240] HaMai D, Bondy SC. Pro- or anti-oxidant manganese: a suggested mechanism for reconciliation. Neurochemistry International. 2004;44:223-9.

[241] Reaney SH, Kwik-Uribe CL, Smith DR. Manganese oxidation state and its implications for toxicity. Chemical Research in Toxicology. 2002;15:1119-26.

[242] Chen J-Y, Tsao GC, Zhao Q, Zheng W. Differential Cytotoxicity of Mn(II) and Mn(III): Special Reference to Mitochondrial [Fe-S] Containing Enzymes. Toxicology and Applied Pharmacology. 2001;175:160-8.

[243] Auerbach M, Ballard H. Clinical Use of Intravenous Iron: Administration, Efficacy, and Safety. ASH Education Program Book. 2010;2010:338-47.

[244] Stansbury EE, Buchanan RA. Fundamentals of electrochemical corrosion. Materials Park, OH: ASM International; 2000.

[245] Lee DBN, Roberts M, Bluchel CG, Odell RA. Zirconium: Biomedical and Nephrological Applications. ASAIO Journal. 2010;56:550-6 10.1097/MAT.0b013e3181e73f20.

[246] Chai F, Yang CF, Su H, Zhang YQ, Xu Z, Yang YH. Effect of Zr addition to Ti-killed steel on inclusion formation and microstructural evolution in welding induced coarse-grained heat affected zone. Acta Metallurgica Sinica (English Letters). 2008;21:220-6.